Proceedings

Guang-Zhong Yang and Ara Darzi (Eds.)

The Hamlyn Symposium on Medical Robotics

1-2 July 2012

Imperial College London, UK

Proceedings of
The Hamlyn Symposium on Medical Robotics
1-2 July 2012, Imperial College
London, UK
ISBN: 978-0-9563776-3-0

Preface

The 5th Hamlyn Symposium on Medical Robotics was held at the Hamlyn Centre for Robotic Surgery and The Royal Geographical Society in London, UK on 1-2 July 2012.

The theme for this year's symposium was "*towards flexible access, bio-inspired design, minimized footprint, and wider clinical uptake*" with an impressive line-up of leading scientists and engineers in bio-inspired robots, and snake robots in particular, as invited speakers. The shape adaptation capability of these robotic platforms can facilitate intraluminal or extra-luminal anatomical curved pathway navigation, which will enable an expansion in applications of the current robotic systems. The speakers invited included Professor Howie Choset, Professor Pierre Dupont, and Dr Vipul Patel, who all provided insights into the cutting edge developments in this field. The keynote was delivered by Professor Shigeo Hirose, who provided an overview of "Biologically Inspired Robots: Snake-like, Spider-like Robots and Others". In addition, this year, Professor Richard Satava gave the inaugural Karl Storz-Harold Hopkins lecture on "Developing Next Generation Robots".

This year, we also introduced clinical abstracts to encourage better interaction of the engineering and clinical communities. A total of 88 papers were submitted and after systematic peer review, 52 papers from 11 countries were selected for presentation at the Symposium. The topics covered ranged from training and clinical outcomes, image guidance, planning and navigation, haptics and perceptual feedback, platform design, training and neuroergonomics, and new clinical approaches.

The Hamlyn Symposium grew out of the original Imperial College's Cross Faculty Workshops on Medical Robotics funded by the Hamlyn Centre for Robotic Surgery. We are delighted that it is now established as an annual international forum for clinicians, engineers and researchers to exchange ideas and explore new challenges and opportunities in healthcare technologies. We were delighted to see that this year senior academics and young research fellows had been working together to organize a series of workshops on topics ranging from Robotic Endovascular Interventions to Clinical Trials and Outcomes, held before and after the Symposium. These workshops provided a forum for focused discussion about specific research and clinical topics of medical robotics, as well as an informal environment for academic networking. Many of these workshops have resulted in further ongoing interactions among the participants and joint research publications.

We would like to thank both the International and Local Programme Committees, the Workshop Organising Committee and the Local Organising Committee for giving up their precious time ensuring timely review of all the papers submitted and helping to provide an excellent symposium programme. The meeting would not be possible without the commitment and hard work of a dedicated team. In particular, we are grateful to Karen Kerr, Su-Lin Lee, Sejal Jiwan, Ruzanna Gulakyan, Raphaele Raupp, Robert Merrifield, Daniel Elson, Hedyeh Rafii-Tari, Alessandro Vandini, Julia Greenwood, Alexandre Vicente, Kumuthan Sriskandarajah and Thomas Cundy for working behind the scenes and for their tireless effort in managing all aspects of the symposium organisation.

Finally, we would like to give our special thanks to Lady Hamlyn. All of this would of course, not be possible without the generous philanthropic support from both the Helen Hamlyn Trust and Lady Hamlyn herself.

It was our pleasure to welcome the Symposium attendees to London.

July 2012, London

Guang-Zhong Yang
Ara Darzi

Organisation

General and Programme Co-Chairs

Professor Guang-Zhong Yang
Lord Ara Darzi

International Programme Committee

Howie Choset	*Carnegie Mellon University, USA*
Kevin Cleary	*The Sheikh Zayed Institute, Washington, USA*
Paolo Dario	*Scuola Superiore Sant'Anna, Pisa, Italy*
Simon DiMaio	*Intuitive Surgical Inc, USA*
Pierre Dupont	*Children's Hospital Boston, USA*
Hubertus Feussner	*Technical University Munich, Germany*
Abe Fingerhut	*Centre Hospitalier Intercommunal, Poissy, France*
Gabor Fichtinger	*Queen's University, Canada*
Dennis Fowler	*Columbia University, USA*
Blake Hannaford	*University of Washington, USA*
Koji Ikuta	*Nagoya University, Japan*
Leo Joskowicz	*The Hebrew University of Jerusalem, Israel*
Jacques Marescaux	*University Hospital Strasbourg, France*
Nassir Navab	*Technical University Munich, Germany*
Bradley Nelson	*ETH Zürich, Switzerland*
Vipul Patel	*Global Robotics Institute, USA*
Cameron Riviere	*Carnegie Mellon University, USA*
Richard Satava	*University of Washington, USA*
Ichiro Sakuma	*University of Tokyo, Japan*
Lee Swanstrom	*University of Oregon, USA*
Mark Talamini	*University of California, San Diego, USA*
Russ Taylor	*Johns Hopkins University, USA*
Ashutosh Tewari	*Weill Cornell Medical College, USA*
Kirby Vosburgh	*Harvard University, USA*
Steve Wexner	*Cleveland Clinic Florida, USA*

Local Programme Committee

Kaspar Althoefer	*King's College London, UK*
Thanos Athanasiou	*Imperial College London, UK*
Colin Bicknell	*Imperial College London, UK*
Nicholas Cheshire	*Imperial College London, UK*
Prokar Dasgupta	*King's College London, UK*
Brian Davies	*Imperial College London, UK*
Daniel Elson	*Imperial College London, UK*
Leonard Fass	*GE Healthcare, UK*
Mohamad Hamady	*Imperial College London, UK*
Andreas Melzer	*Dundee University, UK*
Azad Najmaldin	*St James University Hospital, Leeds, UK*
Geoff Pegman	*RU Robotics, UK*

Reza Razavi	*King's College London, UK*
Ferdinando Rodriguez y Baena	*Imperial College London, UK*
Julian Teare	*Imperial College London, UK*
Justin Vale	*Imperial College London, UK*

Workshop/Tutorial Organising Committee

Su-Lin Lee (Chair)
Hutan Ashrafian
Daniel Leff
Erik Mayer
George Mylonas
Celia Riga
Mikael Sodergren

Local Organising Committee

Karen Kerr
Sejal Jiwan
Ruzanna Gulakyan
Raphaele Raupp

Table of Contents

Invited Papers

Biologically Inspired Robots: Snake-like, Spider-like Robots and Others 1
S. Hirose

Surgical Snake Robots: Faster, Better, Cheaper, and in Control 2
H. Choset

Concentric Tube Robots for Minimally Invasive Surgery 3
P.E. Dupont, A. Gosline, N. Vasilyev, J. Lock, E. Butler, C. Folk, A. Cohen, A. Veeramani, M. Wu, G. Schmitz, R. Chen, P. del Nido

A Decade of Robotic Surgery: Past, Present and Future 5
V.R. Patel

Developing Next Generation Robots 7
R.M. Satava

Training and Clinical Outcomes

The Impact of Trainees on Surgical Outcomes following Robotic Assisted Radical Prostatectomy (RARP)...... 9
L.-S. Lee, G.L. Shaw, D.E. Neal, N. Shah

Short and Long Term Complications of Robotic Abdominal Surgery in Children 11
N. Gattas, C. Smith, N. Alizai, C. Van Wyk, J. Sellors, S. Whiteley, A. Najmaldin

A New Global Ratings Scale for Assessing Virtual Reality Arthroscopy Simulator Performance: Results of a Pilot Study 12
K. Akhtar, S. Bayona, A. Dodds, D. Shier, C. Gupte, F. Bello, R. Emery, J. Cobb

Retrograde versus Antegrade Nerve-sparing during Robot-assisted Radical Prostatectomy: Which is Better for Early Functional Outcomes? 14
A. Sivaraman, Y.H. Ko, R.F. Coelho, S. Chauhan, O. Schatloff, S. Samavedi, C. Giedelman, K. Palmer, V.R. Patel

Image Guidance in Robotic Surgery

Target Tracking in 3D Ultrasound Volumes by Direct Visual Servoing...... 15
C. Nadeau, H. Ren, A. Krupa, P. Dupont

Active Stabilization of Ultrasound Image for Robotically-Assisted Medical Procedures...... 17
C. Nadeau, A. Krupa, P. Moreira, N. Zemiti, P. Poignet, J. Gangloff

Left Atrium Surface Flattening for Assisting Guidance in Catheter Ablation Procedures...... 19
R. Karim, Y.-L. Ma, J. Housden, A. Arujuna, C.A. Rinaldi, M. O'Neill, R. Razavi, T. Schaeffter, K. Rhode

Image-Guided Transoral Robotic Surgery for the Treatment of Oropharyngeal Cancer.................. 21
P. Pratt, E. Edwards, A. Arora, N. Tolley, A. Darzi, G.-Z. Yang

Platform Design and Controls

Raven II™: Open Platform for Surgical Robotics Research 23
H.H. King, L. Cheng, P. Roan, D. Friedman, S. N. Kosari, J. Ma, D. Glozman, J. Rosen, B. Hannaford

Robotic Control of a Traditional Flexible Endoscope 25
J.G. Ruiter, G. M. Bonnema, M.C. van der Voort, I.A.M.J. Broeders

Micro Medical Robot with Magnetic Remote Control in 3D Space... 27
M. Yasui, M. Ikeuchi, K. Ikuta

Lessons Learned Using the Insertable Robotic Effector Platform (IREP) for Single Port Access Surgery.. 29
N. Simaan, A. Bajo, A. Reiter, P. Allen, D. Fowler

New Clinical Approaches and Pilot Studies

Totally Endoscopic Robotic Parathyroidectomy through a Lateral Cervical Approach................... 31
S. Van Slycke, H. Maes, J.P. Gillardin, H. Vermeersch

A Pilot Ex-Vivo Evaluation of a Telerobotic System for Transurethral Intervention and Surveillance.. 33
A. Bajo, R.B. Pickens, S.D. Herrell, N. Simaan

Initial Experience with Robotic Partial Nephrectomy (RPN): A Collaborative Approach drawing on Different Backgrounds... 35
A. Patel, C. Oliver, M. Billia, G. Kooiman, P. Dasgupta, T.S. O'Brien, B. Challacombe

Robotic Tele-Manipulating Devices for Laparoscopy Improve Surgical Performance in Simulated Porcine Laparoscopic Cholecystectomies on the ELITE Simulator................................ 36
K. Sriskandarajah, S. Gillen, A. Di Marco, M. Sodergren, D.R.C. James, J. Clark, H.D. Feussner, A. Darzi, G.-Z. Yang

Planning and Navigation

Improved Visualisation with Shape Instantiation for Robot Assisted Catheter Navigation 38
S.-L. Lee, K.-W. Kwok, C. Riga, C. Bicknell, G.-Z. Yang

Investigation of a CT Compatible Robot for Robot-assisted Surgical Reductions of Joint Fractures.. 40
A. Hinitt, M. Sobhani, S. Dogramadzi, D. Raabe, R. Atkins

Laser Ablation System for Residual Brain Tumour based on the Protoporphyrin Fluorescence Spectrum 42
T. Ando, J. Koike, K. Mizumura, E. Kobayashi, H. Liao, T. Maruyama, Y. Muragaki, H. Iseki, I. Sakuma

Toward Intraoperative Image-Guided TransOral Robotic Surgery 44
W.P. Liu, S. Reaugamornrat, A. Deguet, J.M. Sorger, J.H. Siewerdsen, J. Richmon, R.H. Taylor

Haptics and Perceptual Feedback

The Role of Haptics in Robotics-Assisted Mitral Valve Annuloplasty 46
M.E. Currie, A. Talasaz, A.L. Trejos, R. Rayman, M.W.A. Chu, B. Kiaii, T. Peters, R. Patel

Vibrotactile Perception for Haptics in Virtual Reality Surgical Training.. 48
T. Martin, C.W. Schwingshackl, M.J. Oldfield, F. Rodriguez y Baena

Surgical Instrument Vibrations are a Construct-Valid Measure of Technical Skill in Robotic Peg Transfer and Suturing Tasks 50
K. Bark, E.D. Gomez, C. Rivera, W. McMahan, A.C. Remington, K.M. Murayama, D.I. Lee, K.R. Dumon, N.N. Williams, K.J. Kuchenbecker

Air-Float Stiffness Probe for Tissue Abnormality Identification in Soft Tissue Palpation 52
I.B. Wanninayake, K. Althoefer, L.D. Seneviratne

Poster Presentations

Functional Outcomes following Transoral Robotic Surgery for Obstructive Sleep Apnoea............ 54
A. Arora, B. Kotecha, A. Hassaan, Z. Awad, J. Budge, A. Darzi, N. Tolley

Patient-specific 3D Surgical Planning to Perform Cutting Edge Robotic Surgery........................... 55
M. Carbone, C. Cappelli, V. Ferrari, S. Signori, N. De Lio, V. Perrone, F. Mosca, U. Boggi

Robotic-Assisted Laparoscopic Pyeloplasty in Children: A Single Institution Learning Curve 57
N. Gattas, A. White, S. Whiteley, A. Najmaldin

Can Biometric Measures Predict Feasibility in Transoral Robotic Surgery (TORS)? 59
A. Arora, A. Acharya, S. Khemani, J. Kotecha, A. Darzi, B. Kotecha, N. Tolley

Optimizing Oncological and Functional Outcomes with Robot Assisted Radical Prostatectomy (RALP) in Preoperatively High Risk Prostate Cancer Patients 61
A. Sivaraman, R.F. Coelho, S. Chauhan, O. Schatloff, S. Samavedi, C. Giedelman, K. Palmer, V.R. Patel

From Bench to Bedside: The Novel Use of 3D MRI for Image-Guided Robotic Prostatectomy...... 63
D.C. Cohen, A.N. Sridhar, P. Pratt, B. Khoubehi, J. Vale, G.-Z. Yang, A. Darzi, E.K. Mayer, P. Edwards

Bespoke Fixtures for Robotic Thyroidectomy.. 65
A. Arora, Z. Awad, N. Tolley, V. Luzzato, J. Ahn, F. Ostovari, M. Oldfield, F. Rodriguez y Baena

A Study of Executive Control During Intracorporeal Minimally Invasive Suturing using Functional Near Infrared Spectroscopy (fNIRS) 67
K. Shetty, D.R. Leff, F. Orihuela-Espina, A.W. Darzi, G.-Z. Yang

A Healthcare Mobile Robot with Natural Human-robot Interaction 69
J. Liu, J. Correa, S. McKeague, E. Johns, C. Wong, A. Vicente, G.-Z. Yang

Robotic NOTES: System Concept and Architecture 71
R. Kojcev, E. Wilson, K. Davenport, H. Luo, K. Gary, S. Oonk, K. Cleary

Navigated Endoscopy: Prototype System for Robotically Assisted Ureteroscopy 73
C.A. Peters, A. Burns, E. Wilson, H. Luo, K. LeRoy, J. Goldie, B. LaBrecque, K. Cleary

Preliminary Adhesion Control of a Miniature Intra-abdominal Robot for Laparoscopic Surgery 75
A. Montellano López, R. Richardson, A. Dehghani, R. Roshan, D. Jayne, A. Neville

A Feasibility Study on the Use of Concentric Tube Continuum Robots for Endonasal Skull Base Tumor Removal 77
H.B. Gilbert, P.J. Swaney, J. Burgner, K.D. Weaver, P.T. Russell III, R.J. Webster III

An MRI Compatible Optical Multi-Axis Force/Torque Sensors Robotic Surgery 79
R. Sargeant, H. Liu, K. Althoefer

2DOF MR-Compatible Cardiac Catheter Steering Mechanism 81
A. Ataollahi, Y.L. Ma, L. Seneviratne, T. Schaeffter, K. Rhode, R. Razavi, K. Althoefer

Closed-loop Position Control of an MRI-Powered Biopsy Robot 83
P. Vartholomeos, C. Bergeles, L. Qin, P.E. Dupont

Clinical Study of Prostate Tumour Identification using a Rolling Indentor Robot 85
J. Li, H. Liu, J. Zirjakova, B. Challacombe, P. Dasgupta, L.D. Seneviratne, K. Althoefer

Development of a Novel Hybrid System for Haptics 87
A.I. Skinner, K. Hohenberg, A. Pereira, S. Bowyer, Y. Tenzer, F. Rodriguez y Baena

Extending the Reach and Stability of Manually Steerable Neuroendoscopes Through Robotics 89
P.E. Dupont , S. Chawarski, E.J. Butler, R. Hammond-Oakley, A.H. Gosline, P. Codd, T. Anor, J.R. Madsen, J. Lock

New Evaluation Metrics Applied to Robotic Anastomosis 91
A. Farhat, M. Al-Haddad, G. Younes, T. El-Ghazaly, J. Abi-Nahed, A. Al-Ansari, G. Turkiyyah

Skill Assessment with Proximal Force Sensing for Endovascular Catheterisation 93
H. Rafii-Tari, C.J. Payne, C. Riga, C. Bicknell, S.-L. Lee, G.-Z. Yang

SurgTrak: Synchronized Performance Data Capture for the da Vinci Surgical Robot 95
L.W. White, T.M. Kowalewski, B.H. Hannaford, T.S. Lendvay

Minimally Invasive Surgical Skill Assessment by Video-Motion Analysis 97
S.-K. Jun, M. S. Narayanan, A. Eddib, P. Singhal, S. Garimella, V. Krovi

Eye-Tracked Vergence Response During Active-Stereo Display 99
A.T. Duchowski, B. Pelfrey, D.H. House, R. Wang

Intraoperative Analysis of Locations for 3D Ultrasound-Guided Capture of Foreign Bodies from a Beating Heart 101
P. Thienphrapa, B. Ramachandran, H. Elhawary, A. Popovic, R.H. Taylor

Fusion of Visual and Inertial Measurements for 3D Tissue Reconstruction in Minimally Invasive Surgery 103
S. Giannarou, Z. Zhang, G.-Z. Yang

A Snapshot Endoscopic Polarisation Imaging System 105
N.T. Clancy, D.S. Elson

Quantitative Tissue Measurements in Transoral Robotic Surgery 107
D. Stoyanov, P. Pratt, E. Edwards, G.-Z. Yang, A. Arora, A. Darzi, N. Tolley

Author Index 109

Biologically Inspired Robots: Snake-like, Spider-like Robots and Others

Shigeo Hirose

Tokyo Institute of Technology
Department of Mechanical and Aerospace Engineering

hirose@mes.titech.ac.jp

ABSTRACT

Although the word “robot” was inspired by human workers, we do not need to imitate human figures when we design a practical robotic system for some specific applications. Instead, we should be free from all the preconceptions and we should be creative in the design of the shape of robots.

One of the approaches I found effective was to get inspiration from more wider wild life in general. I made intensive study on the locomotion of real snake in 1970s and based on the study I have been designing many types of snake-like robots such as the amphibious model ACM R-5 which makes 3D swimming in water (Fig.1), the rescue robot Souryu V (Fig.2), and the snake-like multi-joint Float Arm, which is already in use in the assembly line of automobile industry.

I was also inspired by the walking motion of spider and I have desinged several types of spider-like walking robots, including wall climbing robot NINJA II, the 7 ton world largest walking robot TITAN XI (Fig.3), which has been developed for civil engineering tasks on the surface of steep slope, the walking and roller skating hybrid robot Roller Walker, and the walking-crawler hybrid robot TITAN X.

I will also introduce some of our activities to mitigate the disaster of East Japan earthquake and following Fukushima nuclear accident by new types of robotic technology.

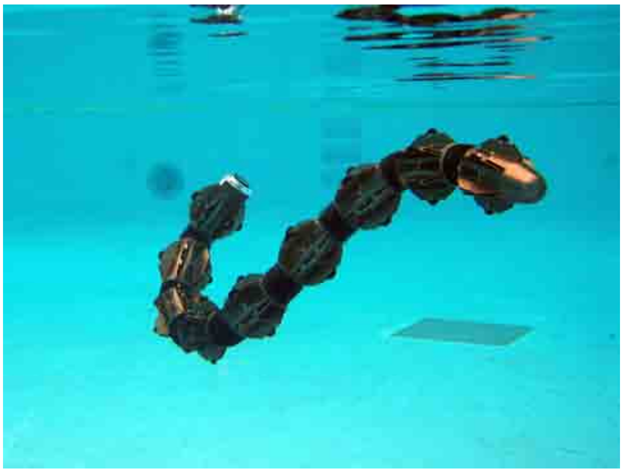

Fig. 1 Amphibious snake-like robot ACM R5

Fig. 2 Snake-like rescue robot Souryu V

Fig. 3 Quadruped robot for construction task TITAN XI

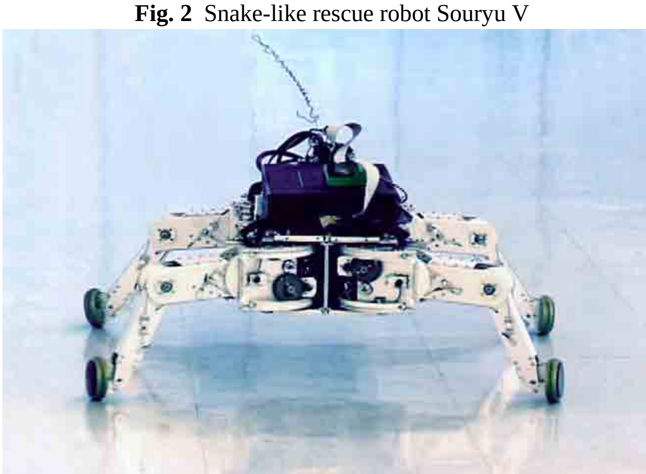

Fig. 4 Walking and roller skating hybrid robot

REFERENCES

[1] S. Hirose, “Biologically Inspired Robots”, Oxford University Press, 1993

Surgical Snake Robots: Faster, Better, Cheaper, and in Control

Howie Choset

Carnegie Mellon University

choset@cs.cmu.edu

INTRODUCTION

Minimally invasive surgery is the greatest advance to the art and science of surgery since Lister introduced antiseptic techniques 150 years ago. By accessing anatomical targets through a small incision with specialized tools, the clinical benefits to patients are profound: less soft tissue disruption, reduced pain, faster healing and recovery, and fewer complications. However, despite their proven track record, minimally invasive devices are still quite limited in that they are rigid or only reach superficial regions in the body. One reason for this is that they are mechanical, lacking true computational capabilities that we have enjoyed in other fields. By developing and combining the mechanical and computational, the robotics field can make true advances to all medical interventions.

This talk will describe a surgical snake robot called the FlexProbe^{TM} which was invented at Carnegie Mellon and is undergoing commercial development by a new startup called Medrobotics, Inc., located in Raynham, MA. The FlexProbe has 102 degrees of freedom and is capable of following a curve in three dimensions. We have performed several experiments on live pigs, and human cadavers to establish the efficacy of this robot for minimally invasive cardiac surgery.

RESULTS

We have performed experiments for minimally invasive cardiac surgery and transoral robotic surgery. For both applications, all animals well tolerated the procedures until their elective euthanasia. For the cardiac surgery in pig, in the navigation trials, the distal apparatus of Flexprobe followed a complex 3-D path from the subxiphoid incision along the ventricular wall to each target. All navigation targets were acquired without complications (e.g., fatal arrhythmia, hypotension, bleeding). The on-board camera provided adequate visualization for navigation.

In the ablation trials, a linear lesion composed of several consecutive "dot-to-dot" lesions at the base of the left atrial appendage was successfully completed. No adverse event was noted during the trials. There was no injury due to the positioning of the robot and the tool's manipulation to the surrounding mediastinal structures (i.e., phrenic nerve, lung, pulmonary artery) upon postmortem examinations.

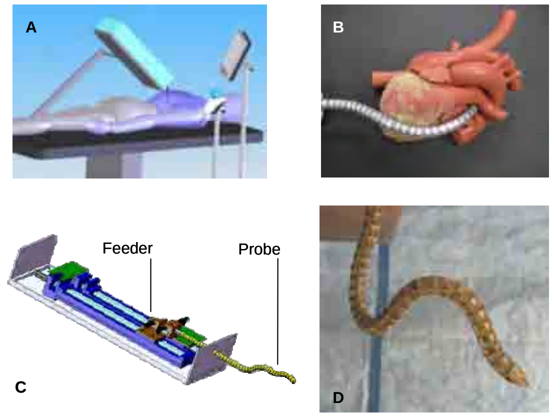

Fig. 1 (A) Flexprobe inside the feeder box and mounted to an operation table (B) Flexprobe driving around a model of a heart (C) CAD Drawing of early feeder design (D) Flexprobe driving in a nonlinear path.

DISCUSSION

We believe that the medical robotics community is just at the beginning. Robot tool-like devices will off-load many of the responsibilities of surgeons onto non-surgical physicians. This will have the benefit of further reducing the costs of the procedures and disseminate medical care. In fact, by democratizing capabilities previously relegated only to surgeons, we will also create more jobs for medical personnel to deliver higher quality care at a lower cost.

REFERENCES

[1] "A Highly Articulated Robotic Surgical System for Minimally Invasive Surgery," T. Ota, A. Degani, D. Schwartzman, B. Zubiate, J. McGarvey, H. Choset, M. Zenati. Ann Thorac Surg, Vol. 87, No. 4, pp. 1253-1256, April, 2009.

[2] "Transoral Highly Articulated Robotic Surgery (THARS) of the Larynx: A Novel Technology and Application," C. Rivera-Serran, B. Zubiate, R Kuenzler, H. Choset, M. Zenati, S. Tully, U. Duvvuri In-press *Laryngoscope,* Feb, 2011

Concentric Tube Robots for Minimally Invasive Surgery

P.E. Dupont[1], A. Gosline[1], N.Vasilyev[1], J. Lock[1], E. Butler[1], C. Folk[2], A. Cohen[2], A.Veeramani[2], M. Wu[2], G. Schmitz[2], R. Chen[2], P. del Nido[1]

[1]Cardiovascular Surgery, Boston Children's Hospital, Harvard Medical School, USA

[2]Microfabrica, Inc., Van Nuys,CA, USA

pierre.dupont@childrens.harvard.edu

INTRODUCTION

The human body was not designed to facilitate surgical repair. Thus, in order to minimize collateral damage to healthy tissue, many interventions require following complex curved paths through tissue and body lumens to reach surgical targets.The smallest existing instrument technologies utilizing this approach are comprised of catheters and endoscopes for passing through body lumens and flexible needles for steering along curved paths through tissue.

While these technologies provide substantial benefit to the patient, they also possess limitations on the types of interventional tasks that they can perform. For example, steerable needles rely on tissue reaction forces to bend and so cannot steer inside a body cavity. Catheters can be designed to steer inside a cavity, but their flexibility limits the forces they can apply to tissue. Thus, both types of devices have similar interventional capabilities– they can deliver a drug or device (e.g., stent) and perform ablation, but they are limited in terms of the surgical tools that they can use and the tissue manipulations that they can perform.

Recently, a new class of robots for minimally invasive surgery has been developed called concentric tube robots. These robots are comparable in diameter to steerable needles and catheters, but differ in construction since they are formed from concentric, telescoping, curved superelastic metal tubes. The shape of these robots is a smooth three-dimensional curve that can be controlled by rotating and translating the individual tubes with respect to each other. While their construction makes these robots significantly stiffer than conventional catheters, the ability to precisely control robot shape enables safe navigation through either tissue or body lumens. Tools and devices are deployed through the central lumen of the robot that serves as a working channel.Consequently, this robotic technology has broad potential for clinical use throughout the body. This paper provides a brief summary of our progress to date in developing this technology.

MATERIALS AND METHODS

The family of shapes that a concentric tube robot can assume is determined by the curvatures, stiffnesses and lengths of the individual tubes that comprise it. Three fundamental principles in designing tube sets are illustrated in Fig. 1. First, each telescoping section is designed to be substantially stiffer than all distal sections. This principle decouples the motion of each section from all of the others. The second principle is for each section to be of piecewise constant curvature. This shape is selected so that the robot can be telescopically extended in a follow-the-leader fashion to avoid producing unnecessary lateral forces either when steering through tissue or when passing through a body lumen. The third principle is to make each telescoping section to be of either fixed curvature or variable curvature (typically varying between straight and a maximum value. This principle is intended to produce the largest workspace with the fewest tubes.

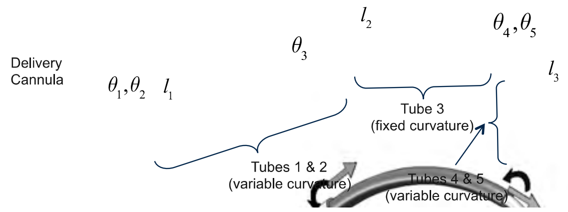

Fig. 1 Concentric tube robot illustrating design principles.

RESULTS

<u>*Design algorithms:*</u> Concentric tube robots are sets of tubes designed for a specific procedure or set of procedures that mount in a common motorized drive system.These tube sets can be made either for single use or for repeated use with sterilization. As illustrated in Fig. 2(a) for a beating-heart intracardiac intervention, many procedures can be decomposed into two parts, (1) navigating through tissue or body lumens to a surgical site, and (2) holding proximal sections fixed while distal sections articulate independently to interact with tissue.

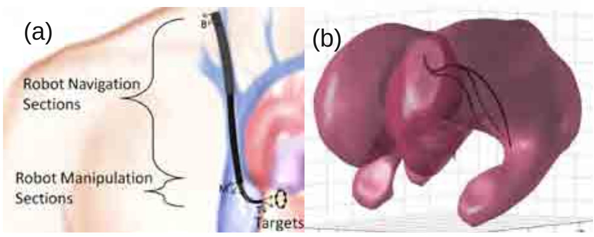

Fig. 2 Algorithmic robot design. (a) Design decomposition for intracardiac beating heart patent foramen ovale closure. (b) Robot design example for intraventricular neurosurgery.

Using this approach, robot design algorithms have been developed utilizing image-based models of the anatomy together with geometric descriptions of the procedure to compute the appropriate lengths, shapes and stiffnesses of individual tubes for procedures in cardiac surgery and neurosurgery.

Modeling and Control: A motorized drive system, compatible with all tube sets (Fig. 4(b)), is used to control the motion of the individual tubes while the surgeon commands the overall motion of the robot using a joystick or keyboard commands. Robot control involves rapid computation of the forward and inverse kinematics. Furthermore, owing to robot compliance, implementing stiffness or force control also requires rapid computation of the relationship between applied loads and robot deformation. Kinematic and quasistatic force models have been developed from Cosserat rod theory and used to implement numerically efficient position and stiffness controllers.

*Surgical Tools:*To enable the use of concentric tube robots for surgery inside body cavities, we are creating a tool set that is matched to both the dexterity of the robots and to the workspace available inside the confines of such cavities. Our tool set encompasses the two fundamental surgical tasks of approximating tissue and removing tissue. Given the challenges of manufacturing at the millimeter scale, we are utilizing a metal MEMS fabrication process that produces fully assembled devices with micron scale features.

Fig. 3 depicts two of our devices. The first is an implant for approximating two layers of tissue. It is comprised of two pairs of expanding spring-loaded wings that are used to pull the tissue layers together. The wing pairs are attached by a ratcheting mechanism that enables the tissue layer approximation distance to be adjusted with submillimeter accuracy. As described below, we have used this device to successfully demonstrate percutaneous beating-heart patent foramen ovale (PFO) closure in a porcine model. Fig. 3(c) depicts a robot-deployed 2 mm microdebrider for tissue removal. The robot lumen is used to power the rotating tool as well as to provide both irrigation and aspiration for entrainment and removal of cutting debris.

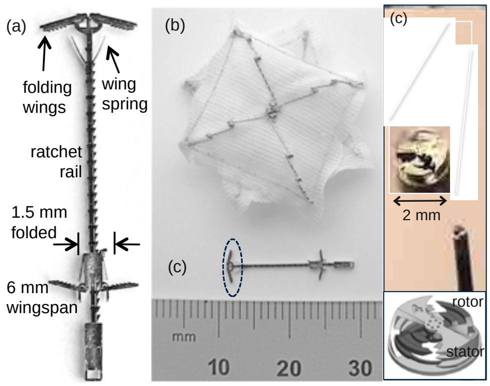

Fig. 3 Metal MEMS surgical tools. (a) Tissue approximation device. (b) size comparison of CardioSeal® catheter-delivered occlusion device and MEMS device. (c) Tissue removal tool.

Beating-heart Intracardiac Surgery Animal Trials: To validate our design algorithms, models, controller, tools and imaging techniques, we have performed a series of successful percutaneous beating-heart PFO closures in a swine model. Following the schematic of Fig. 2(a), we designed the 3-section robot of Fig. 4(a) to enter the right internal jugular vein and navigate to the right atrium. Once inside the atrium, section 1 is locked and sections 2 and 3 are used to approximate the septum secundum and primum by first piercing the secundum and then stretching it laterally to achieve the desired overlap with the septum primum (Fig. 5(a)). The robot then pierces the primum and deploys the device of Fig. 3(a) producing the result shown in Fig. 5(b).

The tissue approximation device of Fig. 3(a) possesses several advantages in comparison to occluder devices such as that of Fig. 3(b). First, in contrast with occluders that rely on spring forces to remain in position, the ratchet mechanism of the MEMS device provides the ability to tailor the approximation to the patient's anatomy. Secondly, to reduce the chance of emboli formation on the left side of the heart, it is desirable to minimize the amount of foreign material exposed there to the blood. While only the distal wings of the MEMS device are present on the left side (Figs. 3(c) and 5(b)), an entire umbrella-like square (Fig. 3(b)) of the occluder is present in the left atrium.

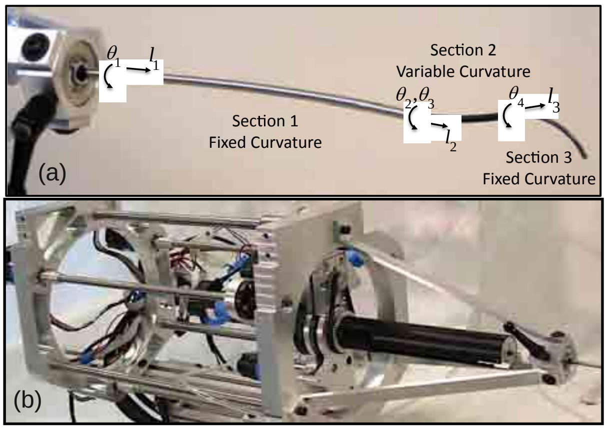

Fig. 4 Robot used for percutaneous PFO closure. (a) Three-section robot design. (b) Motorized drive system.

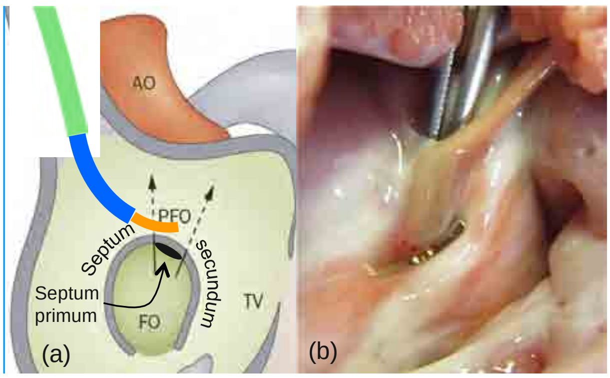

Fig. 5 PFO closure. (a) Robot first pierces septum secundum in depicted location and stretches tissue layer (downward in figure) over primum. (b) Left atrial view showing forceps inserted into PFO channel sealed by device. Visible wings of device are those circled in Fig. 4(c).

ACKNOWLEDGEMENT

This work was supported by the National Institutes of Health under grants R01HL073647 and R01HL087797.

REFERENCES

A list of our publications can be found on our lab website at *robotics.tch.harvard.edu* or *biorobotics.bu.edu*.

A Decade of Robotic Surgery: Past, Present and Future

Vipul R Patel MD

Director - Global Robotics Institute

Professor of Urology - University of Central Florida

INTRODUCTION

It has been slightly more than a decade since the full-fledged introduction of robotic surgery. From very humble beginnings it has progressed rapidly so much so that in the USA about 85% of all prostatectomies are being done robotically. When the technology was introduced the expectations regarding outcomes were much different to what it is now. Initial expectation was that robotic prostatectomy be done in a safe manner in a reasonable time frame with lower blood loss when compared to open surgery. Now both the referring doctors and patients hold us robotic surgeon to far higher benchmarks and expect significant differences in outcomes and more importantly our experience gained in the last 10 years allows us to deliver on these expectations. As our experience has crossed to 5600 robotic prostatectomies we chronicle our journey to achieving optimal outcomes.

CURRENT STATUS OF ROBOTIC SURGERY

Examining current evidence for robotic surgery we realize that there is a paucity of direct head to head comparisons between conventional and robotic surgery. Such randomized trials may never be possible due to patient choice. Hence the bulk of our data is from nonrandomized studies. Evidence from metanalysis has shown that robotic assisted prostate surgery which forms a substantial portion of robotic surgery done world wide has better outcomes in terms of blood loss, hospital stay, catheterization times etc. Moreover data is emerging that the major trifecta outcomes namely cancer control, continence and potency that it is equal to if not better than open surgery.

With long-term oncological outcomes for localized cancer prostate nearing 97% at 15 years the focus has shifted to achieving optimal continence and potency outcomes. Our current continence outcomes of 97% at the end of one year are the sum of introduction of the suspension stitch, bladder neck reconstruction and posterior reconstruction including the modified Rocco stitch.

With regards to potency outcomes we sought to standardize nerve sparing. Our nerve sparing technique mimics that of open surgery where we perform Athermal early retrograde release of the nerve bundle. Initially envisioned as an all or none phenomenon, where the cavernosal nerves may either be preserved or excised, the current concept is that the nerve preservation is graded rather than absolute, where the Neurovascular bundle (NVB) may sustain various degrees of damage during surgery. We developed a nerve-sparing grade(1) with the aid of reliable anatomical land marks (2)that would allow us to objectively inform the patients of the expectations regarding potency outcomes after surgery. Moreover, we also validated surgeon’s perception of grade of nerve preservation to the amount of residual nerve tissue on the final pathological specimen. Such partial nerve preservation and objective grading of nerve preservation is important as it allows us to tailor the nerve preservation to individual cancer status of the patient thereby reducing positive surgical margins.

We realized that the current demands and expectations of patients who desire surgical treatment for prostate cancer are much higher and cannot be adequately addressed with the classic trifecta outcomes alone. Following minimally invasive approaches, patient satisfaction is highly determined by perioperative complications and also by the presence of positive surgical margin (PSM) rates, which can cause significant long-term psychological distress to patients after surgery. A new and more comprehensive methodology for reporting outcomes after RP was proposed: The Pentafecta (3). In the Pentafecta rate, we included complications and surgical margin status, along with the three major outcomes classically reported in trifecta rates: potency, continence, and biochemical recurrence (BCR)–free survival. We believe that Pentafecta outcomes more accurately reflect patient expectations following surgery for prostate cancer. This approach may be beneficial and should be used when counseling patients with clinically localized disease.

LIMITATIONS AND LEARNING CURVE

Primary limitations include considerable cost disadvantages. Lack of competition has resulted in a lack of incentive for the manufacturer to reduce costs. Very few centres are able to consistently make a profit from the robot. However we believe these lacunae can be partially overcome by improving efficiency of robot utilization and increasing volumes. Moreover there is a significant learning curve. This learning curve has to be breached for good outcomes.

FUNDAMENTALS OF ROBOTIC SURGERY

A structured curriculum is essential for training and objectively assessing future robotic surgeons. Currently the certification process to be a robotic surgeon rests with the manufacturer. This process needs to be more structured and hence the process of creating a curriculum for robotic surgery has been initiated. Defining outcomes, curriculum and specific training tasks along with validating the training tasks and measurements with setting up passing criteria are current goals for improving the quality of robotic surgery being performed as well a uniformity of outcomes among the centre's.

CONCLUSION

Robotic surgery has progressed rapidly since its introduction. The robotic surgical outcomes have also kept pace and currently are second to none. To improve uniformity in outcomes a structured curriculum with well-defined tasks and measures is essential.

REFERENCES

[1] Schatloff O, Chauhan S, Sivaraman A, Kameh D, Palmer KJ, Patel VR. Anatomic Grading of Nerve Sparing During Robot-Assisted Radical Prostatectomy. European Urology [Internet]. 2012 Jan 4 [cited 2012 Jan 25]; Available from: http://www.ncbi.nlm.nih.gov/pubmed/22230713

[2] Patel VR, Schatloff O, Chauhan S, Sivaraman A, Valero R, Coelho RF, et al. The Role of the Prostatic Vasculature as a Landmark for Nerve Sparing During Robot-Assisted Radical Prostatectomy. European Urology [Internet]. 2011 Dec 30 [cited 2012 Jan 25]; Available from: http://www.ncbi.nlm.nih.gov/pubmed/22225830

[3] Patel VR, Sivaraman A, Coelho RF, Chauhan S, Palmer KJ, Orvieto MA, et al. Pentafecta: A New Concept for Reporting Outcomes of Robot-Assisted Laparoscopic Radical Prostatectomy. European urology. 2011

Developing Next Generation Robots

Richard M. Satava, MD

Department of Surgery, University of Washington, Seattle, WA, USA

INTRODUCTION

Now that robotics is established in clinical medicine and especially surgery, it is appropriate to analyze the new emerging technological advances and put together a strategy for the next generation systems. In addition, it is imperative to look to other industries for inspiration and to evaluate adopting or adapting current sophisticated systems to clinical practice.

The fundamental principle that brings robotics from the Industrial Age into the Information Age is the concept that a robot is not a machine - it is an information system - with sensors, actuators, controllers, etc, and as such an integrated system, which is what the evolving definition of the science of mechatronics [1] emphasizes. Since energy-based, robotically controlled systems have evolved (though their sensors) as information harvesters, and the information is then used to control the robotic (energy) system (though closed-loop feedback, feed forward, predictive algorithms, etc), robotics facilitates a new relationship between energy and information similar to the famous E=m c2 equation. Perhaps there is an analogous equation (E=i k2 where k is a yet to be discovered constant relationship between energy and information, both of which are intangibles) which might imply a physical relationship (i= m c2/k2) between information and real objects (m); which may imply that information does "exist"; perhaps this is where 3D stereolithography printers (see below) apply. Or is this simply a philosophical relationship similar to the "mind-brain" paradox that tries to determine whether a "thought or "idea" (meme) actually exists?

The current generation of robots is human (or macro) scale, however developments are occurring on both larger hybrid systems as well as "down" into the millimeter and micro- scale.

Robotic systems will become extremely large (room-sized) as we are seeing with the hybrid systems in image guided surgery. SRI International has prototyped an operating room without people - a "robotic cell" in which the surgeon, scrub nurse and circulating nurse robots are integrated into a single system that can be controlled by the surgeon. As robots become larger and more complex, it will be important to adjust thinking from single systems to that of "systems-of-systems engineering" or SOSE (also see below "the robot as an enterprise solution").

In the 'other direction', one aspect of manufacturing has gone to the millimeter and micron scale due to enormous discoveries in micro-electro-mechanical-systems (MEMS) as well as the next generation optical-MEMS. In fact, this scale (for simplicity referred to as "micro")is taking advantage of miniaturization of numerous new energy based devices, such as light emitting diodes (LEDs), micro-fluidics, micro ultrasonic catheter tips, "lab on a chip", etc., into "energy-directed-information-controlled-MEMS" (EDICM) systems. Thanks to this revolution in technology, devices which filled rooms or tabletops are now millimeter sized "chips" which can either be constructed as stand alone hand-held devices or incorporated into larger systems. These systems, by their very nature, are intelligent devices which can perform diagnosis and therapy in real time (milliseconds). As more is learned about the capabilities to precisely select, control and direct the energy sources, it is likely that energy directed therapies (beyond current X-Ray therapy) will lead to the next generation of non-invasive therapy using image guided, hand held (or robotically-controlled for precision) instruments.

Classical robotic instruments will continue to be in the armamentarium of the surgeon. The addition of haptics remains controversial, and continues to be a very difficult engineering challenge. In expanding the scope of a traditional robot, SOSE will allow the creation of much more sophisticated devices, with capabilities of varying levels of automaticity, multi-functional end effectors (Swiss army knife concept), multi-purpose (incorporating simulation, training, surgical rehearsal, pre-op warmup, image guidance including molecular imaging, etc.) and more complete integration into the hospital enterprise (surgical robots are purchased by hospitals, thus are "enterprise investments"). The robot should be viewed as an enterprise solution - by sharing the "data stream" from the robot with Central Supply, Quality Assurance , Risk Management, Hospital Privileging, Training and Assessment, etc.

Physically, the robots will be designed differently with emergence of micro (millimeter size), biomimetic (snake, fish, etc -like), self-assembling and self-repairing systems, to mention a few new directions. Today cell biologists are using femto-second lasers to manipulate mitochondria, Golgi bodies, and even in the nucleus on chromosomes in a preliminary form of genetic engineering. Is the femto-second laser the scalpel of the future? Much has-been speculated about "nano-robots". Though in 1959 Richard Feyman envisioned constructing devices atom by atom[2] to create "molecular machines", creating such "machines" is currently accomplished through batch biochemistry rather than molecule by molecule (robotic assisted) physical assembly.

An interesting new emerging technology is regenerative medicine and specifically tissue engineering - the growth of new organs or tissues from a patient's own stem cells. The latest variation in this science is the use of 3-D stereolithography "printing", using the principles of standard 'ink-jet printing' but filling the ink wells with the necessary different cells and literally "printing" out an organ, layer by layer. Current printing robotic systems are pre-programmed and in-vitro, however the future development may provide a system for in-vivo printing of specific tissues or organs controlled by a surgeon.

DISCUSSION

Although clinically practical, robotic surgery is just in its infancy. The speculations above are all technically feasible and many are in laboratory research. However, it will be a combination of technical feasibility, validation, practicality, behavioral change to accept such radical revolution, fiscal acceptance, and, of course politics, that will determine which of the potential applications will be successful.

REFERENCES

[1] http://en.wikipedia.org/wiki/Mechatronics

[2] Richard P. (1959). "Plenty of Room at the Bottom". Presentation to American Physical Society. http://en.wikipedia.org/wiki/Richard_Feynman. Accessed 10 June, 2012.

The Impact of Trainees on Surgical Outcomes following Robotic Assisted Radical Prostatectomy (RARP)

L.S. Lee*, G.L. Shaw, D.E. Neal, N. Shah

Department of Urology, Addenbrookes Hospital, Cambridge, UK

**luishiong.lee@addenbrookes.nhs.uk*

INTRODUCTION

Surgeons in training have longer operating times and surgical complications in open and laparoscopic surgery[1-3]. Radical prostatectomy as treatment of prostate cancer is a complex procedure with a variable learning curve[4, 5]. Previously, Schroeck et al showed that trainees did not affect selected outcomes following RARP [6]. In the UK, tighter constraints on healthcare resources, and a distinct cancer profile in a non-screened detected population create unique challenges in RARP training.

We hypothesize that patient outcomes following RARP will differ between patients operated solely by an established robotic surgeon versus those operated with trainee participation.

MATERIALS AND METHODS

Consecutive cases of robotic assisted radical prostatectomy by a single established surgeon, in a tertiary institution, from 1st Mar 2010 to 28th Feb 2012 were identified. The study population was classified into cases where trainees were involved as console surgeons (Tr+) , versus those involving only the senior surgeon (Tr-). As a requirement, trainees attended basic robotic surgery training and accrued sufficient first assistant experience prior to console training. The training program consisted of modular components with increasing level of complexity:

(i) Bladder mobilisation and endopelvic fascia dissection
(ii) Bladder neck, seminal vesicles and Denonvillier`s fascia dissection
(iii) Pedicle ligation and nerve sparing
(iv) Dorsal venous complex ligation, urethral transection and urethrovesical anastomosis
(v) Lymphadenectomy

The outcomes analysed include:

(i) Patient demographics, pre-operative PSA levels and ASA grading
(ii) Operative time, frequency of nerve sparing procedures, estimated blood loss (EBL), length of stay (LOS) and complication rates
(iii) Pathological T, N stage and positive surgical margin (PSM) rates

Statistical analysis was performed using a 2 sided T-test with significance defined at $p<0.05$.

RESULTS

There were 146 cases identified, of which N=44 involved trainees (Tr+) and N=102 without trainees (Tr-). There were 5 trainees involved in this study, but only 2 were operating at each time. All trainees had diverse background experience in radical prostatectomy and robotic assisted surgery. Each Tr+ case involved trainees at different levels of competency: one at step (i) and other at step (iii) or beyond.

All patients were ASA classification grade 2 or better. There was no significant difference in patient demographics, prostate weight, oncological profile, operative time or length of stay. In the Tr+ group, there were higher rates of PSM but lower EBL (with no impact on transfusion rates).

DISCUSSION

Despite limitations inherent to its retrospective and non-randomised nature, we observe similar patient characteristics between study groups, and no differences with operative times or length of stay(contrary to previous findings) [1-3].

In the Tr- group, the higher EBL is possibly related to a higher proportion of nerve sparing procedures performed.

Overall PSM rates are higher in the Tr+ group, consistent with the learning curve of RARP. When PSM rates are stratified by pathological T stage, they are comparable with other series.[7-9]

In conclusion, trainee involvement in RARP does not impact peri-operative outcomes, but is associated with higher PSM rates. Although this does not affect overall oncological outcomes when compared to other established series, there may be adverse implications to individual specific quality indices.

REFERENCES

[1] Vriti Advani, S.A., Chad Gonczy, Steven Markwell, Imran Hassan, *Does resident involvement effect surgical times and complication rates during laparoscopic appendectomy for uncomplicated appendicitis? An analysis of 16,849 cases from the ACS-NSQIP*. The American Journal of Surgery. **203**: p. 347-352.

[2] Bridges M, D.D., *The financial impact of teaching surgical residents in the operating room.* Am J Surg, 1999. **199**: p. 28-32.

[3] Scarborough, J.E.M.B., Kyla M. MD; Pappas, Theodore N. MD, *Defining the Impact of Resident Participation on Outcomes After Appendectomy.* Annals of Surgery, 2012. **255**: p. 577-582.

[4] Herrell SD, a.S.J.J., *Robotic-assisted laparoscopic prostatectomy: what is the learning curve?* Urology, 2005. **66**: p. 105-107.

[5] Zorn KC, O.M., Gong EM, et al, *Robotic radical prostatectomy learning curve of a fellowship-trained laparoscopic surgeon.* J Endouro, 2007. **21**: p. 441-447.

[6] Florian R. Schroeck, C.A.P.d.S., Ross A. Kalman, Maitri S. Kalia, and G.E.H. Sean A. Pierre, Leon Sun, Judd W. Moul, and David M. Albala, *Trainees Do Not Negatively Impact the Institutional Learning Curve for Robotic Prostatectomy as Characterized by Operative Time, Estimated Blood Loss, and Positive Surgical Margin Rate.* Urology, 2007. **71**: p. 597-601.

[7] Fatih Atuga, E.P.C., Sudesh K. Srivastavb, Scott V. Burgessa, Raju Thomasa, Rodney Davisa, *Positive Surgical Margins in Robotic-Assisted Radical Prostatectomy: Impact of Learning Curve on Oncologic Outcomes.* Eur Urol, 2006. **49**: p. 886-872.

[8] Michael Liss, K.O., David Ornstein, *Positive surgical margins during robotic radical prostatectomy: a contemporary analysis of risk factors.* BJUI, 2008. **102**: p. 603-608.

[9] Thomas E. Ahleringa, L.E., Robert A. Edwardsa,David I. Leea,Douglas W. Skarecky, *Robotic radical prostatectomy: A technique to reduce pT2 positive margins.* Urology, 2004. **64**: p. 1224-1228.

Table 1. Surgical outcomes following RARP

	Tr+ group	**Tr- group**	**p value**
Number of cases, N	44	102	-
Mean age (SEM), years	59 (1.1)	60 (0.7)	0.16
Mean pre-op PSA(SEM), ng/ml	6.7 (0.4)	7.5 (0.8)	0.36
Pathological Gleason sum			
6	12 (27%)	25 (25%)	0.24
7	29 (66%)	63 (62%)	
8 and above	3 (7%)	14 (13%)	
Pathological T stage			
T2(N,%)	21 (48%)	54 (53%)	0.92
T3(N,%)	23 (52%)	48 (47%)	
Pathological N stage			
N positive (N,%)	3 (7%)	3 (3%)	0.38
N negative (N,%)	41(93%)	99 (97%)	
Positive surgical margins (N,%)	8 (18%)	6 (6%)	0.01*
Negative surgical margins (N,%)	36 (82%)	96 (94%)	
pT2 PSM cases (N,%)	2 (9%)	2 (4%)	0.01*
pT3 PSM cases (N,%)	6 (26%)	4 (8%)	
Nerve sparing procedures (N,%)	38 (86%)	90 (88%)	0.27
Non nerve sparing procedures (N,%)	6 (14%)	12 (12%)	
Mean prostate weight (SEM), g	56 (3.0)	60 (2.7)	0.30
Mean EBL(SEM), ml	253 (32)	326(26)	0.03 *
Transfusion rate (%)	0	0	-
Operating time (SEM), min	182 (5)	179(3)	0.37
Mean LOS (SEM), days	1.2 (0.09)	1.1(0.4)	0.35
Intra-operative complications(N,%)	-	1(1%)	0.56
Post-operative complications (N,%)	1(2%)	3 (3%)	

*Statistically significant

Abbreviations: SEM,standard error of mean; g, grams; min, minutes; PSM, positive surgical margins; EBL, estimated blood loss; LOS, length of stay

Short and Long Term Complications of Robotic Abdominal Surgery in Children

N. Gattas[1], C. Smith[2], N. Alizai[2], C. Van-Wyk[2], J. Sellors[2], S. Whiteley[2], A. Najmaldin[2]

[1]*School of Medicine, University of Queensland, Australia*
n.gattas@uq.edu.au

[2]*Paediatric Surgery, Leeds Teaching Hospitals NHS Trust, United Kingdom*
azad.najmaldin@leedsth.nhs.uk

INTRODUCTION

Robotic assisted surgery has been developed to address the difficulties of laparoscopic surgery. Although well established in adult surgery, the application of robotics in paediatric surgery remains in its early infancy and prospective data on the technique's effectiveness in children are scarce [1-3]. This report presents early and late complications of robotic surgery in one paediatric surgery institution.

MATERIALS AND METHODS

Our unit has a longstanding experience in laparoscopic surgery. Following a few hours of hands-on laboratory practice, we introduced robotic surgery into our practice in March 2006. Since this time, all children who underwent robotic assisted surgery under the care of two surgeons were included in this study. Three arms of the Da Vinci system and an open technique laparoscopy were used in all procedures. 8mm or 5mm robotic instruments were consumed at surgeon's discretion. An additional 3.5mm or 5mm laparoscopic port and instrument was used when necessary. All patients had regular follow up, and data were collected prospectively.

Fig. 1 Position of ports and robotic instruments in robotic excision of choledochal cysts in a small child.

RESULTS

There were 274 procedures in 267 patients. The procedures were carried out independently by either surgeon A (76%), B (17%) or jointly (7%). The operations were urological in 138 (50.4%), billiary and splenic in 54 (19.7%) and gastrointestinal in 82 (30%). The median age was 7.8 years (6 weeks - 16 years) and 20 patients (7.2%) weighed less than 10 kg with the smallest being 5.4 kg. 13% had a history of previous abdominal surgery. The mean robotic and total operating times were 132 (11 - 478) and 204 (47 - 584) minutes respectively. There were no anaesthetic or robotic complications. 12 patients (4.4%) were converted to an open procedure. Of these, 2 (0.7%) were for surgical complications. In hospital complications occurred in 8 patients (3%). All were treated conservatively except one who had a ureteric stent replacement. Post-operative IV or oral morphine were received by 29 (10.6%) and 12 (4.4%) of the patients respectively. The median hospital stay was 2 days (1 - 9 days). This variable was influenced by the pre-existing conditions and socio- geographical circumstances of the patients. To date, 3 patients (1.1%) have required re-do surgery for pyeloplasty (1) and fundoplication (2).

DISCUSSION

These prospective data demonstrate that in an experienced paediatric minimally invasive unit and in selected young and small patients, the short- and long-term morbidity of robotic surgery is low even during the learning period. Robotic surgery may hold more promise for paediatric surgeons than adult surgeons.

REFERENCES

[1] Van Hassteren G, Levine S, Wayes W. Pediatric robotic surgery: early assessment. Pediatrics. 2009,124(6):1642-9.
[2] Meehan JJ, Sandler A: Pediatric robotic surgery: A single-institutional review of the first 100 consecutive cases. Surg Endosc. 2008;22(1):177-82.
[3] Minnillo BJ, Cruz JAS, Sayao RH, Passerotti CC, Houck CS, Meier PM, Borer JG, Diamond DA, Retik AB, Nguyen HT. Long-term experience and outcomes of robotic assisted laparoscopic pyeloplasty in children and young adults. J Urol. 2011; 85(4):1455-60.

A New Global Ratings Scale for Assessing Virtual Reality Arthroscopy Simulator Performance: Results of a Pilot Study

Kash Akhtar[1,2], Sofia Bayona[3], Alex Dodds[1], David Shier[1], Chinmay Gupte[1], Fernando Bello[1], Roger Emery[1], Justin Cobb[1]

[1]*Department of Surgery & Cancer, Imperial College London*

[2]*School of Surgery, London Deanery*

[3]*Department of Computer Architecture and Technology, Computing Sciences, and Artificial Intelligence, Universidad Rey Juan Carlos, Madrid*

surgery@me.com

INTRODUCTION

Surgical training is undergoing significant changes with reduced working hours and an increasing focus on patient safety. Virtual Reality (VR) simulators allow trainees to gain experience in controlled, risk-free environments and their role in orthopaedic training is increasing. Some authors feel the current assessments of intra-operative technique to be somewhat limited in scope however [1] and there is no specific assessment for VR simulated procedures such as knee arthroscopy.

This paper describes the development of a Global Rating Scale of Arthroscopic Performance and the results of applying it to a pilot study. The aim of this scale is to assess specific aspects of technical dexterity. It was designed to be used within the operating theatre and virtual environments.

MATERIALS AND METHODS

We used a Delphi method (consensus of an expert group) to develop a detailed Global Rating Scale for assessing the diagnostic arthroscopy of any joint (Table 1). This consisted of 10 dimensions, each graded on a 5 point scale from 1-5, with the middle and extreme points described explicitly (with 1 the lowest score and 5 the highest).

50 subjects of differing experience performed 3 exercises using a virtual reality arthroscopy simulator (ARTHRO Mentor^{TM}) [2].

Subjects were filmed performing the procedure and the onscreen display was also recorded. These videos were edited so subjects could not be identified, but that hand and body movements could be assessed globally. A split-screen arrangement showed the video of the subject performing the procedure on one side and the simulator display on the other (see Figure 1).

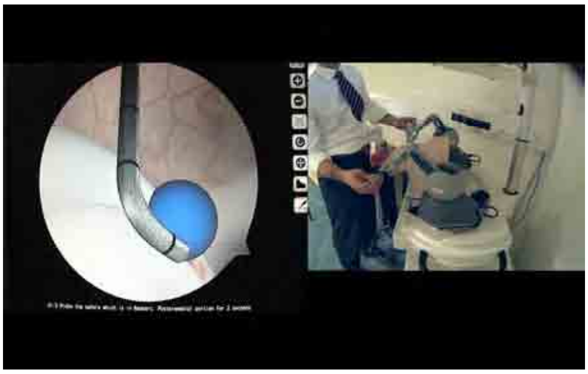

Fig. 1 Split-screen display.
Left: VR ARTHRO Mentor^{TM} simulator display.
Right: view of the participant using the simulator

These videos were given to two experienced arthroscopic surgeons blinded to the identities and experiences of the participants. They each analysed all 50 subjects performing the 3 exercises using the Global Rating Scale of Arthroscopic Performance. The results were then analysed by a blinded researcher.

Results were analysed using two-way analysis of variance (ANOVA) with measures of absolute agreement. The Intra-Class Correlation Coefficient (ICC) was calculated for each exercise to assess inter-rater reliability.

GRS for arthroscopy procedures. Observer id:____ Video name: _______

1. Makes the portals (or inserts the arthroscope and instruments) with the correct angles of insertion to access the targeted space

1- Many unsystematic attempts and very inefficient access to the targeted point with randomly chosen angles of insertion.
2-
3- Several attempts before getting into the targeted space. Once found, maintains the correct arthroscope and instrument angles most of the times
4-
5- Efficient angles of insertion, perfect access to the targeted space within the joint

2. Respect for tissue (looking at the smoothness of the movements)

1- Often used unnecessary force on tissue. Damage caused by inappropriate use of the instruments
2-
3- Careful handling of tissue but occasionally rough movements or caused inadvertent damage
4-
5- Consistently handled tissues appropriately, with minimal damage

3. Proficiency in handling the arthroscope

1- The view of the anatomy is not coherent (for example, randomly oriented upside-down). Incoherent turns of the optics and the camera. Repeatedly makes tentative or awkward movements with the arthroscope
2-
3- Competent use of the arthroscope, coherent view of the anatomy although occasionally appeared stiff or awkward. Inefficient use of the optics turn
4-
5- Fluid moves with the arthroscope, adequate use of camera and optic turns, and no awkwardness. If adequate, takes advantage of using different portals

4. Instrument handling (except the arthroscope)

1- Repeatedly makes tentative or awkward movements with instruments
2-
3- Competent use of instruments, although occasionally appeared stiff or awkward
4-
5- Fluid moves with instruments and no awkwardness

5. Depth perception

1- Constantly overshoots target. Slow to correct
2-
3- Some overshooting or missing of target
4-
5- Accurately directs instruments in the correct plane to target

6. Bimanual dexterity and triangulation

1- Noticeably awkward with non-dominant hand, poor coordination between hands. Unable or great difficulty to locate the instrument
2-
3- Uses both hands but does not maximize interaction between hands. Locates the instrument after a moderate time, but in a systematic way
4-
5- Expertly uses both hands in complementary manner to provide optimum performance. Locates the instrument quickly and efficiently

7. Efficiency and time

1- Many unnecessary, inefficient movements. Constantly changing focus or persisting without progress
2-
3- Slow, but planned movements are reasonably organized with few unnecessary or repetitive movements
4-
5- Confident, clear economy of movement and maximum efficiency

8. Knowledge of anatomy and orientation

1- Deficient knowledge of the anatomy. Feeling of being lost within the joint. Clear mistakes when recognising or looking for anatomical structures
2-
3- No mistakes when recognising the anatomy. Good orientation and knowledge of where the arthroscope and instruments are. Moderate knowledge of the anatomical structures and pathologies
4-
5- Demonstrated familiarity with all the anatomical structures and pathologies. Excellent orientation

9. Knowledge of specific procedure and/or tasks to be performed (related to each particular exercise)

1- Deficient knowledge of the operative steps, even with help.
2-
3- Able to follow the operative steps (or tasks) with moderate help
4-
5- Demonstrated familiarity with all aspects of the operation and the operative steps to be performed

10. Overall individual performance and competence (related to each particular exercise)

1- Very poor
2-
3- Competent
4-
5- Clearly superior

☐ No arthroscopic experience Arthroscopy experience: ☐ Novice ☐ Intermediate ☐ Expert
Other comments:

Table 1. Global Rating Scale of Arthroscopic Performance

RESULTS

The ICC was calculated for each exercise (see Table 2), with an average of 0.91 across all 3 exercises. Internal consistency was high (alpha: 0.918).

Exercise	Cronb-ach's alpha	Intraclass Correlation Coefficient (95% CI)	Signific-ance
Exercise 1	0.9	0.902 (0.826-0.945)	P<0.001
Exercise 2	0.929	0.922 (0.852-0.957)	P<0.001
Exercise 3	0.869	0.844 (0.672-0.920)	P<0.001

Table 2. Results for inter-rater reliability for each exercise.

DISCUSSION

There is a need for valid and reliable methods of assessing technical competence in surgical training. The high values seen for Cronbach's alpha and the Intra-Class Correlation Coefficient demonstrate that the Global Rating Scale of Arthroscopic Performance has great potential as a means of assessing VR simulator performance, with high internal consistency and excellent inter- rater reliability. The Orthopaedic Curriculum & Assessment Project [3] promotes a measured and holistic approach to orthopaedic training in the operating theatre. There are limitations to this approach, however, as it is difficult to standardise operations and the initial steep part of the trainees' learning curves may potentially put patients at risk. There is also a significant cost of training in the operating room and it may be more appropriate to teach generic arthroscopic skills to trainees elsewhere. This is where simulation can be of benefit. The role of VR simulation in surgical training continues to grow and more appropriate tools for quantifying performance in this environment are required. This Global Rating Scale offers a more thorough approach to assessing technical performance on a VR arthroscopy simulator. Blinding of those undertaking rating and data analysis should remove any inherent bias and support its use as a tool for assessment and feedback.

We are currently using the Global Rating Scale of Arthroscopic Performance to test the concurrent validity of this simulator. We are also performing a larger scale validation study with a view to incorporating this assessment within a simulation curriculum for trauma and orthopaedic surgery. It may prove a useful guide as to when a trainee has the appropriate skill-set to progress to operating on patients. Consequently, this may have implications for safeguarding the welfare of both patients and trainees.

Once validated, we intend to test the role of the Global Rating Scale of Arthroscopic Performance in the assessment of arthroscopy in the operating theatre.

REFERENCES

[1] Howells NR, Gill HS, Carr AJ, Price AJ, Rees JL. Transferring simulated arthroscopic skills to the operating theatre: a randomised blinded study. J Bone Joint Surg Br. 2008 Apr;90(4):494-9.
[2] Simbionix, 2012. http://www.simbionix.com
[3] www.ocap.org.uk/curriculum

Retrograde versus Antegrade Nerve-sparing during Robot-assisted Radical Prostatectomy: Which is Better for Early Functional Outcomes?

Ananthakrishnan Sivaraman, Young Hwii Ko, Rafael F. Coelho, Sanket Chauhan, Oscar Schatloff, Srinivas Samavedi, Camilo Giedelman, Kenneth Palmer and Vipul R. Patel

Global Robotics Institute, Celebration, FL, USA
University of Central Florida, School of Medicine, Orlando, USA

OBJECTIVE

To evaluate the impact of the antegrade (from base to apex) and retrograde (from apex to base) nerve sparing (NS) approaches on functional outcomes after robot-assisted radical prostatectomy (RARP).

MATERIALS AND METHODS

From January 2008 to January 2011, a total of 2267 RARPs were performed by a single surgeon who graded the extent of NS as a percentage of nerve bundle preserved (100%, 75%, 50%, 25%, and 0%) on each side. From a cohort of 1118 preoperatively potent men (SHIM>21), 793 patients had a sum of 200% of NS from each side (full NS), and 501 patients had at least one year of follow up. After propensity matching, 344 patients were finally selected, and these patients were categorized into two groups according to whether NS was conducted by antegrade (Group 1, n=171) or retrograde (Group 2, n=173). Validated questionnaires were used for assessment of continence and potency recovery at 1 month, then every 3 months, up to a year.

RESULTS

Groups 1 and 2 were similar in all preoperative baseline characteristics, including age, body mass index, gland size, preoperative AUA and SHIM score, serum PSA level, clinical stage, biopsy Gleason score, D'Amico risk stratification, and presence of diabetes mellitus, hypertension, hyperlipidemia, and coronary artery disease. Intraoperative, while operative time, hospital stay, catheter indwelling period, complication and transfusion rate were similar, blood loss (119.6±34.2 vs. 111.6±31.6 ml, p=0.027) was increased in Group 1. Overall positive margin rates were similar (11.1% vs. 6.9%, p=0.192), and no correlation with NS approach was found in multivariate analysis regarding margin status.

Potency rates at 1 month, 3 months, 6 months, 9 months, and 12 months were 39.7%, 73.3%, 81.4%, 89.5%, and 93.8%, respectively. At 3, 6, and 9 months, it was significantly higher in Group 2 (65.5% vs. 80.9% [p=0.001], and 72.5% vs. 90.2% [p<0.001], and 85.8% vs. 93% [p=0.048], respectively). Multivariable analysis using all preoperative variables also indicated that NS approach was an independent predictor for potency regain along with age, gland size, and concomitance of hyperlipidemia, at 3 and 6 months. After adjusting for other predictors, the hazard ratio for potency recovery for Group 2 relative was 2.264 (95% CI: 1.372 – 3.736, p=0.001) at 3 months, and 3.605 (1.951 – 6.661, p<0.001) at 6 months. The NS approach also affected the recovery of continence at 1 month using same model; the hazard ratio for continence recovery for Group 2 at this time point was 1.581 (1.001-2.496, p=0.049).

CONCLUSIONS

In patients with normal preoperative erectile function and who had full bilateral NS, a retrograde NS approach facilitated early recovery of potency and continence compared with an antegrade approach without compromising cancer control.

REFERENCES

[1] Chauhan S, Coelho RF, Rocco B, Palmer KJ, Orvieto MA, Patel VR. Techniques of nerve-sparing and potency outcomes following robot-assisted laparoscopic prostatectomy. International braz j urol. 2010;36:259–72.

[2] Rabbani F, Stapleton AM, Kattan MW, Wheeler TM, Scardino PT. Factors predicting recovery of erections after radical prostatectomy. J. Urol. 2000 Dec;164(6):1929–34.

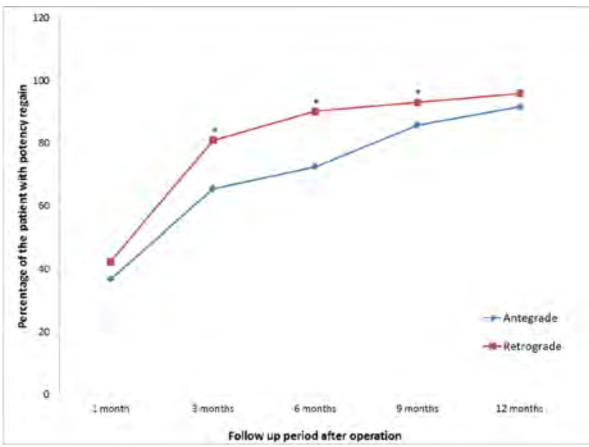

Fig. 1 Summary of potency outcome evaluated at each follow-up, divided by the extent of NS.

Target Tracking in 3D Ultrasound Volumes by Direct Visual Servoing

C. Nadeau[1], H. Ren[2,3], A. Krupa[1], P. Dupont[2]

[1]IRISA, Inria Rennes-Bretagne Atlantique, France

[2]Children's Hospital Boston and Harvard Medical School, Boston, MA, USA

[3]Department of Bioengineering, National University of Singapore, Singapore

(caroline.nadeau, alexandre.krupa)@inria.fr

(hongliang.ren, pierre.dupont)@childrens.harvard.edu

INTRODUCTION

Three dimensional ultrasound (3DUS) guided robotic beating heart surgery is an emerging computer-assisted surgical technique. Motion tracking of both the robot and the heart tissue is one of the key open problems in these procedures and the use of 3DUS imaging offers the possibility to extract, intra-operatively and in real time, the motion of one or more targets.

In this paper, we present a visual servoing approach to track the motion of a single target that can consist of either the surgical robot or cardiac tissues. To deal with the low quality of the 3DUS volumes, our intensity-based approach requires no primitive extraction or image segmentation. This approach does not involve time consuming processing steps and can be applied to a wide range of tissue types and medical instruments.

Unlike previous work [1], where the motion compensation task was realized physically by moving the probe attached to a robotic arm to compensate for abdominal organ motion, we propose here to track the motion of the target using a 3D region of interest (ROI) which is automatically moved within the 3D US volume to compensate for both target and probe motion. This is a new method compared with conventional 3DUS-based target motion tracking or imageless motion tracking as surveyed in [2]. In-vivo animal experiments were conducted to validate the tracking approach.

MATERIALS AND METHODS

3DUS guided robotic beating heart surgical procedure

Image volume sequences were acquired during an in-vivo porcine robotic surgery using a concentric tube robot [3]. The 3D image acquisition system was a Philips IE33 system manufactured by Philips Medical (www.philips.com). The robot was inserted through a small incision in the jugular vein on the neck and then steered inside the right atrium. The surgeon positioned the matrix-array 3D probe epicardially on the heart to image the robotic instrument tip and the intracardiac tissue (Fig. 1). The system was used to acquire US volumes at a frame rate of 25 Hz for durations of 10 sec. These volumes were then loaded in a rendering software we have developed and the tracking performed off line.

Standard settings of the imaging parameters were used during image generation, including 50% overall gain, 50% compression rate, high density scan line spacing, 6 cm image depth, and zero dB power level.

Fig. 1 Beating-heart intracardiac surgery with 3DUS probe manually positioned on the epicardial surface.

Intensity-based visual servoing

In this procedure, the US probe is not actuated and motion tracking is performed in the acquired US volume by moving a ROI to compensate for probe and target motion. An image-based visual servoing strategy is considered for minimizing the error $\mathbf{e}(t) = \mathbf{s}(t) - \mathbf{s}^*$ between a current set of visual features $\mathbf{s}$ and a desired one $\mathbf{s}^*$ by applying an instantaneous velocity $\mathbf{v}_c$ to the ROI. To observe an exponential decrease of this visual error, the classical control law [4] is given by:

$$\mathbf{v}_C = -\lambda \cdot \hat{\mathbf{L}}_s^+ (\mathbf{s} - \mathbf{s}^*)$$

where λ is the gain involved in the exponential decrease of the error and $\hat{\mathbf{L}}_s^+$ is the pseudo-inverse of an estimation of the interaction matrix $\mathbf{L}_s$ that relates the variation of the visual features to the velocity $\mathbf{v}_c$.

To deal with the low quality of the 3D US images, we consider as visual features $\mathbf{s}$ the intensity values of the voxels of the 3D ROI:

$$\mathbf{s} = \{I_{1,1,1}, \cdots, I_{u,v,w}, \cdots, I_{L,M,N}\}$$

Where L, M and N are respectively the width, the height and the depth of the ROI and where $I_{u,v,w}$ is the intensity of the voxel of coordinates *(u,v,w)* in the US volume.

The interaction matrix associated to these intensity features has been modeled in [1] and depends only on the 3D image gradient and the coordinates of the voxels in the US volume.

RESULTS

We conducted experiments to evaluate the ability of the algorithm to track cardiac tissue and to track the robot. The results of the soft tissue tracking task are displayed in Fig. 2. In the first volume provided by the 3D probe, the central image of the volume is displayed to allow the user to delineate the desired anatomic structure by a bounding box used as a basis for the 3D ROI considered in the control law. Then, during the subsequent volumes, the velocity computed by visual servoing is applied to this ROI. Compensated tissue motion is due predominantly to the cardiac cycle. To validate visually the tracking task, we display during the cardiac motion the interpolated US image going through the center of this ROI, first without compensation (c), then with compensation (e). In both cases, the corresponding difference images (d,f) with the desired US view are also computed. The efficiency of the compensation is shown on the difference image (f) where the ROI is roughly gray with no strong gradient, compared to the difference image (d). Moreover a visual error is defined as the Euclidean norm of the visual vector and is displayed on the curve (b).

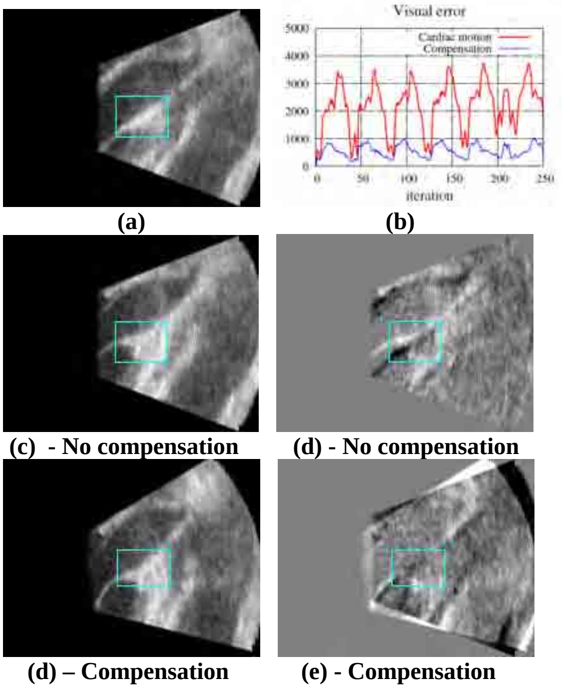

Fig. 2 Tracking results for cardiac tissue. The desired anatomic target is delineated on the central view of the initial US volume (a). The motion compensation is validated by the decrease in visual error (b) and by the difference images (d,f) corresponding to the image extracted from the ROI at iteration 240, respectively without (c) and with (e) compensation.

Experiments were also performed to evaluate intensity-based visual servoing for tracking robot motion during surgery. In this case, we defined the desired ROI to include the tip of the concentric tube robot, as it was navigated inside the right atrium of the beating porcine heart [3]. Robot tip motion is automatically tracked by the proposed intensity approach during its movement. The results are presented in Fig. 3. In each of the acquired 3DUS volumes, the ROI remains centered on the tool tip, which validates the tracking task. Fig. 3(e) shows the decrease of the visual error with the tracking and Fig. 3(f) gives an estimate of the tool motion. This motion corresponds to a forward and backward translation along the direction of the tool shaft.

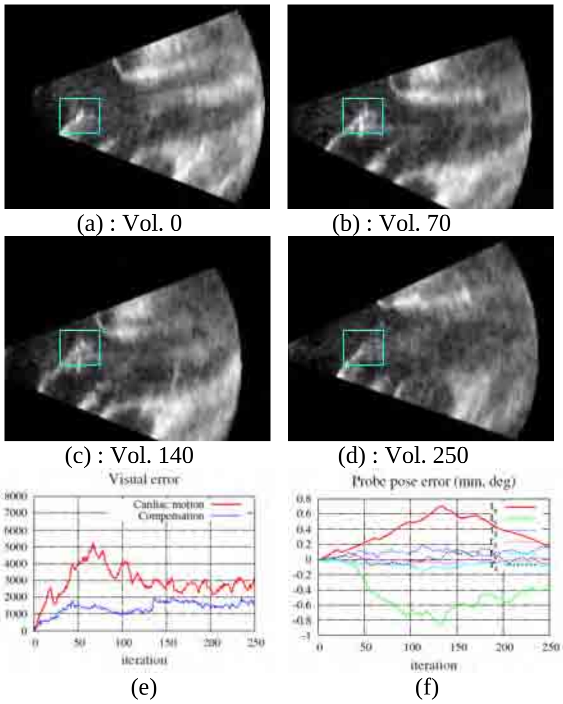

Fig. 3 Tracking results for the robot. The robot tip indicated by the surgeon in the initial US volume (a) is tracked in the successive ones (b,c,d). The tracking task allows the reduction of the visual error (e) and the estimation of the tool pose (f) (the θ**u** representation is considered to describe the orientation, where $\mathbf{u} = (u_x\ u_y\ u_z)^\mathbf{T}$ is a unit vector representing the rotation axis and θ is the rotation angle).

DISCUSSION

We have presented a new direct visual servoing method for the estimation and compensation of rigid motions using 3DUS volume sequences and illustrated its effectiveness using data from robotic beating-heart surgery. These experiments validated the approach both for tracking the rigid motion of robotic tools and also for tracking the quasi-rigid motion of heart tissue.

As a next step, we will investigate extending the method to deal with the non-rigid motions of heart tissue using a deformable grid instead of the rigid ROI.

Acknowledgement

This work was supported by the National Institutes of Health under grants R01HL073647 and R01HL087797 and by the ANR project US-Comp of the French National Research Agency.

REFERENCES

[1] Nadeau C., Krupa A., Intensity-based direct visual servoing of an ultrasound probe. IEEE Int. Conf. on Robotics and Automation, 2011 May; 5677-5682.

[2] Ren H., Vasilyev N. V., and Dupont P. E., Detection of curved robots using 3d ultrasound. IEEE/RSJ Int. Conf. on Intelligent Robots and Systems, 2011.

[3] Dupont P., Lock J., Itkowitz B., and Butler E., Design and control of concentric-tube robots. IEEE Trans. on Robotics, 2010; 26(2): 209-225.

[4] Espiau B., Chaumette F., and Rives P., A new approach to visual servoing in robotics. IEEE Trans. on Robotics, 1992; 8(3): 313-326.

Active Stabilization of Ultrasound Image for Robotically-Assisted Medical Procedures

C. Nadeau[1], A. Krupa[1], P. Moreira[2], N. Zemiti[2], P. Poignet[2], J. Gangloff[3]
[1]*IRISA, Inria Rennes-Bretagne Atlantique, France*
[2]*LIRMM, UMR 5506, CNRS Université de Montpellier 2, 34095 Montpellier, France*
[3]*LSIIT, UMR 7005 CNRS-Université de Strasbourg I, 67400 Illkirch, France*

caroline.nadeau@inria.fr

INTRODUCTION

In the context of robotic assistance to medical gestures, we propose solutions to stabilize the ultrasound (US) image by actively compensating for the physiological motions of the patient. The considered applications are for instance the assistance for diagnoses or hepatic tumor biopsies where the liver and the tumors mainly undergo the respiratory motion. Other clinic applications, such as prostate cancer brachytherapy have been identified in [1] that could benefit from such robotic image stabilization.

The per-operative image provided by the US probe and the contact force applied to the probe are used to control the six degrees of freedom (dof) of the robot. To deal with the low quality of the US images, we propose to use the intensity of the image as visual features in a visual servoing control loop [2][3]. This vision control is associated with a force control to ensure a constant force applied to the probe. Finally, a predictive controller is implemented in the control law to take advantage of the repetitiveness of the physiological motions. We present first ex-vivo robotic results on animal tissues where we compensate for the 3D motions using successively 2D and 3D probes.

MATERIALS AND METHODS

2D and 3D intensity-based visual servoing

In order to avoid time-consuming and difficult US image processing step, we implement an intensity-based visual servoing to control the motions of the probe. This approach is applied first with a classical 2-5 MHz 2D probe (Sonosite, C60) with a frame rate of 25Hz and then with a 3D motorized one (Ultrasonix, 4DC7) that provides 5vol/s.

With a 2D probe, the visual features vector is built with the intensity values of the pixels of a region of interest (ROI) of the US image. The interaction matrix L_s that links the variation of these image features to the motion of the probe is modeled in [2] and used in an image-based visual servoing control law. This interaction matrix is computed from the 3D image gradient that is estimated once at the initial pose of the probe, without being updated during the tracking task.

In the 3D case [3], a 3D deformable grid, containing a set of control points, is attached to the US volume and the intensity-based approach is applied to estimate the control points displacement between the successive volume acquired by the 3D probe. From the displacement of these points, a thin-plate spline model is considered to compute the deformation of the grid that corresponds to the non-rigid motion of the target. A rigid transformation is finally extracted from this motion model and used to control the robot by position-based visual servoing.

Vision/force control

For guaranteeing that a constant force is applied by the probe to the skin during the tracking task, we implement an hybrid vision/force control based on an external control loop approach. In the meantime, it also improves the safety of the task. The force control is used to servo the normal translation motion of the probe while the five remaining dof are controlled by the vision.

Predictive controller

In the classic visual servoing control law, the controller does not take advantage of some knowledge on the disturbance model and more particularly of its periodicity. In this work, we implement in the control loop a repetitive predictive controller (R-GPC) in order to anticipate the effect of the disturbance [4].

RESULTS

The first ex-vivo robotic results on real tissues with the US intensity-based visual servoing are presented here. For this validation, a chicken stuffed with pig liver and kidneys and immersed in a water tank to avoid air gaps inside its body is carried by a 6 dof robot. A 3D periodic motion composed of combined rotations and translations is applied to this phantom. The tracking task is performed successively with a 2D and a 3D US probe, mounted on a six dof anthropomorphic robotic arm, which is also equipped with a force sensor. The experimental setup is presented in Fig. 1. Two optical markers are fixed on the probe and on the phantom and provide the relative pose of both elements thanks to an EasyTrack system. This relative pose is only used as a ground truth to validate the tracking task.

The robotic arm is manually positioned above the phantom and the force control is applied with a desired force of 3N to put the probe in contact with the chicken surface.

Fig. 1 Robotic setup (left) with the animal phantom (right).

A desired ROI is then delineated in the US image and a small back and forth motion is automatically realized to acquire parallel images around the desired image and compute the interaction matrix involved in the control law. A 3D periodic motion along all translations and one rotation (around the probe axis) is applied to the phantom. The disturbance has a period of *8s* and generates amplitudes of motion of *18mm* and *8mm* along horizontal axes and 10mm along the vertical axis with a rotation of the phantom of *4deg*.

The results of one tracking task with the 2D probe are displayed in Fig. 2. The ROI is initialized in the first US image (a) and the visual control is launched. The disturbance motion is applied at *t=20s*, then at *t=160s* the compensation is stopped. To visually validate the task, a visual error is defined as the Euclidean norm of this visual vector and is displayed on the curve (b). After one period of disturbance (at *t=28s*), this error is significantly reduced thanks to the predictive effect of the R-GPC. The curve (c) shows the respect of the force reference throughout the tracking task. Finally the curve (d), obtained thanks to the EasyTrack system, validate the robotic task in terms of pose since the relative pose of the probe with respect to the phantom is maintained constant during the tracking (*t<160s*).

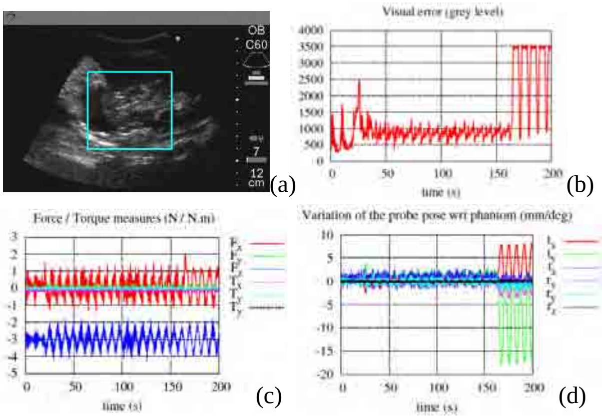

Fig. 2 Ex-vivo results : compensation with a 2D probe.

Experiments were also performed with the 3D probe. In this case, no initialization step is required to compute the image gradient and the visual servoing is launched (at *t=60s*) while a sinusoidal disturbance, of 12.5s of period, occurs. The results of one tracking task are presented in Fig. 3. A 3D grid of 3×3×3 control points is defined in the first US volume provided by the 3D probe (a) to track the motion in successive volumes (see [3]). The central plane of the US volume is shown in (b). The force control ensures a contact force of 3N during the whole robotic task (c) and the EasyTrack system gives a validation of the accuracy of the tracking in terms of pose (d).

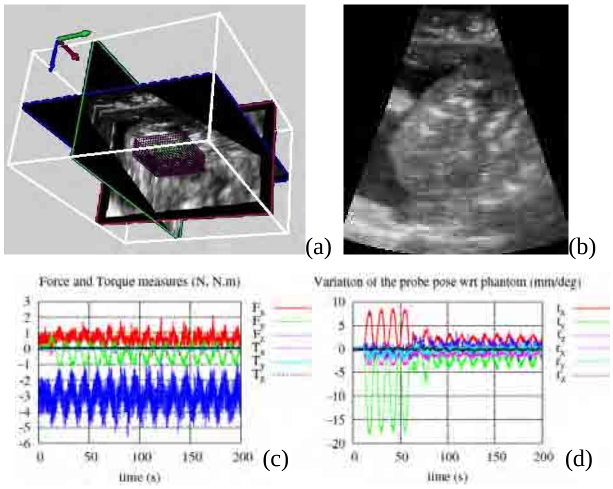

Fig. 3 Ex-vivo results : compensation with a 3D probe.

DISCUSSION

We have presented the first ex-vivo results of actively compensated periodic motions with a robot controlled along five directions with an intensity-based visual servoing and along one direction with force. These results show the asset of the approach that does not require features extraction or segmentation of the image and is therefore well adapted for dealing with any kind of anatomic images. With a 2D probe, a frame rate of 25Hz is reached but an initialization step is required before applying the tracking. The 3D probe, on the other hand, can be used to avoid this step, but the volume rate of 5Hz limits the dynamics of the tracking. In both cases, the vision control has been coupled with a force control running at 1kHz to ensure the contact of the probe.

Acknowledgement

This work was supported by the ANR project US-Comp of the French National Research Agency.

REFERENCES

[1] Krupa A., Fichtinger G., Hager G.D., Real time motion stabilization with B-mode US using image speckle information and visual servoing. Int. Journal of Robotic Research, 2009; 28:1334-1354.

[2] Nadeau C., Krupa A., Intensity-based direct visual servoing of an ultrasound probe. IEEE Int. Conf. on Robotics and Automation, 2011 May; 5677-5682.

[3] Lee D., Krupa A., Intensity-based visual servoing for non-rigid motion compensation of soft tissue structures due to physiological motion using 4D ultrasound. IEEE/RSJ Int. Conf. on Intelligent Robots and Systems, 2011 Sep.; 2831-2836.

[4] Gangloff J., Ginhoux R., De Mathelin M., Soler L., Marescaux J., Model predictive control for compensation of cyclic organ motions in teleoperated laparoscopic surgery. IEEE Trans. on Control System Technology, 2006; 14:235-246.

Left Atrium Surface Flattening for Assisting Guidance in Catheter Ablation Procedures

Rashed Karim[1], Ying-Liang Ma[1], James Housden[1], Aruna Arujuna[2], C. A. Rinaldi[1,2], Mark O'Neill[1,2], Reza Razavi[1,2],Tobias Schaeffter[1] and Kawal Rhode[1]

[1]Division of Imaging Sciences and Biomedical Engineering, Kings College London, UK

[2]Guy's and St. Thomas' Hospitals NHS Foundation Trust, London, UK

rashed.karim@kcl.ac.uk

INTRODUCTION

Minimally-invasive catheter-based interventions are widely used to treat patients with complex cardiac arrhythmias. Traditionally, these procedures have used fluoroscopic imaging with resultant long procedure times and associated radiation exposure. More recently, image-guided navigation has been used for these interventions. Examples include EnSite Velocity (St. Jude Medical, USA), CARTO 3 (Biosense Webster, USA) and EP Navigator (Philips Healthcare, The Netherlands) systems. In each of these systems, three-dimensional (3D) anatomical models of the target cardiac chambers obtained by live catheter tracking, pre-procedural imaging or a combination of both are used to guide the interventions.

3D models displayed on a two-dimensional (2D) screen require frequent interaction from an end-user for switching between views of the chamber of interest. To simplify visualization during navigation, a 2D planar map would allow simultaneous visualization of the entire target anatomical/functional information along with the current interventional device position and any previous treatment points, such as areas that have been ablated. Planar mapping of the left ventricle and brain cortex are common [1]. However, the left atrium (LA) with its complex variable geometry poses a significant challenge to the problem of planar mapping. In our work, we show that it is possible to obtain 2D planar mapping from 3D LA geometry models by parameterizing the surface piece-wise using its smaller segments.

MATERIALS AND METHODS

Prior to the ablation procedure, an MRI examination is carried out and this includes several scans beginning with survey and reference scans, followed by ECG-triggered scans. We utilize two important scans: 1) 3D whole heart respiratory-navigated and cardiac-gated balanced steady-state free precession (bSSFP) scan and 2) delayed-enhancement scan (DE-MRI) for visualization of myocardial fibrosis and scar. The LA geometry is segmented from the bSSFP scan by adapting a mean surface mesh model built from training data [2]. By registering the DE-MRI scan to the bSSFP, delayed-enhancement information can then be projected on the LA surface mesh [3]. This generates a 3D LA surface mesh with DE-MRI scar or fibrosis information available at each mesh polygon. The scar information can be an intensity range [3] or simply binary information from a segmentation algorithm.

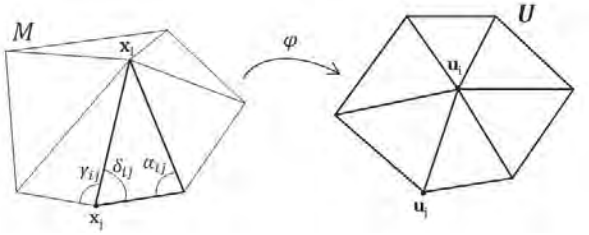

Fig. 1 LA mesh patch (*M*) with its associated flattened planar map (*U*).

Mapping the 3D LA surface mesh to its *square* planar map is possible by considering mesh *patches.* A patch is the immediate neighborhood of a mesh vertex (see patch *M* in Fig. 1 for vertex $\mathbf{x}_i$). Mesh vertices $\mathbf{x}_i$ and $\mathbf{x}_j$ are mapped to their 2D co-ordinates $\mathbf{u}_i$ and $\mathbf{u}_j$ on the planar map by an area and angle-preserving parameterization with a fixed square border [4]. To preserve the area and angles as much as possible, the *distortion* of these between the mesh patch in 3D and its corresponding planar patch in 2D is minimized. This distortion is captured in an energy function consisting of two parts E_A (due to area) and E_X (due to angle):

$$E_A = \sum_{\text{Vertex pairs}(i,j)} \cot\alpha_{ij} |\mathbf{u}_i - \mathbf{u}_j|^2 \qquad (1)$$

$$E_X = \sum_{j \in N(i)} \frac{(\cot\gamma_{ij} + \cot\delta_{ij})}{|\mathbf{x}_i - \mathbf{x}_j|^2} (\mathbf{u}_i - \mathbf{u}_j)^2 \qquad (2)$$

where $\mathbf{u}_i$, $\mathbf{u}_j$ are corresponding planar co-ordinates of $\mathbf{x}_i$, $\mathbf{x}_j$ (see Fig. 1). The total energy $E_T = \mu.E_A + \sigma.E_X$ is then minimized, where μ and σ are weights for the energy functions. It is important to note that the above minimization is for internal vertices only. For boundary vertices, constraints (i.e. boundary conditions) are placed. Since the desired planar map is a square, the boundary vertices of the LA mesh are constrained to the boundary of the square. The LA boundary is the mitral valve annulus, and the mesh is cut in that region. Due to the nature of LA chamber's shape, the boundary is topologically equivalent to a disc which is then mapped and constrained to the boundary of the square of the planar map. The final optimization of E_T, and thus the mapping, is accomplished using the iterative conjugate gradient method [4] and use of Lagrange multipliers for boundary conditions. Finally, the DE-MRI scar information in the 3D LA surface mesh is simply transferred to the planar map using the planar mapping of each vertex in the 3D mesh to its corresponding vertex in 2D.

RESULTS

MRI data from 10 patients presenting for first (n=7) or redo (n=3) ablation procedure were analyzed by using post-ablation scans of first-time and pre-ablation scan of re-do patients. Planar maps were generated from 3D surface LA mesh with scar information. Points were selected on the LA mesh and corresponding locations on planar maps were visually verified (see Fig. 2). The geometry of scar around veins and breaks or gaps in scar was easily visualized in one single view with no interaction necessary.

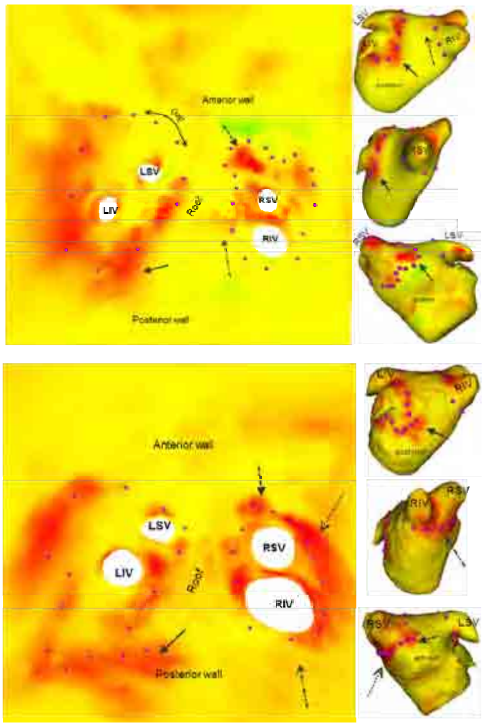

Fig. 2 Planar maps (left) and different orientations of LA mesh (right) from a redo case (top) and post first ablation (bottom). Corresponding regions are labeled with dashed, dotted and filled arrows representing three different regions. Areas in red represent sites of previous ablation (upper panel) and recent ablation (lower panel). A typical lesion set would aim to encircle completely the pulmonary veins as indicated by the stylised purple points. Abbreviations for veins – by convention LSPV, RSPV,LIPV, RIPV, LPVs, RPVs

The planar maps minimize area distortion during mapping but do not preserve distances as it is theoretically impossible to achieve this when mapping to a fixed square border. To measure the amount of distortion in distances between the 2D planar map and its 3D mesh, pairs of points were randomly picked on the planar map and their corresponding locations in 3D determined. The Euclidean distance on the planar map was compared to the *geodesic* (i.e. surface) distance in 3D, and the factor by which the distances differ was determined. The factor or distortion ratio is the ratio of 2D to 3D distance. Fig. 3 segments these distances to three classes: small (< 10 mm), medium (< 25 mm) and large (> 25 mm) for each LA mesh. The smaller distances had the largest variation in distortion: Average [max, min, σ] = [6, 0.2, 1.7]. In comparison, medium distances had lesser varying distortions: [max, min, σ] = [2, 0.1, 0.4]. This likely suggests that distances close to the boundary were distorted greater than internal locations. Medium to large distances span along the entire length of the map and are thus likely to contain regions of both small and large distortions, thereby cancelling out this effect (consider distortion ratios less than 1 to be *negative* distortions). Small distances selected close to the boundary can exhibit large distortions as opposed to only small distortions for points not near the boundary. This explains the high variation in small distances. This degree of distortion near the boundary is also evident in the geometry of scar near boundaries (see Fig. 2).

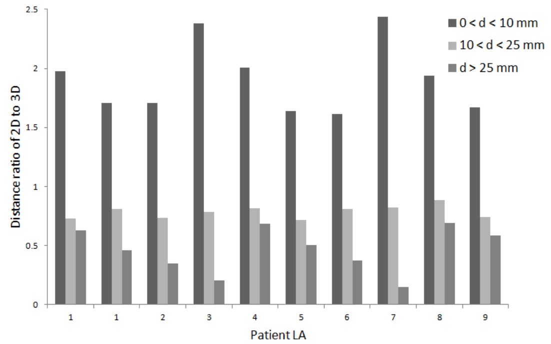

Fig. 3 Distance distortion ratios for all 10 patient LA meshes analyzed ablation (bottom). Within each patient, geodesic distances (*d*) on the LA meshes were classified separately as small ($d < 10$), medium ($10 < d < 25$) and large ($d > 25$).

CONCLUSIONS

The work presents a novel approach to visualize LA geometry along with scar information on a 2D planar map. Procedural guidance using a 3D mesh can be cumbersome and demands constant interaction with the geometry. The use of planar maps with point-by-point catheter technologies (manual or robotic) could decrease the complexity of navigation and even improve navigation by less experienced operators. Future work will look into deforming the square map to a universal square template with three/four holes of fixed radii representing pulmonary veins. This may further simplify and standardize the map for navigation.

REFERENCES

[1] B Fischl, M. Sereno and A. Dale, Cortical surface-based analysis: Inflation, flattening, and a surface-based coordinate system, NeuroImage 9(2), 1999.

[2] J. Peters, et al., Automatic whole heart segmentation in static magnetic resonance image volumes," Proceedings of MICCAI 2007, pp. 402–410, 2007

[3] Knowles B., Caulfield D, et al, Three-dimensional visualization of acute radiofrequency ablation lesions using MRI for the simultaneous determination of the patterns of necrosis and edema, IEEE Trans. Bio. Eng., 57(6) 2010.

[4] M Desbrun, M. Meyer and P Alliez. Intrinsic parameterizations of surface meshes. Eurographics 21(3), 2002.

Image-Guided Transoral Robotic Surgery for the Treatment of Oropharyngeal Cancer

Philip Pratt[1], Eddie Edwards[2], Asit Arora[2], Neil Tolley[2], Ara Darzi[2], Guang-Zhong Yang[1]

[1]Hamlyn Centre for Robotic Surgery, Imperial College London
[2]Department of Surgery and Cancer, Imperial College London
p.pratt@imperial.ac.uk

INTRODUCTION

Transoral Robotic Surgery (TORS) represents a new treatment paradigm for patients with head and neck cancer. Increasingly, it is being adopted to perform minimally invasive oropharyngeal, nasopharyngeal and skull base tumour resection. TORS overcomes many of the limitations associated with conventional surgery [1]. Safe and accurate tumour localisation is of paramount importance due to the inherent anatomical constraints, close proximity of important neurovascular structures and the significant risk of functional morbidity. Two-dimensional image-guided TORS has been shown to facilitate tumour resection [2]. Building on the effective three-dimensional visualisation and registration system already developed for robotic partial nephrectomy [3], the objective of this study is to investigate the feasibility of the approach in TORS, including an assessment of the degree of tissue deformation and the identification of key navigational targets.

MATERIALS AND METHODS

The 3-arm *da Vinci* Si Surgical System robot (Intuitive Surgical, Sunnyvale, CA, USA) was used to perform TORS in a 58 year old male patient diagnosed with a T2N0 oropharyngeal squamous cell carcinoma involving the left tonsil. Figure 1 shows the intra-operative view at 4 key stages following insertion of the Boyle Davis mouth gag and 12mm 30° stereo endoscope. Resection was performed using 5mm endo-wrist instruments (Maryland forceps and monopolar spatula). The initial incision (a) was made lateral to the anterior tonsillar pillar in line with the pterygo-mandibular raphe. Dissection proceeded (b) along the lateral aspect of the pharyngeal constrictor muscles which were transected over the prevertebral fascia (c) to achieve an adequate posterolateral tumour resection margin. The lateral resection margin was the medial pterygoid muscle (lateral to which runs the internal carotid artery). Branches of the pharyngeal venous plexus and facial artery were controlled with clip ligation prior to excising the specimen (d) en-bloc. The following targets were identified for image guidance using augmented reality overlay:

- Tumour - in particular, rapid localisation thereof, penetration depth and relevant adjacent anatomy;
- Vessels - accurate visualisation of internal/external carotid artery and internal jugular vein; and
- Appropriate registration anatomy - including the lateral pharyngeal fat pad, teeth and hyoid bone.

In order to ensure an adequate resection margin while avoiding major vascular structures, these targets have the potential to be used to help mark the excision boundary. This is of particular relevance for submucosal oropharyngeal tumours which are not directly visible, and large (T3/4a) oropharyngeal lesions.

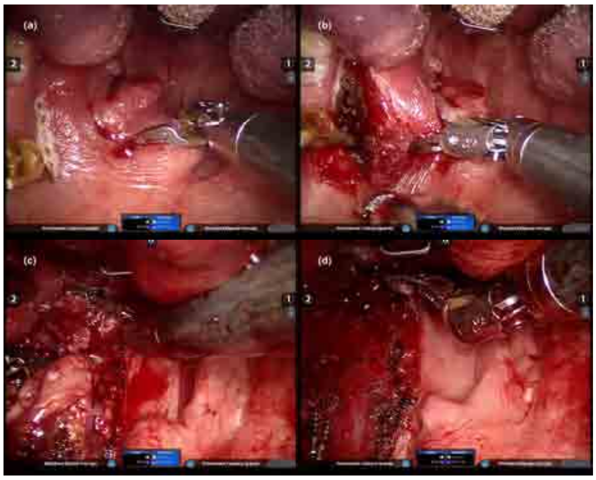

Fig.1 Key procedural stages (left-to-right from top): marking of excision boundary with cautery spatula; initial dissection between muscle planes; base-of-tongue posterior dissection; and wall defect following tumour removal.

The NVIDIA Quadro Digital Video Pipeline [4] forms the basis of the guidance system architecture. The same two-stage, semi-automated registration scheme used in the partial nephrectomy study [3] was employed. Mesh geometry for the chosen navigational targets was created from MRI and PET/CT preoperative imaging. Single corresponding features located in the geometry and stereo surgical scene were used to fix the translational degrees of freedom. The remaining rotational degrees of freedom were adjusted manually in order to achieve real and virtual lumen structural alignment.

In addition to mesh-based rendering, support for direct volume rendering was provided using the Fovia High Definition Volume Rendering® (HDVR®) engine [5]. Both simple alpha blending and *inverse realism* [6] were used to fuse the endoscopic and rendered views. Footage was recorded in full stereo HD (1920×1080i), while subsequent retrospective analysis was performed at SXGA (1280×1024) resolution.

RESULTS

Figure 2 illustrates MRI segmentation and semi-transparent mesh visualisation, and contrasts this with direct volumetric rendering of the equivalent PET/CT image. In each modality, the target lesion was clearly identifiable, with MRI offering marginally better differentiation of tissue characteristics.

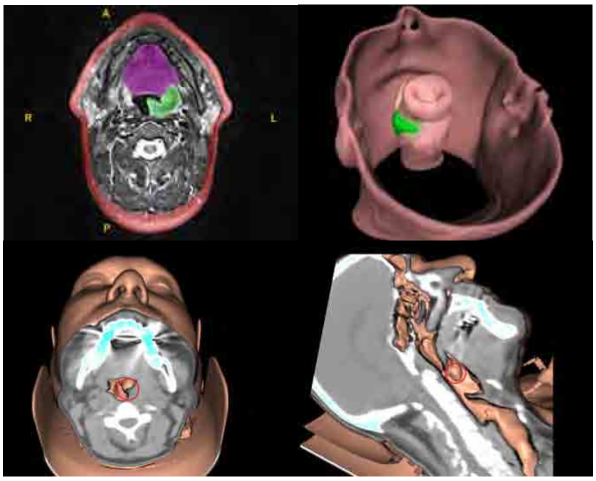

Fig.2 Preoperative analysis (left-to-right from top): segmented MRI showing tumour, tongue and surface of head; mesh-based model of lumen showing depth of tumour penetration; volumetrically rendered PET-CT axial cross-section; and corresponding sagittal cross-section (tumour circled in red).

Figure 3 shows post-registration examples of augmented reality overlay, including simple alpha blending, *inverse realism*, mesh-based models and direct volumetric rendering. Tissue 'windows' were painted manually.

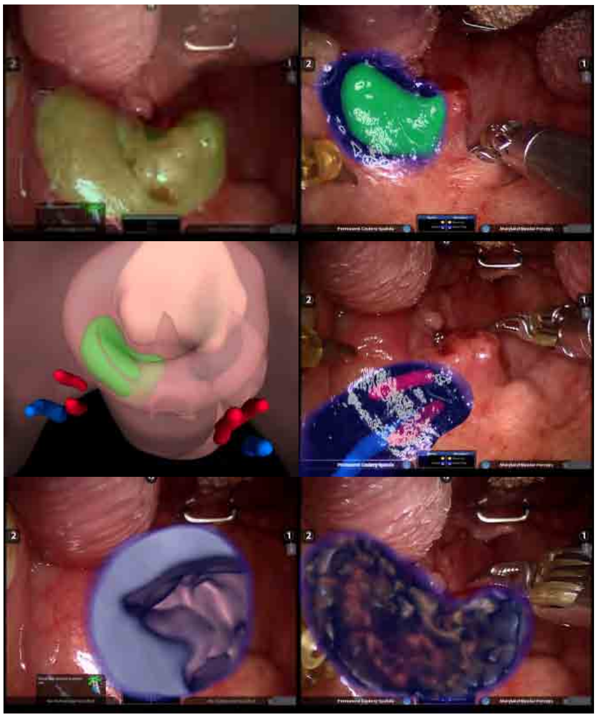

Fig.3 Augmented reality visualisations (left-to-right from top): blended overlay of registered tumour model; painted inverse realism window; vessel models; corresponding registered overlay; volume rendered PET/CT lumen overlay; and MRI volume showing tumour boundary (white edges).

In each case, only one of the two stereo channels is shown. In practice, pairs of stereo visualisations are produced in accordance with the calibrated endoscope intrinsic and extrinsic camera parameters. During the MRI segmentation and model-building phase, the axial voxel spacing of 5.2mm was found to be barely adequate. Unfortunately, for this initial study, it was not possible to control the acquisition protocol.

DISCUSSION

Retrospective analysis of procedure footage and preoperative imaging indicates that there are beneficial opportunities for image guidance in TORS. There are sufficient anatomical landmarks to fulfill the requirements of the registration scheme. The degree of tongue muscle deformation induced by gag placement is significant, but the lumen morphology remains relatively intact, sufficiently so for immediately useful augmented reality overlay. With the ultimate view of achieving translation into live human cases, the following enhancements are also planned:

- Development of improved preoperative image acquisition protocols to ensure high-fidelity mesh-based and volumetric rendering;
- Better registration automation through stereo depth map recovery and geometry alignment;
- Rendering from virtual viewpoints through texture capture and scene reconstruction;
- Better manipulation of volume transfer functions;
- Use of 2D/3D transoral ultrasound; and
- Use of image-constrained biomechanical models to account for intraoperative tongue deformation.

Detailed quantitative validation experiments will be performed to confirm that satisfactory levels of semi-automated registration accuracy, similar to those observed in the context of partial nephrectomy [3], can be achieved without disruption of surgical workflow.

ACKNOWLEDGEMENTS

The High Definition Volume Rendering® SDK is used under licence from Fovia, Inc.. The authors extend their gratitude to Professor Wladyslaw Gedroyc and also the theatre staff at the Wellington Hospital, London.

REFERENCES

[1] Arora, A., Cunningham, A., Chawdhary, G., Vicini, C., Weinstein, G., Darzi, A., Tolley, N.: Clinical applications of Telerobotic ENT-Head and Neck surgery. Int J Surgery (2011) 9:277-284

[2] Desai, S., Sung, C.K., Genden, E.: Transoral robotic surgery using an image guidance system. The Laryngoscope (2008) 118:2003-2005

[3] Pratt, P., Mayer, E., Vale, J., Cohen, D., Edwards, E., Darzi, A., Yang, G.Z.: An effective visualisation and registration system for image-guided robotic partial nephrectomy. J Robotic Surgery (2012) 6:23-31

[4] http://www.nvidia.com/object/quadro_dvp.html

[5] http://www.fovia.com

[6] Lerotic, M., Chung, A., Mylonas, G., Yang, G.Z.: pq-Space based non-photorealistic rendering for augmented reality. MICCAI Part II (2007) LNCS 4792:102-109

Raven II™: Open Platform for Surgical Robotics Research

H. Hawkeye King[1], Lei Cheng[1], Philip Roan[1], Diana Friedman[1], Sina Nia Kosari[1], Ji Ma[2], Daniel Glozman[2] Jacob Rosen[2], Blake Hannaford[1]

[1]*University of Washington, Seattle, WA, USA*

[2]*University of California, Santa Cruz, CA, US*

INTRODUCTION

In this paper we present a new platform for surgical robotics research: the Raven II™. The goal of this work is to provide a robot with which researchers can explore new techniques in telerobotic surgery by modifying the hardware and software to meet their needs.

The first generation RAVEN[1] was designed for experiments in long distance, Internet based telepresence surgery. Several studies using RAVEN by our team, demonstrated feasibility of Internet based teleoperation to remote and extreme environments [2]. Investigations using the Raven also measured the impact of common Internet latencies on surgical performance and explored interoperability among a wide range of telesurgery master/slave robots [3,4].

Raven II is a second-generation system that includes all the same Internet telepresence capabilities, and features many improvements that make it better suited for a wide range of telesurgery research.

With support from the US National Science Foundation Computing Research Infrastructure program, seven Raven II systems were built, and in February 2012 they were distributed to US based researchers at Harvard University, Johns Hopkins University, University of Nebraska, University of California (UC) Los Angeles, UC Berkeley, UC Santa Cruz, and University of Washington. Having the Raven II hardware creates a new opportunity for groups to share design improvements, replicate results, and collaborate on research. Having a common open-source code base allows new developments to be shared among multiple institutions. The authors believe this is the best route to continued innovation in telerobotic surgery.

Design of the Raven II is described in Materials and Methods below. Project completion is described in the Results section, and the significance of this new platform is treated in the Discussion.

MATERIALS AND METHODS

Raven II evolved from the original RAVEN surgical system. Mechanically Raven II differs from the RAVEN in several significant respects. The system inertia, especially due to reduced mass of a linear-actuation guide rail, was significantly reduced from RAVEN to Raven II for improved control performance. Link mass of RAVEN was 4.6 kg, compared to 2.0 kg for Raven II. In addition, the Raven II mechanism was designed to accommodate either two or four arms. Optimization was performed for mechanism isotropy over the ranges of motion in laparoscopy, as well as maximizing common workspace among the four maniplators. (For complete details see [5].) A new, patented tool design provides six degrees of Cartesian motion and grasping [6]. A unique feature of the tool is a wrist design that eliminates cable coupling between degrees of wrist actuation.

The RAVEN used Maxon EC40 with 12.25:1 gear reduction and EC32 DC brushless motors. Brushless motors such as these provided better torque-to-weight ratio than brushed motors. However, they require significant additional cabling and complex expensive motor controllers. Raven II uses Maxon RE40 and RE30 brushed DC motors with a 12:1 and 3.7:1 gear ratio respectively. This has not made noticeable difference in performance, and has reduced cabling and electronics complexity.

Raven II electronics have many of the same features as RAVEN, but in a compact form factor more easily situated in a laboratory environment or carried to the field (Figure 1). A single nineteen-inch desktop rack holds the robot power supply, motor controllers and I/O for the two arms and a Linux PC. As in RAVEN, a key hardware safety feature is a DL05 programmable logic controller that monitors the robot inputs and outputs and has the capability to trigger fail-safe brakes on the frist three (gross positioning) mechanism joints. Z6A6 and Z12A8 servo amplifiers (Advanced Motor Control, Camarillo, CA) drive the robot’s smaller and larger motors at six and twelve amps respectively. I/O with the computer is via a custom designed eight channel USB I/O board. This board can read 8 encoder signals and write 8 analog motor outputs in less than 125 µs.

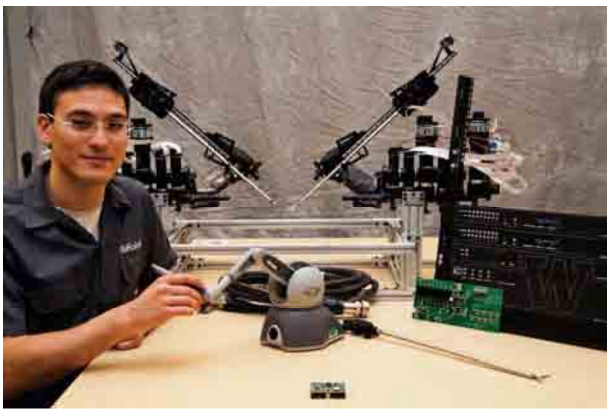

Fig. 1 Raven II: a second-generation surgical robotics research platform.

Raven II software has been dramatically revised from RAVEN. As with RAVEN, the basic sensor-actuator control loop is closed through the Linux PC at one thousand hertz. To achieve the necessary speed and determinism RAVEN used an RTAI Linux kernel module. Now, Raven II uses CONFIG_PREEMPT_RT, a hard real-time patch for the Linux Kernel. The patch satisfies all timing requirements, providing an accurate 1kHz control loop. It also allows real-time software to execute in user space with minimal modification, thus simplifying the software development environment.

In addition the Raven II software has been integrated with Robot Operating System (ROS) [5]. ROS is a modular, open source robotics middleware package that makes it very easy to combine the Raven II software with other robotics software libraries. For example, Raven II state information is output using ROS message passing mechanisms, and can be plotted in real time using "rosbag" or used by a teleoperation system to calculate force-feedback. In addition a robot visualization tool (shown in Figure 2) was developed using the "rviz" ros module. The ROS parameter server is used for initial gains configuration of the robot. Despite integration with ROS raw UDP sockets are also supported for teleoperation control, since our research has shown slightly better performance this way.

The Raven II control software was rewritten in C++, with the goal of making it easy for collaborators to implement new controllers and features. At the same time, much of the modularity of the original RAVEN code was maintained. All Raven II partners have access to a common source code repository that will include future contributions from all sites.

Several Internet-based collaboration tools foster communication among research peers and provide peer-to-peer support for the new systems. A wiki has been created to hold documentation and keep it up to date. An online discussion forum, integrated with the wiki is also in place, and has proven crucial to supporting the deployed systems and sharing information. Finally a blog kept participants up-to date as the robots were developed, and is now used for periodic news updates.

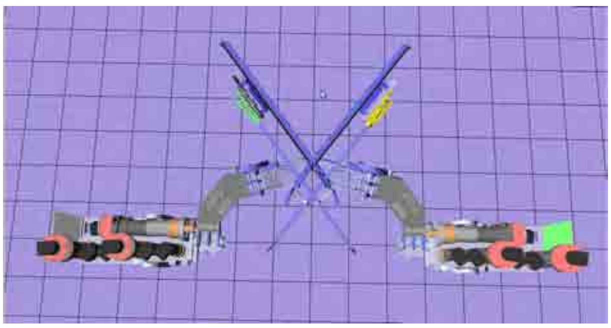

Fig. 2 Integration with Robot Operating System makes the software compatible with many off-the-shelf robotics packages. This figure shows the use of the "rviz" package for visualization of the robot.

RESULTS

Dual-arm Raven II systems were completed in February 2012 and provided to seven institutions around the United States. One robot suffered damaged to two motor encoder shafts which were replaced. In all partner locations, the robots are set up and running and new research is being devised and implemented.

Community participation via dedicated Internet forums has been active with over one hundred posts in February and March. This hints strongly at further collaboration among groups.

DISCUSSION

Raven II is a major improvement over the original RAVEN system and is a robust platform for MIS robotics research. Open-source control software simplifies development of new modules, and ROS integration means it's easy to directly interface with many existing robotics packages.

In the future, revisions are planned to fix some minor hardware anomalies. Also, many new avenues of research are being pursued on this platform involving haptic feedback for improved control, machine learning, image guidance and more.

Raven II is now a common surgical robotics research platform in use by seven leading U.S. based research groups with more to follow. This forms the basis of a promising new research network.

REFERENCES

[1] M. Lum, D. Friedman, G. Sankaranarayanan, H. King, K. Fodero, R. Leuschke, B. Hannaford, J. Rosen, and M. Sinanan, "The Raven- Design and Validation of a Telesurgery System," Int. J. of Robotics Research, v.28, No.9, pp. 1183–1197, 2009.

[2] C.R.Doarn, M. Anvari, T. Low, and T.J. Broderick, "Evaluation of Teleoperated Surgical Robots in an Enclosed Undersea Environment," Telemedicine and e-Health, May 2009, v.15 No. 4, pp. 325-335.

[3] H. H. King, B. Hannaford, K.-W. Kwok, G.-Z. Yang, P. Grifths, A. Okamura, I. Farkhatdinov, J.-H. Ryu, G. Sankaranarayanan, V. Arikatla, K. Tadano, K. Kawashima, A. Peer, T. Schauß, M. Buss, L. Miller, D. Glozman, J. Rosen, and T. Low, "Plugfest 2009: Global interoperability in telerobotics and telemedicine," ICRA 2010.

[4] M.J.H. Lum, J. Rosen, T.S. Lendvay, M.N. Sinanan, B. Hannaford, "Effect of Time Delay on TeleSurgical Performance", ICRA 2009.

[5] Z. Li, C. Glozman, C. Milutinovic, and J. Rosen, "Maximizing Dexterous Workspace and Optimal Port Placement of a Multi-Arm Surgical Robot", ICRA 2011.

[6] M. Quigley, B. Gerkey, K. Conley, J. Faust, T. Foote, J. Leibs, E. Berger, R. Wheeler, and A. Ng, "ROS: an open-source robot operating system," Open-source software workshop of ICRA 2009.

[7] M.R. Moreyra, "Wrist with decoupled motion transmission", Nov. 2005, US Patent 6,969,385.

Robotic Control of a Traditional Flexible Endoscope

J.G. Ruiter[1,2], G.M. Bonnema[1], M.C. van der Voort[1], I.A.M.J Broeders[1,3]

[1]*University of Twente, Enschede*

[2]*DEMCON advanced mechatronics, Oldenzaal*

[3]*Meander Medical Centre, Amersfoort*

j.g.ruiter@utwente.nl

INTRODUCTION

In flexible endoscopy the interior surfaces of the gastrointestinal, reproductive and respiratory tracts are assessed. The physician uses a flexible endoscope with a camera at the steerable distal tip that is introduced in the natural body openings. Instruments can be inserted in the endoscope. These protrude from the tip and enable performing interventions, like resection of small polyps. Current commercial available flexible endoscopes and its instruments have limited capacity to execute procedures that require advanced maneuverability. For that reason surgical procedures, like endoscopic submucosal dissection (ESD) of large lesions, are not generally adopted by gastroenterologists. The recent concept of natural orifice transluminal endoscopic surgery (NOTES) that asks even more dexterity is still in its infancy because of the lack of user-friendly sophisticated tools [1]. Main usability problems are related to the control section at the proximal end. Because of the configuration of control elements the physician often faces handling problems. For instance, approximately 20% of the physicians are using both hands for the control section, while an assistant manipulates shaft and instruments according to spoken instructions [2]. Drawback of this workflow is that the physician is missing valuable force feedback information on tissue interaction, and in addition communication errors easily occur. At present there are no flexible endoscopes available that can be controlled in an intuitive and user-friendly way by one person. Robotic technology has the potential to improve current practice and is likely to play a major role in performing advanced interventions easily and safely. Computer techniques, like motion scaling, can be implemented to support physicians. We propose a robotic system that interacts with a traditional flexible endoscope. In this way current endoscope qualities, like cleanability and good image quality, are maintained and costs related to replacement of endoscopic equipment is prevented.

Previous work [3] concentrated on redesign of the control section to obtain single person endoscope steering for diagnosis. With the addition of instruments in therapeutics, single person control can only be obtained if the flexible endoscope can be operated with one hand and instruments with the other. We combined the robotic steering module that actuates the distal tip in [3] with a newly designed robotic module that actuates

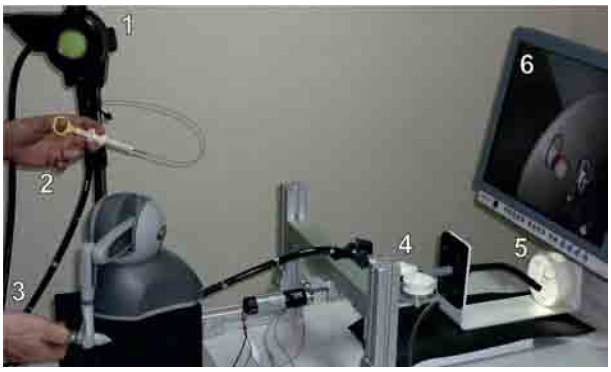

Fig. 1 Robotic control flexible endoscope: (1) Traditional endoscope with driving means for tip steering, (2) Manual instrument control (3) Multi-DOF controller for tip steering and shaft control, (4) Driving means for shaft actuation, (5) Training model, (6) Monitor.

the shaft of the flexible endoscope. The physician uses one multi-degrees-of-freedom (multi-DOF) input controller to steer, advance, rotate, and maintain the position of the motorized flexible endoscope, while the other hand is able to manipulate instruments, as shown in Fig. 1. The control handle of the input controller resembles the endoscope tip. The operator experiences control like directly holding the camera at the distal tip and movements of the physician’s hand and the camera are matched to obtain intuitive manipulation.

Robotic control is not intended for endoscope advancement in diagnosis that requires precise interpretation of interaction forces between endoscope and lumen, but it enables the physician to intuitively manipulate the tip of the endoscope in the operating area. It creates a stable endoscopic platform without the need of an assistant and allows for small robotic movements of the distal tip when the spatial range of the instruments is too small. We evaluated the usability of the robotic endoscope to perform these tasks compared to current flexible endoscopy.

MATERIALS AND METHODS

In Fig. 1 the complete system is depicted that is used in our experiment to assess the intuitiveness and user-friendliness of robotic flexible endoscopy. The driving means for the endoscope tip consist of a motor unit that is connected to the navigation wheels of the endoscope to actuate left/right and up/down movements. The endoscope shaft is clamped between two V-shaped wheels that are actuated to advance the shaft. Axial rotation of the shaft is achieved by rotating the frame on which the wheels are positioned. A Phantom Omni haptic device (Sensable Technologies) is a suitable input controller to steer these four degrees of freedom (4-DOF). We used position control as transfer function between user input and end effector displacement. Position control is most intuitive in tasks that require accurate manipulation in a limited workspace and is implemented for tip as well as shaft control [4]. A hold-to-run button on the control handle prevents unintended movements of the endoscope and locks it into position when releasing the input device.

We tested three setups in our experiment. In one setup we used conventional endoscope operation with assisted instrument control as a reference for robotic flexible endoscopy. The second setup allows 4-DOF robotic steering and shaft control with one hand and manual instrument control with the other hand, as described in this paper. The third setup uses the robotic steering module of [3] with a Phantom Omni controller to obtain 2-DOF single handed tip steering. The shaft is manually operated with the other hand and the instrument by an assistant. The last setup is added to evaluate the influence of bimanual endoscope control by the physician. The intuitiveness is expected to be higher when steering as well as shaft control is performed singlehandedly, as in the second setup.

Subjects, without experience in endoscope handling, were asked to perform 2 tasks that require advanced endoscope maneuverability. The absence of experience enabled testing of intuitiveness. First, subjects had to pick up a specific ring from a pion with a grasper and place it on a designated pion. Secondly a ring had to be guided from one end of a tortuous wire loop to the other end. Instrument control was limited to opening and closing the grasper. Each of the six possible orders of the three setups was performed equally often to correct for learning effects and fatigue. The 12 subjects (aged 19-50 years, 2 women and 10 men) were asked to perform task 1 once as exercise before the evaluation was started. Our focus was to test the control usability of the robotic endoscope. Usability is defined by the International Standardization Organization (ISO) as: ”the extent to which a product can be used by specific users to achieve goals with effectiveness, efficiency, and satisfaction in a specified context of use”. In our experiment the following dependent variables were measured:

- Tasks completed (effectiveness)
- Time required for tasks (efficiency)
- Workload analysis based on a modified NASA Task Load Index, measuring mental and physical demand [5] (efficiency)
- Rank interfaces to preference (satisfaction)

RESULTS AND DISCUSSION

The quantitative results of the experiment are depicted in Table 1. The results show that robotic control improves efficiency and satisfaction. All participants were able to complete the tasks with all setups, so improved effectiveness is not demonstrated in this experiment. The results of the 2-DOF robotic setup show no significant differences compared to the 4-DOF setup. However, almost all subjects preferred the 4-DOF setup. Participants valued its intuitiveness, its accuracy, the feeling of being in control, and its single person setup. Additionally, about 50% of the subjects indeed complained about the 2-DOF robot being more mentally demanding. Some of them constantly switched between tip steering and shaft manipulation during the procedure. What subjects missed in all setups was independent axial rotation of the grasper to orient it to grasp a ring. Axially rotating the shaft resulted in translational movements of the tip when it was bent. In the 4-DOF robotic setup this could be compensated for by actuating tip steering in the opposite direction. This was not implemented yet.

Table 1. Quantative results experiment

Setup	conventional	robotic 2-DOF	robotic 4-DOF
Task 1 (sec.)[a]	356 (200)	158 (133)	148 (114)
Task 2 (sec.)[a]	183 (109)	98 (98)	84 (75)
Workload (max. 25) [a]	20 (4)	12 (3)	10,5 (2)
Preference (no.1/2/3)	0/1/11	1/10/1	11/1/0

[a] Values are represented as median (standard deviation)

The robotic system presented in this paper showed its usability, but is not ready to be implemented in the current clinical workflow. We are working on translating this proof-of-principle into a product, that takes safety, cleanability, and easy positioning close to the patient into account. Additionally all controls of the current endoscope for functions like insufflation, suction and rinsing are integrated in the control handle of the multi-DOF input controller. Expert testing is required to test performance in clinically relevant advanced procedures.

ACKNOWLEDGMENTS

The authors would like to thank Michel Franken, Rob Reilink, Koen Swinkels, Chris Nieuwenhuis and Kevin Voss for their contribution in building the robotic system. This research is funded by the Dutch Ministry of Economic Affairs and the Province of Overijssel, within the Pieken in de Delta (PIDON) initiative.

REFERENCES

[1] Swanstrom LL. Novel endoscopic platforms for endoluminal and NOTES Surgery. Proc. of the Hamlyn Symposium on Medical Robotics. 2009 Jun:5-6.

[2] Liberman AS, Shrier I, and Gordon PH. Injuries sustained by colorectal surgeons performing colonoscopy. Surgical endoscopy. 2005 Oct;19(12):1606-1609.

[3] Ruiter JG, Rozeboom ED, van der Voort MC, Bonnema GM, Broeders IAMJ. Design and evaluation of robotic steering of a flexible endoscope. Biorob 2012. In preparation.

[4] Zhai S. Human performance in six degree of freedom input control. Ph.D. dissertation. Dept. of Industrial Engineering, University of Toronto. 1995.

[5] Hart SG, Staveland LE. Development of NASA-TLX (Task Load Index): Results of empirical and theoretical research. In Human Mental Workload. 1988:239-250. Amsterdam: North Holland Press.

Micro Medical Robot with Magnetic Remote Control in 3D Space

M. Yasui[1], M. Ikeuchi[2], K. Ikuta[2]

[1]*Graduate School of Frontier Biosciences, Osaka University*

[2]*Research Center for Advanced Science and Technology, The University of Tokyo*

Ikuta@rcast.u-tokyo.ac.jp

INTRODUCTION

We can control magnetic micro robots by using external magnetic fields. This means that magnetic micro robots are remotely controllable, and do not require batteries and electrical wires. Due to these characteristics, we expect that magnetic micro robots will be applied for minimally invasive surgery. Fig. 1 shows the concept of the micro robot. An operator can observe and control this micro robot in real time through a microscope. The micro robot can drive by a rotational magnetic field, because it is a helical structure and magnetized radial direction.

Our group succeeded in controlling the screw-type micro robot in a micro capillary [1,2]. The micro robot was fabricated by using microstereolithography (MSL) and magnetically photocurable (MPC) polymer. MSL is a micro fabrication technology in which a UV laser cures photocurable resin layer by layer fabricating a 3D microstructure (Fig. 2(a)). MPC polymer contains magnetic particles and a viscosity increasing agent (Fig.2 (b)).

To apply this magnetic micro robot for minimally invasive surgery, we need to control the magnetic micro robot 3 dimensionally, not only in a micro capillary. In this report, we report 1) newly developed density controllable MPC polymer, 2) 3D control of a magnetic micro robot, and 3) cell size magnetic micro robot.

DENSITY CONTROLLABLE MPC POLYMER

Since gravity affects on the control property of micro robot, it is important to adjust the density of micro robot. We developed density controllable MPC (DMPC) polymer to realize neutral buoyancy. To compound DMPC polymer, we added hollow microcapsules (F-80SDE, Matsumoto Yushi-Seiyaku Co., density 0.03 g/cm^3, average diameter 20μm) into MPC polymer (Fig.3 (a)). We used ferrite particles, fumed silica and SCR770 (D-MEC) as magnetic particles, viscosity increasing agent and photocurable polymer.

To understand the effect of microcapsules on the relative density of DMPC polymer, we inspected the relationship between the concentration of microcapsules and the relative density of DMPC polymer. Fig. 3(b) shows the relationship between relative density of DMPC polymer and concentration of microcapsules with different concentration of ferrite particles (0-30wt%). This result indicates that we can control the density by adjusting the concentration of microcapsules.

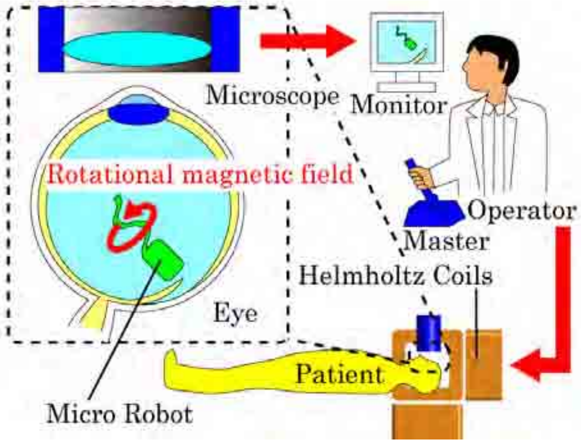

Fig. 1 Concept of 3D and remote controllable magnetic micro robot

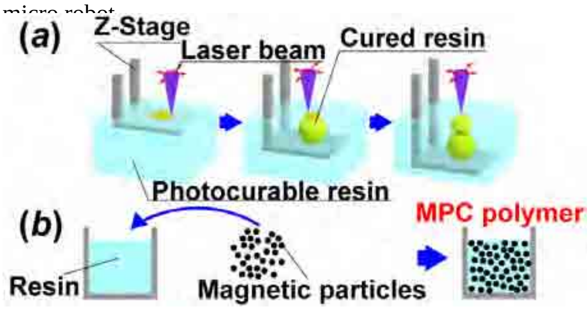

Fig. 2 (a) Microstereolithography, (b) Magnetically photocurable (MPC) polymer.

(a)

(b)

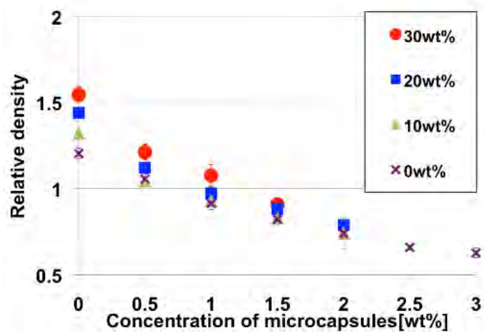

Fig. 3 (a) Density controllable MPC polymer, (b) The relationship between relative density and concentration(0-3wt%) of microcapsules with different concentration(0-30wt%) of magnetic paticles.

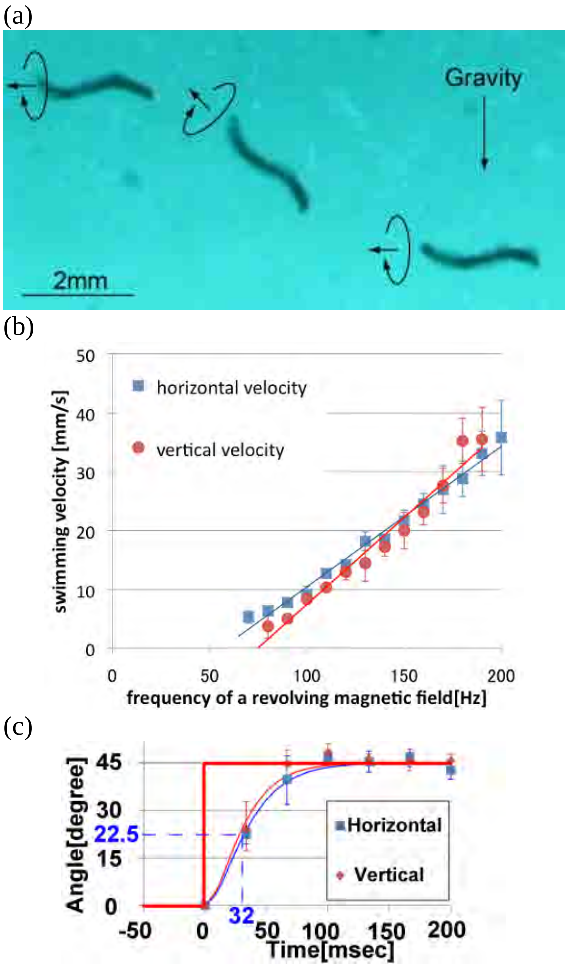

Fig. 4 (a) 3D control of magnetic micro robot in water, (b) Driving characteristics of micro robot, (c) Dynamic property.

3D CONTROL OF MICRO ROBOT

We fabricated magnetic micro robot with neutral buoyancy by using DMPC polymer (microcapsules: 1.5 wt%, ferrite particles 30 wt%) and MSL, and magnetized the micro robot in a radial direction. Then, we applied a rotational magnetic field into this micro robot in water. As shown in Fig. 4 (a), this micro robot drove 3 dimensionally in water.

Next, we investigated the relationship between vertical and horizontal driving velocity of the magnetic micro robot and frequency of the rotational magnetic field (3.4 mT). Fig. 4 (b) indicates the relationship between driving velocity and frequency of the revolving magnetic field. The magnetic micro robot did not drive over 200 Hz. Experimental results show that the horizontal and vertical driving properties are almost the same value. This result means the magnetic micro actuator possesses neutral buoyancy.

We investigated the dynamic characteristics when the direction of a rotational magnetic field (3.4 mT, 50 Hz). Fig. 4(c) indicates the dynamic characteristics of magnetic micro robot's changing angle 45 degrees from horizontal to vertical direction, and from horizontal to horizontal direction. From Fig.4 (c), we can see that the

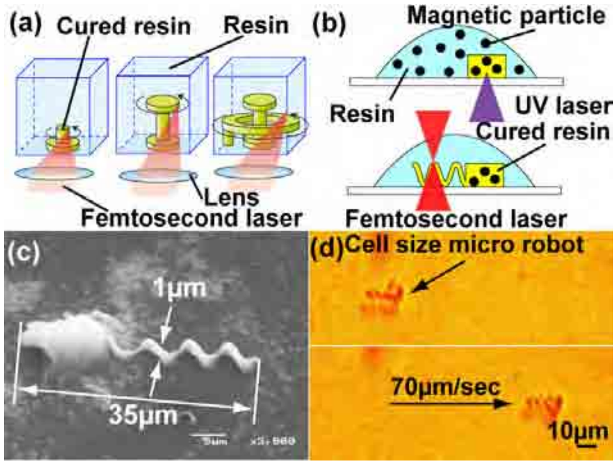

Fig. 5 (a) 2 photon microstereolithography, (b) minituarizing process, (c) cell size magenetic micro robot, (d) driving in water.

dynamic characteristics do not depend on the direction. Furthermore, the delay time was 32 msec in both horizontal and vertical directions. These characteristics are useful to control the magnetic micro robot three-dimensionally.

CELL SIZE MICRO ROBOT

We have developed a fabrication process for miniaturizing magnetic micro robot. We used two-photon microstereolithography (2P-MSL). In 2P-MSL, only the focused point of femtosecond laser cures, and by scanning the point we can get a 3D microstructure (Fig. 4(a)). In the miniaturizing process, first we fabricate a magnetic dot structure by MPC polymer and MSL, and then fabricate a 3D microstructure (Fig. 4(b)). Fig. 4(c) shows the fabricated cell size magnetic micro robot. We also succeeded in driving this micro robot in water (Fig. 4(d)). The amplitude and frequency of rotational magnetic field is 15 mT and 75 Hz.

CONCLUSION

We have developed the world's first density controllable magnetically photocurable polymer, and fabricated a magnetic micro actuator possessing neutral buoyancy. Moreover, we constructed 3D driving control system, and we verified the driving properties of the micro robot. Finally, we developed a fabrication process to miniaturize the magnetic micro robot, and succeeded in driving the cell size magnetic micro robot in water.

REFERENCES

[1] K. Kobayashi, K. Ikuta, Three-dimensional magnetic microstructures fabricated by microstereolithography, Applied Physics Letters, Vol. 92, (2008), pp. 6951-6953.

[2] K. Kobayashi, K. Ikuta, 3D Magnetic Microactuator Made of Newly Developed Magnetically Modified Photocurable polymer and Application to Swimming Micromachine and Microscrewpump, MEMS 2009, IEEE 22nd International Conference, 2009, pp. 11-14.

Lessons Learned Using the Insertable Robotic Effector Platform (IREP) for Single Port Access Surgery

N. Simaan[1,2], A. Bajo[1,2], A. Reiter[3], P. Allen[3], D. Fowler[4]

[1]A.R.M.A. Laboratory, Dept. of Mechanical Engineering, Vanderbilt University

[2] Vanderbilt Initiative for Surgery and Engineering (VISE)

[3]Dept. of Computer Science, Columbia University

[4]Dept. of Surgery, Columbia University

nabil.simaan@vanderbilt.edu

INTRODUCTION

Single Port Access Surgery (SPAS) is driven by the potential for additional patient benefits due to reduction of the number of access incisions to only one (or to no incisions when using a natural orifice). These potential benefits include improved cosmesis, reduced risk of incisional hernia and wound site infection, and reduced pain compared to open surgery or laparoscopic minimally invasive surgery. To validate these patient benefits, new technologies are needed to address the technical demands of SPAS. As an effort towards achieving this goal, our team has developed the Insertable Robotic Effector Platform (IREP), Figure 1.

The IREP, we believe, is currently the smallest system for SPAS requiring an access port of only ∅15 mm while offering dual arm dexterous operation with sub-millimeter accuracy, 3D visualization, and automated instrument tracking. The total number of actuated Degrees-of-Freedom (DoF) of the IREP is 21. These include seven actuated DoF per a dexterous surgical arm, three actuated DoF for deploying and controlling the pan/tilt of a 3D vision module, two actuated DoF for each gripper, and two DoF are used for axial insertion of each dexterous arm.

The IREP was designed using past experience in minimally invasive surgery (MIS) of the throat [1]. The design considerations of this system have been described in [2] and [3]. Design requirements included the coverage of a workspace of at least 50 mm in each Cartesian direction, roll of the gripper about its longitudinal axis to enable intracorporeal suturing in confined spaces, ability to triangulate both surgical arms, ability to apply a 2N lateral force in correspondence with surgical tissue manipulation forces and suturing [4], and ±0.25mm in positioning accuracy to allow micro-surgical interaction.

The IREP uses a unique mechanical architecture that includes continuum robots with push-pull actuation, parallel linkages, and passively flexible actuation stems. The design avoids the use of serially connected motorized joints (such as in [5],[6]) in order to limit backlash and to enhance sterilizability. The IREP also provides a controllable distance between the bases of its dexterous surgical arms to increase kinematic dexterity and to enhance dual arm triangulation compared to other designs (e.g. [7], [8]) with dexterous arms emanating from a single lumen. The IREP has also been designed as a platform for multi-modal use including energy and drug delivery and suction. This is achieved through the use of tubular access channels within each surgical arm.

The following is a description of lessons learned during early evaluation experiments using the IREP.

Fig. 1 Experimental setup showing the IREP on a Cartesian stage.

MATERIALS AND METHODS

To evaluate the functionality of IREP, we used two tasks of the Fundamentals of Laparoscopic Surgery (FLS) Manual Skills testing component (Peg Transfer and Simple Suture with Intracorporeal Knot). In addition, vision tracking algorithms as in [9]-[10] and micro-manipulation ability were also tested. Figure 2 shows the Peg Transfer experiment. Six rubber triangular parts with ∅6.3 mm holes were transferred from one side to the other side of a peg board with ∅3.2 mm pegs.

The IREP was tested in extreme conditions assuming that the only available gross movement of the device is along the trocar's longitudinal axis. We did not use all the four DoF available to standard minimally invasive instruments since we wanted to discern the IREP's dexterity and workspace without reliance on these additional DoF. The peg transfer task consists of grasping a plastic ring with one hand, removing the ring from the peg, transferring the ring to the other hand, and then placing the ring on another peg without dropping the ring. The Simple Suture and Intracorporeal Knot module consists of placing a suture through a dot on a rubber drain followed by tying intracorporeally a surgeon's knot and two square knots. Using these two modules, we could assess functionality of the robotic device under direct vision. If completed, we would record the time to complete each module.

RESULTS AND DISCUSSIONS

The experiment validated that the grippers of the IREP were able to firmly hold the triangular objects, the movement of the dexterous arms was sufficient to allow object transfer, and that each dexterous arm could cover the entire FLS peg board (64x103 mm). The experiment however did reveal that the telemanipulation code suffered from several flaws that included: a) an unnecessarily high scaling 5:1 ratio between the master and slave, b) coupling of motion between the master and slave was not direct, c) rotation of the grippers about their axis slightly affected the gripper tip position, d) although movement in the mid-range of the trocar's longitudinal insertion axis was intuitive for both hands, at the extremes of the range of movement in this axis, the movement generated by the Cartesian stage carrying the IREP could only be controlled by the right master. Flaws (a-b) have been later fixed during debugging phases of the telemanipulation code. Flaw c is related to calibration of the continuum robotic arms and the fact that we used a Phantom Omni as the master interface, which made it difficult for the surgeon to rotate his hand in space without inducting translations. We have since then implemented an orientation telemanipulation mode. Exact calibration of the dexterous surgical arms remains a minor issue to address since our experience has shown that telemanipulation under surgeon vision allows for intuitive compensation for system imperfections.

The experiments in passing circular needles and knot tying revealed that the grippers were able to stabilize the circular needles, but the limited roll of the gripper wrist within a range of ±60° made circular needle passing and hand exchange difficult. This highlighted the need for a redesign of the distal wrist to provide a larger rotation workspace. We have since then redesigned the wrists, but the new design has not been integrated yet.

Figure 3 shows telemanipulation experiments of the IREP gripper under a microscope. The user was able to follow a line 100μm thick by manipulating a 70μm wire held against a 500μm grid paper.

Figure 4 shows preliminary experiments carried out to demonstrate gripper tracking using a single 2D image. Future algorithms will take advantage of 3D tracking using both IREP cameras.

Near future evaluation the IREP will include quanitification of payload capabilities, telemanipulation RMS errors and latency, and clinical evaluation on animals. Additional detailed evaluation of our ongoing work is also available at [11].

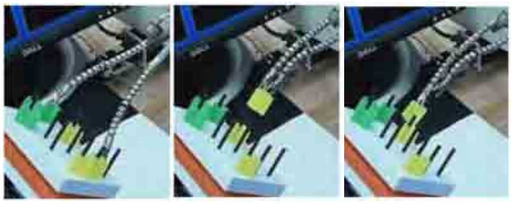

Fig. 2 Dexterity peg board used for FLS evaluation.

Fig. 3 The IREP robot tele-manipulating a 70μm wire along a straingt line.

Fig. 4 Visual tracking of the IREP's dexterous arms.

REFERENCES

[1] N. Simaan et al., "Design and Integration of a Telerobotic System for Minimally Invasive Surgery of the Throat," Int. J. of Rob. Res., vol. 28, no. 9, pp. 1134-1153, 2009.

[2] K. Xu, et al. "System Design of an Insertable Robotic Effector Platform for Single Port Access (SPA) Surgery," Proc. Int. Conf. on Int. Rob. Sys., 2009, pp. 5546-5552.

[3] J. Ding, et al., "Design, Simulation and Evaluation of Kinematic Alternatives for Insertable Robotic Effectors Platforms in Single Port Access Surgery." Proc. Int. Conf. Robotics & Automation, pp. 1053-1058, 2010.

[4] A. Dubrowski et al., "Quantification of motion characteristics and forces applied to tissues during suturing.," Am. J. of Surg., vol. 190, no. 1, pp. 131-6, 2005.

[5] M. Piccigallo et al., "Design of a Novel Bimanual Robotic System for Single-Port Laparoscopy," IEEE/ASME Trans. on Mechatronics, vol. 15, no. 6, pp. 871-878, 2010.

[6] A. C. Lehman et al., "In vivo robotics for natural orifice transgastric peritoneoscopy," Stud. Health. Technol. Inform., vol. 132, pp. 236-241, 2008.

[7] A. P. Kencana et al., "Master and Slave Robotic System For Natural Orifice Transluminal Endoscopic Surgery," Proc. IEEE Conf. on Robotics Automation and Mechatronics, 2008, pp. 296-300.

[8] D. Abbott, et al., "Design of an endoluminal NOTES robotic system." Proc. Int. Conf. Intelligent Robots & Systems, 2007, pp. 410-416.

[9] A. Reiter et al., "A learning algorithm for visual pose estimation of continuum robots," Proc. Int. Conf. on Intelligent Robots and Systems, 2011, pp. 2390-2396.

[10] A. Reiter and P. K. Allen, "An online learning approach to in-vivo tracking using synergistic features," Proc. Int. Conf. on Intelligent Robots & Systems, 2010, pp. 3441-3446.

[11] A. Bajo et al., "Integration and Preliminary Evaluation of an Insertable Robotic Effectors Platform for Single Port Access Surgery," Proc. Int. Conf. Robotics & Automation, 2012.

Totally Endoscopic Robotic Parathyroidectomy through a Lateral Cervical Approach

S. Van Slycke[1,2], H. Maes[1], J.P. Gillardin[1], H. Vermeersch[2]

[1]*OLV Clinic Aalst, Belgium, Department of General and Endocrine Surgery*

[2]*Department of Head and Neck Surgery, University Hospital Ghent, Belgium*
sam.van.slycke@olvz-aalst.be

INTRODUCTION

New minimally invasive techniques for parathyroidectomy are a hot topic. Robotic assisted parathyroidectomy has only been reported by an extra cervical approach so far. We would like to present our early experience with a Totally Endoscopic Robotic Parathyroidectomy through a Lateral cervical Approach (TERPLA)**.**

MATERIALS AND METHODS

This is a prospective single center study of all 10 patients diagnosed with primary hyperparathyroidism (PHPT) who underwent TERPLA. After a thorough preoperative assessment with medical imaging, including ultrasonography, scintigraphy and SPECT CT, patients with PHPT due to a solitary posteriorly localized parathyroid adenoma were selected for TERPLA. The procedure requires general anesthesia. A 10 mm incision is made laterally in the neck on the anterior side of the sternocleidomastoid muscle. Through this incision, a dissection is performed, providing an access medially of the carotid artery and laterally of the strap muscles. Through two extra 5 mm incisions, two working trocars can be placed cranially and caudally from the central incision. Then the optical trocar is placed and fixated with a seam around the central incision, preventing an air leak. This seam is held under tension by placing a clamp near the skin. Optionally, the ends of the wire can be fixated to the optical trocar by a second clamp, keeping the optical trocar in place (Fig. 1). The working space is continuously insufflated until 8 mmHg CO_2. The robotic instruments then can be docked under endoscopic control: a grasper is placed in the left arm and a monopolar cautery hook is placed in the right arm. Through a blunt dissection, the adenoma can be freed from the surrounding structures, and the vascular pedicle is cut by coagulation. The trocars and the adenoma are then removed, and the skin is closed.

The resection specimen is transported dry to the pathological laboratory, where a frozen section procedure is performed.

The value of PTH is followed on baseline moments described in the NACB guidelines with detection in the blood taken by the anesthesiologist through an intravenous line in the great saphenous vein, or through an arterial line placed in the radial artery. The moments are at intubation (T1), at incision (T2), just before resection of the adenoma (T3), 5 minutes after resection (T4), 15 minutes after resection (T5) and optionally 30 minutes after resection (T6). [2] In our institution, an extra sampling of PTH is performed four hours postoperatively.

RESULTS

We performed TERPLA on 10 patients, starting from September 2011 until March 2012. One patient was converted to a cervicotomy because of difficult dissection after previous neck surgery, with an adenoma incrusted in the thyroid gland. All patients achieved a normal value of serum PTH-level 4 hours postoperatively. All resection specimens were confirmed as a parathyroid gland adenoma on pathological protocol. All patients reached a normocalcemia in the short term follow up. No major complications occurred. Esthetic outcome was excellent. Median follow up time is 47 days (3-85). Mean operating time if no conversion was 72 minutes (±30). All patients were cured. The mean value of calcemia was 11.6 mg/dl (±0.83) preoperative and 9.80 mg/dl (±0.55) postoperative, with a normal range between 8.6-10.3 mg/dl. Nine out of ten patients were discharged on the first postoperative day (POD), including the patient that was converted. One patient was discharged on the second POD. No patients reported any postoperative pain at all, measuring from the first postoperative day.

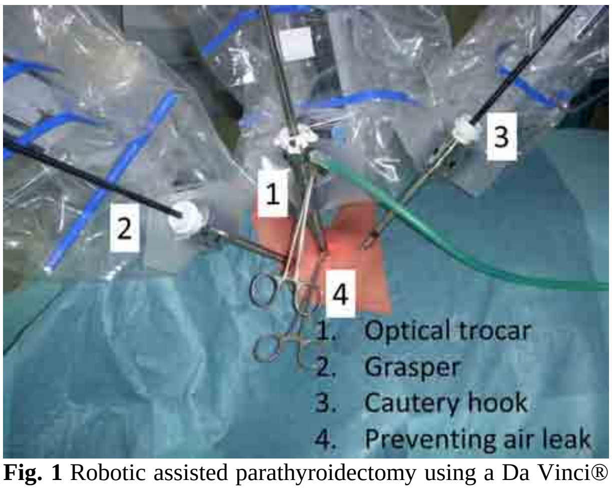

Fig. 1 Robotic assisted parathyroidectomy using a Da Vinci® surgical robot.

DISCUSSION

TERPLA has shown to be a safe and feasible procedure in patients with a posteriorly localized parathyroid adenoma. Considering the existing techniques for minimal invasive parathyroid surgery, we have seen still a small margin for improvement. When compared to the technique described by Henry [1], we believe that the robotic system adds several advantages to the classic endoscopic approach. The use of a high definition three-dimensional imaging improves the accuracy. Another advantage is the articulation of the instruments, which makes it possible to manipulate the parathyroid gland from more directions compared to the endoscopic straight instruments. The combination of these both advantages facilitate the dissection, even in difficult cases where the adenoma is adherent to the thyroid gland. In our experience of more than twenty cases where we used the totally endoscopic approach [1] as a standard procedure, we encountered many times the difficulty of conflicts between the working instruments and the endoscope. It is hard to find an ergonomic position for both the surgeon holding the working instruments and the assistant holding the endoscope. By using a robotic approach we eliminated this problem.

When looking into the future, we expect that the use of peroperative fluorescence imaging techniques [3] can contribute to the further development of minimally invasive endocrine surgery in the very near future.

At the present, there are still some disadvantages of the robotic approach. First of all, there is a bigger cost to perform the robotic technique. In our institution, this extra cost has not yet been passed on to the patient in any way in the case of robotic parathyroid surgery.

Second, we have seen a longer mean operating time in the robotic procedure (72 minutes) compared to the classic endoscopic parathyroidectomy (49 minutes) we performed in more than 20 cases. We believe that we are still in a learning curve, and we expect this difference to become minimal. The assumption is often made that the installation of the robotic system is very time consuming, but we can refute this assumption. In a well-organized operation theatre, the three components of the robot can already be positioned before the procedure. While the patient is brought under general anesthesia, the sterile drapes of the robot arms can already be put in place. Installation of the patient is parallel to the classic endoscopic approach [1]. By the moment the operating time starts, the robot arms can be rolled in ready to perform, with a time loss of less than 30 seconds.

A third disadvantage is the total length of skin incision. In the technique described by Henry [1], two 3 mm incisions are made, and one 10 mm incision. In our technique, the two working port incisions are 5 mm, which brings the total incision length to at least 20 mm. Compared to the classic endoscopic approach, this is an augmentation of 4 mm more scare, which seems to diminish the cosmetic advantage of minimal invasive surgery. Nevertheless, as already has been stated before: minimally invasive parathyroid surgery is not only a question of length of the incision [4]. All patients were satisfied about the cosmetic result, and the residual scars of the two 5 mm ports were practically invisible one month postoperative (Fig. 2). Hopefully, the further development of the robotic instruments may even provide us with smaller working tools, which reverses this aspect.

At this moment, we did not yet make a comparison between the TERPLA and the totally endoscopic parathyroidectomy as described by Henry [1]. However, we believe we can provide enough data to justify a randomized clinical trial comparing these two techniques.

Fig. 2 Satisfying cosmetic result one month after total endoscopic robotic parathyroidectomy, showing only a residual scar of the 10 mm incision. The two lesser incisions are almost invisible.

We conclude that totally endoscopic robotic parathyroidectomy through a lateral cervical approach is a safe and feasible procedure in patients with a posteriorly localized parathyroid adenoma. This technique reveals new aspects in minimal invasive surgery and should be further investigated in the near future.

CONFLICTS OF INTEREST

There were no conflicts of interest.

REFERENCES

[1] Henry JF. et al., Endoscopic parathyroidectomy via a lateral neck incision. Ann Cir. 1999; 53(4): 302-306

[2] Nichols JH et al., National Academy of Clinical Biochemistry Laboratory Medicine Practice Guidelines: Evidence Based Practice for Point of Care Testing. Clin Chim Acta 2007; 379(1-2):14-28

[3] Prosst R. et al., Fluorescence-guided minimally invasive parathyroidectomy: clinical experience with a novel intraoperative detection technique for parathyroid glands. World J Surg 2010; 34:2217–2222

[4] Henry JF., Minimally invasive thyroid and parathyroid surgery is not a question of length of the incision. Langenbecks Arch Surg 2008; 393:621–626

A Pilot Ex-Vivo Evaluation of a Telerobotic System for Transurethral Intervention and Surveillance

A. Bajo[1,3], R. B. Pickens[2], S. D. Herrell[2,3], N. Simaan[1,3]

[1]A.R.M.A. Laboratory, Dept. of Mechanical Engineering, Vanderbilt University,

[2]Dept. of Urologic Surgery, Vanderbilt University Medical Center

[3]Vanderbilt Initiative for Surgery and Engineering (VISE)

nabil.simaan@vanderbilt.edu

INTRODUCTION

In this paper, we present a pilot evaluation of a novel telerobotic surgical system for Transurethral Resection of Bladder Tumor (TURBT). In 2012, the number of newly diagnosed bladder cancer patients and deaths in the US is estimated to be 73,510 and 14,880 respectively [1]. TURBT procedures (see Fig. 1) provide access to the bladder via the resectoscope, a telescopic straight instrument with a diameter typically between 8 to 9 mm.

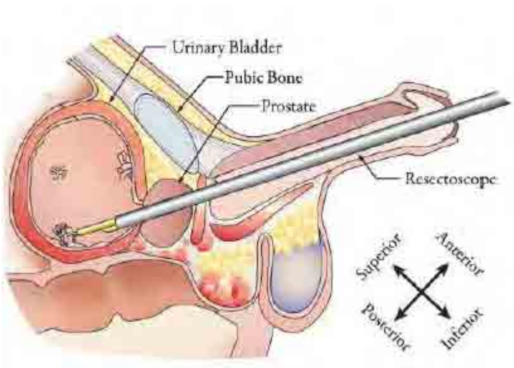

Fig. 1 Overview of the TURBT procedure. The resectoscope is inserted through the urethra to access the bladder [2].

The resectoscope dramatically reduces distal dexterity by limiting lateral movement and allowing only for translation and rotation along/about its longitudinal axis. Accuracy of the resection, therefore, highly depends on the particular position of the carcinoma inside the bladder and on surgeon's skills and experience. Moreover, one drawback of current practice of TURBT is that tumor resection is carried out piecemeal and, therefore, possibly contributing to seeding other cancer sites [3]. Although resection in one piece (en-block) during TURBT was recently demonstrated clinically [4], transurethral en-block resection remains challenging or impossible depending on lesions location and surgeon's technical expertise.

In this study, we present a pilot evaluation of a novel system for robotically-assisted TURBT. The system includes a dexterous two-stage continuum robot with multiple access channels that are used for visualization, instrument deployment, and energy delivery. The master-slave architecture allows for telemanipulation of the slave robot using a Sensable Phantom Omni and a pedal switch for initiating manipulation. Preliminary evaluations on two bovine bladders demonstrated the ability of the system to target all quadrants, delivery laser energy, and perform biopsies.

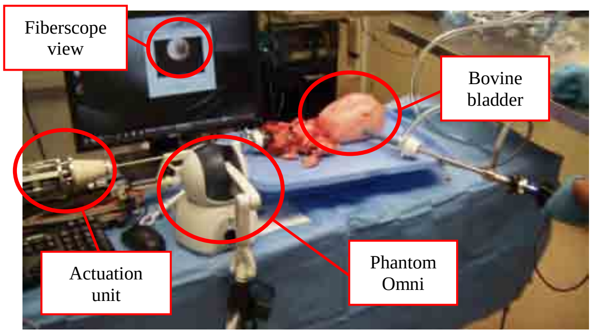

Fig. 2 Overview of the experimental setup.

MATERIALS AND METHODS

The proposed telesurgical system for TURBT is shown in Fig. 2. The figure shows the slave robot's actuation unit, the master manipulator (Sensable Phantom Omni), a monitor showing the view from the on-board fiberscope, an inflated bovine bladder, and an additional laparoscope for improved visualization. The scope of this pilot study was to demonstrate the basic surgical tasks such as coverage, energy delivery, and resection during TURBT.

The robotic slave was deployed inside the bovine bladder through a standard resectoscope. The bovine bladder was inflated with air and kept at constant pressure for the entire procedure. Visualization feedback was obtained from both the on-board 1.2 mm fiberscope prototype and the external laparoscope. Because of the low resolution of this first fiberscope prototype, external visualization was required for successfully operating inside the bladder.

A 0.55 mm laser probe was deployed through one of the access channels and energy was delivered to the superior, anterior, and posterior quadrants of the bladder. Indigo blue dye was manually injected with a syringe to define the target resection area. The slave was then tele-manipulated to fire the laser on the target area as shown in Fig. 3. The inferior quadrant was reached and surveillance was demonstrated.

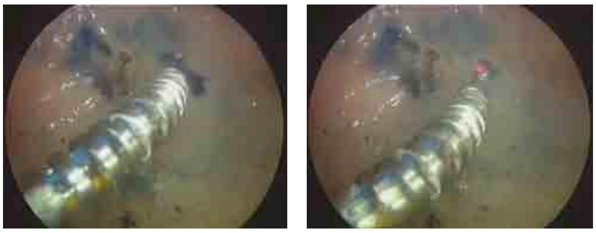

Fig. 3 Laser delivery experiments. (Left) Indigo blue dye was used to delineate the resection area. (Right) Laser energy was delivered over the entire target area.

Additional experiments were carried out to demonstrate the feasibility of cancer resection and biopsy. A ∅1.8 mm disposable biopsy forceps were delivered through the third access channel. Tissue was gripped and laser was delivered to resect the sample as shown in Fig. 4. The dexterity of slave allows for pivoting about the contact point and successfully completing en-block biopsy/resection.

Fig. 4. Deployment of biopsy forceps (Left). View of the system grasping tissues and delivering laser delivery (Right).

RESULTS AND DISCUSSIONS

The preliminary results demonstrated the ability of the proposed robot to complete critical surgical tasks required during TURBT. These tasks include: surveillance, energy delivery, biopsy, and resection of cancerous areas.

At the current state, the main limitation of the robot is the on-board 1.2 mm fiberscope prototype with embedded light source. The limited cross section requires a tradeoff between fibers used for visualization and fibers used for illumination. Although, the fiberscope was useful to examine tissue and maneuver the end-effector locally on the tissue, its short focal distance does not allow one to use it for gross motion.

Energy delivery to the superior, anterior, and posterior quadrants was successfully carried out. Figure 5 shows pictures of some of the targeted area. The bovine bladder was cut after the experiments and the targeted areas examined. The picture shows localized energy delivery to the predetermined areas only.

Biopsy and resection was also successfully demonstrated as shown in Fig. 4. The slave manipulator allows for the delivery of a standard 1.8 mm biopsy forceps. The biopsy forceps allows for grasping and removing large areas of tissue using the laser. By pivoting about the contact point, it is possible to ablate larger areas than using the forceps only. Figure 6 shows the slave manipulator grasping the resected tissue outside the bovine bladder. The tissue sample was pulled out along with the slave manipulator at the end of the procedure. The size of the resected tissue is larger than conventional samples that can be obtained with biopsy forceps alone. The size of the tissue is compared next to a "one dime" of Ø18 mm.

Future designs will improve dexterity in the inferior quadrant by adding a wrist at the end-effector. Additional research will focus on depth controlled resection, enforcement of safety telemanipulation zones (virtual fixtures/active constraints), and on detailed clinical evaluation of the benefits of robotic assistance for transurethral resection and surveillance.

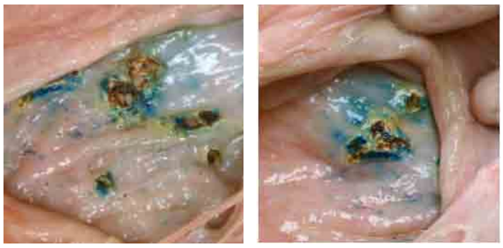

Fig. 5 Clinical view of a target area after completion of the laser experiments

Fig. 6 Clinical view of a sample tissue removed with combined grasping and laser delivery.

REFERENCES

[1] NIH, "National Cancer Institute," 2012. [Online]. http://www.cancer.gov/cancertopics/types/bladder.

[2] R. E. Goldman, A. Bajo, L. K. Suh, and N. Simaan, "Design and Evaluation of a Minimally Invasive Telerobotic Platform for Transurethral Surveillance and Intervention," *IEEE Transaction on Biomedical Engineering*, vol. submitted, 2012.

[3] E. R. Ray and T. S. O'Brien, "Should Urologists Be Spending more Time on the Golf Course?," *BJU International*, vol. 100, no. 4, pp. 728-729, 2007.

[4] R. Ukai, E. Kawashita, and H. Ikeda, "A new technique for transurethral resection of superficial bladder tumor in 1 piece," *The Journal of Urology2*, vol. 163, no. 3, pp. 878-879, 2000.

Initial Experience with Robotic Partial Nephrectomy (RPN): A Collaborative Approach drawing on Different Backgrounds

A. Patel[1], C. Oliver[1], M. Billia[1], G. Kooiman[2], P. Dasgupta[1], T.S. O'Brien[1], and B. Challacombe[1]

[1]Urology Centre, Guy's and St Thomas' NHS Foundation Trust, London
[2]Department of Urology, King's College Hospital, London
amit.patel@gstt.nhs.uk

INTRODUCTION

The surgical, nephrological and oncological results from laparoscopic nephron-sparing surgery are encouraging [1,2] but concerns remain regarding the technical difficulty of intracorporeal suturing resulting in prolonged warm ischaemic times(WIT). Previous work has demonstrated that suturing with the da Vinci robotic system is easier compared with standard laparoscopy[3]. At our institution we have drawn from our experience from open and laparoscopic PN, and robotic pelvic surgery to develop the RPN program. We report on the first 28 patients undergoing RPN.

PATIENTS AND METHODS

28 patients with renal masses had RPN from June 2010-March 2012. 24 were exophytic, 1 cystic 2 predominantly endophytic and 1 completely endophytic. The median PADUA score[4] was 7-8. The principles of traditional open surgery were followed. The renal vessels were occluded with bulldog clamps and warm ischaemia used in all cases. Sliding clip rennorhaphy and Evicel (J&J) were used for hemostasis. A tumour base biopsy was taken at the deep resection margin.

RESULTS

19 men and 9 women with a median age 53 years (range 37-80). 26 patients underwent a transperitoneal and 2 retroperitoneal approach. Median operative time and WIT were 170 minutes (150-220) and 19 minutes (12-28) respectively. Median estimated blood loss was 150mls (20-500) and median length of stay 3 days (3-9). There were no conversions to open surgery, laparoscopic radical nephrectomy or peri-operative blood transfusions. There were 1 Clavien grade III (ureteric stent) and 2 grade 1 complications. No patients had an eGFR decline of greater than 5% post operatively. Median tumour size was 27mms (6-60). Pathology revealed 18 clear cell carcinomas, 2 chromophobe, 2 papillary, 3 angiomyolipoma,1 mature haematoma and 2 oncocytoma. 1 surgical margin was focally positive, however deep margin biopsies were clear. To date, no recurrences have been seen.

CONCLUSIONS

Robotic partial nephrectomy is a safe and low morbidity alternative to open partial nephrectomy in selected patients with small renal tumours.

Despite being in the initially phase of our learning curve of RPN, WIT, oncological and functional outcomes are good and comparable to other world centres[3].

REFERENCES

[1]. I.S. Gill, L.R. Kavoussi, B.R. Lane, et al.. Comparison of 1,800 laparoscopic and open partial nephrectomies for single renal tumors. J Urol 178 (2007) (41 - 46)

[2]. B.R. Lane, I.S. Gill. 7-year oncological outcomes after laparoscopic and open partial nephrectomy. J Urol 183 (2010) (473 - 479)

[3] B.M. Benway, S.B. Bhayani, C.G. Rogers, et al.. Robot assisted partial nephrectomy versus laparoscopic partial nephrectomy for renal tumors: a multi-institutional analysis of perioperative outcomes. J Urol 182 (2009) (866 - 872)

[4] V. Ficarra, G. Novara, S. Secco, et al.. Preoperative aspects and dimensions used for an anatomical (PADUA) classification of renal tumours in patients who are candidates for nephron-sparing surgery. Eur Urol 56 (2009) (786 - 793)

Robotic Tele-Manipulating Devices for Laparoscopy Improve Surgical Performance in Simulated Porcine Laparoscopic Cholecystectomies on the ELITE Simulator

K. Sriskandarajah[1], S. Gillen[2], A. Di Marco[1], M. Sodergren[1], D.R.C. James[1], J. Clark[1], H.D. Feussner[2], A. Darzi[1], G.-Z. Yang[1]

[1]Hamlyn Centre for Robotic Surgery & Global Health Innovation, Imperial College London
[2]Department of Surgery, Klinikum rechts der Isar, Technische Universität der TUM, Munich
k.sriskandarajah@imperial.ac.uk

INTRODUCTION

Laparoscopy has afforded many advantages to patients but has made some operations more technically challenging for the surgeon. One factor that has increased complexity is that surgeons can only view the target tissue or organ displayed via a video monitor. The surgeon must rely on the laparoscope assistant to not only show the necessary anatomy and instruments, but also maintain a stable horizon and move smoothly, so that the operation can be performed safely and accurately [1,2]. Despite the assistant being aware of their important role, they still cannot control the motion of the laparoscope identically to what the surgeon would have done if they were in control. In addition, the assistant cannot compensate for the effects of physiological tremor and fatigue. Thus surgeon-controlled robotic laparoscope holders (tele-manipulating devices) may provide a solution to this problem. The aim of this study was to objectively test the hypothesis that for a common laparoscopic operation, namely, the laparoscopic cholecystectomy a robotic tele-manipulating device may improve surgical performance and not add to the overall cognitive workload of the surgeon performing the operation.

METHODS

The AKTORmed SOLOASSIST device was selected as the commercially available robotic tele-manipulating system to test the hypothesis (Figure 1). Fourteen surgical residents with prior average experience in laparoscopic surgery of over five hundred cases were trained in the use of the SOLOASSIST device. This involved utilisation of the SOLOASSIST device to complete a modified peg transfer task (Task 1) of the Fundamentals in Laparoscopy Surgery (FLS) program [3]. The subjects completed their training after they obtained the defined proficiency standard for the task as outlined in the FLS program [3,4].

Each of the 14 surgeons performed the laparoscopic cholecystectomy twice, i.e. with the aid of the SOLOASSIST and a senior surgical resident with experience in performing the operation over one hundred times. The surgeons were randomised into group A (who would perform the operation with the SOLOASSIST first followed by the conventional surgical assistant), and group B (surgical assistant first, followed by the SOLOASSIST).

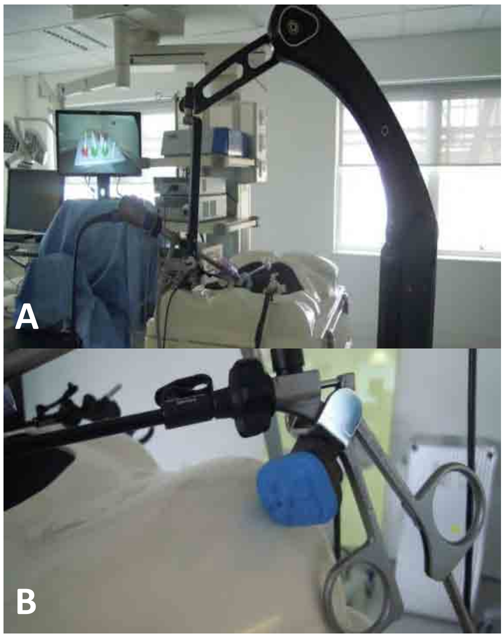

Fig. 1 A) AKTORmed SOLOASSIST device setup controlling a laparoscope in a box trainer. **B)** SOLOASSIST surgeon control pad attached to a generic laparoscopic grasper. It is attached on the instrument that is changed the least during the operation. Thus, for a laparoscopic cholecystectomy this is the left hand instrument.

The subjects performed the laparoscopic cholecystectomies in the endoscopic–laparoscopic interdisciplinary training entity (ELITE) simulator on a cadaveric porcine model (See Figure 2) [5]. Retention tests were done immediately prior to the study to ensure that surgeon performance on using the SOLOASSIST was still above the FLS proficiency standard.

The performance metrics of task time and total path length were obtained by use of the previously validated Imperial College Surgical Assessment Device (ICSAD) [6]. The number of task errors (e.g. dissection into the hepatic parenchyma and cholecystotomies) were accounted for by two independent trained assessors experienced in performing the operation. In addition, the NASA TLX workload index was completed following each task.

Fig. 2 Setup of the cadaveric porcine livers in the ELITE simulator with the SOLOASSIST device and ICSAD.

All statistical analyses were performed using IBM Statistics SPSS V 19.0.0. Mann-Whitney *U*, Chi squared and Fisher's Exact Tests were used for data analyses. Alpha levels were set at 0.05, 95% confidence.

RESULTS

All surgeons completed their proficiency training for the SOLOASSIST device and passed the retention tests to the same level prior to performing the laparoscopic cholecystectomies. There was no statistically significant difference in age, gender, handedness, 'years since qualified' and laparoscopic experience between the two groups A and B as demonstrated in table 1.

Table 1 Demographics

Group	A	B	P Value
Median Age	33.0	32.0	P=0.435
Handedness (L:R)	2:5	2:5	p=0.720
Gender (M:F)	6:1	6:1	P=0.769
Median Years Qualified	7.00	8.00	P=0.651
Median Laparoscopic Experience	516	581	P=0.848

Comparing the performance of the subjects using the SOLOASSIST versus the surgical assistant revealed a tendency towards shorter task time and greater efficiency in movements (path length); nonetheless these results did not reach statistical significance. However, when comparing the total number of errors, the use of the SOLOASSIST was associated with a statistically significantly lower incidence of errors. These results are summarised in table 2 below.

Table 2 Results of ICSAD performance metrics, observed errors and NASA TLX workload index

Metric		SOLOASSIST	Assistant	P Value
Task Time /sec	Median	879.5	887.0	P=0.291
	IQR	394.0	543.8	
Total Path Length	Median	91.43	119.6	P=0.81
	IQR	43.64	104.8	
Total no. of errors	Median	0	2	**P=0.021***
	IQR	1.25	3.00	
Unweighted TLX	Median	142.5	155.0	P=0.345
score	IQR	73.75	87.50	

*Significance level of P value <0.05

The unweighted TLX scores did not show any statistical difference between the SOLOASSIST and the assistant tasks. 86% of the study participants declared on an anonymised questionnaire that they would recommend the use of the robotic tele-manipulator for laparoscopic surgery.

DISCUSSION

This stable robotic laparoscope platform that can be controlled by the surgeon appears to improve performance by reducing surgical errors in this simulated cadaveric experiment. This beneficial effect may arise from removing problems associated with communication, the surgeon deciding the best view, rather than the assistant guessing or being told continuously. Furthermore, the benefits of having a stable horizon and no physiological tremor may also contribute to the effect seen in this study. Despite this system possibly helping surgeons by reducing errors, as suggested by the results in this study, the ergonomic outcome parameters such as path length were unaffected by the use of this system. Thus the potential advantages have to be balanced against greater cost and surgeon preference.

Yurko et al (2010) demonstrated that increased cognitive workload on the surgeon resulted in worse performance during laparoscopic operations [7]. Importantly, the effect of the robotic tele-manipulator was not detrimental on the cognitive workload of the surgeon as supported by the NASA TLX workload scores.

Further study in vivo is required to determine if these benefits are clinically relevant and transferable to the operating room.

REFERENCES

[1] Zhang L, Cao CG. Effect of automatic image realignment on visuomotor coordination in simulated laparoscopic surgery. Appl Ergon. 2012 Feb 26. [Epub ahead of print]

[2] Sodergren MH, Orihuela-Espina F, Mountney P, Clark J, Teare J, Darzi A, Yang GZ. Orientation strategies in natural orifice translumenal endoscopic surgery. Ann Surg. 2011; 254(2):257-66.

[3] http://www.flsprogram.org/

[4] Xeroulis G, Dubrowski A, Leslie K. Simulation in laparoscopic surgery: a concurrent validity study for FLS. Surg Endosc. 2009; 23(1):161-5.

[5] Gillen S, Wilhelm D, Meining A, Fiolka A, Doundoulakis E, Schneider A, von Delius S, Friess H, Feussner H. The "ELITE" model: construct validation of a new training system for natural orifice transluminal endoscopic surgery (NOTES). Endoscopy. 2009; 41(5):395-9.

[6] Taffinder, N, Smith SG, Huber J, *et al*. The effect of a second-generation 3D endoscope on the laparoscopic precision of novices and experienced surgeons. Surg Endosc. 1999; 13(11):1087-92.

[7] Yurko YY, Scerbo MW, Prabhu AS, Acker CE, Stefanidis D. Higher mental workload is associated with poorer laparoscopic performance as measured by theNASA-TLX tool. Simul Healthc. 2010; 5(5):267-71.

Improved Visualisation with Shape Instantiation for Robot Assisted Catheter Navigation

Su-Lin Lee[1], Ka-Wai Kwok[1], Celia Riga[2], Colin Bicknell[2], and Guang-Zhong Yang[1]

[1]Hamlyn Centre for Robotic Surgery, Imperial College London, UK

[2]Academic Division of Surgery, Imperial College London, UK

su-lin.lee@imperial.ac.uk

INTRODUCTION

The recent introduction of robotic catheter navigation systems, such as the Hansen Sensei (Hansen Medical) [1], has assisted the manipulation of catheters through complex anatomy with improved accuracy and consistency. However, visualization of key target areas is still reliant on X-ray fluoroscopy. This provides a 2D projection of the 3D arterial anatomy, which is unable to demonstrate through-plane motion of the catheter and boundaries of the vessels without frequent use of nephrotoxic contrast.

The introduction of 3D arterial models for navigation purposes is complicated by subject-specific anatomical deformation. Models generated from preoperative imaging tend to be static and require updating using intra-operative data. Real-time shape instantiation has been developed for the prediction of the dynamic 3D shape intra-operatively using only sparsely sampled data. Preoperative models are used to determine the optimal scan planes or features to be tracked intra-operatively. During intervention, these sparsely sampled data can be used to instantiate the entire 3D anatomy, thus significantly reducing the ionising radiation and the use of contrast agent.

In practice, a further issue to be tackled for effective endovascular navigation is that while a 3D model of the vasculature of interest and its dynamics can assist with navigation, an overlay of such a model to the fluoroscopic image requires the reorientation of the projection plane from multiple angles. However, the availability of the 3D data would permit an endoscopic view from the catheter tip. In this paper, the technical details for achieving such a visualisation scheme are presented. Validation is performed on nine subjects to demonstrate the positive effect of the method on navigation quality and efficiency.

MATERIALS AND METHODS

A silicone vascular phantom (Elastrat Sàrl, Geneva, Switzerland) was scanned using a 3D CT imaging protocol in a GE Innova 4100 interventional X-ray machine. Five scans were obtained at five simulated dynamic positions, generated by placing inserts next to the ascending aorta. The phantom and the average mesh used in the training set are shown in Figure 1. The dynamic shape instantiation framework [2], using features extracted from fluoroscopic images as input, was used to generate a simulated respiratory cycle based on the breathing pattern developed by Lujan *et al.* [3]. A linear Kalman filter [4] was used to generate a predictive dynamic motion model over time.

This dynamic predictive motion model was used along with a kinematic model of a robotic catheter to make up the simulation environment; this environment allowed for detailed assessment of the potential benefits of the motion model and virtual endoscopic view. Manipulation of the robotic catheter was via an Omni Phantom device (SensAble Tech. Inc., USA) and the operators were advised of the risks of making arterial wall contact with the catheter.

Nine subjects (all right-hand dominant) were recruited to assess their performance when using the system to cannulate the left subclavian artery (LSA). Each subject performed the procedure twice – with and without the virtual endoscopic view – and operators were allowed to adjust the orientation of the 3D model during the procedure. The setup of the experiment is shown in Figure 2.

The following performance indices were recorded:

- Completion time
- Path length
- Mean optimal path deviation
- Number of mesh collisions
- Duration along the walls

The Kruskal-Wallis test was used to assess differences between procedures performed with and without virtual endoscopy.

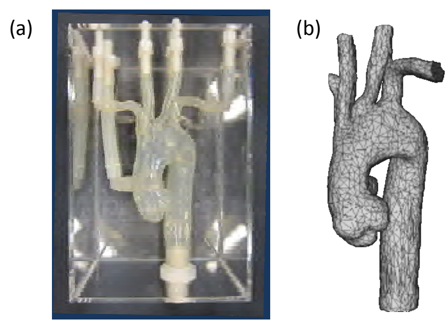

Fig. 1 The phantom used for the experiments and the average mesh from the training set.

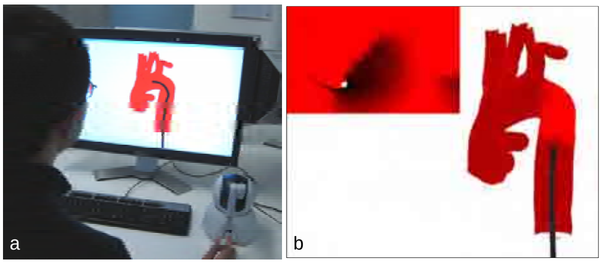

Fig. 2 The setup of the user evaluation experiments: (a) the user evaluation experiment setup with the Omni Phantom (without virtual endoscopy) and (b) a screenshot of the experiment with virtual endoscopy in the top left corner.

RESULTS

A summary of the performance indices recorded is shown in Table 1; the means and standard deviations of each index are shown both with and without virtual endoscopy. Overall, performance metrics improved significantly during cannulation of the LSA using virtual endoscopy (Kruskal-Wallis; $p<0.05$). Most importantly, the number of mesh collisions and the duration of time the catheter tip was pressed against the vessel wall reduced markedly, suggesting improved safety of cannulation. All subjects commented on how virtual endoscopy made the procedure easier and all chose not to reorient the 3D model when using virtual endoscopy.

Table 1 Summary of the performance indices in the user evaluation experiments.

	Without Virtual Endoscopy		**With Virtual Endoscopy**	
	Mean	**SD**	**Mean**	**SD**
Completion time, s	107.8	46.3	**71.8**	**36.3**
Path length, mm	882.9	648.8	**395.0**	**147.0**
Path deviation, mm	10.9	4.0	**5.8**	**0.8**
No. of mesh collisions	8.4	9.5	**1.3**	**2.2**
Duration along walls, s	4.2	3.4	**0.6**	**0.9**

In Figure 3, a comparison of the catheter tip travel paths for Subject 4 is shown. The red path (with virtual endoscopy) is much smoother than the blue path (without virtual endoscopy) and there are fewer repetitious catheter tip movements used to cannulate the left subclavian.

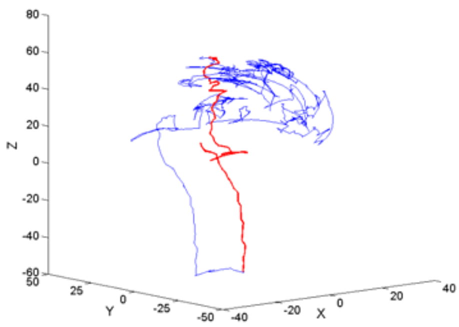

Fig. 3 A comparison of the catheter tip travel path for Subject 4 with (red) and without (blue) the virtual endoscopic view.

DISCUSSION AND CONCLUSION

To conclude, we have assessed a virtual endoscopic view of the aortic arch coupled with a dynamic shape instantiated model. The dynamic shape instantiation is able to provide shapes outside the training set and hence forms a robust base for the ideal motion model for endovascular navigation. The use of an endoscopic view with shape instantiation has been demonstrated to reduce the amount of time and manipulations required to perform a robotic endovascular task. It has also reduced the number of mesh collisions and catheter tip duration along the arterial walls, hence potentially reducing the risk of embolization and vessel trauma.

REFERENCES

[1] Riga CV, CD Bicknell, MS Hamady, et al. Evaluation of robotic endovascular catheters for arch vessel cannulation. Journal of Vascular Surgery. 2011; 54 (3): 799-809.

[2] Lee S-L, A Chung, M Lerotic, et al. Dynamic Shape Instantiation for Intra-operative Guidance. Medical Image Computing and Computer-Assisted Intervention (MICCAI). 2010; LNCS 6361: 69-76.

[3] Lujan AE, EW Larsen, JM Balter, et al. A method for incorporating organ motion due to breathing into 3D dose calculations. Medical Physics. 1999; 26 (5): 715-720.

[4] Kalman RE. A New Approach to Linear Filtering and Prediction Problems. Transactions of the ASME - Journal of Basic Engineering. 1960; 82 (Series D): 35-45.

Investigation of a CT Compatible Robot for Robot-assisted Surgical Reductions of Joint Fractures

A. Hinitt[1], M. Sobhani[1], S. Dogramadzi[1], D. Raabe[2], R. Atkins[3]

[1]Bristol Robotics Laboratory, University of the West of England, UK

[2]Berufsakademie Sachsen, University of Cooperative Education, Germany

[3]Bristol Royal Infirmary, University Hospitals Bristol, UK

Sanja.Dogramadzi@brl.ac.uk

INTRODUCTION

The joints of the body are frequently involved in bone breaks. For the joint to function properly again, the broken pieces must be put back together as perfectly as possible. We have designed and presented a robotic system for a minimally invasive joint reduction surgery using a rigorous surgical workflow analysis [1]. The system utilizes three compact parallel robots that can move fragments of the broken joint through sets of pre-calculated trajectories (Figure 1). All three robots are Stewart platforms with 6 DOFs actuated by metal strut actuators. During fracture surgery the surgeon performs intra-operative CT scans of the fractured area.

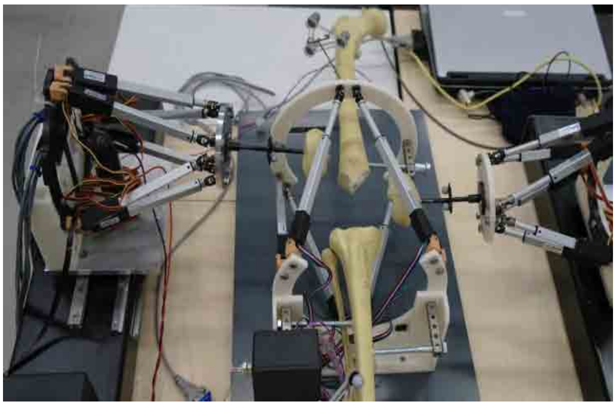

Fig. 1 Robot-assisted system for joint fracture reductions

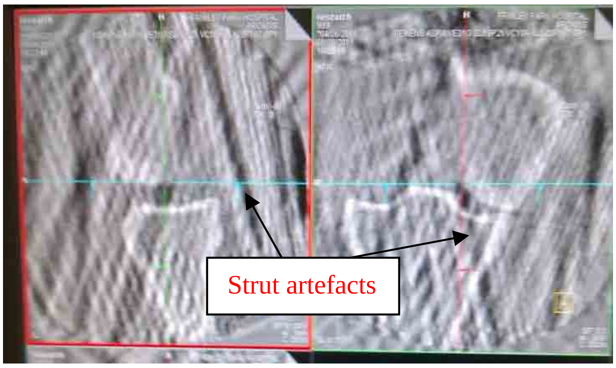

Fig. 2 A CT image of the system from Figure 1. Metal struts of the parallel robot distort the image.

Metal linear actuators in each leg of the robotic platform, to some extent, obstruct the visibility of the bones and, more importantly, produce a distortion in the CT images (Figure 2).

CT scanners use the density of the objects to produce an image of the scanned structures. Having any metal object of high density in the CT environment, is leading to obscured parts of the subject structure and streaking, caused by the metal, produces degradation of quality of the whole image.

MATERIALS AND METHODS

To solve these problems two methods, both based on the idea of reducing metal area under CT scanner, have been investigated. First approach was to reduce the number of the platform legs by using a parallel mechanism with lower DOFs and the second method was to develop a CT compatible actuation system.

To this end, two types of metal-free linear actuating methods have been considered - string and pulley and pneumatic actuation. Taking into account intrinsic compliance and not so precise position control of pneumatic actuation system, string and pulley have been selected as a method of choice. Stiffness and resolution of string and pulley actuation system have been investigated by a purposely made test rig. Two types of strings of polyester braids with dyneema core have been tested by putting the strings under tension and measuring force and displacement. Stiffness of strings under tension has been empirically evaluated. Accuracy and precision of the tensioned strings have been investigated when driven by two servo motors.

In terms of mechanism design, two parallel mechanisms have been studied, namely 3RPS and 3UPU. Although these manipulators have satisfactory features, considering their structure and controllability, they have not enough DOFs for the assigned task. Therefore, to have a system with similar capability in motion to the current Stewart platform with 6 DOFs and high load capacity, a novel mechanism has been designed based on the idea of having two Stewart-Gough platforms in hybrid configuration with a common moving platform in the middle (Figure 3).

In the new mechanism each leg of Stewart platform has been replaced by one under tension opposing string pair to produce a cable driven manipulator. Inverse kinematics of the mechanism has been solved as inverse kinematics of two Stewart platforms by imposing a constraint of having one moving platform in between the two fixed bases. The mechanism motion has been simulated in Matlab before building a prototype. .

RESULTS

The prototype is built with 12 servo motors that articulate the six string pairs which control of the moving frame. These motors alter the length of the strings via set of pulleys. The zero position of the moving frame is calibrated by pre-tensioning all strings in the system and effectively locking the frame between the opposing strings. The system uses Matlab to calculate the inverse kinematics solution of the hybrid system and generate the string lengths for a required position and orientation of the middle frame. A series of via points are calculated for a particular motion. The string lengths are converted into the servo motor positions and applied to the servo motors using an Arduino AVR microcontroller that produces pulse trains for each of the motors. These are sent to the Arduino by MATLAB using a USB serial port interface. The position shifts to a new via point after a defined time interval providing precise control of the frame position

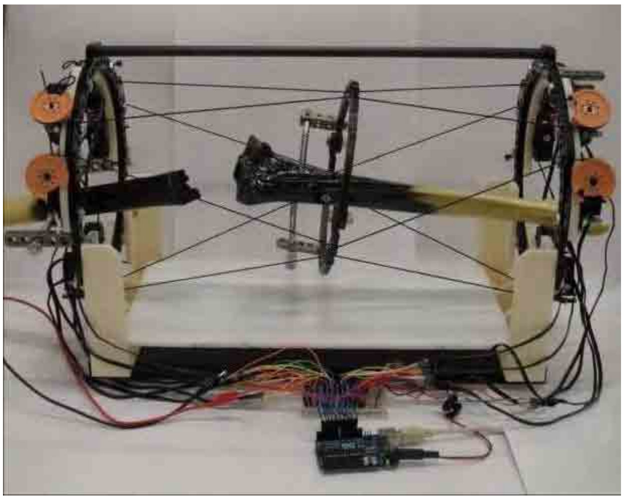

Fig. 3 New, string-actuated parallel robot

This novel mechanism with six DOFs has been tested in motion and it shows high rigidity along with a good positioning performance.

A CT scan of Sawbones using new robot has confirmed that the only distortion occurs around the Schank metal screws that attach the bone to the moving frame. The fixating metal screws will be replaced by non-metal fixations to avoid streaking.

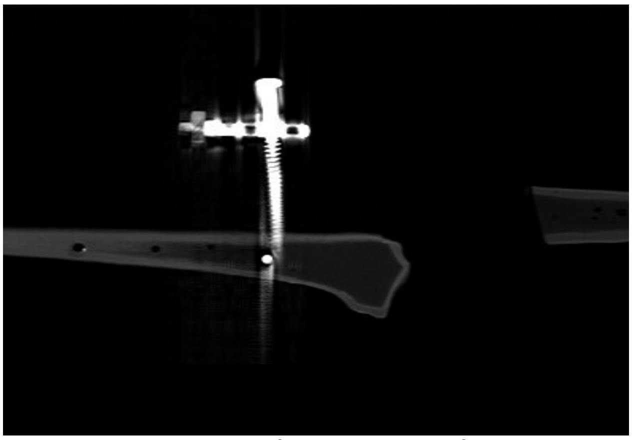

Fig. 4 A clear CT image of the parallel robot from Figure 3

DISCUSSION

Computer and robotic assisted systems developed for minimally invasive surgery often rely on high contrast medical images of the operating area to allow segmentation of anatomical objects resulting in an improved positioning accuracy and patient's safety. When using magnetic resonance or computer tomography for the image feedback, metallic construction of robots causes substantial image artefacts (Fig.2). MR and CT compatible mechanisms have been investigated for various surgical procedures [2-3] to improve image quality. Cable driven parallel robots are often used to remotely actuate components. This principle has also been investigated for the actuation of the MR compatible robots [4].

In this paper we presented our initial prototype of a new cable-actuated parallel robot that shows a good performance with the positional accuracy of less than 1mm. The actuating system is scalable and allows a clear view of the operating field.

REFERENCES

[1] Raabe D, Dogramadzi S and Atkins R. Semi-automatic percutaneous reduction of intra-articular joint fractures – an initial analysis, accepted for Int. Conf. Robotics and Automation (ICRA), 2012.

[2] Zemiti N, Bricault I, Fouard C, Sanchez B, Cinquin P. LPR: A CT and MR-Compatible Puncture Robot to Enhance Accuracy and Safety of Image-Guided Interventions. *Mechatronics, IEEE/ASME Transactions on* , vol.13, no.3, pp.306-315,2008.

[3] Koseki Y, Tanikawa T, Chinzei K. MRI-compatible micromanipulator: Positioning repeatability tests & kinematic calibration. Proc IEEE Eng Med Biol Soc. 2009.

[4] Chapuis D, Gassert R, Ganesh G, Burdet E and Bleuler H Investigation of a Cable Transmission for the Actuation of MR Compatible Haptic Interfaces,

Acknowledgment: The authors would like to thank the Bristol Royal Infirmary for their help in creating CT scans.

Laser Ablation System for Residual Brain Tumour based on the Protoporphyrin Fluorescence Spectrum

Takehiro Ando[1], Junki Koike[1], Kousuke Mizumura[1], Etsuko Kobayashi[1], Hongen Liao[1], Takashi Maruyama[2], Yoshihiro Muragaki[2], Hiroshi Iseki[2] and Ichiro Sakuma[1]

[1]*Graduate School of Engineering, The University of Tokyo*

[2]*Faculty of Advanced Techno-Surgery, Tokyo Women's Medical University*

take_and_o@bmpe.t.u-tokyo.ac.jp

INTRODUCTION

Recently, 5-aminolaevulinic acid (5-ALA)-induced protoporphyrin IX (PpIX) fluorescence has been used for visualizing brain tumours intraoperatively [1]. Some studies demonstrated that PpIX fluorescence spectrum is important in identifying the tumour region more precisely. However, because manual resection has limited spatial accuracy, precise resection remains difficult even if the instrument enables measurement of the spectrum from a very tiny region. To achieve precise resection, some previous studies attempted to use a micrometre band laser for tumour ablation. Because micrometre band light is highly absorbed by water, such a system enables very precise ablation.

This study proposes an integrated diagnostic and therapeutic system that enables identification and ablation of a brain tumour during a single operation. Although a previous report described development of an integrated system to perform both measurement and ablation [2], their system was too large for clinical application. In contrast, the robotic system developed in this study has an endoscope-like shape, which makes it suitable for insertion into restricted spaces.

MATERIALS AND METHODS

1. System Configuration

Our system deals with removal of residual tumour tissues that cannot be resected manually. Therefore, the system has to be suitable for use inside the cavity created by manual resection. Our system has an endoscope-like shape that enables side irradiation of the light to identify and ablate the tumour tissue inside such a narrow region. Because the light path is coaxially set in the device, spectrum measurement and ablation can both be achieved without positional adjustment.

Figure 1 shows an overview of the system. Our system consists of a fluorescence measurement section, an ablation laser unit, a scanning unit and a controlling computer. A laser diode with a wavelength of 405 nm was used to excite PpIX, and a spectrometer (B&W TEK Inc/ WTC-111E) was used for spectrum measurement. A dichroic mirror (cut-off wavelength: 550 nm) enabled coaxial measurement of the fluorescence spectrum. A long pass filter was used to prevent intense reflection of the excitation light. Both the spectrometer and excitation light were connected by optical fibres. An erbium-doped yttrium aluminium garnet (Er:YAG) laser was used as the ablation laser, which was also connected by optical fibres. In order to achieve a coaxial light path, the lights were switched by a dielectric multilayer mirror, controlled by a computer. Because this system uses a wide wavelength band (405 nm–2.97 μm), custom-made lenses are necessary to prevent large chromatic aberrations. In this study, two lenses were designed by optimizing the curvature, thickness and materials to minimise any aberration between 405 nm and 2.97 μm. Consequently, the objective lenses comprised two lenses made from sapphire and calcium fluoride.

A tube with an outer diameter of 8 mm was used to allow insertion into a narrow cavity. The objective lenses described above were fixed inside the tube, and an aluminium-coated mirror was placed at the tip of the tube at an angle of 45° to reflect the excitation light and ablation laser. The system has two degrees of freedom. A hollow shaft stepper motor rotates the objective lens unit, which enables circumferential scanning, and a linear stage moves the objective lens unit back and forth, which enables scanning along the direction of insertion.

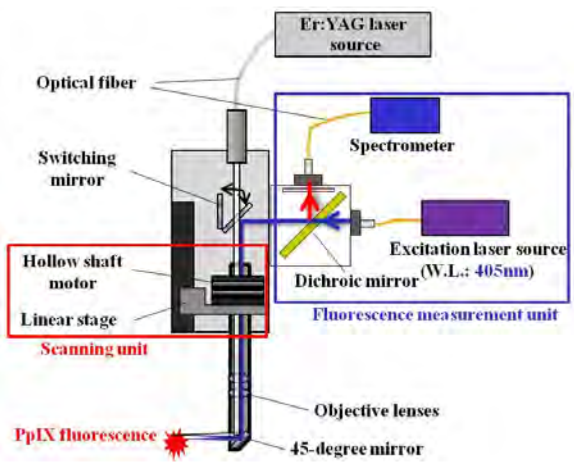

Fig. 1 System overview

2. Evaluation experiment

A Spectrum measurement

In order to confirm the performance of the system in spectrum measurement, the fluorescence spectrum was measured using an optical phantom having similar scattering properties to brain tissue. The optical phantom was made of agar gel and was prepared as follows: 1.5 g of agar powder was dissolved in 47.85 mL of boiled pure water. After the agar had completely dissolved, 1.15 mL of Intra Lipid was poured into the agar solution. Next 1 mL of PpIX solution (200 μg/mL) was added to the agar solution and the mixture cooled slightly. The concentration of Intra Lipid was chosen so that the optical phantom had the same scattering coefficient μ'_s as a brain tumour, which is approximately 3 [1/cm].

B Spot diameter

Although spot diameter can be estimated from the optical design of the lenses, the actual diameter may be larger than designed because of assembling errors. In order to measure the actual diameter, fluorescence intensity was measured where it crossed the border of an optical phantom having two regions, with and without fluorescence. The spot diameter was defined as the distance at which the fluorescence intensity is 5%–95%. Furthermore, the spot diameter of the ablation laser was also measured. A stainless-steel sheet was fixed on an XY stage and moved at 0.1-mm intervals in front of the tip of the device. Because the laser is blocked gradually, the laser power acquired behind the board will decrease. The spot diameter of the ablation laser was defined as the distance at which the laser power reached 5%–95 %.

C Ablation experiment

To confirm ablation performance, an isolated porcine brain was used as an object of ablation. The distance between the device tip and object was set to 15 mm and the Er:YAG laser activated. The experiment was repeated, changing the pulse repetition frequency and peak energy.

RESULTS

Figure. 2 shows examples of the fluorescence spectra of the optical phantom measured by the device. The results demonstrate that our system enables measurement of the PpIX fluorescence spectrum.

The results of spot diameter measurement show that spot size reached a minimum of 1.6 mm at a position 15 mm from the tip. The ablation spot diameter was 1.4 mm at a position of 12–18 mm.

Figure. 3 shows an example of the ablated brain surface at different laser settings. The ablated diameter was almost the same and was around 0.8 mm when only pulse changed. Conversely, when pulse energy changed, the ablated diameter increased with increasing pulse energy and the diameter was approximately 1.2 mm at 200 mJ/pulse.

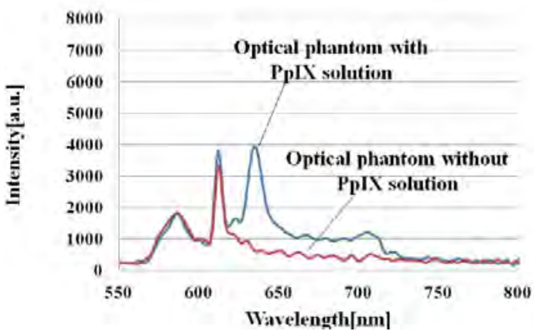

Fig. 2 Results of spectrum measurement

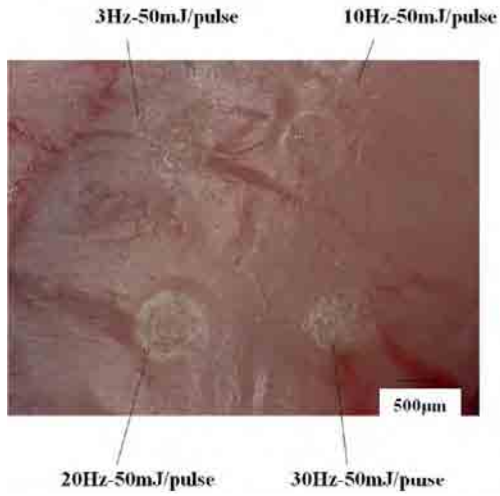

Fig. 3 Results of ablation

DISCUSSION

The actual spot diameter of the excitation light was 1.6 mm and that of the ablation laser was also larger than the designed value (0.7 mm). These enlargements of spot size may be due to stray light. This problem can be solved by inserting some diaphragms in the middle of the light pathway.

ACKNOWLEDGEMENT

This work was partly supported by a Grant-in-Aid for Japan Society for the Promotion of Science (JSPS) Fellows and the Translational Systems Biology and Medicine Initiative (TSBMI) of the Ministry of Education.

REFERENCES

[1] Stummer W, Pichlmeier U, Meinel T, Wiestler OD, Zanella F, Reulen HJ, ALA-Glioma Study Group. Fluorescence-guided surgery with 5-aminolevulinic acid for resection of malignant glioma: a randomised controlled multicentre phase III trial. Lancet Oncol. 2006; 7:392-401.

[2] Liao H, Noguchi M, Maruyama T, Muragaki Y, Kobayashi E, Iseki H, Sakuma I. An integrated diagnosis and therapeutic system using intra-operative 5-aminolevulinic-acid-induced fluorescence guided robotic laser ablation for precision neurosurgery. Med Image Anal. 2012; 16:754-66.

Toward Intraoperative Image-Guided TransOral Robotic Surgery

W.P. Liu[1*], S. Reaugamornrat[1], A. Deguet[1], J.M. Sorger[4], J.H. Siewerdsen[1,3], J. Richmon[2], R.H. Taylor[1,3]

Departments of [1]Computer Science, [2]Otolaryngology-Head and Neck Surgery, [3]Biomedical Engineering, Johns Hopkins University, Baltimore, USA
[4]Intuitive Surgical Inc., Sunnyvale, USA
**wen.p.liu@jhu.edu*

INTRODUCTION

TransOral robotic surgery (TORS) is a minimally invasive surgical intervention to treat oropharyngeal cancer, including resection of base of tongue tumors. It is a progressively more viable option in addressing a trend of increasing oral cancer association with the human papilloma virus (HPV), accounting for 70% of oropharyngeal carcinoma in 2000, compared to 16% in the 1980s. The impact of HPV on the epidemiology of oropharyngeal cancer has resulted in younger patients (40 to 60 years) [1], whose treatment options must equally consider cure and longer term quality of life compared to HPV-negative cases (typically older and smoking-related). TORS offers an increasingly attractive treatment modality with minimal morbidity and reduced toxicity compared to conventional regimens of chemo+radiotherapy [2].

However, contraindications, including poor tumor visualization, large tumor size, and involvement of the carotid artery or other critical structures, remain. Most base of tongue tumors are buried deep in the musculature of the tongue, presenting a challenge to clear visualization of all but the most superficial aspects of the tumor and an inability to palpate the tongue base during robotic surgery. The resulting challenge to reliably delineate tumor margins is compounded by the fact that pre-operative imaging of the tongue in repose may not accurately reflect the tumor position when the tongue is retracted and deformed during surgery. Expert surgeons rely on experience to remain oriented with respect to critical anatomy, even after tissue deformation, by intuitively mapping preoperative data to the (highly deformed) surgical field. Such practice leaves considerable room for improvement and may lead to compromised margins and ultimately recurrent disease.

We propose using cone-beam computed tomography (CBCT) [3] to capture intraoperative patient deformation. Critical structures (e.g., the tumor and adjacent arteries) can be either segmented directly in CBCT or in preoperative CT/MR followed by deformable registration to the intraoperative scene. Augmentation of TORS endoscopic video with image and planning data defining the target and critical structures offers the potential to improve navigation, spatial orientation, confidence, and tissue resection, especially in the hands of less experienced surgeons. This paper presents initial development and evaluation of video augmentation on the stereoscopic *da Vinci S* System for base of tongue tumor resection in TORS.

MATERIALS AND METHODS

I. System Overview

Our system builds from the *cisst*/SAW software infrastructure developed at Johns Hopkins University in collaboration with Intuitive Surgical Inc. (ISI) [4]. Stereoscopic video augmentation is achieved by extending the *cisst 3DUserinterface* (3DUI), using Visualization Toolkit (VTK), to support manual registration of segmented intraoperative planning data of critical structures (Fig. 1a) to the endoscope. SAW and the *da Vinci* robot communicate through the ISI application programming interface to relay joint positions of the slave arms, endoscope and master controllers. Currently, CBCT data is registered to the robotic camera space through rigid point-based registration by locating fiducials with the master controls in 3DUI. VTK objects associated with planned data (i.e., the target and critical structures) are stippled for transparency, overlaid on stereo video captured from the *da Vinci* cameras, and streamed to the master console to follow the endoscope joint positions in real time.

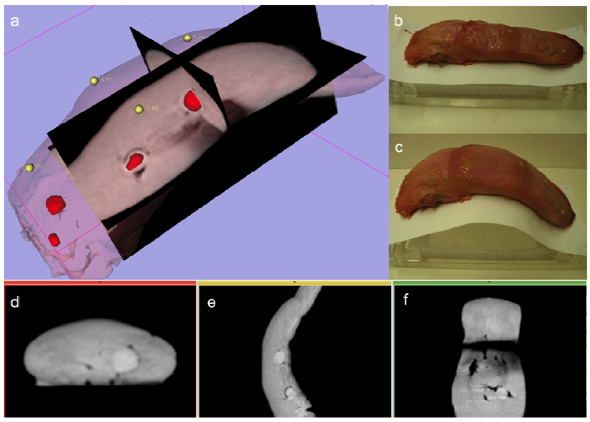

Fig. 1 (a) Surgical plan, in (a,d,e,f) 3D Slicer (na-mic kit, Brigham & Women's Hospital, Cambridge MA**)**, with surface and target VTK meshes segmented from the intraoperative CBCT of a (b,c) pig tongue specimen, embedded with spherical targets.

II. Evaluation of video overlay accuracy

A rigid anthropomorphic skull phantom derived from 3D rapid prototyping modeled from a cadaver CT scan was used to assess the accuracy of the video overlay. Evaluations measured the reprojection distance (RPD), (i.e., the shortest distance between the overlaid CT targets and rays through the visible target seen through both cameras). From five different camera poses, the mean RPD of three manually segmented fiducials embedded near the soft palate of the phantom was measured at (1.82±0.92) mm.

III. Experiment on the TORS Robot

Experimentation using porcine tongue phantoms with a *da Vinci S* robot was conducted to evaluate the effect of intraoperative imaging and navigation through video augmentation. A custom phantom built from an acrylic base, supported two foam templates allowing tongue specimens to be imaged in the preoperative (flat, Fig. 1b) and intraoperative (curved and distended, Fig. 1c) positions. Three porcine tongues (each embedded with eight soft-tissue targets) were imaged with CBCT. A fellowship-trained base-of-tongue surgeon expert in use of the *da Vinci S* was tasked to place a needle in each target of the curved tongue phantom with variants in image guidance as given in Table 1. Phantom 1 represents current practice with preoperative image data+no overlay while phantom 2 replaces preoperative with intraoperative images+no overlay. Phantom 3 characterizes our proposed workflow with intraoperative CBCT+video overlay. In each case, the target localization error (TLE) was measured as the distance between the needle point and the closest edge of the target (with needles placed on or inside the target treated as a TLE of zero).

Phantom	Image Data	Overlay	TLE [mm]		
			Mean	STDDev	Max
1	Preop	No	4.92	4.57	15.03
2	Intraop	No	3.90	3.26	9.94
3	Intraop	Yes	1.70	1.77	4.05

Table 1 Experiments with TORS tongue phantoms.

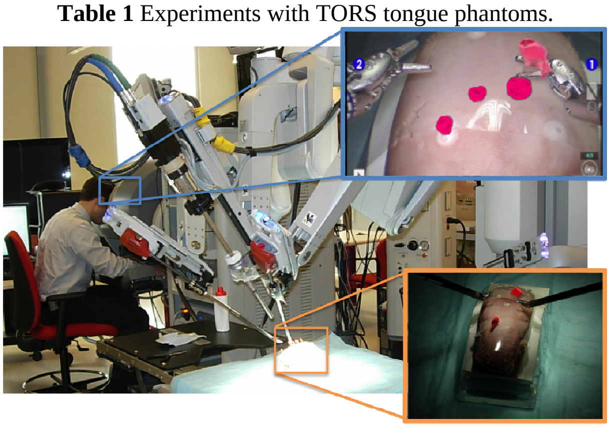

Fig. 2 Experimental setup using a *da Vinci* S system with stereoscopic video overlay of spherical soft-tissue targets (magenta) segmented from intraoperative CBCT.

RESULTS

Initial experimental results measuring TLE is summarized in Table 1 with box plots in Fig. 3. The position of needles and target edges were determined by manual segmentation from CBCT of each tongue following the experiment. Mean TLE for phantom 1 was (4.92±4.6) mm, compared to phantom 2 (3.90±3.26) mm, and phantom 3 (1.70±1.77) mm. This shows the potential value of intraoperative imaging and navigation through video augmentation to improve target localization in TORS. A p-value of 0.048 between phantom 1 and phantom 3 demonstrated statistical significance between simulated current practice (unregistered preoperative imaging) and the proposed image guidance system.

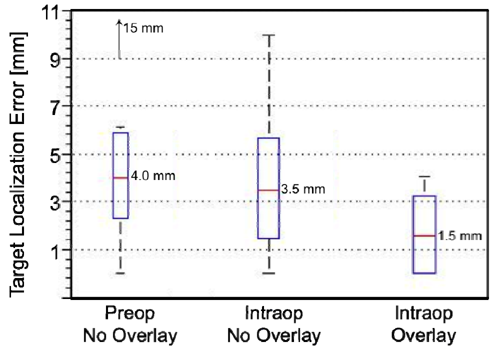

Fig. 3 Target localization error in the three experimental scenarios**.**

DISCUSSION

A system with intraoperative image-guidance for TORS has been presented. Experiments show improved target localization using intraoperative imaging and video augmentation with the potential to address challenges of anatomical displacement. Future work includes improving rigid video to CT registration and kinematics-based tracking with vision-based 3D reconstruction. Research on deformable registration between preoperative CT/MR, including segmented surgical plans, and intraoperative CBCT is underway. Potential error sources and sensitivity analysis will be investigated in order to characterize systematic performance and accuracy.

ACKNOWLEDGEMENTS

This research is supported in part by Intuitive Surgical Inc. and by Johns Hopkins University. The authors extend sincere thanks to Dr. Iulian Iordachita et. al., Woo Jin Kim for assistance with tongue phantom fabrication, and to Dr. Sebastian Schafer for CBCT acquisitions. The C-arm CBCT prototype was developed in academic-industry partnership with Siemens XP (Erlangen, Germany) with thanks to Dr. Rainer Graumann and Dr. Gerhard Kleinszig. Infrastructure support was provided from NIH-R01-CA-127444, NSF EEC9731748 and the Swirnow Family Foundation.

REFERENCES

[1] Westra, W. H., "The Changing Face of Head and Neck Cancer in the 21st Century: The Impact of HPV on the Epidemiology and Pathology of Oral Cancer," in *Annual North American Socity of Head and Neck Pathology Companion Meeting*, Boston, 78-81 (2009).

[2] Weinstein, G. S. and O'Malley, B. J. W., *Transoral Robotic Surgery (TORS)*. San Diego, CA, USA: Plural Publishing Inc., (2012).

[3] Siewerdsen, J. H., Moseley, D. J., Burch, S., Bisland, S., Bogaards, A., Wilson, B. A., and Jaffray, D. A., "Volume CT with a flat-panel detector on a mobile, isocentric C-arm: Pre-clinical investigation in guidance of minimally invasive surgery," *Medical Physics*, 32(1) , 241-254 (2005).

[4] Kazanzides, P., Jung, M. Y., Deguet, A., Vagvolgyi, B., Balicki, M., and Taylor, R. H., "Component-based software for dynamic configuration and control of computer assisted intervention systems," *Insight Journal* June (2011).

The Role of Haptics in Robotics-Assisted Mitral Valve Annuloplasty

Maria E. Currie[1,3], Ali Talasaz[2,3], Ana Luisa Trejos[2,3], Reiza Rayman[1], Michael W.A. Chu[1,4], Bob Kiaii[1,3,4], Terry Peters[5], Rajni Patel[2,3,4]

[1]*Division of Cardiac Surgery, Department of Surgery, London Health Sciences Centre, London, Ontario, Canada*

[2]*Dept. of Elect. & Comp. Engineering, Western University, London, Ontario, Canada*

[3]*Canadian Surgical Technologies & Advanced Robotics, Lawson Health Research Institute, London, Ontario*

[4]*Dept. of Surgery, Schulich School of Medicine & Dentistry, Western University, Canada*

[5]*Medical Imaging Laboratory, Robarts Research Institute, Western University, Canada*

INTRODUCTION

In the currently used minimally invasive surgical robotic system (the da Vinci® from Intuitive Surgical Inc.), the master-slave configuration and the absence of haptic feedback prevent the transmission of tool-tissue interaction forces to the surgeon [1]. This may be particularly deleterious in dexterous fine movements such as intracorporeal suturing and knot tying, which require accurate control of applied forces and instrument positions [2]. Without haptic feedback, excessive forces may be applied to tissue leading to increased trauma and damage to tissue [1, 2]. This could be particularly important in robotics-assisted mitral valve repair, which requires fine motor skills to suture an annuloplasty band to the cardiac tissue along the mitral valve annulus.

Therefore, the objective of this study is to determine the effect of direct haptic feedback and visual force feedback on the amount of force applied to mitral valve tissue and the time to perform *ex vivo* mitral valve annuloplasty using robotics-assisted techniques. In addition, our aim is to determine whether these effects are consistent between novices and experts in robotics-assisted cardiac surgery.

MATERIALS AND METHODS

Mitral valve annuloplasty test-bed

A cardiac surgery test bed was constructed to measure forces applied by test subjects performing robotics-assisted mitral valve annuloplasty. The tissue test bed consisted of a porcine mitral valve mounted on a six-axis force/torque sensor (ATI Industrial Automation, Apex, NC) to measure applied forces in the *x*, *y*, and *z* directions.

Haptics-enabled robotic surgery system

The haptics-enabled master-slave surgical system used for trials is shown in Figure 1. This setup consists of two Mitsubishi PA10-7C robots as the slave system controlled remotely over a dedicated network through two customized Quanser Haptic Wands as the master interface [3]. The structure of the Haptic Wand, its workspace and force reflection capability have been described in a previous publication [4].

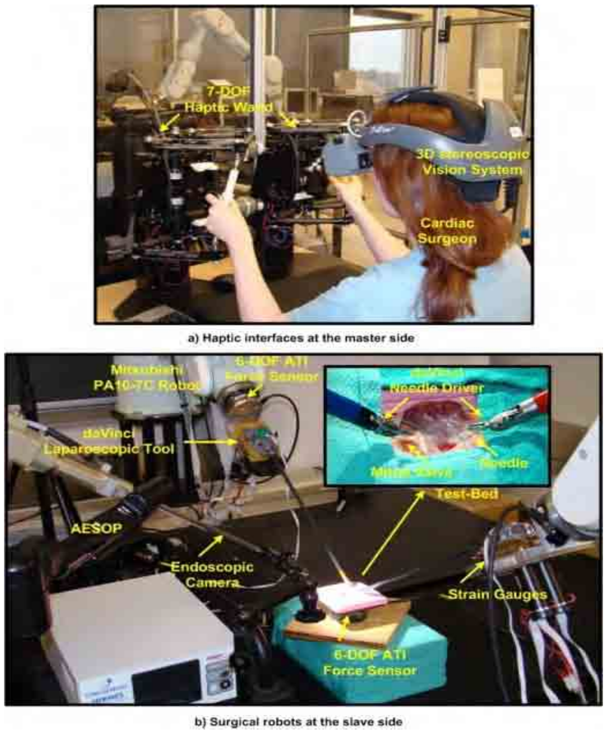

Fig. 1 Haptics-enabled robotic surgical system

Stereoscopic visualization was provided by a zero-degree endoscope (Intuitive Surgical, Sunnyvale, CA) and a ProView XL50 head-mounted display (Kaiser Electro-Optics Inc, Carlsbad, CA).

Assessment of forces and time required for mitral valve annuloplasty tasks

Cardiac surgeons with experience in both conventional and robotics-assisted cardiac surgery and medical trainees with no experience in robotics-assisted surgery used the master-slave robotic system to pass four sutures through the porcine mitral valve annulus and an annuloplasty band and tied the stitches in place. The forces applied by the study subjects and the time required to complete each task were recorded. Subjects performed tasks with or without force feedback, or with visual force feedback, direct force feedback, or both visual and direct force feedback. The order in which force feedback was presented was randomized. Throughout all trials, all actions were captured on video and the positions of the master (Haptic Wand) and the slave robot were also recorded.

RESULTS

The results obtained to date from novice trials revealed that there was no significant difference in the time required to complete either suturing (Figure 2) or tying (not shown) using either visual or direct force feedback, or no force feedback ($p = 0.9$). However, visual, direct, and combined visual and direct force feedback significantly reduced the amount of force applied to cardiac tissue during suturing ($p = 0.07$; Figure 3) and suture tying by novices when compared to surgery without force feedback ($p = 0.09$; Figure 4).

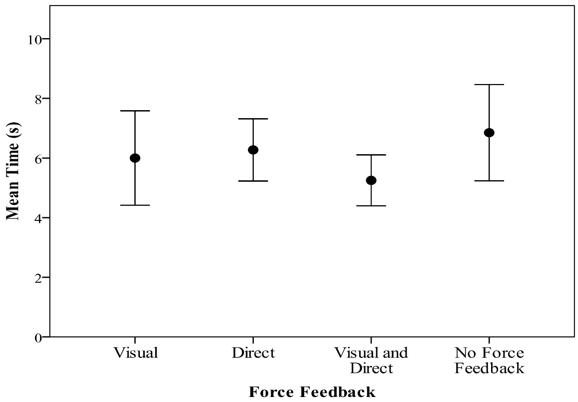

Fig. 2 Mean time required to suture mitral valve annulus.

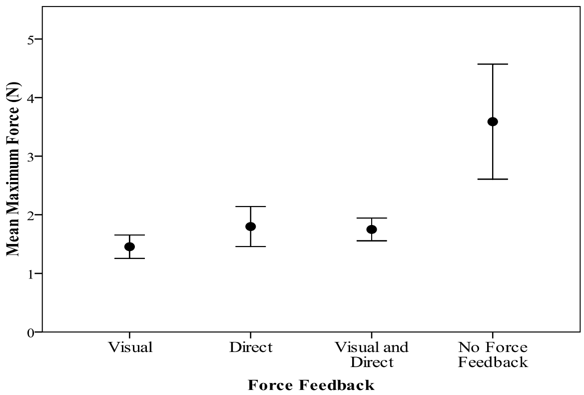

Fig. 3 Mean maximum force applied during suturing of the mitral valve annulus.

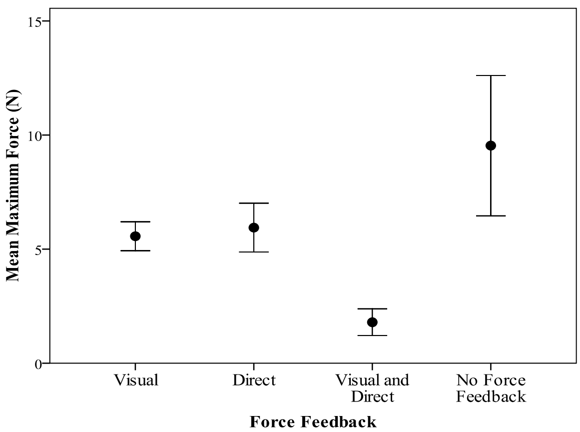

Fig. 4 Mean maximum force applied during suture tying along the mitral valve annulus.

DISCUSSION

Our preliminary results from novice trials suggest that when comparing robotics-assisted mitral valve annuloplasty with and without force feedback, use of the former mode results in significantly less force applied to cardiac tissue during suturing and suture tying. In addition, the amount of force applied during suturing and suture tying was more consistent with force feedback (Figures 3, 4). Previous studies of porcine tissue have reported visible tissue damage with the application of an 11 N force over an area of 2.4 cm^2 [5]. In this study, potentially damaging forces were applied to cardiac tissue during suture tying using robotics-assisted techniques without force feedback. However, consistently less force was applied to cardiac tissue when all modes of force feedback were used. In particular, the use of both visual and direct force feedback during robotics-assisted mitral valve annuloplasty resulted in a greater decrease in forces applied to cardiac tissue when compared to visual or direct force feedback alone. There was no statistically significant difference in the amount of time required or force applied to cardiac tissue between visual and direct force feedback (Figures 3, 4). Finally, while the addition of force feedback decreased the amount of damaging force applied to cardiac tissue during robotics-assisted mitral valve annuloplasty, it did not significantly increase the time required to complete suturing and tying tasks.

The implication of these preliminary findings is that in order to achieve better control of interaction forces on cardiac tissue during robotics-assisted surgery, force feedback may be required. In our future work, we expect that these findings will be more pronounced with the completion of all trial experiments with both experts and novices. In addition, we will determine how these effects vary for subjects with varying levels of expertise in robotics-assisted surgery.

REFERENCES

[1] Westebring-van der Putten EP, Goossens RH, Jakimowicz JJ, and Dankelman J. (2008) Haptics in minimally invasive surgery--a review. Minim Invasive Ther Allied Technol. 17(1): 3–16.

[2] Trejos AL, Patel RV, and Naish MD. (2009) Force sensing and its application in minimally invasive surgery and therapy: a survey. Proc. IMechE Part C: J Mech Eng Sci.; 224(7): 1435–1454.

[3] Talasaz A. (2012) Haptics-Enabled Teleoperation for Robotics-Assisted Minimally Invasive Surgery. PhD thesis, Western University.

[4] Bassan H, Talasaz A, and Patel RV. (2009) Design and characterization of a 7-DOF haptic interface for a minimally invasive surgery test-bed. IEEE/RSJ Conference on Intelligent Robots and Systems. Oct 10-15: 4098–4103.

[5] Trejos AL, Jayender J, Perri MT, Naish MD, Patel RV, and Malthaner RA. (2009) Robotics-assisted tactile sensing for minimally invasive tumour localization. Int J Robot Res. 28 (9): 1118–1133.

Vibrotactile Perception for Haptics in Virtual Reality Surgical Training

T. Martin, C. W.Schwingshackl, M. J. Oldfield, F. Rodriguez y Baena

Department of Mechanical Engineering, Imperial College London, UK
f.rodriguez@imperial.ac.uk

INTRODUCTION

The advance of simulators for surgical training requires constant improvement in the quality, accuracy and magnitude of sensory feedback to the user. The use of vibration reproduction as a method of haptic feedback is still underdeveloped [1], with most existing systems operating on a direct 'live' loop where vibrations are measured and simultaneously displayed through the haptic interface. Whilst producing convincing results, these systems lack the ability to recreate the sensations 'off-line' at a later time [2]or in a simulated surgical environment. This work differs further from [2] in that the tool response is also investigated. In order to achieve this, the higher frequency elements of measurements taken at the tip of surgical tools are required, which need to be analyzed and reproduced so that their contribution in surgery (e.g. navigation, diagnosis, perception) can be assessed. Work has been done on the signals reproduced when surgical probes tap different surfaces and the resulting vibrations' dependence on the surface properties. This has been done for both tactile and force feedback systems [3]. Whilst being useful, these results have yet to be implemented in a system, in part due to the limitations presented by current actuators, both in terms of their size and their ability to output large accelerations. First, an investigation into the steady state, low force exploration of a surface with a representative probing tool is presented. Subsequently, a system is presented that attempts to recreate only the higher frequency components of vibrotactile perception.

MATERIALS AND METHODS

In order to investigate the high frequency (50 – 1,000 Hz) haptic response on a representative probe, an experimental system was created. A Microscribe® G2 (CNC Services, Inc.) six degrees of freedom mechanical digitizer was chosen as the basis for capturing the 3 dimensional position data, and a three axis Integrated Circuit - Piezoelectric (ICP) accelerometer was used to capture vibration information. The Qt™ (Nokia inc.) open source graphics library was used to design and implement a computer interface using the Visualization Toolkit (VTK, Kitware, inc.) for graphical display and visual feedback, on a Windows 7 PC. With the software, Microscribe interface and a representative tool point, the response of different surfaces could be measured with a DataPhysics® data capture card and the associated SignalCalc™ 240 Dynamic Signal Analyzer data capture software. The response of the accelerometer could then be related to the position and velocity of the tip for the duration for the capture.Four surfaces were chosen for exploration. These were MDF, aluminum, perspex and rubber. The samples were all prepared on an MDF base of the same size (0.2 × 0.2m). These surfaces were first registered against a common coordinate system using a closed-form three-point plane registration. Data was then captured by dragging the tool tip over the surfaces. The movement of the tool over the surface was split into three sections; acceleration; steady state with approximately constant velocity; deceleration towards the end of the capture. The acceleration data from the accelerometer were truncated over the steady state period and examined for their frequency content following windowing and DC offset removal (to account for drift in the acceleration data). A normalized, discrete fast Fourier transform (DFFT) was used to analyze the data, in conjunction with a power spectrum density analysis using the Welch spectrum object.

RESULTS

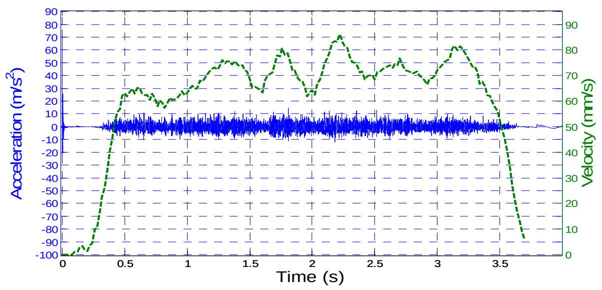

Fig. 1 Example acceleration response (blue)and velocity (green) oftool tip during straight line exploration of MDF.

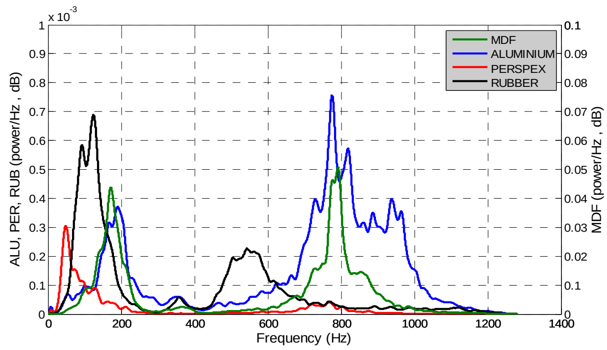

Fig. 2 Power Density Spectrums of typical responses of the four test materials on split axes.

Figure 1 shows that the magnitude of the acceleration response appears to correlate well with the magnitude of the velocity of the tool tip. This is true for all data collected on tested materials. Overall, ten tests were conducted on each material, with the average velocity of all captured data remaining constant between tests at 65-70 mm/s. The DFFTs of the data show a frequency response profile which centers around two main peaks. Analysis of the frequency information in the steady state exploration by focusing on the power density spectrum of the data, as shown in Figure 2, confirms this trend. There are two distinct peaks at 180 Hz and 800 Hz. The frequency content of the signal as shown in Figure 2 is not restricted to MDF, as very similar peaks are found at the same frequencies for MDF and Aluminum, 100 Hz and 550 Hz for rubber and 50 Hz for Perspex.

DISCUSSION

In this study, the sensations being measured rely on a 'distal perception approach", where it assumed that the user uses the tool as an extension of their tactile senses. In order to be able to recreate the measured vibrations in a haptic system, it is important to understand the nature of tool interactions. Two possibilities exist. Firstly, the perceived response is related to the speed of the tool over the surface and the texture of the surface itself; increasing the speed of the tool would thus increase the frequency of the measured vibrations, which occur as a result of the tool tip being able to travel along the three-dimensional texture of the sample. Secondly, the tool undergoes multiple small impacts as it travels along the surface, generating hundreds of broadband excitations of the tool tip per second. These are independent of the speed of the tool and simply excite the natural response of the system instead, which is a function of the system's geometry and materials. Across multiple tests on the same material, the limited range of force imparted on the surface does not significantly affect the consistency of the measured frequency response.

The frequency domain results of data acquired while dragging the probe tip over the selected materials demonstrates that the force profile imparted on the tool point excites what appear to be the natural responses of the system, at 180 and 800 Hz. Indeed, the main difference in vibrotactile response between surfaces is in the amplitude of the frequency response around the natural frequencies. For example, aluminum has a response ten times smaller than MDF, where the amplitude is proportional to the roughness of the surface. This suggests that the response of the tool tip is independent of the transversal speed, as the same frequency content exists regardless of material or speed of the tool. The response for rubber and Perspex are possibly erroneous due to the deformation of the rubber and the tip slipping during the Perspex capture. Further tests must be completed on other deformable and smooth surfaces in order to verify if these effects affect the forcing of the system. The implication for haptic recreation is that, to model the sensation of stroking bone or tissue in a surgical simulation, one must know the specific tool's natural response as well as the amplitude of excitation from that material. It is not necessary to model and reproduce the surface and its

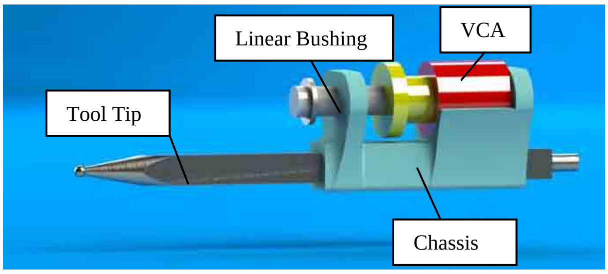

Fig. 3 Render of the voice coil actuator (VCA) system still to be implemented.

mechanical properties in full for tactile feedback. In order to investigate this hypothesis, a vibro-tactile haptic system is currently under development (Figure 3). The system will be used to excite the same probe that was used for the vibration measurement experiments. The mechanical design for the system includes a voice coil (MotiCont LVCM-013-013-02) mounted on a chassis and centered around an equilibrium position by two restoring springs. The axis of actuation, according to the distal approach, is irrelevant as the human hand cannot sense the direction of vibrations[4].

CONCLUSIONS AND FUTURE WORK

Experiments have been conducted to measure the high frequency vibrations occurring at the tool point of a representative surgical instrument. The aim was to identify key parameters which affect perception during stroking of a surface, which is a common task in diagnostic procedures (e.g. knee arthroscopy with a hooked probe). Without considering surface deformation or the first impact, results suggest that the frequency components of the vibration profile only depend on the system's natural frequencies (which are in turn a function of geometry and materials) and not of the surface texture itself.

This finding will inform the development of novel haptic displays for surgical training. The haptic system will be used to conduct perceptual tests on a wide sample base of textures, with both a 'black box' and a control scheme approach. The black box approach will directly recreate the accelerations measured at the probe tip with direct output and no control. The control scheme will excite only the natural frequencies of the system at the desired magnitude required to simulate a particular surface.

REFERENCES

[1] E. Shaer, et al., "Tangible user interfaces",*Foundations and Trends in HCI*, vol. 3, no. 1-2,2010.
[2] K. Kuchenbecker, et al., "VerroTouch: High-Frequency Acceleration Feedback for Telerobotic Surgery",*EuroHaptics*, vol. 6191,pp. 189-196,2010.
[3] S. Jeon, et al., "Extensions to haptic augmented reality: Modulating friction and weight", *World Haptics Conference (WHC), 2011 IEEE*, pp. 227-232, June 2011.
[4] J. M. Loomis. "Distal attribution and presence",*Presence: Teleoperators and Virtual Environments*, vol. 1, pp 113–119, 1992

Surgical Instrument Vibrations are a Construct-Valid Measure of Technical Skill in Robotic Peg Transfer and Suturing Tasks

Karlin Bark, Ernest D. Gomez, Charlotte Rivera, William McMahan, Austin C. Remington, Kenric M. Murayama, David I. Lee, Kristoffel R. Dumon, Noel N. Williams, and Katherine J. Kuchenbecker

University of Pennsylvania, Philadelphia, Pennsylvania, USA

kbark@seas.upenn.edu, egomez@mail.med.upenn.edu, kuchenbe@seas.upenn.edu

INTRODUCTION

Traditional surgical skill assessment relies on observation of a surgeon's performance, a method that is both subjective and time consuming. The growing demand for robotic minimally invasive surgery has increased the need for objective methods of assessing technical skill for surgical training [1,2]. Several prior skill assessment studies have analyzed the kinematic motion of the robot to calculate performance metrics such as economy of motion and instrument speed [3,4]. However, these metrics do not account for interactions between the instruments and the surgical environment.

One possible method of objectively accounting for the quality of these interactions and classifying instrument handling skills is to measure the transient mechanical vibrations of the robotic instruments. These vibrations primarily result from instrument contact with objects in the environment, such as collisions and needle hand-offs, with larger vibrations generally signifying *rougher* interactions. *Abrupt* movements of the surgical instruments also cause measurable vibrations. Our work on VerroTouch, a system for providing real-time auditory and haptic feedback of instrument vibrations [5], has shown that robotic instrument vibrations can easily be measured with low-cost accelerometers mounted on the patient-side robot.

Preliminary analysis of data collected in a previous study of VerroTouch [5] showed that instrument vibration magnitude is a construct-valid metric of technical skill for a needle passing task [6]. To determine whether this metric is construct valid for a wider range of training tasks, this paper analyzes the peg transfer and suturing tasks from that prior study.

MATERIALS AND METHODS

As fully detailed in [5], twelve surgeons performed three box-trainer-style tasks (peg transfer, needle pass, and suturing) with an Intuitive Surgical da Vinci S robot augmented with our system for measuring and feeding back instrument vibrations. Participants consisted of seven novice surgeons with no prior da Vinci experience and five experienced robotic surgeons (with experience ranging from 50 to 2400 cases). Each task was performed by each subject four times under different feedback conditions. This retrospective analysis focuses on the peg transfer and suturing tasks, and feedback condition is not considered.

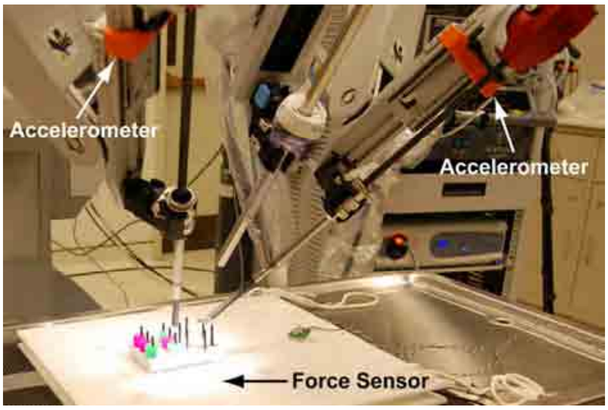

Fig. 1. A da Vinci S robot augmented with accelerometers that measure instrument vibrations. Task materials are mounted to the white board, which is equipped with a force sensor.

Accelerometers attached to the robot arms measured the high-frequency accelerations of the left and right needle driver instruments, and a force-torque sensor mounted within the task board measured the forces applied to the task materials (Fig. 1). For each trial we calculated the average root-mean-square (RMS) vibration magnitude of the two instruments and the RMS force applied to the task board over the duration of the task, as described in [5]. Only vibrations exceeding 0.2 m/s^2, the empirically determined noise ceiling of the sensors, were included in the RMS calculations. Video of each trial was recorded, and the completion time was noted.

To verify the skill level of the participants, two experienced robotic surgeons who participated in the study two years prior were recruited as raters; both were blinded to subject identity and experience level. The raters scored video recordings of the 48 suturing trials on paper surveys using a modified combination of the Objective Structured Assessment of Technical Skill (OSATS) global rating scales [7] and the Global Evaluative Assessment of Robotic Skills (GEARS) scale [8]. The following OSATS categories were used: *Respect for Tissue, Time and Motion, Instrument Handling,* and *Flow of Operation and Forward Planning*. The GEARS items used were *Depth Perception, Bimanual Dexterity, Efficiency, Force Sensitivity*, and *Robotic Control*. The peg transfer task was not rated due to the simplicity of the task.

Table 1. Comparison of RMS instrument vibrations, RMS forces, and time to completion for novice and experienced robotic surgeons doing peg transfer and suturing tasks. Suturing skill was also rated using OSATS and GEARS.

	Novice	Experienced	p value
Peg Transfer			
RMS Vib (m/s²)	0.9 ± 0.2	0.8 ± 0.1	0.049
RMS Force (N)	3.3 ± 1.3	2.3 ± 1.2	<0.0001
Time (s)	121 ± 32	87 ± 21	<0.0001
Suturing			
RMS Vib (m/s²)	0.8 ± 0.2	0.6 ± 0.1	0.023
RMS Force (N)	1.5 ± 0.8	1.0 ± 0.4	0.015
Time (s)	113 ± 24	60 ± 15	<0.0001
OSATS (%)	0.5 ± 0.1	0.8 ± 0.1	<0.0001
GEARS (%)	0.5 ± 0.1	0.8 ± 0.1	<0.0001

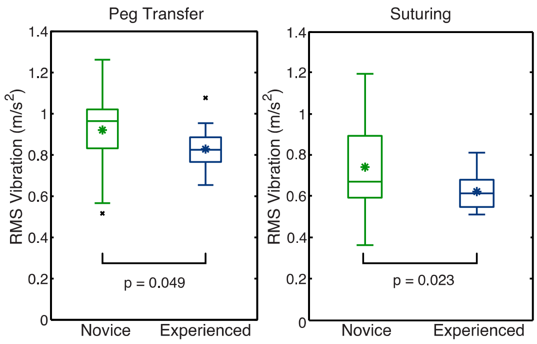

Fig. 2. Box plots of the average measured RMS instrument vibrations for the peg transfer and suturing tasks. The mean value for each group is marked with *, and outliers are indicated with an x. Experienced robotic surgeons caused significantly lower instrument vibrations than novices in both tasks (p-values indicated on plots).

Independent-sample t-tests were conducted on the task data to compare the instrument vibrations of novice and experienced surgeons. Applied force, completion time, and rated skill were also compared to determine whether differences existed between the two groups.

RESULTS

Experienced robotic surgeons recorded significantly lower instrument vibrations than the novice surgeons for both the peg transfer and suturing tasks, (Peg Transfer: $t(46) = 2.02$, $p = 0.049$, Suturing: $t(46) = 2.34$, $p = 0.023$). Box plots of the RMS vibration data for both tasks are provided in Fig. 2. Experienced surgeons also recorded lower RMS forces and task completion times, as seen in Table 1.

Blinded OSATS and GEARS evaluations verified that experienced robotic surgeons performed the suturing task with greater assessed technical skill than novices. Inter-rater reliability was very good, with an Intraclass Correlation Coefficient (ICC) of 0.80 (95% CI 0.71 – 0.86). Average skill ratings and results of the t-test are also found in Table 1.

DISCUSSION AND CONCLUSIONS

The presented results demonstrate that instrument vibrations, as measured by VerroTouch, are a construct-valid measure of technical surgical skill during robotic in vitro training tasks. Although differences in RMS vibration magnitude appear to be small for these tasks, some novices' slower coordinated actions may have resulted in lower vibrations for certain manipulation events. We believe overall skill level depends on multiple measures, so novices should improve their coordination while completing tasks quickly, efficiently, with low forces, and with low instrument vibrations.

In contrast to the kinematic measures recorded by the robotic system, instrument vibrations indicate the quality of instrument handling and interaction with the operative environment. Furthermore, evidence that visual feedback of skill measures may increase a surgeon's ability to improve their performance [4] suggests that the real-time audio and haptic feedback of instrument vibrations provided by VerroTouch could also enhance the training of robotic surgeons. Studies to verify this are currently in progress.

ACKNOWLEDGMENTS

This research is supported by the Pennsylvania Department of Health via Health Research Formula Funds, by the National Science Foundation via grant #IIS-0845670, by a Translational Research Award from the Coulter Foundation, and by Intuitive Surgical via the donation of instruments and accessories.

REFERENCES

[1] Schreuder HWR, Wolswijk R, Zweemer RP, Schijven MP, Verheijen RHM. Training and learning robotic surgery, time for a more structured approach: a systematic review. BJOG. 2012; 119(2):137-149.

[2] van Hove PD, Tuijthof GJM, Verdaasdonk EGG, Stassen LPS, Dankelman J. Objective assessment of technical surgical skills. Br J Surg. 2010; 97:972-987.

[3] Kumar R, Jog A, Malpani A, Vagvolgyi B, Yuh D, Nguyen H, Hager G, Chen CCG. Assessing system operation skills in robotic surgery trainees. Int J Med Robot. 2012; 8:118-124.

[4] Judkins TN, Oleynikov D, Stergiou N. Enhanced Robotic Surgical Training Using Augmented Visual Feedback. Surg Innov. 2008; 15(1):59-68.

[5] McMahan W, Gewirtz J, Standish D, Martin P, Kunkel JA, Lilavois M, Wedmid A, Lee DI, Kuchenbecker KJ. Tool Contact Acceleration Feedback for Telerobotic Surgery. IEEE Transactions on Haptics. 2011; 4(3):210-220.

[6] Gomez ED, Bark K, Rivera C, McMahan W, Remington A, Lee DI, Williams NN, Murayama KM, Dumon KR, Kuchenbecker KJ. Construct Validity of Instrument Vibrations as a Measure of Robotic Surgical Skill. Accepted to the American College of Surgeons 98th Annual Clinical Congress, 2012.

[7] Martin JA, Regehr G, Reznick R, Macrae H, Murnaghan J, Hutchison C, Brown M. Objective structured assessment of technical skill (OSATS) for surgical residents. Br J Surg, 1997; 84(2):273–278.

[8] Goh AC, Goldfarb DW, Sander JC, Miles BJ, Dunkin BJ. Global Evaluative Assessment of Robotic Skills: Validation of a Clinical Assessment Tool to Measure Robotic Surgical Skills. J Urol, 2012; 187(1):247-252.

Air-Float Stiffness Probe for Tissue Abnormality Identification in Soft Tissue Palpation

I.B. Wanninayake, K. Althoefer, L.D. Seneviratne

Centre for Robotic Research, Kings College London

i.wanninayake@kcl.ac.uk

INTRODUCTION

Robot-assisted minimally invasive surgical techniques are designed and developed to provide outcomes that are equivalent to those resulting from conventional surgical techniques such as open surgery while enabling a shorter rehabilitation time,less pain anda less risk of post operative infection. Recent advances in robotic-assisted surgical systems such as the da Vinci[TM] (Intuitive Surgical [1]) have further revolutionized the medical field by offering number of advanced features such as 3D vision, high distal dexterity with 7 degrees of freedom, motion scaling, and natural hand-eye alignment at the surgical console. However, the lack of tactile and force feedback still remains as a majordrawback of robotic-assisted surgical systems currently in clinical use. This limits the application of such systems in many surgical procedures as the surgeon has to rely solely on the visual information to assess tool tissue interaction forces during a surgery.Surgeon can no longer use the long established techniques such as tissue palpation to inspect the surgical field and identify tissue abnormalities and hidden pathological lesions such as tumors. However, a number of attempts to achieve palpation capability through robotic devices are reported in the literature [2]-[3]. The primary goal of this paper is to present a novel optical fiber based air-float palpation probe designed to measure stiffness variation of a soft tissue while rolling over the tissue surface in any direction in a near frictionless manner. The probe can concurrently measure the indentation depth and surface profile variations and experiments carried out using simulated soft tissues showed that the probe can accurately identify tumors embedded inside non-flat tissue surfaces.

MATERIALS AND METHODS

Air-float stiffness probe consists of fourfiber optical displacement sensing elements D_1, D_2, D_3, and S_1. The sensing elements D_1, $D_2$and D_3 are used to measure tissue surface profile variations while S_1 is used to measure indentation depth. Two fiber optic cables in parallel configuration are used to measure the displacement of each sensing element. Structure and working principle of the probe is illustrated in Fig. 1. Spherical indenter is held at the tip of the probe by a steady stream of air. It is free to rotate in any direction and the air flow through the tunnel ensures a friction free movement of sphere within tunnel. Three surface profile sensors D_1, D_2, D_3, are mounted in the shield

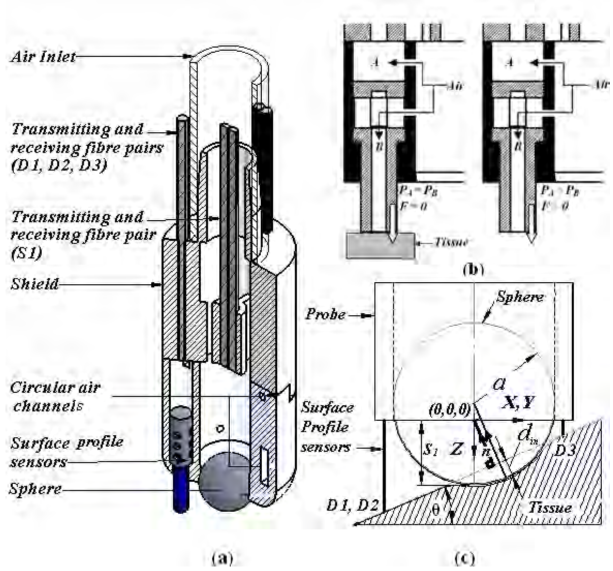

Fig. 1 (a). Longitudinal section of the stiffness probe indicating four fiber optic displacement sensors, S1,D1,D2,D3, (b). Behavior of the surface profile sensors when in contact with tissue and also when sensor tip is open allowing air to flow through (c). Modeling of the indentation depth acquisition system

surrounding the indenter at 120° to each other. Each profile sensor consists of a hollow cylindrical rod and an optical displacement sensor. Profile sensors are designed and mounted inside the shield in such a way that they are free to move along the axial direction of the probe and can deliver and discharge air out at the tip. Airflow through the rods creates an air-cushion at the tips and ensures that rods float just above the tissue surface without indenting into it. As illustrated in Fig. 1(b), during a palpation activity, surface profile of the tissue is approximated by the plane $D_1D_2D_3$, generated by three surface profile sensors. The Plane $D_1D_2D_3$ can be used to estimate the normal distance n,from the probe face to the tissue surface and also θ,the angle of the tissue plane with respect to the probe axis. Hence using the parameters n and θ, the effective indentation d_{in} of the indenter can be evaluated as

$$d_{in} = a - [n + (a - s_1)\cos\theta], \quad (1)$$

where $s_1$is the axial displacement of the indenter from the origin.If the supply air pressure is maintained constant the parameter d_{in} is a direct function of the stiffness of the tissue under investigation.

To calibrate the four sensing elements, the prototype probe was attached to the distal tip of a 6-DOF (Degree of freedom) robotic manipulator (Mitsubishi RV-6SL) to allow accurate motion control and the robot arm was slowly advanced towards and retrieved from a flat work piece rigidly mounted to a workbench. As the indenter and the surface profile sensors gradually pushed into their channels by the work piece, voltage output of each displacement sensing element $D_1, D_2, D_3,$ and S was collected and recorded respectively. The calibration results are shown inFig. 2.

To evaluate the efficiency of the tumor identification, a silicon phantom with two embedded tumors was constructed using the RTV6166 gel. Dimensions of the phantom, size and depth of the tumors are shown in Fig. 3. During the experiment, the robotic manipulator was used to drive the probe to slide across the silicone sample. Initially, the probe was navigated on to the silicon phantom and lowered until the tip of the probe was only 1mm away from the tissue surface. Then, air pressure was increased gradually until the indenter achieves its maximum displacement. During the experiment, scanning was done along the curved surface of the silicone sample to cover the area under which nodules tumors were buried. As the scanning is carried out, effective indentation depth was generated using Eq.1. Fig. 4 shows a map of the tissue surface profile and relative stiffness profile for two scan cycles.

RESULTS

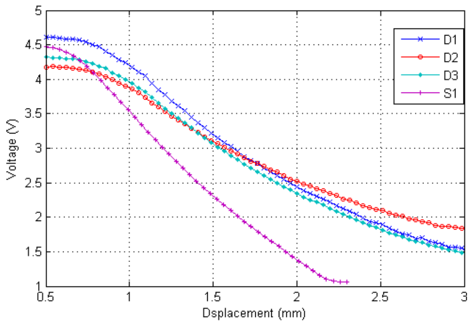

Fig. 2 Calibration results of the three surface profile sensors, D1, D2, and D3 and the stiffness sensor S1

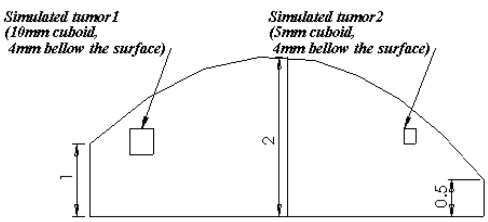

Fig. 3 Cross-sectional diagram of the tissue indicating the position, size, and the depth of the two embedded tumors.

According to Fig. 4. (b), the probe canidentify stiffness variation above the two tumors. There is a clear peak at tumor one. However, the subsequent noisy region makes tumor two difficult to identify. A positive correlation between the generated tissue height profile and the silicone sample design data is also evident from Fig. 4 (a). However,the generated height profile is flat at the center and there is a significant error existing between the two profiles. This error is mainly due to the saturation of the optical amplifiers at higher light intensities. The optical amplifiers saturate when the tissue surface is very close to the probe face. It can be corrected by re-tuning the amplifiers for the full range of the surface profile sensors. This modification to the surface profile sensor would overcome the sharp variations present in the Fig. 4 (b) and would effectively make the tumor two more identifiable.

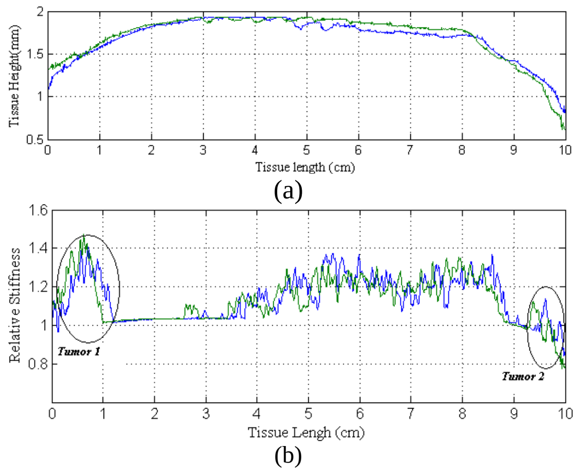

Fig. 4 (a). Tissue surface height profile, (b). Relative stiffness of the tissue generated through the indentation depth measuring system.

DISCUSSION

Considering the results from the validation experiments, it is clear that the air-float probe has the potential to identify the tumors hidden inside tissue surfaces. Further, as the sensing system operates under air pressure, tissue scanning can be carried out with the probe kept at any orientation. All these factors suggest that the air-float probe has the potential to aid the surgeon in identifying and locating hidden tumors. However, the current diameter of the system is 15mm and further work including miniaturization is necessary to tune the sensor to meet the requirements for minimally invasive surgery. It is also noted that, due to the dynamic nature of the open system the air pressure regulation is challenging. This could have a direct effect on the indention sensed by S_1. These interactions have not yet been evaluated and further work is being done to evaluate and model these interactions.

REFERENCES

[1] G.S. Guthart, and J.K. Sailsbury, "The intuitive TM telesurgery system: Overview and application", Proc. IEEE Int Conf. Robotics and Automation, 2000, pp. 618-21.

[2] R.D. Howe, W.J. Peine, D.A Kantarinis, and J.S. Son, RemotePalpation Technology," IEEE Magazine in Medicine and Biology, vol.14, no.3, 1995, pp. 318-23,

[3] D. Zbyszewski, P. Polygerinos, L.D Seneviratne, and K. Althoefer, A Novel MRI Compatible air-cushion tactile sensor for Minimally Invasive Surgery, "IEEE/RJS Int. conf. on intelligent Robots and Systems" 2009, pp.. 2647-52

Functional Outcomes following Transoral Robotic Surgery for Obstructive Sleep Apnoea

A. Arora[1], B. Kotecha[2], A. Hassaan[3], Z. Awad[1], J. Budge[1], A. Darzi[3], N.Tolley[1]

[1]*ENT Department, St Mary's Hospital, Imperial College Healthcare NHS Trust, London*

[2]*Royal National Throat Nose and Ear Hospital, London*

[3]*Department of Biosurgery and Surgical Technology, St Mary's Hospital, Imperial College London*

asitarora@doctors.org.uk

INTRODUCTION

Transoral Robotic Surgery (TORS) has been successfully used to address the limitations associated with conventional surgery of the oropharynx and supraglottis in head and neck cancer (1). The objective of this pilot study was to evaluate the functional outcome of patients with obstructive sleep apnoea (OSA) undergoing airway surgery using TORS.

MATERIALS AND METHODS

An ethically approved prospective non randomised cohort study was conducted between July 2010 and March 2012. Seven patients who had failed CPAP and previous surgery were recruited. Pre-operative sleep nasendoscopy was used to guide patient selection. The primary outcome measure was cure defined as greater than 50% reduction in the baseline apnoea-hypopnoea index (AHI) and Epworth sleep score (ESS). Secondary outcome measures included operative time and complications. Patient reported measures of voice, swallow and quality of life were recorded using validated assessment tools. Mean follow up was 9 months (range 3-18 months).

RESULTS

All patients were male; the mean age was 52 years and mean BMI was 27.5. The mean baseline AHI was 20.3 (C.I 7.5-33) and ESS was 14.6 (range 11-23).TORS involved tongue base resection (n=7) +/- epiglottoplasty (n=5). The cure rate following TORS was 86%.There was a significant reduction in the mean AHI (3.6; C.I 1.6-6.6) at 4 months ($p=0.04$). The mean ESS also demonstrated significant reduction ($p=0.02$). The mean operative time was 70 minutes. Three patients required overnight post operative intubation. Nasogastric tube insertion and tracheostomy were not required. All patients were discharged within 72 hours with no major complications. Transient dysphagia occurred in 2 patients which resolved by 4 weeks. Another patient developed dysgeusia which resolved within a similar timeframe. All quality of life parameters significantly improved compared to baseline levels from 2 weeks ($p=0.03$).

DISCUSSION

TORS represents a new treatment paradigm for patients with OSA who fail conventional treatment using Continous Positive Airway Pressure (CPAP). This can occur in up to 80% of patients and if left untreated, is associated with a significant mortality risk (2,3). The conventional transoral approach has demonstrated limited success particularly when the cause is multisegmental involving the tongue base and epiglottis (4). The external surgical approach is associated with significant morbidity. In comparison, the morbidity associated with TORS is minimal. The 86% cure rate reported in this series compares favourably to the literature which ranges from 40-69% (4,5). The AHI is an objective measure derived from overnight sleep polysomnography perfomed at standarised time intervals before and after TORS. The high success rate reflects careful patient selection using sleep nasoendocopy to identify the anatomical level(s) of collapse. Furthmore, the mean BMI in this series is significantly lower than in comparable series. The results of this pilot study suggest that TORS represents a promising treatment option for selected patients with OSA. Long term prospective evaluation in a large patient cohort is necessary to validate the findings of this preliminary study.

REFERENCES

[1] Arora A, Cunningham A, Chawdhary G, Vicini C, Weinstein GS, Darzi A and Tolley N. Clinical applications of Telerobotic ENT-Head and Neck surgery. Int J Surg 2011 (9):277-284.

[2] Hannifa M, Lasserson TJ and Smith I. Interventions to improve compliance with continuous positive airway pressure for obstructive sleep apnoea. Cochrane Database Syst Rev. 2009(4):CD003531

[3] He J, Kryger MH, Zorick FJ, Conway W and Roth T. Mortality and apnoea index in obstructive sleep apnoea. Experience in 385 male patients. Chest 1998 94(1):9-14

[4] Elshaug AG, Moss JR, Southcott AM and Hiller JE. Redefining success in airway surgery for obstructive sleep apnoea: a meta analysis and synthesis of the evidence. Sleep 2007 30(4):461-467

[5] Vicini C, Dallan I, Canzi P et al. Transoral robotic surgery of the tongue base in obstructive sleep apea-hypopnea syndrome: anatomic considerations and clinical experience. Head Neck 2012 34(1):15-22

Patient-specific 3D Surgical Planning to Perform Cutting Edge Robotic Surgery

M. Carbone[1], C. Cappelli[2], V. Ferrari [1], S. Signori[3], N. De Lio[3], V. Perrone[3], F. Mosca[1], U. Boggi[3]

[1]EndoCAS – University Hospital of Pisa

[2] Division of Diagnostic and Interventional Radiology - University Hospital of Pisa

[3]Division of General and Transplant Surgery in Uremic and Diabetic Patients - University Hospital of Pisa

marina.carbone@endocas.org

ABSTRACT

We report the results obtained in two cutting-edge robotic interventions to underline the clinical value of patient-specific segmented 3D-models for preoperative planning in challenging surgery.

INTRODUCTION

The value of patient-specific three-dimensional (3D) models, obtained segmenting radiological images, for surgical planning is nowadays assessed by multiple studies[1-3]. Segmentation methods characterize each voxel basing on its intensity and on its nature, enabling visualization advantages to thoroughly understand the segmented anatomy.

Detailed knowledge of patient-specific anatomy is of overwhelming importance during minimally invasive major surgeries, that can nowadays be safely performed laparoscopically, but the use of the da-Vinci[4] surgical system could make these challenging operations even safer.

Planning the procedure using segmented images allows the surgeon to earn better awareness on patient anatomy and to choose the optimal surgical approach.

MATERIALS AND METHODS

Patient-specific 3D-models were generated using the semiautomatic tool the authors integrated into the open-source software ITK-SNAP1.5 [5-6]. It is based on the modified *region growing* algorithm appropriately parameterized for each organ. The segmentation process is performed by the radiologist. During segmentation, the result is validated on the fly and corrected if necessary, steering the appropriate parameters. Inside the software, it is also possible to simulate cutting planes and to perform volume estimations of each segmented structure.

RESULTS

1. Renal autotransplant

A 38-year-old woman presented with multiple bilateral aneurysms of the renal arteries(RAs), caused by severe fibromuscular dysplasia. The optimal treatment was extracorporeal repair of RAs followed by autotransplantation.

The operation was planned with our patient-specific 3D-model, Fig.1. The main objective was to identify the best match between the anatomy of each RA, after resection of all aneurysms, and putative autologous jump grafts. The ideal substitute would have been a branched internal iliac artery (IIA) graft. After segmentation, in a simulation environment, each IIA was overlapped on each RA tree to select which segment was more similar to each renal bifurcation.

The planning allowed the surgical team to manage the entire in-vivo operation laparoscopically and robotically: the surgeon decided to repair the right kidney first, using the right IIA. The left kidney was planned for repair after a follow-up period to ensure that the other was functioning properly.

The kidney was procured laparoscopically, repaired at a back-table, and transplanted by robot-assisted laparoscopy.

2. Robotic liver resection

A 49-year-old man who would have not accepted transfusions for religious reasons presented with a quickly growing hepatic angioma nearly replacing the right liver lobe.

The patient-specific 3D-model showed exactly vessels convolution around the angioma, Fig 2. The surgeon planned the hepatic resection and decided for a robotic intervention: a right hepatectomy which was carried out without complication with an estimated blood loss of 300mL.

DISCUSSION

Even if it is still a time-consuming task to be afforded in any intervention, the value of patient-specific 3D-models is invaluable to plan and to evaluate the feasibility of cutting-edge interventions. The robotic approach is becoming not just an alternative to traditional surgery, but an instrument to perform new kind of interventions previously unaffordable. New surgical devices are introducing new kind of interventions, for which new planning instruments are required.

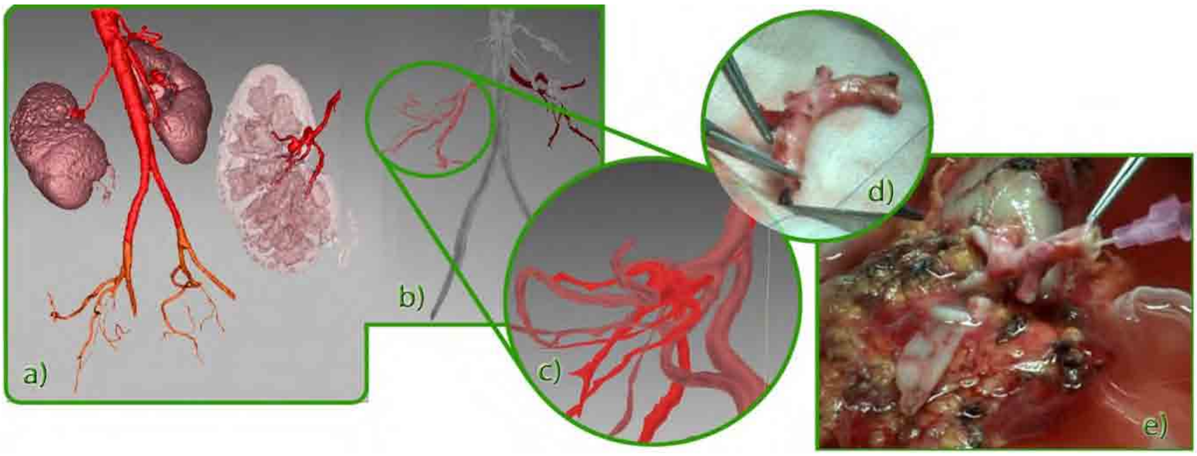

Fig. 1 a) the 3D-model includes: the abdominal aorta, the kidneys and the iliac arteries and a zoom on the right kidney transparent to highlight the aneurysmatic pathology; b) the simulation environment where the internal iliac arteries were studied to be overlapped to the renal arteries; c) a detail of the right IIA on the right RA; d) the right IIA on the operating table; e) the right IIA were substituted on the kidney ex-vivo and then re-inserted in the patient

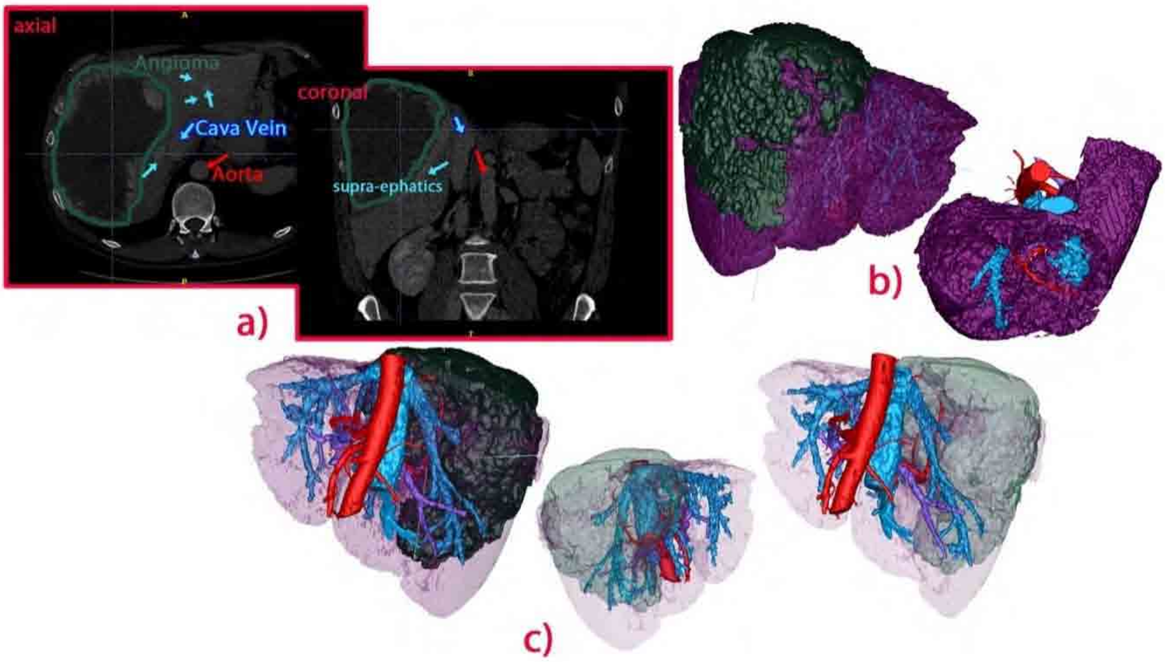

Fig. 2 Robotic liver resection - a) two CT slices of the datasets; b) the 3D-model from different points of view with and without the angioma; c) the 3D model were the liver parenchyma is totally transparent to see the inner vasculature and its relationship with the lesion.

REFERENCES

[1] V. Ferrari, *et al.*, "Value of multidetector computed tomography image segmentation for preoperative planning in general surgery," *Surgical Endoscopy and Other Interventional Techniques,* Sep 23 2011.

[2] P. Lamata, *et al.*, "Use of the Resection Map system as guidance during hepatectomy," *Surgical Endoscopy and Other Interventional Techniques,* vol. 24, pp. 2327-2337, Sep 2010.

[3] M. A. Muller, *et al.*, "State of the art 3D imaging of abdominal organs," *JBR-BTR,* vol. 90, pp. 467-74, Nov-Dec 2007.

[4] http://www.intuitivesurgical.com/.

[5] P. A. Yushkevich, *et al.*, "User-guided 3D active contour segmentation of anatomical structures: Significantly improved efficiency and reliability," *Neuroimage,* vol. 31, pp. 1116-1128, Jul 1 2006.

[6] V. Ferrari, *et al.*, "An anatomy driven approach for generation of 3D models from multi-phase CT images," in *International Journal of Computer Assisted Radiology and Surgery*, 2008.

Robotic-Assisted Laparoscopic Pyeloplasty in Children: A Single Institution Learning Curve

N. Gattas[1], A. White[2], S. Whiteley[2] and A. Najmaldin[2]

[1]*School of Medicine, University of Queensland, Australia*
n.gattas@uq.edu.au

[2]*Paediatric Surgery, Leeds Teaching Hospitals NHS Trust, United Kingdom*
azad.najmaldin@leedsth.nhs.uk

INTRODUCTION

Robotic-assisted pyeloplasty (RAP) is an emerging alternative to laparoscopic pyeloplasty in paediatric patients with pelviureteric junction obstruction (PUJO) [1,2]. We acquired the Da Vinci Surgical System in March 2006 and report our learning curve to evaluate the effect of surgeon and hospital experience and on operative times and patient outcomes.

MATERIALS AND METHODS

All patients requiring primary pyeloplasty for PUJO from 2006 to 2011 were included. The procedure was performed by a single paediatric surgeon with an interest in urology and prior experience in minimal access surgery (ASN). The technique included open insertion of the primary port, transperitoneal (paracolic or transmesocolic) reduction pyeloplasty with percutaneous nephrostomy, interrupted suture anastomosis, double-layer continuous suture reconstruction of the pelvis, and closure of the peritoneum and wounds. Theatre set-up, anaesthetic, assisting and scrubbed staff changed regularly during the study. All patients received regular follow-up including ultrasound scan occurred at 1 and 4 months and yearly thereafter, with isotope renogram as necessary. For the purpose of analysis cases were divided per year of operation (2006-07, 2008, 2009, 2010, 2011) and one-way ANOVA with Tukey's multiple comparisons analysis was applied. Data were collected prospectively.

RESULTS

There were 72 children (male/female 48/24; right/left 28/44) with no significant demographic variation between years. The average age was 7.4 years (range 1/12 – 15). 9% were less than one year of age and 21% had giant hydronephrosis. The procedure was converted to an open technique twice due to robotic mechanical failure (1) and inability to stent ureter (1). There were no other intraoperative complications or blood loss. Mean console and total operating time reduced significantly from 195 to 145 ($p=0.001$) and 256 to 213 ($p=0.01$) minutes respectively, while set-up time remain unchanged and docking time reduced from 7.3 to 4.5 minutes ($p=0.02$). Avoidable non-operative delays in theatre times were frequent throughout the study (range 12 – 60 minutes, incidence 27-61% per year) and usually due to inexperienced assistants or lack of non-robotic theatre equipment. Postoperative morphine was used on demand in 21% of patients for up to 12 hours. Mean hospital stay was 39 hours (range 16 – 72). In hospital complications included surgical emphysema (1), urinary retention (1) and a premature dislodged stent (1). To date, one patient developed recurrent obstruction that was treated robotically.

Fig. 1 Suture anastomosis in robotic-assisted pyeloplasty for left PUJO (transmesocolon approach).

DISCUSSION

In the hands of a laparoscopic surgeon, robotic-assisted pyeloplasty produces good results with low morbidity even during the learning period. Contrary to previous reports, our operating time continued to fall significantly beyond five years. This effect may be specific to procedure, surgeon or institution. Dedicated theatre staff and dedicated theatre resources are expected to result in further improvements if implemented.

REFERENCES

[1] Lee RS, Retik AB, Borer JG, Peters CA. Pediatric robot assisted laparoscopic dismembered pyeloplasty: comparison with a cohort of open surgery. J Urol. 2006;175(2):683-68.

[2] Mufarrij PW, Woods M, Shah OD, Palese MA, Berger AD, Thomas R, Stifelman MD. Robotic dismembered pyeloplasty: a 6-year, multi-institutional experience. J Urol. 2008;180(4):1391-96.

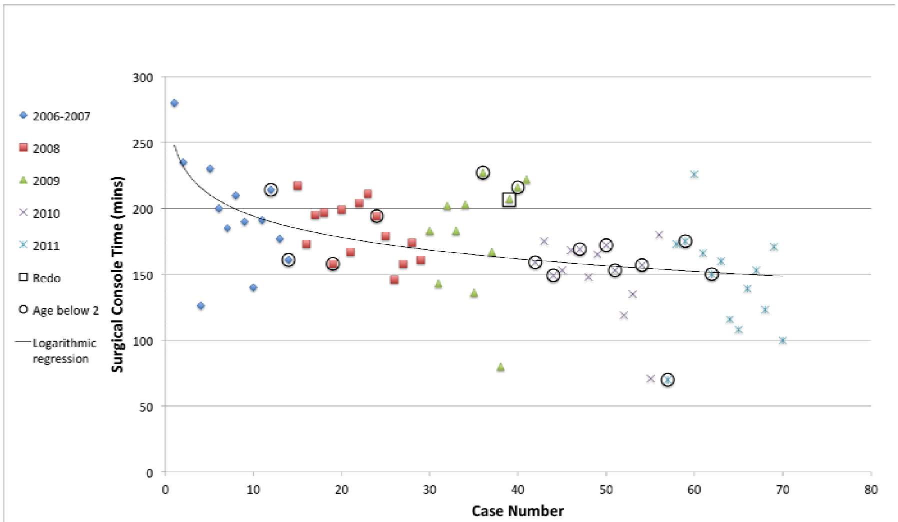

Fig. 2 The learning curve for robotic-assisted laparoscopic pyeloplasty in a paediatric population. Surgical console time included time taken to place the stent and drain. A logarithmic regression model is also shown ($y = -32.25\ln(x) + 255.09$; $r^2 = 0.3277$). Cases are shown by calendar year from 2006 to 2011. Cases with patients ≤2 years of age and the single redo procedure are also shown.

Can Biometric Measures Predict Feasibility in Transoral Robotic Surgery (TORS)?

A. Arora[1], A. Acharya[2], S. Khemani[3], J. Kotecha[1], A. Darzi[2], B. Kotecha[4], N. Tolley[1]

[1]*Dept. Of Otolaryngology, Imperial College Healthcare NHS Trust*

[2]*Division of Surgery, Imperial College London*

[3]*Dept. Of Otolaryngology, Surrey and Sussex NHS Trust*

[4]*Royal National Throat Nose and Ear Hospital, London*

asitarora@doctors.org.uk

INTRODUCTION

Transoral robotic surgery (TORS) overcomes several limitations associated with the established surgical modalities for treating oropharyngeal cancer (OPC) and obstructive sleep apnoea (OSA) [1,2]. Using the da Vinci robot, 2 instrument arms and a 12mm dual channel endoscope (Fig 1a) are inserted transorally using a Boyle-Davis mouth gag or FK retractor (Fig 1b).

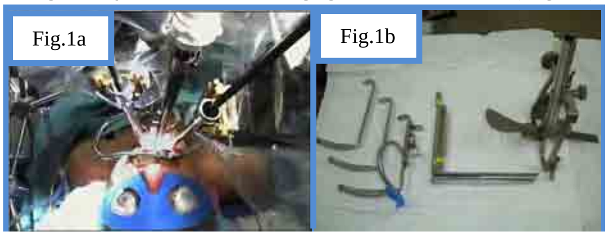

Fig 1a TORS set up in the operating room
Fig 1b Mouth gags used in TORS

The early clinical data suggests improved patient outcome in terms of morbidity and cure. TORS feasibility is conventionally assessed by an EUA (examination under anaesthetic). In 6-10% of cases suboptimal visualisation of the target region precludes its application [2]. The objective of this study was to establish whether feasibility could be assessed using biometric measures.

MATERIALS AND METHODS

Fifty cadavers were prepared using a soft fix embalming technique. Seven anthropometric measurements were recorded using fixed anatomical landmarks (Fig 2).

Key
M = angle of mandible
RW= ramus width
SM= symphysis mentis
H= hyoid
T= thyroid cartilage
C= cricoid cartilage
S= suprasternal notch

Fig 2 Seven fixed anatomical landmarks for anthropometric measurements

Cadaver position was standardised; supine with the neck extended and head flexed. Mallampati class was recorded; this defines the extent to which the tongue obscures the oral cavity (Fig 3) [3].

Fig 3 Mallampati class (1-4)

Three head and neck surgeons blinded to biometric assessment appraised TORS feasibility. The sequence of assessment was randomised to limit order effects. Evaluation comprised a difficulty impression score (0=feasible 1=unfeasible) based on body habitus, mouth opening and dentition.

Visualisation of 4 target regions (tonsil, tongue base, vallecula and epiglottis) using the Boyle-Davis and FK retractor was then performed. A 0/1 binary score was used to represent suboptimal/full visualisation.

The consistency of subjective evaluation was assessed with the Intra-class Correlation coefficient (ICC) and Kappa coefficient. The Spearman's rank correlation coefficient was used to assess the relationship between difficulty impression and actual visualisation of 4 target regions. The student's t-test was used to identify significant differences in the mean anthropometric measures between full visualisation and sub-optimal visualisation groups.

Logistic regression was performed to generate 'cut-off' values using the biometrics measures demonstrating predictive value.

RESULTS

The ICC demonstrated concordance in the surgeons' subjective assessment of TORS feasibility (average measures correlation=0.57, 95% CI= 0.28-0.75).

However, the Kappa coefficient was 0.29 demonstrating that agreement between surgeons was weak. Full visualisation of the tonsil precluded statistical evaluation. Spearman's rank correlation demonstrated a significant positive correlation between subjective difficulty impression and actual visualisation for the 3 remaining target regions (Table 1).

Gag	Boyle-Davis			FK		
Site	Base of Tongue	Vallecula	Epiglottis	Base of Tongue	Vallecula	Epiglottis
rho	0.45	0.29	0.29	0.39	0.40	0.41
p-value	<0.01	0.04	0.04	<0.01	<0.01	<0.01

Table 1 Spearman's rank correlation coefficients

Three anthropometric measurements were identified whose mean values were significantly different between full and suboptimal visualisation groups (Table 2).

Parameter	Site	Gag	Visualisation	Mean	t	p-value
Hyoid-mental Distance	Base of Tongue	Boyle-Davis	Full	5.5	2.41	0.02
			Sub-optimal	4.8		
	Epiglottis	FK	Full	5.5	2.02	0.05
			Sub-optimal	4.9		
Neck Circumference	Base of Tongue	Boyle-Davis	Full	38.7	-2.08	0.04
			Sub-optimal	42.1		
	Epiglottis	Boyle-Davis	Full	36.8	-2.1	0.04
			Sub-optimal	41.2		
Ramus Width	Base of Tongue	Boyle-Davis	Full	2.6	2.18	0.03
			Sub-optimal	2.2		
	Epiglottis	FK	Full	2.7	2.64	0.01
			Sub-optimal	2.2		

Table 2 Anthropometric measures demonstrating significant differences between full and sub-optimal visualisation groups

Logistic regression identified 'cut-off' values for these parameters which independently predicted TORS feasibility (Table 3).

Parameter	Cut-off (cm)	% Correctly Predicted
Ramus Width	>3.7	85
Hyoid-mental Distance	>5.5	85

Table 3 Cut-off values for anthropometric measures which predict TORS feasibility.

The mean Mallampati grade was significantly higher in the suboptimal visualisation group for all target regions irrespective of the mouth gag used (Table 4).

Site	Gag	Visualisation	Mean	t	p-value
Base of Tongue	Boyle-Davis	Full	1.3	-4.15	<.01
		Sub-optimal	2.1		
	FK	Full	1.5	-2.17	<.01
		Sub-optimal	2.1		
Vallecula	Boyle-Davis	Full	1.1	-4.28	<.01
		Sub-optimal	1.8		
	FK	Full	1.1	-4.94	0.04
		Sub-optimal	1.9		
Epiglottis	Boyle-Davis	Full	1.1	-4.52	<.01
		Sub-optimal	1.8		
	FK	Full	1.2	-4.62	<.01
		Sub-optimal	2.1		

Table 4 Mallampati class comparison between full and sub-optimal visualisation groups

DISCUSSION

The application of TORS in OPC and OSA requires careful patient evaluation. Predictive biometric measures are useful in the clinical setting to guide patient selection. Subjective evaluation of TORS feasibility is important and there was a significant positive correlation between difficulty impression and actual visualisation for three target regions. However, the observed inter-rater agreement was weak. This supports the need for a reliable framework of assessment based on validated objective measures to guide patient selection.

The results suggest that transoral visualisation of tongue base, epiglottis and vallecula are challenging in cadavers with a short, thick neck and a narrow mandible ramus. Limited mouth opening as defined by the Mallampati class is another important factor. This is a simple bedside clinical test used by anaesthetists to predict difficult intubation [3].

The effect of rigor mortis using human cadavers was substantially reduced by the embalming technique (phenol-glycerine) which produces realistic tissue pliability. Further clinical evaluation in a large patient cohort is warranted to validate these results. The identification of 'cut-off' anthropometric values could be used in conjunction with the Mallampati grade to predict feasibility whilst avoiding the need for an EUA.

REFERENCES

[1] Quon H, O'Malley BW, Weinstein GS. Transoral robotic surgery and a paradigm shift in management of oropharyngeal squamous cell carcinoma. J Robotic Surgery. 2010; 4:79-86

[2] Arora A, Cunningham A, Chawdhary G et al. Clinical applications of Telerobotic ENT-Head and neck surgery. Int J Surg. 2011; 9: 277-84

[3] Anaesthesia UK. *Laryngoscope Technique* 2004

Optimizing Oncological and Functional Outcomes with Robot Assisted Radical Prostatectomy (RALP) in Preoperatively High Risk Prostate Cancer Patients

Ananthakrishnan Sivaraman, Rafael F. Coelho, Sanket Chauhan, Oscar Schatloff, Srinivas Samavedi, Camilo Giedelman, Kenneth Palmer and Vipul R. Patel

Global Robotics Institute, Celebration, FL, USA
University of Central Florida, School of Medicine, Orlando, USA

OBJECTIVE

Use of nerve sparing (NS) prostatectomy in high-risk prostate cancer (HRCaP) is controversial, due to the higher incidence of extra prostatic extension of tumor. However we believe that in a subset of HRCaP, with clinically localized disease , favourable biopsy characteristics and disease which is macroscopically feasible for resection that it is possible to perform a NS-RALP without compromising oncological safety. We analyzed our outcomes in preoperative high-risk patients according to D'Amico risk stratification and nerve preservation.

MATERIALS AND METHODS

An institutional review board (IRB) approved, prospective robot assisted radical prostatectomy (RARP) database was analyzed retrospectively. Of 1720 patients who underwent RARP, 147 patients had a PSA > 20, Gleason 8 or more and clinical stage T2c – T4. Bilateral full nerve sparing (BNS) and partial nerve sparing (PNS) was performed when oncologically feasible. Biochemical Recurrence (BCR) was defined as > 0.2ng/ml; Continence as the use of 'no pads'; potency as the ability to achieve and maintain satisfactory erections firm enough for sexual intercourse for more than 50% of the times, with or without the use of PDE 5 inhibitors.

RESULTS

The mean followup (± SD) was 19 months (6.9). Mean serum psa was 8.5 ± 7.32. Bilateral, partial and non-nerve sparing was done in 22.1%, 40% and 37.9% respectively. Histopathological evaluation showed 52.1% of tumors to be organ confined. Extra prostatic extension was present in 24.3 % and overall positive surgical margins (PSM) were present in 21.4% of which pT2 PSM rate was 5.4%. Overall BCR rate was 16.4% and ranged from 22.9% in NNS, 12.54% in PNS and 12.9% BNS. This difference was not significant. The overall potency rates were 66.1% for PNS and 87.1% for BNS. Overall continence rates were for both PNS and BNS were above 90%. The trifecta was achieved in 60% of PNS and 71% of BNS.

CONCLUSION

Nerve sparing in RARP is feasible without compromising oncological safety in selected preoperatively high-risk patients. The short term outcomes are comparable to open series with similar cohorts. Surgeon experience and precise preoperative characterization tumor is essential to identify the subset of patients in whom nerve sparing is feasible.

REFERENCES

[1] Loeb S, Schaeffer EM, Trock BJ, Epstein JI, Humphreys EB, Walsh PC. What Are the Outcomes of Radical Prostatectomy for High-risk Prostate Cancer? Urology. 2010 Sep;76(3):710–4.

[2] Kane CJ, Presti JC, others. Changing nature of high risk patients undergoing radical prostatectomy. The Journal of urology. 2007;177(1):113–7.

Table 1 Outcomes

Variables		Nerve Sparing						Total		p value
		NNS(n = 53)		PNS(n = 56)		BNS(n = 31)				
		Count	%	Count	%	Count	%	Count	%	
Potency	Potent	7	13.3%	40	71.4%	28	90.3%	75	53.5%	0.0001
	Not Potent	46	86.7%	16	28.6%	3	9.7%	65	46.5%	
Continence	Continent	45	84.9%	54	96.5%	28	90.3%	127	90.7%	0.124
	Not Continent	8	15.1%	2	3.5%	3	9.7%	13	9.3%	
BCR	No Cancer	41	77.3%	49	87.5%	27	87.1%	117	83.5%	0.378
	Cancer Recurrence	12	22.7%	7	12.5%	4	12.9%	23	16.5%	
Trifecta	Achieved	5	9.4%	38	67.8%	23	74.2%	66	47.2%	0.001
	Not Achieved	48	90.6%	18	32.2%	8	25.8%	71	52.8%	

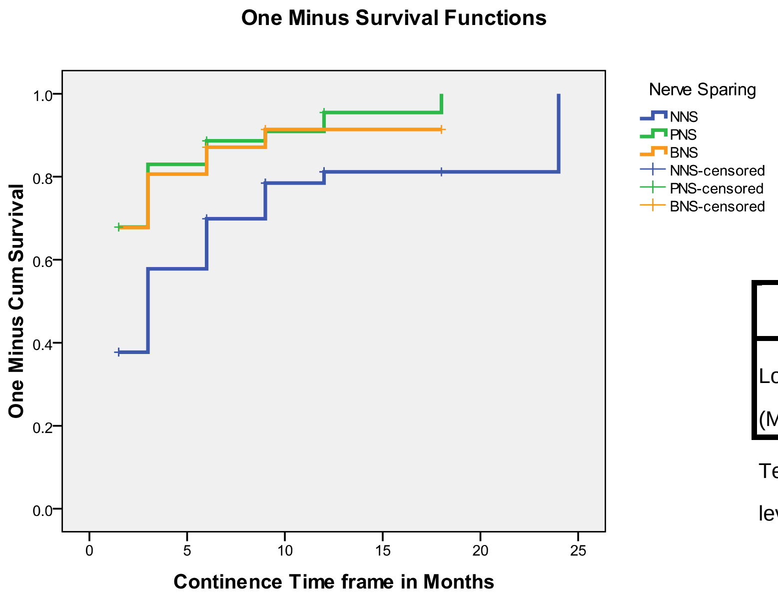

Overall Comparisons

	Chi-Square	df	Sig.
Log Rank (Mantel-Cox)	11.566	2	.003

Test of equality of survival distributions for the different levels of Nerve Sparing.

Fig 1 Trifecta time frames

From Bench to Bedside: The Novel Use of 3D MRI for Image-Guided Robotic Prostatectomy

D.C. Cohen[1], A.N. Sridhar[1], P. Pratt[2], B. Khoubehi[3], J. Vale[3], G.-Z. Yang[1], A. Darzi[1,2], E.K. Mayer[1], P. Edwards[1]

[1]Division of Surgery, Imperial College London
[2]Hamlyn Centre for Robotic Surgery, Imperial College London
[3]Department of Urology, Imperial College Healthcare Trust
daniel.cohen@imperial.ac.uk

INTRODUCTION

Technological advances in robotics have raised expectations that robotic-assisted laparoscopic prostatectomy (RALP) will deliver improved functional and oncological outcomes in the future. One such advance is augmented reality (AR), which enables live, patient-specific anatomical images to be superimposed on the surgeon's view intraoperatively. This has the potential to improve outcomes by providing surgical navigation. MRI is the imaging modality of choice in prostate cancer; we have previously established a protocol for MRI imaging, segmentation and reconstruction.[1,2] Feasibility of image overlay was demonstrated in seventeen retrospective cases.[3] We now present the first reported examples of live intraoperative AR overlay using 3D MRI models.

PATIENTS AND METHODS

Three patients underwent preoperative 3T MRI scans which were ultimately utilised as a live intraoperative overlay. MRI images were manually segmented to identify relevant anatomy, including prostate, urethra, neurovascular bundles, rectum, bladder and bony pelvis. Segmented MRI images were reconstructed into 3D models. Images of relevant anatomy were overlaid onto the stereo view of the da Vinci console under the control of a foot pedal at the request of the operating surgeon. Intraoperative alignment was achieved by manual registration of a point on the pubic symphysis with subsequent rotation matching the visible pelvic rim.

RESULTS

Live AR during RALP under the surgeon's control was achieved in three cases, which are the first of their kind (Figures 1 and 2). There was minimal delay to the operative procedure. The system functioned robustly; image overlay was achieved with good stereo perception of the real and virtual scenes. A manual registration protocol is presented. Studies demonstrated a repeatability of 2-3mm in the region of the pelvic rim.

CONCLUSION

AR guidance of RALP is a technological advance that has potential to improve the safety and outcome of RALP. We have established a protocol for all stages of such guidance - imaging, segmentation, registration and visualisation - and present the first three cases of live overlay of MRI-derived 3D models during RALP. Future work will develop live intraoperative vision-based endoscope tracking and registration methods to compensate for tissue motion.

This project was funded by Cancer Research UK Project no. C24520/A8087.

REFERENCES

[1] Cohen D, Mayer E, Chen D, Anstee A, Vale J, Yang GZ, Darzi A, Edward PJ. Augmented Reality Image Guidance in Minimally Invasive Prostatectomy. LNCS: Prostate Cancer Imaging (2010): 101-110

[2] Mayer EK, Cohen DC, Chen D, Anstee A, Vale JA, Yang GZ, Darzi AW, Edwards P. (Mar 2011). Augmented reality image guidance in minimally invasive prostatectomy. Eur Urol Suppl 2011;10(2):300

[3] Sridhar AN, Cohen DC, Chen D, Pratt P, Khoubehi B, Vale JA, Yang GZ, Darzi AW, Mayer EK, Edwards P. Development of an augmented reality system for robotic prostatectomy: Towards reducing the learning curve. Eur Urol Supp 2011;10:576-70

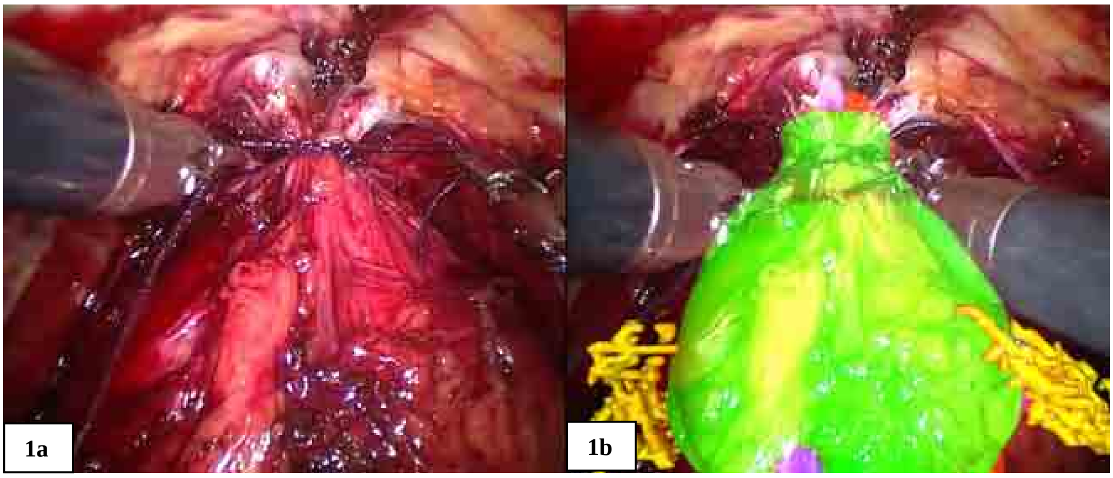

Fig. 1 a: Ligation of the dorsal venous complex; **b**: live intraoperative image overlay, showing prostate (green), neurovascular structures (yellow) and urethra (purple)

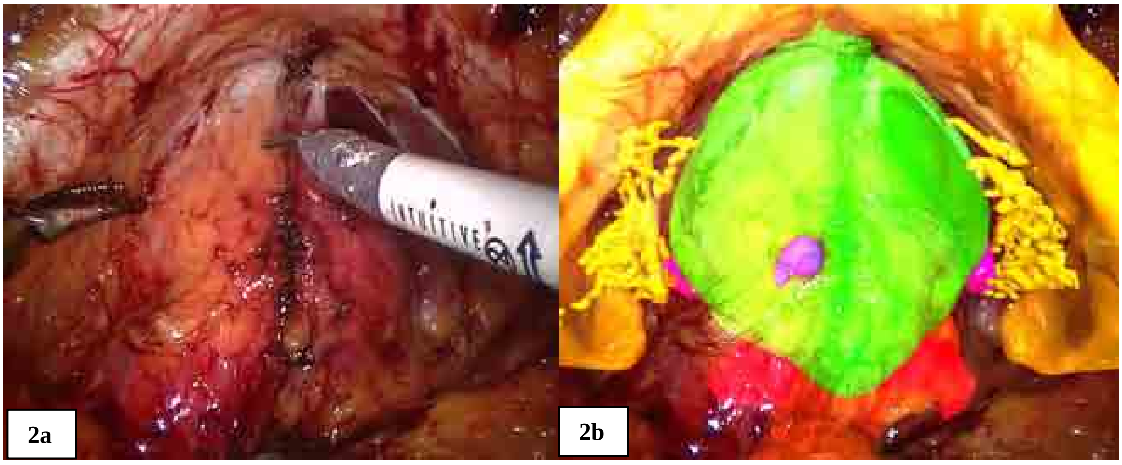

Fig. 2 a: Incision of right side endopelvic fascia; **b**: live intraoperative image overlay on the right, showing prostate (green), neurovascular structures (yellow),urethra (purple), bony pelvis (gold) and seminal vesicles (red)

Bespoke Fixtures for Robotic Thyroidectomy

A. Arora[1], Z. Awad[1], N. Tolley[1], V. Luzzato[2], J. Ahn[2], F. Ostovari[2], M. Oldfield[2], F. Rodriguez y Baena[2]

[1] Department of Otolaryngology, St Mary's Hospital, Imperial College Healthcare NHS Trust, London, UK

[2]Department of Mechanical Engineering, Imperial College London, UK

asitarora@doctors.org.uk

INTRODUCTION

After a century of performing thyroidectomy in a similar way as described by Theodor Kocher in 1912, thyroid surgery has evolved. The morbidity associated with hypertrophic scar formation in a visible area such as the anterior neck is underestimated [1]. Various 'scar-less in the neck' endoscopic techniques have been devised to address this issue [2]. The most common extra-cervical approach to the thyroid gland is the trans-axillary robotic-assisted technique. Chung *et al*. pioneered the approach in 2008 using a custom designed lifting device inserted through the axillary incision. The Chung retractor creates sufficient exposure for dissection without gas insufflation. Several thousand robotic thyroidectomies have been performed in South Korea. Small thyroid nodules (<1cm) account for the vast majority due to a routine population screening programme.

In contrast, the treatment rationale in the UK and US differs with significantly larger thyroid nodules undergoing surgery in a patient population which has a significantly larger BMI [3]. These factors account for the limitations encountered when the Chung retractor is applied to a Western population. A novel retraction device is required which overcomes these existing limitations, improves surgical exposure and thereby allows the technique to become more widely disseminated.

The objective of this feasibility study is to design a novel retractor for robotic thyroidectomy which addresses these issues.

MATERIALS AND METHODS

In order to identify and address the limitations associated with the existing retractor device, critical appraisal of the existing robotic thyroidectomy and parathyroidectomy technique was conducted. The following key shortcomings were identified:

- The lack of lateral support leads to tissue laxation, which interferes with the robotic slave manipulators.
- An assistant is required to keep the internal jugular vein outside of the working envelope of the robot.
- The Chung retractor requires 10-15 minutes for assembly and positioning before robot docking.
- The Chung retractor, being bed-mounted, is cumbersome and has a large footprint – thereby creating a sterility risk during setup.

The next step in the development of a new retractor was to estimate the loads sustained during normal use. A cadaver study was performed at Charing Cross hospital (London, UK), where the load required for tissue retraction and the overall working volume for trans-axillary access to the thyroid gland were measured. This data is included in Table 1.

(a)

Parameter	Load
Average	8.425 kg
Standard Deviation	0.112 kg

(b)

Parameter	Average Measurement	Standard Deviation
Left of incision to clavicle	86.7 mm	4.7 mm
Centre of incision to clavicle	81.6 mm	4.7 mm
Right of incision to clavicle	95.0 mm	7.1 mm

(c)

Data Set	Average	Standard Deviation
1	11.3 mm	0.5 mm
2	10.3 mm	0.5 mm
3	15.0 mm	0.8 mm
Overall	12.2 mm	2.0 mm

Table 1 Retracting load for a 4.5 cm maximum height incision (a), gross anatomical dimensions for repeated measurements (b), and clavicle diameter for three skeletons (c).

These measurements were used to refine the concept of a novel retractor design illustrated in Figure 1.

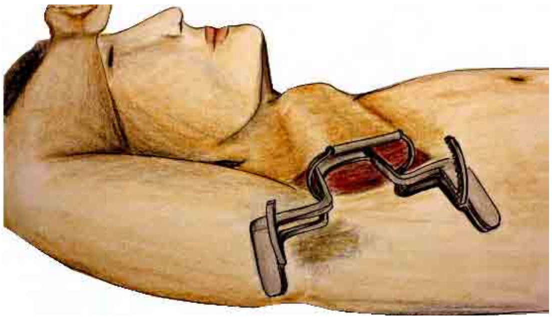

Fig. 1 Concept design of a novel retractor for robotic assisted thyroidectomy using a trans-axillary approach.

The retractor is designed to rest on the clavicle to avoid bed-mounted fixation and compression of the patient's thorax. Having both lower and upper blades provides lateral tension in the tissue, which in turn avoids lateral tissue relaxation.

To assess some of the key assumptions behind the design concept, two successive prototypes were manufactured at Imperial College, which were assessed during a further set of cadaver trials. Results from this study formed the basis of a further design currently being manufactured following a Medical Engineering Research Kick-start grant from Imperial College London.

RESULTS

Although the early prototypes (Figure 2) fulfilled the primary surgical requirements, certain aspects still required refinement. These included the tip geometry and overall footprint. The prototype was subsequently optimised to produce the further design illustrated in Figure 3.

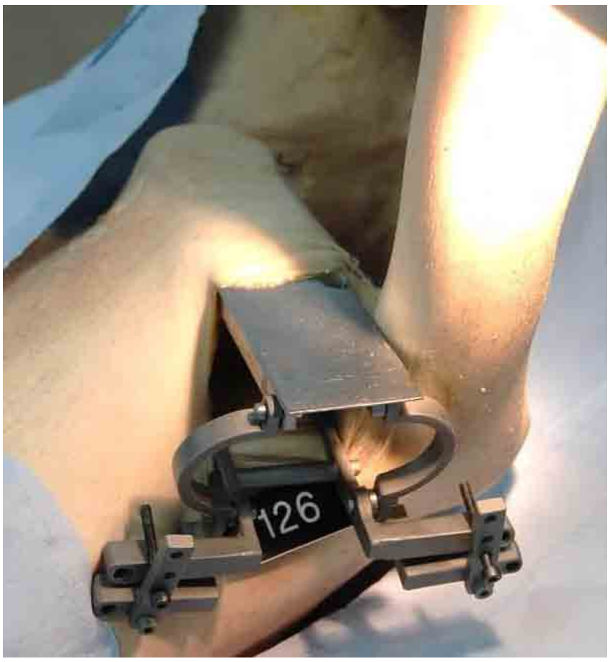

Fig. 2 Test of early surgical retractor prototype.

Additionally, in an analysis aiming to compare the working envelope between the Chung's Retractor and the novel design, it was discovered that for a 6 cm incision and 5 cm skin elevation a volumetric increase of greater than 30% was witnessed, principally due to the lateral support.

DISCUSSION

Cadaver trials of early prototypes demonstrate that the fundamental concept of a novel portable retractor for robotic-assisted minimally invasive thyroidectomy is valid and feasible. The design showcases a number of novel features, including a clavicle-hooking system implying a 'non-bed mounted' setup, and a modular design which can be fitted to a range of anatomy (illustrated by the range of measurements in Table 1b-c). Through cadaver trials, it was also shown that the new fixture produces a larger field of view, has shorter setup time, a diminished risk of contamination and enhanced compatibility for robotic head and neck surgery.

Further prototype development is on-going. This includes modifying the retractor slants to improve clavicle purchase. Variable retractor arm lengths are essential to suit a range of patient morphology as there can be a significant variance in relative locations between the axilla and thyroid gland. Optimising retractor design for clinical evaluation may ultimately reduce post-operative recovery and improve remote access. It is envisaged that this will enable dissemination of the technique to a wider patient population thereby enhancing the impact of robotics in Head&Neck surgery.

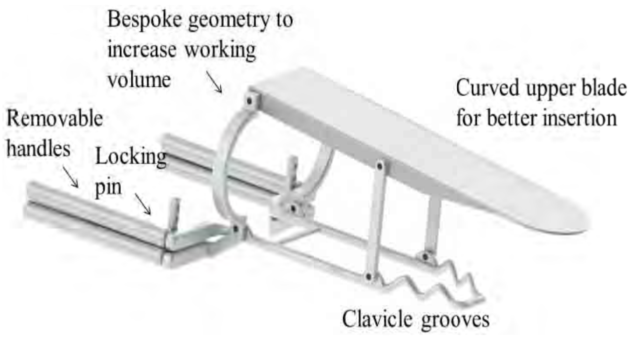

Fig. 3 Diagram illustrating the design of the retractor following two sets of cadaver trials.

REFERENCES

[1] Lawrence JW, Fauerbach JA, Heinberg L et al. Doctor M. Visible vs hidden scars and their relation to body esteem. *J Burn Care Rehabil* 2004;25:25-32.

[2] Tolley, N, Arora A, Palazzo F et al. Robotic-assisted parathyroidectomy: a feasibility study. *Otolaryngol Head Neck Surg* 2011;144(6):859-866.

[3] Arora A, Cunningham A, Chawdhary et al G, Vicini C, Weinstein GS, Darzi A and Tolley N. Clinical applications of Telerobotic ENT-Head and Neck surgery. Int J Surg 2011 (9):277-284.

A Study of Executive Control during Intracorporeal Minimally Invasive Suturing using Functional Near Infrared Spectroscopy (fNIRS)

K. Shetty, D.R. Leff, F. Orihuela-Espina, A.W Darzi, G-Z. Yang
Hamlyn Centre for Robotic Surgery, Imperial College, London
Corresponding author: g.z.yang@imperial.ac.uk

INTRODUCTION

'Neuroergonomics' describes the study of brain behaviour at work, which when applied to surgery examines the impact of new interfaces in minimally invasive surgery on the operator[1]. However, before new technologies can be meaningfully assessed, an understanding of the brain responses evoked by complex surgical tasks is invaluable. Functional Near Infrared Spectroscopy (fNIRS), a non-invasive optical imaging metholodology has been successfully applied to study brain function in surgeons during open and minimally invasive surgery MIS[1, 2, 5, 6]. A more detailed appreciation of the cortical response to complex tasks such as intra-corporeal suturing (LS) is required in order to determine which sub-tasks are most attention demanding and therefore which episodes need focused additional training time and /or technological assistance.

As with complex procedures, in this experiment LS was divided into three subcomponents namely insertion of needle, double throw knot and a pair of single throw knots[4]. We aimed to examine which aspect of the task evoked most pre-frontal cortex (PFC) activity amongst novices. We hypothesized that the technically more challenging aspect of the task, the double throw knot would evoke a greater response than the other two.

MATERIALS AND METHODS

15 medical students with a mean age of 21.6+/-1.4 (years +/-SD) were recruited from Imperial College. All participants were right hand dominant and laparoscopically naive. The task consisted of placing three interrupted LS across an enterotomy formed in a piece of artificial bowel within a box trainer. A 24 channel optical tomography system (ETG-4000, Hitachi Medical Corp., Japan) detected relative change in oxy- and deoxyhaemaglobin (HbO_2 and HHb) over the PFC. Each subject initially observed a video tutorial and later trained for two hours on a box trainer, with guidance from a trainer. Performance of the task was assessed using a Fundamentals of Laparoscopic surgery score[4] and video rated by two laparoscopic experts using a validated score[3]. For each NIR channel, PFC cortical activation was defined as a statistically significant task induced increase in HbO_2 coupled to a statistically decrease in HHb ($p<0.05$).

RESULTS

12 of 15 participants successfully completed the task after a single training session. The remaining three participants were invited for an additional two hours training period before undergoing the assessment. PFC activation by task sub-component is displayed in Figure 1, illustrating broader activation during laparoscopic needle insertion versus knot-tying maneuvers. Figure 2 illustrates that despite the group trend considerable inter subject variability in cortical responses was observed. All participants who were invited for an additional training session (N= 3/15) demonstrated marked excitation in all three of the task subcomponents.

DISCUSSION AND CONCLUSIONS

The PFC is recruited when motor performance is unrefined and attention demands are high[5]. Unlike, the results obtained by Ohuchida et al[6] , the current study suggests that for novice surgeons there are aspects of intra-corporeal knot-tying that demand attention and executive control. Contrary to our hypothesis, the most attention-demanding manoeuvre appeared to be that of needle insertion instead of reef knot-articulation. A further longitudinal study is required to examine the pattern of changes in brain behaviour that are associated with improvements in technical skill and amelioration of cognitive load with learning.

REFERENCES

[1] James DR et al. The ergonomics of natural orifice translumenal endoscopic surgery (NOTES) navigation in terms of performance, stress, and cognitive behavior. Surgery. 2011 Apr; 149(4):525-33.
[2] Leff DR et al. Functional prefrontal reorganization accompanies learning-associated refinements in surgery: a manifold embedding approach. Comput Aided Surg. 2008 Nov; 13(6):325-39.
[3] Kroeze SG et al. Assessment of laparoscopic suturing skills of urology residents: a pan-European study. Eur Urol. 2009 Nov; 56(5):865-72
[4] Korndorffer JR Jr et al. Simulator training for laparoscopic suturing using performance goals translates to the operating room. J Am Coll Surg. 2005 Jul; 201(1):23-9
[5] Leff DR et al. Changes in prefrontal cortical behaviour depend upon familiarity on a bimanual co-ordination task: an fNIRS study. Neuroimage. 2008 Jan 15; 39(2):805-13
[6] Ohuchida K et al. The frontal cortex is activated during learning of endoscopic procedures. Surg Endosc. 2009 Oct; 23(10):2296-301

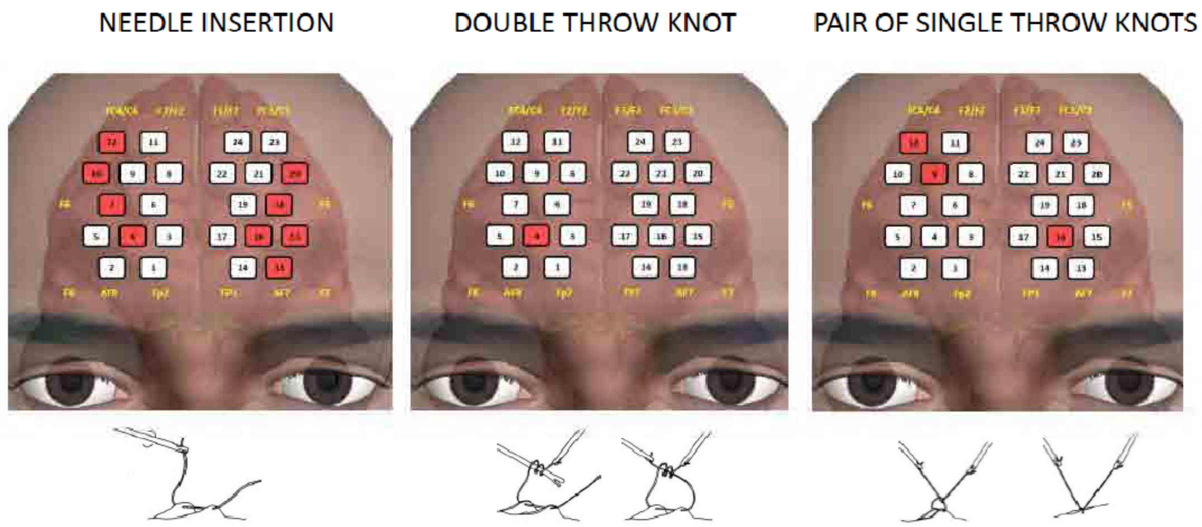

Fig. 1 Group-averaged activation map for each phase of the task. Diagrammatic representation of the technical aspect involved for each phase (bottom panel) and the each corresponding activation maps (upper panel). Channel areas denoting either an HbO_2 increase or HHb decrease in which one Hb species reached statistical threshold ($p<0.05$) are shaded. All other patterns of haemodynamic change (i.e. non-activation based) aren't shaded. International 10-10 marker positions are highlighted (yellow).

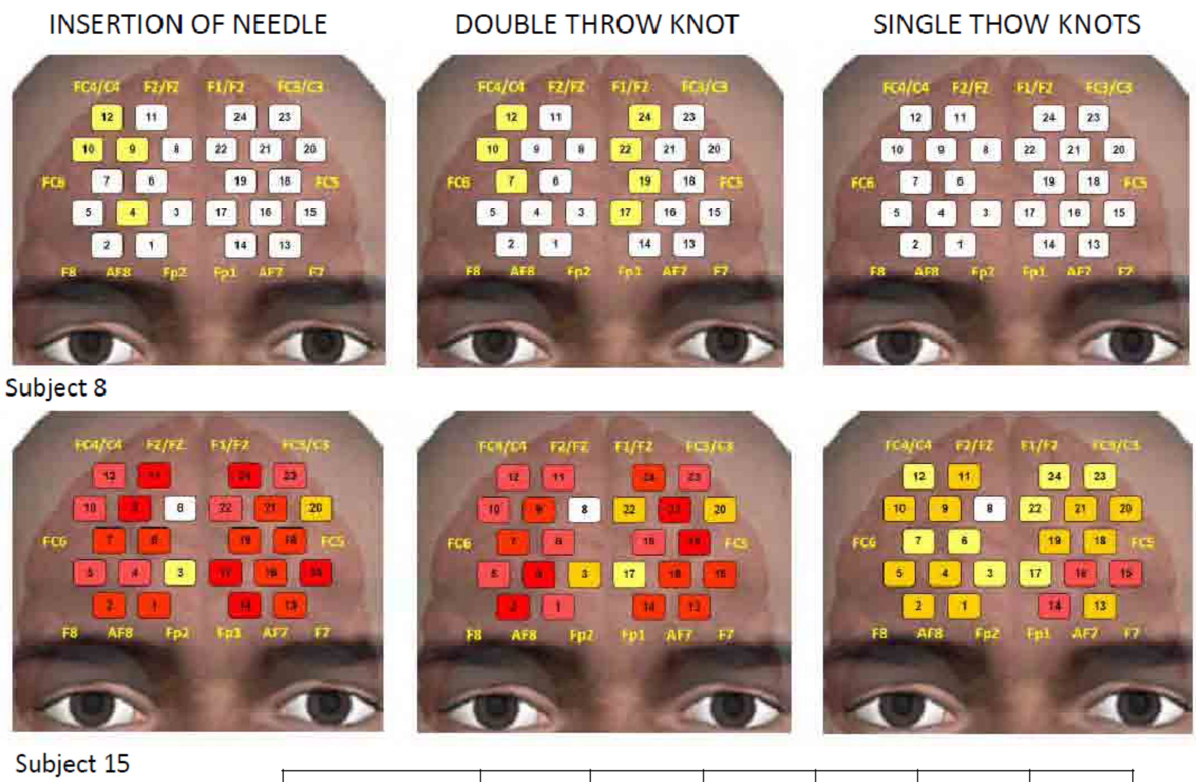

Increase in HbO_2	<20	20-40	41-60	61-80	81-100	>100
Colour grade						

Fig. 2 Inter-subject variability from the group trend as seen in subjects 8 and 15. Subject 15 who underwent an addition training session displays marked excitation for all 3 sub-tasks. Visual analysis by author KS of rise in HbO_2 during each phase of the task. Degree of rise in HbO_2 is denoted by a colour grade.

ACKNOWLEDGMENTS

This work was funded in part by the Academy of Medical Sciences.

A Healthcare Mobile Robot with Natural Human-robot Interaction

J. Liu, J. Correa, S. McKeague, E. Johns, C. Wong, A. Vicente, G.-Z. Yang

Hamlyn Centre for Robotic Surgery, Imperial College London

[j.liu, jc310, sjm05, ej09, charence, apv110, gzy]@imperial.ac.uk

INTRODUCTION

The ageing population presents a significant challenge to the future of healthcare. By 2050, one-in-four people living in the UK will be over the age of 65 [1]. One potential solution to this challenge is the development of assistive mobile robots. Although the very concept of mobile assistive robots have been explored for the last decade [2], most systems are still restricted to laboratory use. Two of the biggest challenges of the current systems are the lack of (i) a natural means of Human-Robot Interaction (HRI) and (ii) an adaptive autonomous scheme for the robot to deal with dynamic environments. In this paper, a mobile robot that provides natural human-robot interaction and an adaptive learning ability is presented.

Five key technical issues are explored in the system: (i) autonomous navigation with human-like behaviour, (ii) gesture recognition within crowded environments, (iii) distant speech recognition with room reverberation and background noise, (iv) adaptive visual scene recognition and (v) the integration of Body Sensor Networks (BSN) with mobile robots. Fig. 1 shows a concept of the system when used in a hospital environment, demonstrating the range of different modes of interaction between human and the robot.

SYSTEM ARCHITECTURE

Fig. 2 shows a schematic diagram of the structure of the whole system. It is hierarchically organised between low-level sensor inputs and modular functions. In this paper, the main emphasis is on HRI and adaptive algorithms for dynamic environments.

Robot Navigation using Human-like Behaviour

For assistive robots, failing to consider the dynamics of an environment or the implicit social rules while navigating can yield sub-optimal solutions. In the worst case scenario, the robot may freeze as no valid solution can be found. In practice, the robot is not only expected to move in the environment, but also to follow some basic social rules. Not getting to close to people or disturb a group of people talking or moving together is undesirable. To take into account the movement of people and social rules, the Dynamic Window Approach (DWA) cost function was extended to include a dynamic and a social component. The dynamic component takes care of avoiding moving people in the environment, while the social component takes care of doing it in a socially acceptable way. Simulations were carried out to test the performance of the proposed social navigation approach. These simulations show the robot is able to complete a path in a dynamic

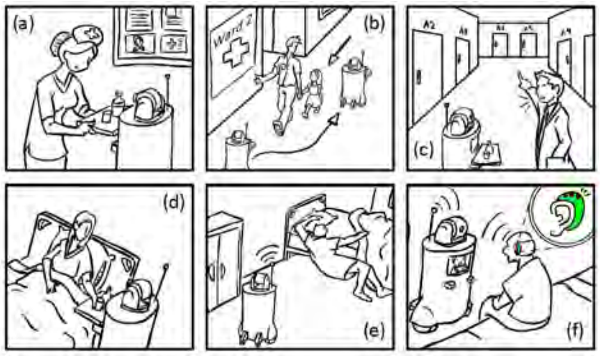

Fig. 1 Concept of a healthcare robot in a hospital environment. The robot delivers drugs (a). En route, it avoids people with minimal disturbance (b). The robot understands natural gesture and speech commands (c) and plans the route to the destination (d). Emergency situations, such as falls detected through pervasive sensors, can alter a robot's priorities (e) and the robot can act as a remote presence between doctors and patients (f).

environment faster, while keeping a greater distance to people. To compare our approach, the classic DWA with no social or dynamic considerations was used.

Reverberation-robust Speech Recognition

Although artificial speech recognition has been well explored for human-computer interaction for many years, it still has many limitations when applied to mobile robots in realistic environments with unavoidable artefacts due to reverberation. Existing models trained with anechoic speech signals can easily deteriorate when people talk to the robot located a few meters away. The speech recognition needs to be robust to these changes as the robot roams around in different rooms. Inspired by the finding on precedence effects of humans, an attenuated statistical room impulse response (IR) model is proposed that can match the real room IR according to the reverberation time T_{60}, i.e. the time it takes for the energy of the sound to reduce by 60 dB after a sound source is switched off. The proposed speech recognition model is trained with simulated room IRs with different T_{60}s and tested on real room IRs. See system details and results in [4].

Gesture Recognition in Cluttered Background

Gesture recognition provides a natural means for non-technical users to command and control mobile robots. This is particularly important in noisy, dynamic environments. For example, a doctor may want, for example, to point towards the room where he wants a robot to travel to in order to clarify their verbal command.

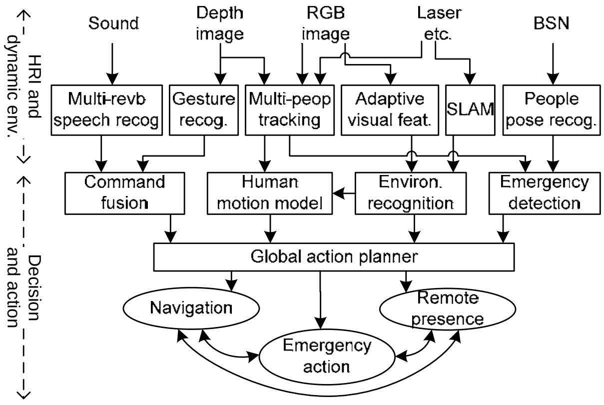

Fig. 2 Schematic system structure

Several sub-problems have been explored in the overall gesture recognition system. These include the detection, tracking and association of hands and people. Traditional approaches to these problems have used colour cameras as an input source, which introduces problems such as illumination constraints and depth ambiguity. The proposed robot uses recently introduced depth cameras to overcome these problems and increase the discriminative capacity of the system.

Object detection in crowded environments is a challenging problem. We have introduced a hand detector specifically designed for robust detection in such situations. Furthermore, to compensate for the increased occlusions and detection ambiguities in our target environment, our hand-body association method makes use of available temporal information.

Adaptive Visual Scene Recognition

Visual scene recognition has a wide range of applications in mobile robotics including appearance-based Simultaneous Localisation and Mapping (SLAM), loop closure in metric SLAM and interaction with the environment. For ensuring natural behaviour in practical applications, it is important that the robot can update its long-term understanding of the environment's appearance as dynamic elements appear in or disappear from a scene. An approach whereby local visual features extracted from an image are tracked across adjacent nodes in a topological map and quantised to form visual words is adopted. A graphical model is then learned for the appearance of each tracked feature by incorporating the relative locations of other contextual features in an image. As dynamic changes (both short-term e.g. people and long-term e.g. furniture rearrangements) occur in the environment, the likelihood of features occurring and co-occurring can be updated to reflect the new scene appearance. Furthermore, for outdoor scenes, the appearance of each feature is learned with respect to the time of day so that illumination effects such as shadows and reflections can be incorporated.

Integration with Wearable and Ambient Sensors

Pervasive wireless sensors worn by a patient can be used to assess wellbeing. For example, to assess the likelihood of an elderly patient falling [7] and to detect falls [8]. Pervasive sensors have also been used to detect activity, monitor patient recovery and perform biomechanical analysis. Support for Body Sensor Networks (BSN) enables the robot to obtain a much more in-depth insight of a patient's health. Whilst certain aspects may be detected solely through the robot's on-board sensors, previous work demonstrated the advantages of incorporating pervasive sensors to classify abnormal gaits [9].

DISCUSSION

A mobile robot has been built to test the proposed system and each modular function. Figure 3 shows a remote interface and the robot profile. The remote user can control the robot in either autonomous or manual mode. Information about the robot, its surroundings and nearby patients can be accessed via the interface.

Fig. 3 The remote presence interface (left) and the uncovered health care robot (right).

In future, further work will be directed to human attention detection, recognition of subtle gestures, environment dependent speech and behaviour learning, and deeper integration of BSN health monitoring with the mobile robot. More detailed results of our previous work can be found in the cited works [4][5][7][8][9].

REFERENCES

[1] M. Lali and L. Atkinson, "The Ageing Population," 2010.

[2] Y. Sakagami, R. Watanabe, et al, "The intelligent ASIMO: system overview and integration," in IROS 2002, pp. 2478-2483 vol.3.

[3] T. Djelani, J. Blauert, and A. Seestern, "Modelling the direction-specific build-up of the precedence effect," in Forum Acusticum, Sevilla, Spain, 2002.

[4] J. Liu, N. D. Gaubitch, and G.-Z. Yang, "Robust Speech Recognition in Reverberant Environments Using Multi-model Selection," in IROS2012 (under review)

[5] E. Johns and G.-Z. Yang, "Place Recognition and Online Learning in Dynamic Scenes with Spatio-Temporal Landmarks," in BMVC 2011, pp. 10.1-10.12.

[6] J. Sivic and A. Zisserman, "Video Google: A text retrieval approach to object matching in videos," in ICCV 2003, pp. 1470-1477 vol. 2.

[7] R.C. King, L. Atallah, C. Wong, F. Miskelly, and G.-Z. Yang , "Elderly Risk Assessment of Falls with BSN," in BSN 2010, pp. 30-35.

[8] M. Tolkiehn, L. Atallah, B. Lo, and G.-Z. Yang, "Direction Sensitive Fall Detection Using a Triaxial Accelerometer and a Barometric Pressure Sensor," in EMBC 2011, pp. 369-372.

[9] C. Wong, S. McKeague, J. Correa, J. Liu, amd G.-Z. Yang, "Enhanced Classification of Abnormal Gait Using BSN and Depth," in BSN 2012, pp. 166-171.

Robotic NOTES: System Concept and Architecture

R. Kojcev[1], E. Wilson[1], K. Davenport[1], H. Luo[1], K. Gary[2], S. Oonk[3], K. Cleary[1]

[1]Sheikh Zayed Institute for Pediatric Surgical Innovation, Children's National Medical Center, Washington, DC, USA

[2]Department of Engineering, Arizona State University, Phoenix, Arizona, USA

[3]American GNC Corporation, Simi Valley, California, USA

kcleary@childrensnational.org

INTRODUCTION

Surgery continues to evolve towards minimizing the invasiveness of the procedure. The minimally invasive revolution started with laparoscopic surgery in the 1980s. Single incision laparoscopic surgery (SILS) is a rapidly developing field that may represent the future of laparoscopic surgery [1]. The major advantage of SILS over standard laparoscopic surgery is cosmesis, with surgery becoming essentially scarless if the incision is hidden within the umbilicus [1]. In addition, the concept of natural orifice transluminal endoscopic surgery (NOTES) has been introduced clinically [2]. While NOTES has its limitations with current instruments, it has been proposed that NOTES could be facilitated by the introduction of robotics technologies. In this paper, we describe our work in developing a system concept and architecture for Robotic NOTES.

MATERIALS AND METHODS

A proposed solution for a tele-operated R-NOTES system is shown in Figure 1. This system consists of two robotic components: 1) an external gross positioning robot and 2) an internal mini-robot with a surgical tool. The robotic components will be controlled by two input devices: 1) a six degree of freedom mouse (SpaceNavigator) for control of the external robot; and 2) a six degree of freedom force reflecting device (Mantis Haptic) for control of the internal robot. Both of the input devices are connected to the Master Control computer, which serves as the hub of the system. The mini-robot is connected to the external robot through a Magnetic Anchoring and Guidance System (MAGS) [3]. In this concept the external robot is used for gross positioning and the internal robot for fine positioning and carrying out the surgical procedure.

One novel feature of the proposed system is the use of the Zigbee wireless protocol to communicate between the master control station and the internal mini-robot. ZigBee is a suite of communication protocols using low-power digital radios based on an IEEE standard for personal area networks. Zigbee transceivers are now available in small integrated circuits, such as the Texas Instruments CC2530 used in this work. Others have also proposed ZigBee for robotic capsular endoscopy [4].

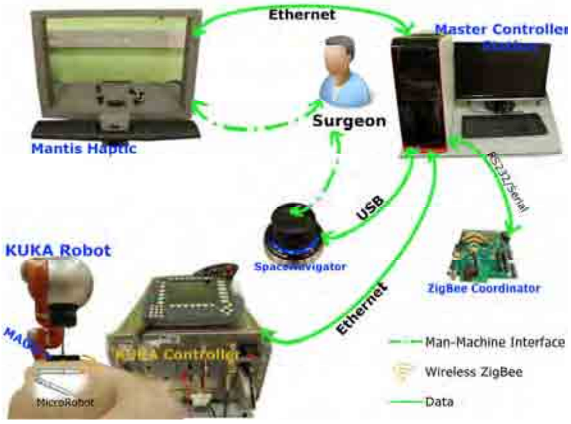

Fig. 1 System block diagram showing the components.

RESULTS

Several components have been developed to date, including a MAGS component, control of the external robot using the SpaceNavigator, and a Zigbee implementation. A MAGS handle was fabricated and an internal magnet module was created using off-the-shelf parts. Magnets were purchased from K&J Magnetics (Philadelphia, PA) and Aluminum parts from McMaster Carr (Santa Fe Springs, CA). Strong N52 grade NdFeB permanent magnets were used and consisted of two 1" diameter x 1" length cylinder magnets for the handle component and two 3/8" diameter x 3/8" thickness magnets for the internal component. The internal magnets were embedded within a cylindrical rod to simulate a potential camera module. A piece of porcine meat of 20 mm thickness was used to simulate the tissue layer. Using weights, we measured the force required to decouple the internal magnet [5] (Figure 2).

Fig. 2 MAGS test with handle on top, meat in middle, and one DOF module on bottom with weight attached.

Subsequently, we tested the concept on an expired spine using a multi-DOF passive module (Figure 3). We also attached the MAGS system to a 7-DOF Kuka lightweight robot and showed the robot could maintain a constant force against an abdominal phantom.

Fig. 3 MAGS concept using expired swine and multi-DOF module. The module is held in apposition to the abdominal wall through the use of the external magnet.

For wireless communication, Zigbee was selected after a review of the options. The Zigbee protocol operates on a 2.4 GHz radio band and can achieve a maximum 250 kbps data rate. A network of Zigbee devices can be formed with three types of devices: Coordinator, Router, and EndDevice. In our concept, the Coordinator would be the Zigbee module attached to the Master Controller Station. Then, each degree of freedom would be a separate Zigbee node and function as an EndDevice.

Since the Zigbee transceiver includes output ports, it can also be used to provide Pulse Width Modulation (PWM) for motor control. The printed circuit board for the internal mini-robot will be circular and contain the TI CC2530, motor driver MPC17C724, and DC voltage regulator. To test the ZigBee network we have developed a custom made printed circuit board incorporating the CC2530 and the AN043 antenna shown in Figure 4. The performance of the ZigBee network for the custom made PCB has been evaluated in laboratory environment. The results were then compared with the TI CC2530 evaluation board. In the test setup we have placed the custom made CC2530 and the evaluation board inside an anthropomorphic phantom. After analyzing the results we have concluded that there was no significant difference in the error rate and the received signal strength between the custom made board and the evaluation board. These results confirmed that the custom made printed circuit board enables reliable data transfer over the ZigBee network.

The mini-robot is under development and the proposed design consists of a 3 DOF module with four links. The base link will contain the magnets for anchoring the mini-robot to the abdominal wall. The second link will be a pitch joint that will move the mini-robot into the abdominal cavity. The third link will be a yaw joint that will move the mini-robot laterally within the cavity. The fourth link will activate a gripper to grasp the target tissue. The goal is to incorporate force sensing into the mini-robot. The force signal could be sent back to the haptic master using the A/D capability of the CC2530 Zigbee transceiver.

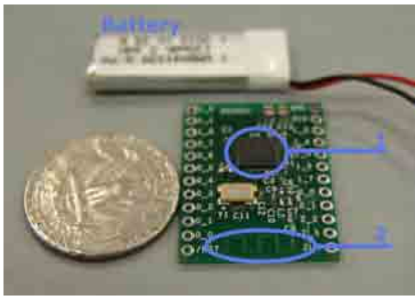

Fig. 4 Custom made PCB board with 1) CC2530 Zigbee transceiver; and 2) Chipcon AN043 antenna.

DISCUSSION

In this paper we have described the system architecture for a Robotic-NOTES system. The development of this demonstration system and these concepts may eventually lead to new techniques for minimally invasive surgery. Our next steps are to complete our prototype system and evaluate the system in phantom and animal studies.

REFERENCES

[1] N. Greaves and J. Nicholson, “Single incision laparoscopic surgery in general surgery: a review,” Ann R Coll Surg Engl, vol. 93, no. 6, pp. 437–440, Sep. 2011.

[2] R. R. Watson and C. C. Thompson, “NOTES spin-off for the therapeutic gastroenterologist: natural orifice surgery,” Minerva Gastroenterol Dietol, vol. 57, no. 2, pp. 177–191, Jun. 2011.

[3] S. L. Best, W. Kabbani, D. J. Scott, R. Bergs, H. Beardsley, R. Fernandez, L. B. Mashaud, and J. A. Cadeddu, “Magnetic anchoring and guidance system instrumentation for laparo-endoscopic single-site surgery/natural orifice transluminal endoscopic surgery: lack of histologic damage after prolonged magnetic coupling across the abdominal wall,” Urology, vol. 77, no. 1, pp. 243–247, Jan. 2011.

[4] E. Susilo, P. Valdastri, A. Menciassi, and P. Dario, “A miniaturized wireless control platform for robotic capsular endoscopy using advanced pseudokernel approach,” Sensors and Actuators A: Physical, vol. 156, no. 1, pp. 49–58, Nov. 2009.

[5] H. Luo, E. Wilson, and K. Cleary, “Simulation, design, and analysis for magnetic anchoring and guidance of instruments for minimally invasive surgery,” SPIE Medical Imaging 2012, Image-Guided Procedures, Robotic Interventions, and Modeling (Proceedings Volume 8316).

ACKNOWLEDGMENT

This project is a collaboration between Children’s National Medical Center and American GNC Corp., funded as a Phase II STTR W81XWH-09-C-0161. We also would like to acknowledge the contributions of Ali Bigdelou, Tobias Reichl, and Nassir Navab from the Technical University of Munich.

Navigated Endoscopy: Prototype System for Robotically Assisted Ureteroscopy

C.A. Peters[1], A. Burns[1], E. Wilson[1], H. Luo[1], K. LeRoy[2], J. Goldie[2], B. LaBrecque[2], K. Cleary[1]

[1]*Sheikh Zayed Institute for Pediatric Surgical Innovation, Children's National Medical Center, Washington, DC, USA*

[2]*Infoscitex Corporation, Boston, Massachusetts, USA*

kcleary@childrensnational.org

INTRODUCTION

The term "navigation" refers to the use of a tracking system for determining the position of surgical instruments relative to the anatomy and displaying this information on a computer monitor. In this respect navigation can be used to aid surgical localization the same way that GPS is used for automobile guidance. Image-guided systems for navigation have been developed by multiple companies over the last twenty years and some commercial success has been seen. The concept of "navigated endoscopy" was introduced at least ten years ago [1] and many papers have been written on this topic. Navigation systems for functional endoscopic sinus surgery, bronchoscopy, and colonoscopy for example have been introduced. However, navigation is still not routinely used at most medical centers.

Flexible endoscopy is a ubiquitous means of diagnosis and therapy in nearly all aspects of medicine. Endoscopic systems from the major manufacturers are similar with controls based on simple flexion of the tip of the endoscope, rotational control, and in and out translational movement. These three movements are controlled by the operator at the head of the instrument and are all distinct in their character, making intuitive control difficult to learn and perform (Figure 1). Efficient and safe control could be enhanced by a control interface that permits intuitive movements with faithful visual feedback (e.g. when the instrument is rotated, the visual field is rotated as well and when a target is identified, it can be reached smoothly). Because of the complexity of movements needed for many applications, integration of a navigation system has the potential to enhance the safety, efficacy, and efficiency of these instruments. While physicians who do endoscopy every day become quite skilled at the contortions that can be needed for effective placement of the instrument tip, the shortcomings of the current approach extend the time required for procedures [2], increase user fatigue, and have the potential to increase the frequency of errors. For those physicians who perform endoscopy on an occasional basis, the need for a more user-friendly, intuitive means of control becomes even more pronounced.

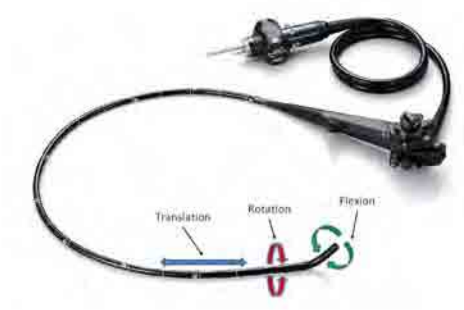

Fig. 1 Typical ureteroscope design. Translation is controlled by physically moving the scope in/out, rotation by physically rotating the scope, and tip flexion by a small knob on the side of the scope.

Flexible endoscopy is commonly performed in all aspects of medicine and includes ureteroscopy, colonoscopy, gastroscopy, duodenoscopy, bronchoscopy, ventriculoscopy, and sinus endoscopy. Uretero-renoscopy is used widely with flexible ureteroscopes for access and manipulation in the ureter and kidney. Uses include stone removal, diagnosis for bleeding or malignancy, as well as direct biopsy and destruction of malignant lesions. In stone disease, ureteroscopy is becoming more widely used than the other minimally invasive means to remove stones in both adults and children [3]. Control is performed with two hands, one to move the ureteroscope in and out, and the other to rotate and flex the ureteroscope (Figure 2). This leaves no hand free to perform manipulations through the working port, which can include stone basketing, laser lithotripsy, tumor fulguration, or biopsy. In many clinical situations, the entire interior of the kidney must be carefully inspected to avoid leaving stone fragments or residual tumor. This requires moving the ureteroscope into each of the 10 to 12 calyces in the human kidney. Such delicate control requires significant skill, particularly in the lower pole of the kidney where the instrument must be tightly flexed and then rotated and pulled back to move into the lower calyces. One paradigm for making navigation more available for endoscopic procedures is to develop an "add-on" package to provide mechanical control and a navigation capability. Here we describe our work developing a prototype system for navigated ureteroscopy. Similar concepts have been explored by other researchers [4].

Fig. 2 Clinical lead Dr. Craig Peters manipulating the ureteroscope during kidney exploration in the operating room. Dr. Peters is looking at the video image from the ureteroscope.

MATERIALS AND METHODS

A block diagram of our system is shown in Figure 3. The system consists of a movement control mechanism, a motion control system, a tracking system, a 3D mouse, a personal computer, and a graphical user interface. The requirements of the movement control mechanism are: 1) Securing of the endoscope in the mechanism must be easy and fast to accomplish – no fumbling by the endoscopist; 2) The mechanism must provide controlled motion in three degrees of freedom: (a) translation for advancement/withdrawal (4 inches), (b) 360° of roll rotation (to adjust plane of flexion), and (c) +/- 180° flexion itself; 3) Translation and angular incremental motions of 0.1 mm and 2 degrees; 4) Must not represent an impediment to necessary direct access to patient; and 5) Standard medical device requirements (e.g., electrical, mechanical fail-safe).

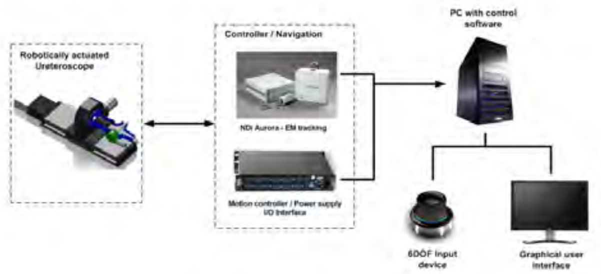

Fig. 3 Integrated system concept showing the ureteroscope and movement control system on the left, the motion control interface and electromagnetic tracking system in the middle, and the user interface / control computer on the right.

RESULTS

A prototype movement control system was designed using Solidworks. The parts were constructed by a contract machine shop and the movement control system was assembled in our lab. Three Maxon DC brushless motors (ECmax16 8W) were attached to control each axis of motion and limit switches were added. A GP22C 690:1 reduction ratio Maxon gearbox was used for the rotation and flexion links and a GP22C 84:1 reduction ratio gearbox was used for the translation stage. The rotation and flexion stages are mounted on a linear lead screw platform (SMI4Motion Inc., Corona, CA). A Galil four-axis motion controller (DMC-4143, Galil Motion Control, Rocklin, CA) and servo amps were connected for control. The prototype system is shown in Figure 4. The controller was connected to a 6 DOF mouse (Space Navigator) and preliminary tests were done using a kidney phantom (IdealAnatomic Inc.). The preliminary tests showed the feasibility of the control concept.

Fig. 4 Prototype movement control system.

DISCUSSION

Navigated endoscopy has multiple applications in medicine. The development of an add-on package for existing endoscopes may facilitate the introduction of this technology. Our next steps are to develop the navigation interface and evaluate the system in a kidney inspection task phantom and animal studies. System validation will be performed using surgical phantoms to assess the anticipated benefits. The metrics include ease of use and workflow, efficiency in terms of task-times, accuracy based on stereotypes task performance such as object retrieval, and efficacy in terms of ensuring complete calyceal system surveillance as would be needed in screening for malignancy. We will also assess the role of user experience in flexible endoscopy to determine the relative benefits for differing experience levels. Animal testing will be then undertaken to confirm the utility of the system for typical uretero-renoscopic procedures.

REFERENCES

[1] T. Yoshida, H. Inoue, Y. Kumagai, and T. Iwai, “Image-navigated endoscopic surgery: introduction of the face-mounted display system with picture-in-picture capabilities,” *Hepatogastroenterology*, vol. 47, no. 32, pp. 375–377, Apr. 2000.

[2] G. C. Harewood, K. Chrysostomou, N. Himy, and W. L. Leong, “Impact of operator fatigue on endoscopy performance: implications for procedure scheduling,” *Dig. Dis. Sci.*, vol. 54, no. 8, pp. 1656–1661, Aug. 2009.

[3] K. Kerbl, J. Rehman, J. Landman, D. Lee, C. Sundaram, and R. V. Clayman, “Current management of urolithiasis: progress or regress?,” *J. Endourol.*, vol. 16, no. 5, pp. 281–288, Jun. 2002.

[4] K. Olds, A.T. Hillel, E. Cha, M. Curry, L.M. Akst, R.H. Taylor, and J.D. Richmon, “Robotic endolaryngeal flexible (Robo-ELF) scope: a preclinical feasibility study,” *Laryngoscope*, vol. 121, no. 11, pp. 2371-4, Nov. 2011.

Preliminary Adhesion Control of a Miniature Intra-abdominal Robot for Laparoscopic Surgery

A. Montellano López[1], R. Richardson[1], A. Dehghani[1],
R. Roshan[1], D. Jayne[2], A. Neville[1]

[1]School of Mechanical Engineering, University of Leeds, Leeds, United Kingdom

[2]Academic Surgical Unit, St. James's Hospital, University of Leeds,
Leeds, United Kingdom
mnaml@leeds.ac.uk

INTRODUCTION

Laparoscopic procedures have been reported to be beneficial for both patients – fewer scars and reduced trauma – and hospitals – shorter recovery times [1, 2]. Traditionally, these procedures have been performed by a surgeon manoeuvring tools through 2-3 mm incisions with visual feedback from a camera. A more advanced development of traditional laparoscopic surgery is to use robots to help surgeons operate more precisely and comfortably. Over the last 25 years robotic assistants have been progressively introduced in the operating theatre. These robots follow a design pattern in which several floor-mounted arms manoeuvre a series of tools inside the body through small surgical ports. Instead of the surgeon directly manoeuvring the tools, in a robotic system these are controlled by the surgeon from a console receiving visual feedback from a camera. However, these techniques are generally cumbersome, require a very large capital cost and the manoeuvrability of the tools are limited by their anchorage external to the human body.

Recent reserach to overcome these limitations has led to the development of miniature devices for intra-corporeal operation. Two of these robots are: the Nebraska Wheeled Robot [3], able to travel on the surface of the abdominal organs, and HeartLander, a robot that crawls on the surface of the beating heart [4].

In this paper, the robot called Rasso applies a novel design principle to attach and/or detach to the peritoneum (the inner part of the abdominal wall) and move against gravity on its surface carrying a camera (see Fig. 1) [5,6].

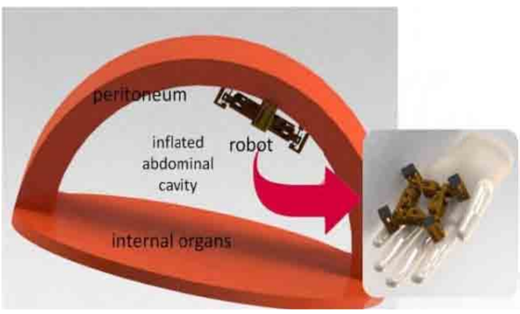

Fig. 1 Sketch of a cross section of the inflated abdomen during a laparoscopic procedure, showing the conceptual design of Rasso.

MATERIALS AND METHODS

Bio-inspired surfaces/pads are used to attach the robot to the peritoneum. The surface that provides adhesion to the robot is a bio-compatible polymer nano-imprinted with a pattern inspired by tree frogs (Fig. 2) [6].

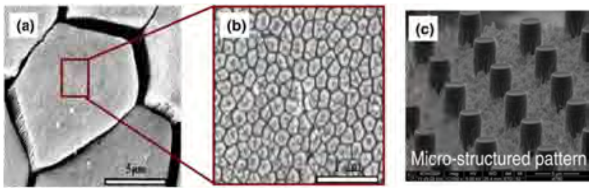

Fig. 2 (a) shows the morphology of tree frog hexagonal epithelial cells, (b) a single hexagonal cell showing peg-like projections can be seen [7], and (c) is a 3D image of the bio-inspired surface [6].

The adhesive pads are attached to the feet of the robot and each pad is moved towards and away from the peritoneum and across its surface by two Squiggle® linear motors (New Scale Technologies Inc.). This paper presents the results of an adhesion control test for one feet of the robot moving perpendicularly to the peritoneum. Fig. 3 shows the experimental set-up for the adhesion test. Here, *F* is the force measured by the load cell.

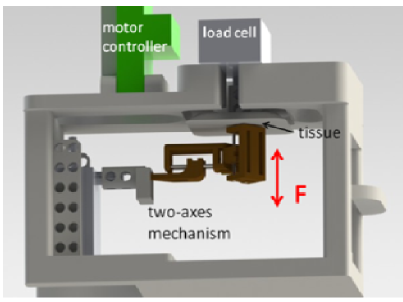

Fig. 3 Experimental set-up for the effect of preload on adhesion test. *F* is the force applied by the motor and measured by the load cell.

A series of values of preload was applied by the robot on the pad measuring the effect on adhesion. For the test rat (human-like) peritoneum was employed as an attachment surface. In order to facilitate contact between the adhesive pad and the peritoneum a 3.5mm-thick layer of Tempur® memory shape foam is placed between the pad and the foot mechanism. A load cell (Transducer Techniques Inc. GSO-100) was used for the measurements of horizontal force applied to the pad (preload) and adhesion force. The pad is square-shaped with an approximate area of $100mm^2$.

The motor is actuated to moves towards the rat peritoneum sample resulting in attachment with a certain value of preload. This is registered as compression force by the load cell, as shown by negative values in Fig. 4. The motor is then actuated in the opposite direction. The motor pulls the pad until the pad returns to its initial position. From that moment on, the motor will have to overcome the adhesion force between tissue and pad to obtain full detachment. The peak of tension force on the load cell is the adhesion force value (see Fig. 4).

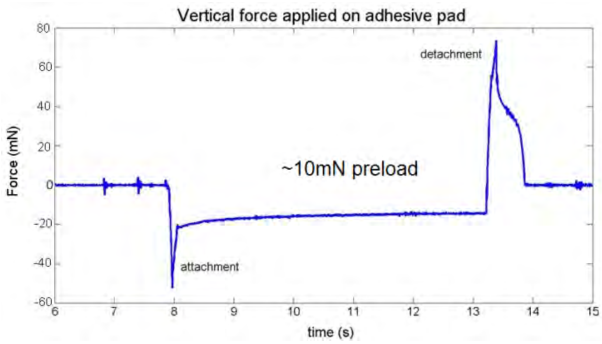

Fig. 4 Vertical force applied by the linear motor and the peritoneal tissue on the adhesive pad.

RESULTS AND DISCUSSION

The pad was preloaded and detached for five consecutive times. In Fig. 5 the average and standard deviation values for the tests performed for a preload of 10 to 70 mN are shown. Adhesion increases by an average of 25% for each 80% average increment in preload. This direct proportionality is true until a value of 70mN of preload is reached, suggesting that pressure favours the formation of links between the two surfaces until excessive force starts breaking them. This range of forces 10–70mN is to be used to control adhesion when in contact with the peritoneum.

Preliminary adhesion control results for a leg of the intra-abdominal robot show the potential of controlling adhesion using the combination of a miniature mechanism and a bio-inspired surface that adheres to biological tissue. Such a capability will enable stable and reliable locomotion of Rasso, paving the way to the implementation of a fully functional mobile device for abdominal surgery.

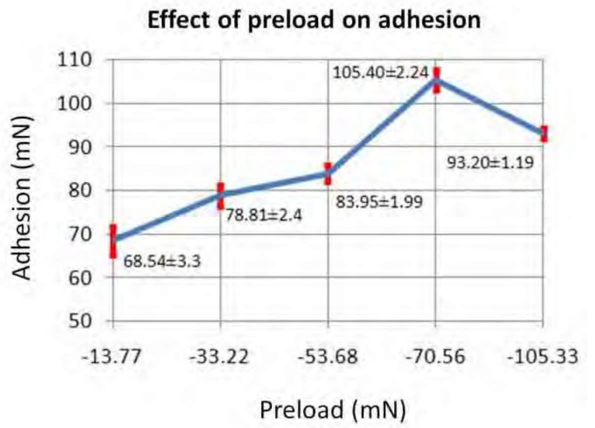

Fig. 5 Effect of preload on adhesion from the pad. The preload is applied by the mechanism of the robot. Adhesion increases with preload for force values between 10 and 70mN.

REFERENCES

[1] P. Dasgupta, "Advanced laparoscopic surgery using tha da Vinci robotic system," in *Robotics in Surgery. State of the Art.*, London, 2010.

[2] J. Gilbert, "Robots in laparoscopic surgery," in *Robotics in Surgery. State of the Art.*, London, 2010.

[3] M. Rentschler, J. Dumpert, S. Platt, K. Lagnernma, D. Oleynikov, and S. Farritor, "Modeling, analysis, and experimental study of in vivo wheeled robotic mobility," *Robotics, IEEE Transactions on,* vol. 22, pp. 308-321, 2006.

[4] N. Patronik, T. Ota, M. Zenati, and C. Riviere, "A miniature mobile robot for navigation and positioning on the beating heart," *Robotics, IEEE Transactions on,* vol. 25, pp. 1109-1124, 2009.

[5] A. Montellano López, M. Khazravi, R. Richardson, A. Dehghani, R. Roshan, T. Liskiewicz, A. Morina, D. Jayne, A. Neville, "Locomotion Selection and Mechanical Design for a Mobile Intra-abdominal Adhesion-Reliant Robot for Minimally Invasive Surgery". Towards Autonomous Robotic Systems." vol. 6856: Springer Berlin / Heidelberg, pp. 173-182.

[6] R. Roshan, D. G. Jayne, T. Liskiewicz, G. W. Taylor, P. H. Gaskell, L. Chen, A. Montellano-Lopez, A. Morina, and A. Neville, "Effect of tribological factors on wet adhesion of a microstructured surface to peritoneal tissue," *Acta Biomaterialia,* vol. 7, pp. 4007-4017.

[7] W. Federle, W. Barnes, W. Baumgartner, P. Drechsler, and J. Smith, "Wet but not slippery: boundary friction in tree frog adhesive toe pads," *Journal of The Royal Society Interface,* vol. 3, p. 689, 2006.

A Feasibility Study on the Use of Concentric Tube Continuum Robots for Endonasal Skull Base Tumor Removal

Hunter B. Gilbert[1]*, Philip J. Swaney[1]*, Jessica Burgner[1], Kyle D. Weaver[2]
Paul T. Russell III[2], and Robert J. Webster III[1,2]

[1]Mechanical Engineering, Vanderbilt University
[2]Vanderbilt University Medical Center

*Contact: philip.j.swaney@vanderbilt.edu, *Shared First Authorship*

INTRODUCTION

We evaluate the ability of a robotic system with needle-diameter, tentacle-like manipulators [1] to remove pituitary tumors endonasally. The robot consists of precurved superelastic tubes that can be axially rotated and telescopically extended to create controllable bending and elongation of the manipulator.

Pituitary tumors account for 15-20% of all diagnosed primary brain tumors [2], and 1 in 5 people are likely to have one in their lifetime [2], with 1 in 120 of these growing large enough (>1cm) to require surgery [3]. In contrast to traditional transcranial and transfacial surgical approaches, the endonasal approach results in no disfigurement to the patient; rather than entering through large tunnels bored into the patient's forehead or cheek, surgical instruments enter through the patient's nostril(s). However, the endonasal procedure is only deployed in a small fraction of all pituitary tumor cases because of the challenge of manually manipulating multiple straight, rigid instruments through the constrained nostril entry port, while performing complex surgical motions at the skull base.

A robotic approach to this procedure has the potential to reduce technical barriers and bring the benefits of endonasal surgery to many more patients. As has been demonstrated in other surgical applications, robots can do this by accurately manipulating small tools (e.g. [4]) and enhancing dexterity (e.g. [5]) in constrained spaces inside the patient. Systems have recently been introduced specifically for middle ear surgery [4] and throat surgery [5], among others.

Endonasal surgery is a particularly challenging application for a robotic system, because of the small nostril access port and the dexterity required at the skull base. Some prior results exist on the use of robotic systems to aid in bone drilling to open access paths to the skull base (see e.g. [6]), and to assist in endoscope manipulation [7]. These are complementary to our approach [1], which is deployed after the surgical site is opened.

MATERIALS AND METHODS

Concentric tube robots, also called active cannulas in view of their uses in medicine, are a type of continuum robot that uses a series of concentric, precurved super-elastic tubes (typically made of nitinol) that translate and rotate inside one another, creating "tentacle-like" motion (i.e. elongation and controllable bending) [8, 9]. The concentric tube manipulator used in this study (Figure 1) consists of three tubes, resulting in a six degree-of-freedom manipulator. The workspace required inside the skull for endonasal procedures and an example tube design method for endonasal surgery were given in [1], and our tube curvatures were selected to closely match the values suggested in that study. The robot is teleoperated using a resolved rates control approach [1] via a haptic device (Phantom Omni, Sensable, Inc., USA) with visualization provided by a standard endoscope (see Figure 2).

Fig. 1 A continuum robot made from three precurved elastic tubes. The robot is able to elongate and bend controllably as the tubes axially rotate and extend. A ring curette similar to those typically used in pituitary surgery is attached to the robot's tip.

The robot shown in Figure1 was used by two experienced skull base surgeons to resect simulated pituitary tumors from a skull model. Suction was used to remove the resected tissue, as is typical in endonasal skull base procedures. The phantom tumor tissue was made from a combination of 1 part SIM-TEST (Corbin, Inc., USA) ballistic test media, and 5 parts water. This mixture provided a soft phantom that the experienced endonasal skull base surgeons judged to be qualitatively similar to the consistency of a pituitary tumor. An anatomical skull model (#A20, 3B Scientific, Germany) was prepared using a bone drill by an experienced surgeon, to closely replicate conditions at the start of pituitary tumor resection. The simulated tumor was then inserted.

Figure 2 shows the experimental setup at the start of tumor resection, and Figure 3 the endoscope view. The surgeon operating the system was instructed to move the active cannula through the nasal passage to the pituitary and remove as much of the simulated

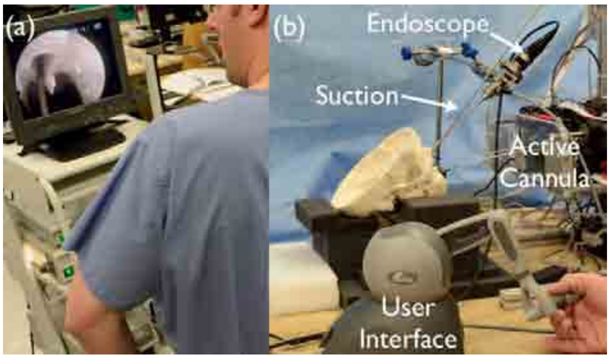

Fig. 2 (a) The surgeon performing a resection used an endoscope view for visualization as shown.(b)The experimental setup consisted of the endoscope, suction, and the active cannula robot, with a Phantom Omni serving as the user interface for teleoperation of the cannula.

tumor as possible, using only endoscope images for visualization. The skull and endoscope were held in place during the experiment, while the suction device was used periodically to clean the curette. The suction was not at any time used to directly remove the simulated tumor itself.

Fig. 3 An endoscopic view collected during tumor removal – the tumor was located through the hole called out with an arrow on the endoscope view. The robot with curette tipis shown on the right side of the image, approaching the tumor.

RESULTS

Two phantom tumor resections were performed according to the procedure described in the Methods section above. In both cases, all tumor was removed other than a thin film of material on the bone surface and in crevices at the back of the sella. To determine the percentage of tumor removed, the skull was weighed before insertion of the simulated tumor, after resection, and after washing to remove tumor residue. In trial 1, one surgeon performed the procedure individually start to finish, with 308 milligrams of an initial tumor mass of 1.4 g remaining after resection (78% removal). In trial 2, two surgeons took turns performing the resection, and 693 milligrams of an initial tumor mass of 2.1 g remaining after resection (67%removal). While no time limit was suggested or imposed and the duration of the resections was not timed, both were completed in a time period comparable to that of a clinical endonasal pituitary tumor removal.

DISCUSSION

To the best of our knowledge, this experiment is the first robotic transphenoidal pituitary tumor phantom resection study. In assessing the results, it is important to note (1) that pituitary tumors are nearly always benign, and (2) that surgeons are often unable to remove 100% of the tumor using current surgical practices. However, clinical outcomes are good, because the goal is decompression of structures like the optic nerve and the carotid arteries (among other structures), and these tumors are often slow-growing. While percentage tumor removal is difficult to quantify in vivo, one clinical study revealed "definite tumor remnants or at least suspicious findings" in 42% of patients in post-operative MRI scans [10]. Thus, while numbers are not available for resection percentages in vivo (because there is no known way to accurately quantify them) we believe our resection percentages are likely in-line with current clinical results. Opportunities for enhancements to our system in future work include the use of a skull with a geometrically accurate sella (surgeons were not able to scrape along the back wall in our phantom as they typically would in vivo), enhancements to tube optimization [1] to include a dexterity metric in addition to reachability, and the potential for dexterity enhancement through the addition of a rotational degree of freedom for the curette about the cannula tip axis.

REFERENCES

[1] Burgner J., et al. "A Bimanual Teleoperated System for Endonasal Skull Base Surgery." IEEE/RSJ International Conference on Intelligent Robots and Systems,2517-23, 2011.

[2] "American Brain Tumor Association (ABTA)," 2011. [Online]. Available: http://abta.org

[3] Ezzat S., et al."The prevalence of pituitary adenomas." Cancer, 101:613–619, 2004.

[4] Miroir M., et al. "RobOtol: from design to evaluation of a robot for middle ear surgery." IEEE/RSJ International Conference on Intelligent Robots and Systems, 850–56, 2010.

[5] Simaan N., et al. "Design and Integration of a Telerobotic System for Minimally Invasive Surgery of the Throat." International Journal of Robotics Research, 28(9):1134–53, 2009.

[6] Matinfar M., et al. "Robot-assisted skull base surgery."IEEE/RSJ International Conference on Intelligent Robots and Systems, 865–70, 2007.

[7] Nimsky C., et al. "Adaptation of a hexapod-based robotic system for extended endoscope-assisted transsphenoidal skull base surgery." Minimally Invasive Neurosurgery,47(1):41–46, 2004.

[8] Dupont P. E., et al. "Design and Control of Concentric-Tube Robots." IEEE Transactions on Robotics, 26(2):209–25, 2010.

[9] Rucker D. C., et al. "A Geometrically Exact Model for Externally Loaded Concentric-Tube Continuum Robots." IEEE Transactions on Robotics, 26(5):769–80, 2010.

[10] Fahlbusch R., et al. "Intraoperative Magnetic Resonance Imaging during Transsphenoidal Surgery." Journal of Neurosurgery, 95(3):381-90, 2001.

An MRI Compatible Optical Multi-Axis Force/Torque Sensors Robotic Surgery

Ramon Sargeant, Hongbin Liu, Kaspar Althoefer

King's College London, UK
{Ramon.sargeant, hongbin.liu,k.althoefer} @kcl.ac.uk

INTRODUCTION

This paper introduces the design of a MRI compatible force sensor that uses fiber optic guided light and linear polarizer materials to measure the applied forces on the tool. The sensor is also capable of measuring the contact direction between the sensor and the object. The developed sensor has wide application such as robotic grasping, MRI guided prostate needle biopsy and MRI-guided cardiac catheterization where the lateral force and displacement on the tool can be measured simultaneously. The sensor's design and operating principles are explained and experimental data is given to verify the proposed operating principle. The experimental data shows that the proposed force sensor performs well. (The research leading to these results has been supported by the handle project, which has received funding from the european community's seventh framework programme (fp7/2007-2013) under grant agreement ict 231640.)

MATERIALS AND METHODS

The multi-axis sensor is based on a 3UPU (Universal-Prismatic-Universal) parallel mechanism sensing structure and uses fiber optic light and linear polarizers as the main sensing element. The sensor has a diameter of 11mm, height of 10mm and weight of 0.6g and is constructed of plastic and flexible nitinol strips (flexures) as shown in Fig. 1. The combination of the plastic components and parallel configuration makes the sensor strong, light but yet still strong and also MRI-compatible since plastic and nitinol are MRI compatible materials.

The forces applied to the sensor twist the nitinol flexures which produce bending moments in the joints. These bending moments can be calculated by the angle that the joints twist from their default positions. The torque required to twist a rectangular strip is given by

$$T = \frac{JG\theta_r}{L} \tag{1}$$

where T is the required torque, G is the shear modulus of the material, L is the length of the twisting protion of the material, θ_r is angle of twisting in radians and J is the torsional stiffness of the material's structure [1]. The output of the linear polarizers is given by

$$I(\theta) = \eta_p I_0 \cos^2(\theta) \tag{2}$$

where $I(\theta)$ is the output intensity and angle θ (in degrees), η_p is the proportion of the light passing

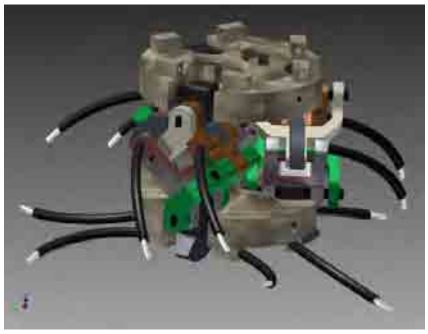

Fig. 1 A 3D illustration of the multi-axis sensor showing the positions of the optical fibers and the linear polarizers.

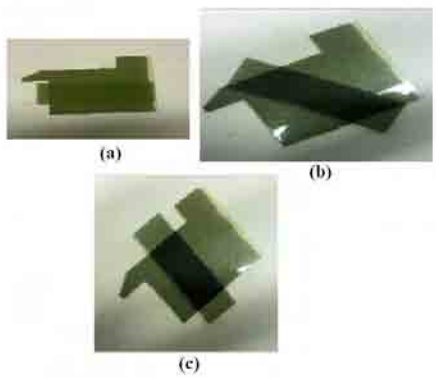

Fig. 2 Photo of the consecutive polarizer films being rotated through 90 °. (a) 0 °. (b) 45 °. (c) 90 °.

through two consecutive aligned polarizers, I_0 is the maximum intensity of the incident beam. Fig. 2 shows photos of two consectuive linear polarisers being rotated through 90 °. The mathematical modelling of I_0 is given in [2],[4],[5]. Substituting eqn (2) into (1) for the angle θ gives

$$T = \frac{JG}{L}\Theta_r\left(\cos^{-1}\sqrt{\frac{I(\theta)}{\eta_p I_0}}\right) \tag{3}$$

where $\Theta_r(\theta)$ is the function to convert from degrees to radians. Each leg is comprised of flexures that twist with the applied force (see Figs. 2 and 3) with the amount of twisting depending on the applied force vector and location. The flexures in the universal joints are arranged orthogonally to each other in the x-y plane so vertical forces (F_z) are transmitted to the prismatic joints only. The vector loop for each leg is shown in Fig. 4. Vector $\mathbf{t_i}$ is the vector from the center of the top surface to a universal joint, vector $\mathbf{B_i}$ is the vector from the center of the bottom surface to a universal joint, vector $\mathbf{r}$ is the vector between the centers of the bottom and top surfaces and vector $\mathbf{d_i}$ is the vector between the corresponding bottom and top universal joints. Solving for $\mathbf{d}_i$ gives the distance and orientation of the moving platform and hence the forces experienced by each flexure. The mathematical modeling of the 3UPU device is given in [3].

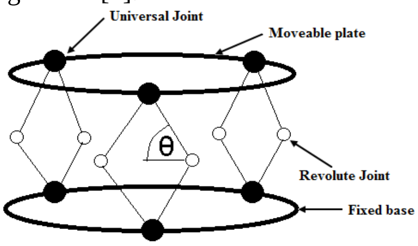

Fig. 3 The prismatic legs of the structure are replaced by revolute joints in order to use the linear polarizers as sensing elements.

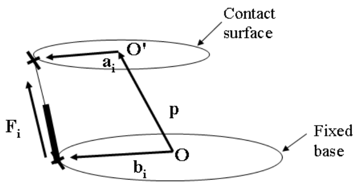

Fig. 4 Vector analysis of one leg of the sensing structure.

RESULTS

To test the structure the multiaxis sensor was subjected to a purely vertical force and the displacement, applied force and polarizer output voltage were measured. Fig. 5 shows the graph of applied force (measured using a Nano17 force/torque sensor) necessary to compress the sensing structure. Fig. 6 shows the corresponding voltage output of the linear polarizers of the prismatic legs for the same distance used during the force test (see Fig. 5). Fig. 7 shows the calibration curve of the 3UPU sensing structure which indicates that the applied force can be correlated to a measured polarizer output voltage.

DISCUSSION

This paper presented a multi-axis force sensor based on a 3-UPU parallel sensing structure and using fiber optic cables and linear polarizer elements as the sensing mechanism. Fig. 5 shows that the applied force produced a linear displacement on the sensing structure which indicates that the prismatic joints function correctly and that the universal joints transmit forces to the prismatic joints without deforming. Fig. 6 also shows that the linear polarizers produce a linear response of to the change in the sensor displacement. This feature is useful because it simplifies the calculation of the applied force. The final graph shows the calibration curve for the sensor where, for a given polarizer voltage, the applied linear force can be easily calculated. The next stage of the research is to modify the 3UPU structure to a 3UPS (Universal-Prismatic-Spherical) structure to create a 6-DOF sensing structure that can also measure the applied torque. The sensor can also be mounted on a robotic grasper to detect the change in surface shape of soft tissue.

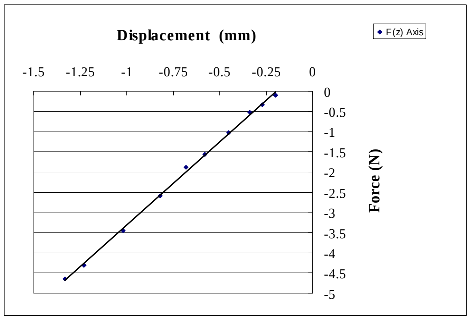

Fig. 5 The results for the displacement test of the sensor

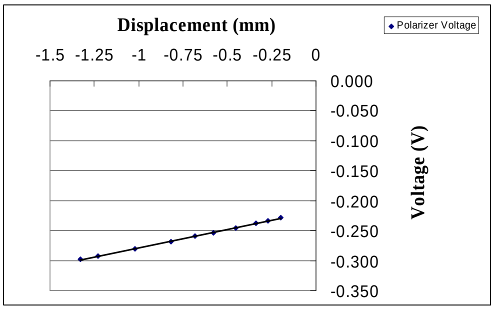

Fig. 6 The change in polarizer output voltage with increased vertical displacement.

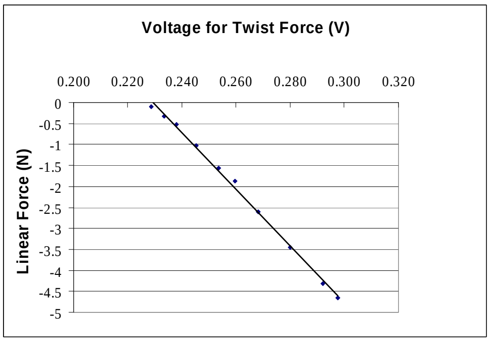

Fig. 7 Calibration curve for the sensor giving a relationship between voltage for the twist force and the applied linear force.

REFERENCES

[1] Young WC, Budynas RG. Roark's Formulas for Stress and Strain 7th Ed. New York: McGraw-Hill, 2002, pp. 109-406.

[2] Saleh BEA, Teich MC. Fundamentals of Photonics. New Jersey: John Wiley & Sons, 2007, pp.73-363.

[3] Tsai L, Joshi S. Kinematics and Optimization of a Spatial 3-UPU Parallel Manipulator. Journal of Mechanical Design, 2000 Dec; 122:439-446.

[4] Polygerinos P, Seneviratne LD, Althoefer K. Modeling of Light Intensity-Modulated Fiber-Optic Displacement Sensor. IEEE Transactions on Instrumentation and Measurement, 2011; 60(4):1408–1415.

[5] Puangmali P, Althoefer K, Seneviratne LD. Mathematical Modeling of Intensity-Modulated Bent-tip Optical Fiber Displacement Sensors. IEEE Transactions on Instrumentation and Measurement, 2010;59(2):283-291.

2 DOF MR-Compatible Cardiac Catheter Steering Mechanism

A. Ataollahi, Y. L. Ma, L. Seneviratne, T. Schaeffter, K. Rhode, R. Razavi, and K. Althoefer

Engineering Department, King's College London

Rayne Institute, King's College London

ali.ataollahi@kcl.ac.uk

INTRODUCTION

Cardiac catheterization is a minimally invasive surgery (MIS) procedure performed using flexible, thin and long tubes called catheters. The catheter can be inserted through a small incision into the femoral vein which leads to the heart. The number of degrees of freedom is limited as the catheter can only rotate and slide through the trocar port. Most commercial catheters are rather simple devices consisting of a flexible plastic body and a maneuverable tip that is manipulated with pre-configured guide-wires, single tendon or permanent magnet tip [1]-[3]. There are also several patents [4]-[6] that present the conceptual designs of catheters that are being developed in industry. One of these products, the Artisan Extend^{TM} Control Catheter is able to adjust its tip position in three dimensions using 4 tendons. This comes at a cost of a larger outer diameter of 11.5Fr and is not MR-compatible [7]. The conventional catheterization procedure uses imaging devices such as X-ray fluoroscope for catheter navigation. Despite the high resolution images provided, the X-ray fluoroscopy technique returns only 2-D projected image with poor soft tissue contrast. In addition, the patient and medical group are exposed to X-ray radiation [8]-[9]. This work presents the design and prototype MR-compatible cardiac catheter steering mechanism with two degrees of freedom which can be navigated in 3D space using tendons. The proposed catheter steering mechanism (See Fig. 1) is based on stacked helical structure segments which are made using rapid prototyping technique. The catheter segment design and tip trajectory is presented in this paper.

STEERING MECHANISM DESIGN

This paper presents the structure design and experimental study of a novel 2-DOF MR-compatible cardiac catheter steering mechanism. The steerable structure is tendon driven and consists of miniature deflectable segments created by a high precision rapid prototyping machine (Projet HD3000 Plus, 3D Systems Co., USA). Fourteen helical segments with four integrated 250 µm tendon channels, 1.7 mm central lumen, and outer diameter of 3 mm (9Fr) are printed of ABS polymer using this machine. Fig. 2 (Left) shows the helical segment design. The novel structure allows the deflection of segment in all directions away from its long axis using four tendons. The assembly design is shown in Fix. 2 (Right). The final prototype catheter has the deflectable length of 126 mm. Four silk string is used as tendon for actuation. A 300um carbon fiber rod is used to improve its repeatability, by providing a backbone for the continuum manipulator at its central channel. As a result of having two degrees of freedom catheter twist is not necessary during navigation which improves the catheterization time and accuracy. In order to compenstae the segment twist cause by tendon tension two different segments with clockwise and counter clockwise helical structure is used in the catheter assembly to avoid positioning error (Fig.2 (Right)). A polymer tube is also used in central channel to fill the gap between carbon fiber rod and the channel wall. This is to be replaced with multi lumen polymer extruded tube to allow implementation of other features at the catheter-tip such as RF ablation wires, tracking coil, etc. A 9 Fr. nylon braided tube is used for catheter shaft with the length of 80 cm.

Fig. 1 The prototype steerable mechanism.

The components are all made of polymer and non-conductive materials to be capable of being employed for applications inside MRI scanner. MR-compatibility tests performed inside a 1.5T MRI scanner, confirm the MR-compatibility of the prototype catheter (Fig. 3).

RESULTS

The proposed prototype catheter steering mechanism is used to investigate the trajectory of the catheter-tip in 3D space. A commercial 3-axis magnetic coil tracking system (Aurora® EM, NDI Co., Canada) is employed to measure the position of the catheter-tip; A robotic actuator made of four stepper motor and microcontroller motion controller is developed to manipulate the tendons precisely in trajectory experiment. The first experiment is performed by actuating a single tendon, similar to the traditional catheters, and the 2D trajectory of the catheter-tip is recorded using magnetic tracking system. The catheter-tip trajectory in 2D plane is presented in Fig. 5. Similarly, by actuation two adjacent tendons the catheter can deflect in 3D space between those two tendons. Fig.4 (Left) shows a schematci demonstration of the catheter deflection based on the tendons directions. The recorded tip trajectory of the catheter in 3D space is also shown in Fig.4 (Right) which is showing a 3D surface similar to a semisphere. This shows that the catheter-tip can be navigated inside the patient's heart without being twisted.

DISCUSSION

This paper presents a novel MR-compatible 2-DOF catheter steering mechanism based on stacked 9 Fr helical segments made of polymer. The proposed tendon driven catheter has ability of being deflected in 3D space without required twist at the insertion point. This feature improves the maneuvarability and accuracy of the catheterization and decreases the procedure time. Moreover, the proposed catheter is benefiting from being MR-compatible to be used in MRI scanners. The future development to be implemented is to have complete robotic cardiac catheter which can be used in cardiac ablation procedures inside the MRI scanner for in-vitro experiments.

REFERENCES

[1] P. Polygerinos, A. Ataollahi, T. Schaeffter *et al.*, "MRI-Compatible Intensity-Modulated Force Sensor for Cardiac Catheterization Procedures," *Biomedical Engineering, IEEE Transactions on*, vol. 58, no. 3, pp. 721-726, 2011.

[2] C. Yi, *et al.*, "Multi-turn, tension-stiffening catheter navigation system," in *Robotics and Automation (ICRA), 2010 IEEE International Conference on*, 2010, pp. 5570-5575.

[3] J. Driller, "Kinetics of magnetically guided catheters," *Magnetics, IEEE Transactions on*, vol. 6, pp. 467-471, 1970.

[4] M. A. Martinelly and W.C. Haase, "Method and system for navigating a catheter probe," U.S. RE40,852, July 14, 2009.

[5] Sheldon D. Gould and Garry T. Riggs, "Curving Tip Catheter," U.S. Patent 4,586,923, May 6, 1986.

[6] M. Eng, R. R.Viswanathan, P. R. Werp, I. Tunay, A. K. Pandey, and G. T. Munger, "Electrophysiology Catheter," U.S. Patent 6,980,843, Dec. 27, 2005.

[7] P. Kanagaratnam, *et al.*, "Experience of robotic catheter ablation in humans using a novel remotely steerable

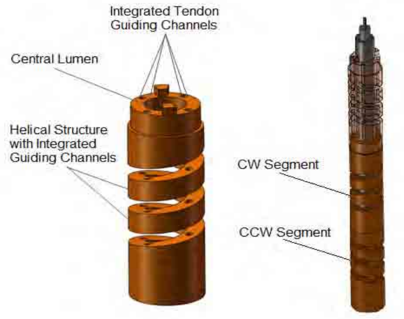

Fig. 2 Helical segment design with integrated tendon channels (Left). The schematic stacked segments forming steerable catheter structure (Right).

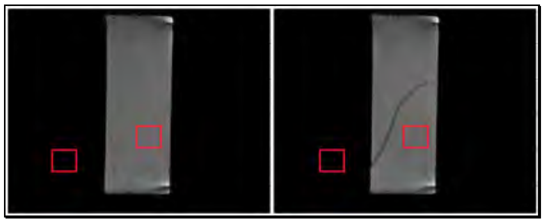

Fig. 3 The normal Phantom (left) and the catheter installed phantom (right). The red rectangles are 30x30 pixels sampling area.

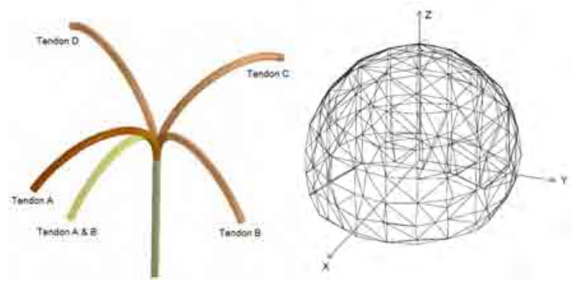

Fig. 4 The Schematic demonstration of the two degrees of freedom deflection using four tendons (Left). three dimensional Trajectory experiment result (Right).

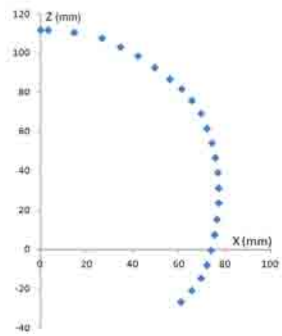

Fig. 5 The catheter-tip trajectory in 2D plane using single tendon.

catheter sheath," *Journal of Interventional Cardiac Electrophysiology*, vol. 21, pp. 19-26, 2008.

[8] R. Razavi, *et al.*, "Cardiac catheterisation guided by MRI in children and adults with congenital heart disease," *The Lancet*, vol. 362, pp. 1877-1882, 2003.

[9] T. Schaeffter and H. Dahnke, "Magnetic Resonance Imaging and Spectroscopy," in *Molecular Imaging I*. vol. 185/1, W. Semmler and M. Schwaiger, Eds., ed: Springer Berlin Heidelberg, 2008, pp. 75-90.

Closed-loop Position Control of an MRI-powered Biopsy Robot

Panagiotis Vartholomeos[1], Christos Bergeles[1], Lei Qin[2] and Pierre E. Dupont[1]

[1]Childrens Hospital Boston, Harvard Medical School, Boston, MA USA

[2]Dana Farber Cancer Institute, Harvard Medical School, Boston, MA USA

panagiotis.vartholomeos@tch.harvard.edu

INTRODUCTION

Clinical MRI scanners can provide large amounts of electromagnetic energy that potentially could be used for actuation as well as imaging and so provide a complete environment for robotic interventions. The idea of using MR scanner magnetic gradients for actuating and tracking millimeter or micrometer size ferromagnetic particles was initially proposed and performed by Martel et al. [1] for drug-delivery applications. In parallel, many groups have developed MRI compatible robots for interventional applications (see reviews in [2,3]).

Inspired by this existing body of work, our group developed an MRI-powered robotic actuator, which was introduced in [4]. Our design leverages the force generation principles studied in [1] to perform the interventional procedures described in [2,3]. In this paper, we introduce closed-loop position control in the context of driving a biopsy needle into tissue. The approach utilizes interleaved actuation and imaging pulse sequences to drive a needle a specified displacement using image-based feedback of a fiducial marker that moves with the needle.

MATERIALS AND METHODS

Principle of operation and prototype: The proposed MRI powered actuator is comparable to an electric motor. It consists of a stator, which comprises the MRI scanner together with the fixed supports of the actuator, and a rotor, which is the rotating portion of the actuator and contains a ferromagnetic sphere. The actuator is rotated through the application of rotating magnetic field gradients that induce a force on the ferromagnetic sphere. A prototype actuator was constructed using LEGO components as shown in Fig. 1. LEGOs offer a fast, convenient and reliable way to build MRI-compatible mechanisms. The small ferrous sphere is located outside the imaging field of view and so does not affect imaging quality.

The actuator itself is wireless and compact. Its principle of operation, its dynamics and capabilities are described in [4]. For the experiments described here, the actuator is placed near the isocenter of the scanner with the plane of the rotor aligned with the X-Z plane of the scanner reference frame. Using the maximum gradient of a clinical MRI, 40 mT/m, the actuation pulse sequence shown in Fig. 3 produces a force on the rotating ferrous sphere (Fig. 1) on the order of 10mN, which is amplified using a gear train and converted to linear coordinates using a rack and pinion. Our open-loop experiments with this prototype have demonstrated needle forces up to 1.2 N.

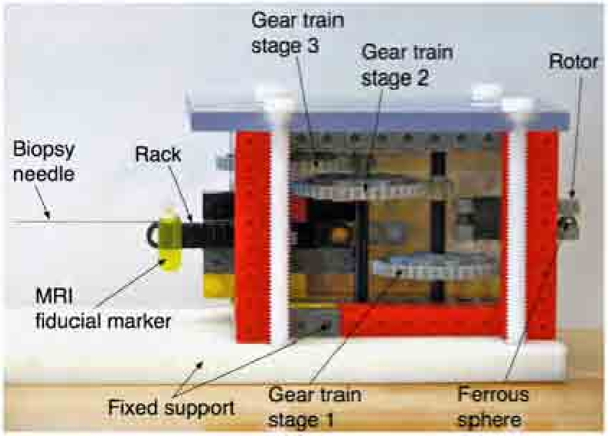

Fig. 1 LEGO prototype. The rotor contains a ferrous sphere and its rotational motion is converted into linear motion using a rack and pinion configuration. The marker on the rack serves as a fiducial for localization of the needle attached on the rack.

Closed-loop position control: The closed loop control architecture and its components are depicted in Fig. 2. Experiments were conducted in a 1.5T clinical MRI scanner. To track the relative displacement of the needle tip, an 8 mm-wide MR-SPOTS fiducial marker (Beekley Medical, CT) was attached to the rack component holding the needle as shown in Fig. 1. While it is also possible to track the needle tip, the use of a passive fiducial marker simplifies the image processing requirements. Since, in our approach, the MR scanner alternates between driving the actuator and tracking its state, reducing the tracking overhead facilitates a higher controller rate.

As shown in Fig. 3, the tracking algorithm employs a gradient echo pulse sequence to generate single-dimensional projections of the field of view. The advantage of this pulse sequence is that it does not contribute to the net motion of the ferrous sphere. Following a background suppression filter to remove the influence of the tissue, the marker is localized using the mean value of a Gaussian function fit to the signal values whose magnitudes are in the top 45%.

Position control experiments were conducted inserting an MRI-compatible needle (MReye, Cook Medical) into chicken breast. The needle was first driven into the tissue to an arbitrary initial location. A gradient echo imaging sequence was then used to image the needle and to determine the distance in the image coordinate frame that the needle must travel to reach a target selected in the image. This displacement command (set point in Fig. 2) was then sent to the external computer for closed-loop execution.

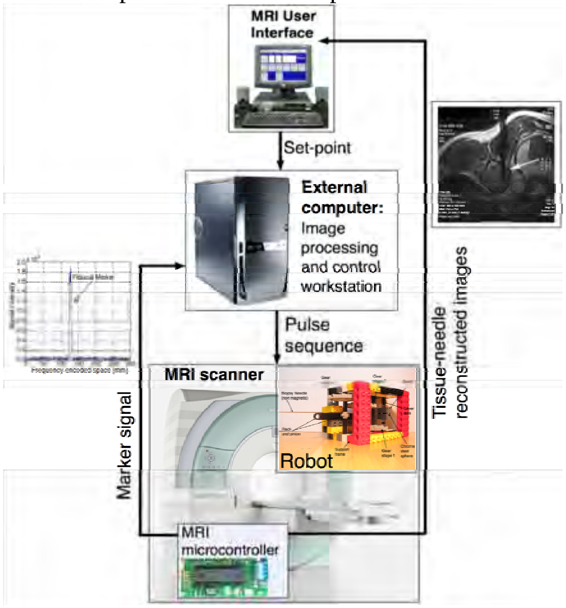

Fig. 2 Closed loop architecture of the MRI-powered robot.

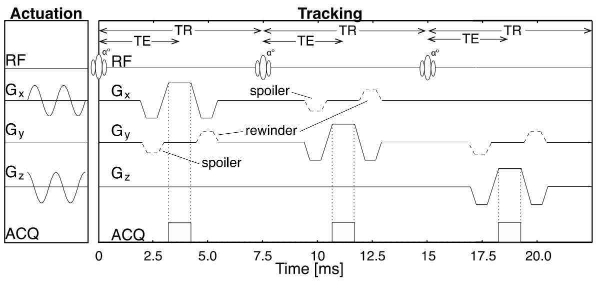

Fig. 3 Actuation and tracking pulse sequences.

RESULTS

Each actuation cycle consists of a single sinusoidal cycle of magnetic gradients which equates to a needle displacement of 250µm. With a field of view in each coordinate direction of 300mm corresponding to 512 voxels, the maximum imaging resolution is 580µm/voxel. Consequently, needle displacements that correspond to less than three actuation cycles (750µm) are not observable. Preliminary localization experiments demonstrated that tracking precision was 1.2mm, due to noise in the imaging signal. Therefore, the imaging pulse was set to follow a sequence of five successive actuation pulses, which correspond to 1.25mm of needle motion. This value is within the tracking capabilities, and indicates the worst-case experimental precision.

An example trial is shown in Fig. 4. Figure 4(a) shows an MR image acquired using gradient-echo imaging, wherein a 10 mm desired needle displacement is selected. This distance corresponds to 8x5 actuation cycles. The displacement was monitored by the tracking algorithm, which terminated the motion when the estimated distance travelled was 9.95mm.

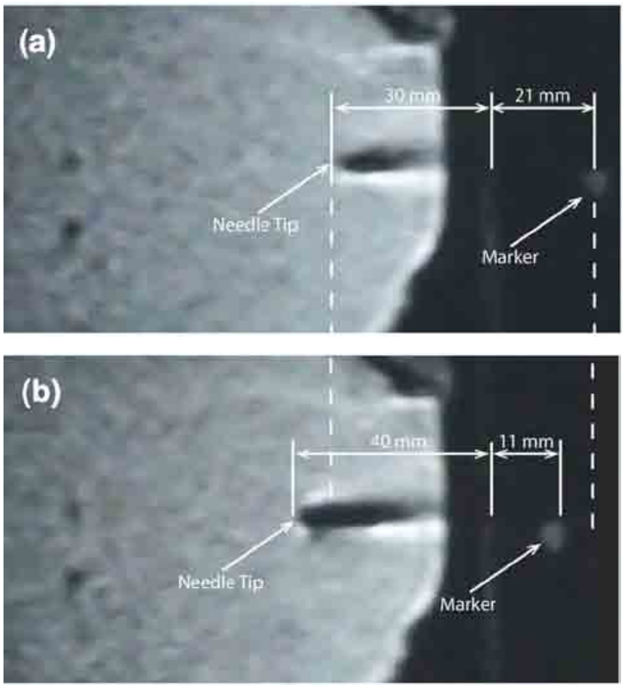

Fig. 4 Illustration of an automated biopsy procedure using gradient-echo imaging, MRI-powering and marker tracking.

DISCUSSION

This paper has presented the effective use of a passive fiducial marker for implementing closed-loop position control of MRI-powered needle displacement in a clinical scanner. These successful experiments provide direction for our future work which will focus on implementing rotor commutation control in order to maximize output force as well as increase actuator output resolution. In addition, we plan to develop techniques for implementing independent position control of multiple degrees of freedom.

REFERENCES

[1] Martel S., et al., "Automatic navigation of an untethered device in the artery of a living animal using a conventional clinical magnetic resonance imaging system", Applied Physics Letters, vol. 90, no. 11, 114105 (3 pages), March 12, 2007.

[2] Nikolaos V. Tsekos, et al., "Magnetic Resonance–Compatible Robotic and Mechatronics Systems for Image-Guided Interventions and Rehabilitation: A Review Study", Annual Review of Biomedical Engineering, Vol. 9: 351-387, 2007.

[3] Fischer GS, Krieger A, Iordachita I, Csoma C, Whitcomb LL, Gabor F, "MRI compatibility of robot actuation techniques: a comparative study", Med Image Com. Assist Interv. 2008; 11: 509-17.

[4] P. Vartholomeos, L. Qin, and P. E. Dupont, "MRI-powered actuators for robotic interventions," IEEE/RSJ IROS, pp. 4508–4515, 2011.

Clinical Study of Prostate Tumour Identification using a Rolling Indentor Robot

Jichun Li[1], Hongbin Liu[1], Jelizaveta Zirjakova[1], Benjamin Challacombe[2], Prokar Dasgupta[2], Lakmal D. Seneviratne[1], Kaspar Althoefer[1]

[1]Centre for Robotics Research, King's College London

[2]Departments of Urology and Histopathology, Guys and St Thomas Hospital

[3]MRC Centre for Transplantation, NIHR Biomedical Research Centre, Guy's Hospital

jichun.li@kcl.ac.uk

INTRODUCTION

Dynamic force feedback is integral to traditional open surgical practice. Minimally invasive techniques usually reduce this sense of touch drastically and in the case of robotic-assisted surgery, remove it altogether, at least in current commercially-available systems, such as the da Vinci Surgical system by Intuitive Surgical. This paper reports on research conducted on a portable rolling indentor robot for three dimensional scanning of soft tissue, capable to evaluate the geometry and mechanical properties of organs in an ex-vivo condition. The employed robotic device comprises a six-degree-of-freedom (DOF) passive robotic arm (Phantom Omni), a data acquisition system and a set of lightweight and potentially minimally invasive rolling probes [1-6]providing haptic feedback. These probes have the potential to discriminate between malignant and benign prostatic tissues and have been validated in an ex vivo setting involving human prostate samples.

MATERIALS AND METHODS

A schematic overview of the rolling indentor robot is shown in Fig. 1. The haptic probe of the rolling indentor robot is attached to a passive robotic arm (Phantom Omni (SensAble)) and consists of a spherical roller and an ATI Nano 17 six-axis force/torque sensor (resolution 0.003N). The Phantom Omni device provides 6 degrees of freedom position sensing.

In our study, we examined prostate samples from male patients having undergone robotic-assisted radical prostatectomy. All patients provided written informed consent allowing the post-operative examination of the extracted prostate samples. The study was given full ethical approval to be conducted at the Department of Urology and Histopathology, Guys and St Thomas Hospital, London. Immediately following surgical prostate removal, rolling indentation experiments were carried out on the extracted human prostates, Fig.2. Real time mechanical property data was collected employing the haptic probe being passed over the excised specimen in a standardized manner covering perimeter large organ surface area. During the rolling indentation, the measured tissue reaction forces were recorded along with the positional information of conducted rolling paths; force and path information were then fused to generate rolling force feedback maps showing the stiffness distribution employing a Matlab visualization package.

The investigator who performed the rolling experiments was blind to the clinical data. After the experiments were completed, the specimens were sent to the pathology department for an independent histological examination. As part of the conducted study, the resultant rolling force feedback maps were correlated

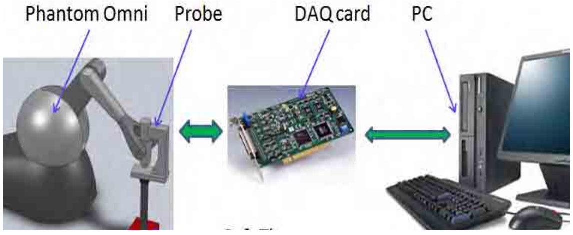

Fig. 1 Schematic of a rolling indentor robot

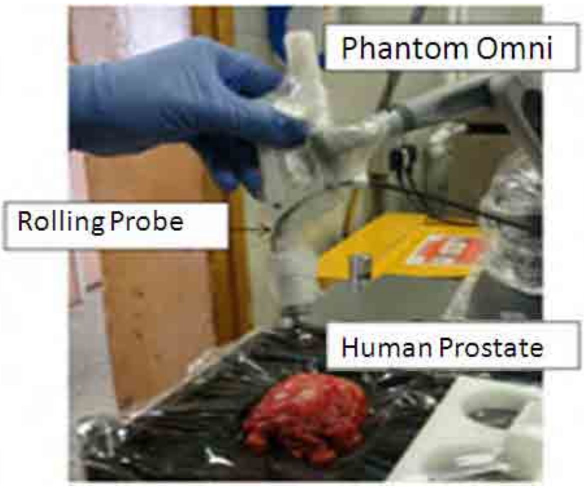

Fig. 2 Rolling indentation experiments conducted on human prostate.

with pre-operative clinical examination, ultrasound guided prostate biopsies, staging MRI and histopathology.

RESULTS

In total the prostates of 23 male patients were examined in the outlined way following robot-assisted radical prostatectomy. The generated rolling force feedback maps were correlated with digital rectal examination, MRI appearances and transrectal US guided prostate biopsy results using a proforma. Correlation was performed using a visual scale by researchers blinded to the purpose of the study. Since, generally, tumors are stiffer than the surrounding tissue, the tumor areas were expected to show up as distinctly red colored areas (higher stiffness) on the rolling force feedback maps. Fig.3 shows a three dimensional colour-coded rolling mechanical image which indicates force feedback and tumour locations of a human prostate.

Fig. 4 shows the outcome of a study comparing the results of our rolling indentation experiments with the clinical reporting proforma on a selected prostate conducted by clinicians at Guy's Hospital.

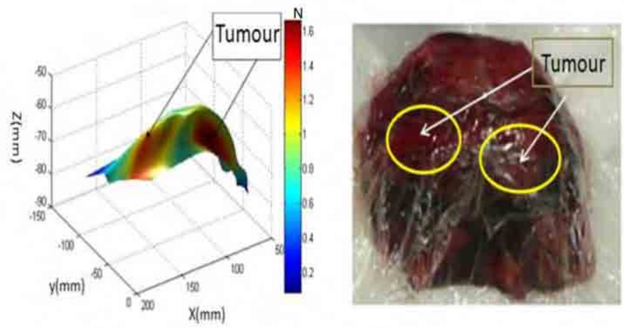

Fig. 3 3D mechanical image of the examined prostate and tumour areas detected by rolling indentation approach on a selected prostate.

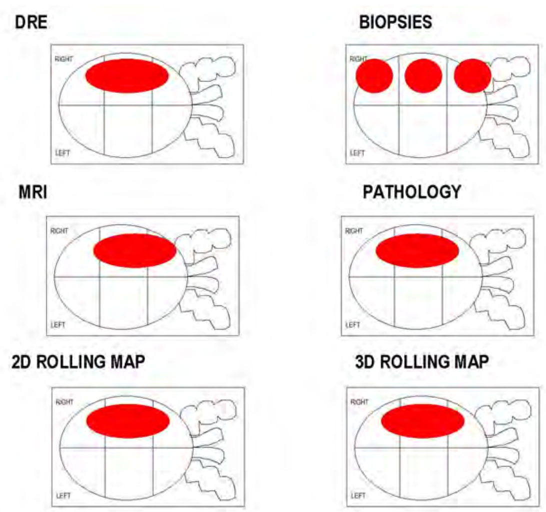

Fig. 4 A comparative result of rolling indentation with clinical reporting proforma on a selected prostate.

The conducted experimental study shows that there was good correlation of the outcome of our rolling indentation based method with the clinical reporting proforma, in particular for index lesions greater than 1 cm in size.

DISCUSSION

The proposed method proves to be a promising tool in organ diagnosis clearly showing its capability to distinguish between cancerous and healthy tissue in soft organs, and, generally, to discriminate pathological tissue variations. The method is currently under development to augment haptic feedback during robotic-assisted radical prostatectomy. Employing this approach during RMIS, may eventually reduce positive margins and allow more accurate nerve sparing to be performed. In vivo laparoscopic testing is planned.

REFERENCES

[1] Jichun Li., et al. "A Passive Robotic Platform for Three-Dimensional Scanning of Ex-vivo Soft Tissue", 2nd IEEE/ASME International Conference on Reconfigurable Mechanisms and Robots, accepted for publication.

[2] Jichun Li, Hongbin Liu., et al. "A Stiffness Probe for Tissue Abnormality Identification in Laparoscopic Surgery", World Automation Conference (WAC2012), accepted for publication.

[3] Hongbin Liu,Jichun Li., et al. "Rolling IndentationProbe for Tissue Abnormality Identification during Minimally Invasive Surgery", IEEE Transactions on Robotics (T-RO), 2011 June: 450-460.

[4] Hongbin. Liu, J. Li., et al."Miniaturized Force-Indentation Depth Sensor for Tissue abnormality identification" IEEE Int. Conf. on Robotics and Automation 2010: 3654-3659

[5] Hongbin. Liu, D. Noonan, L. Seneviratne, P. Dasgupta, K. Althoefer, Rolling Indentation for Tissue Abnormality Localization during Minimally Invasive Surgery, IEEE Trans. Biomedical Eng., 2010,**57**(2): 404 - 414.

[6] Jichun Li, Hongbin Liu., et al" Results of Kidney Lesion Experiments with Haptic Probe", the 59th annual meeting of Society of Academic & Research Urology,2011.

Development of a Novel Hybrid System for Haptics

A.I. Skinner[1], K. Hohenberg[1], A. Pereira[1], S. Bowyer[1], Y. Tenzer[2], F. Rodriguez y Baena[1]

[1]*Department of Mechanical Engineering, Imperial College London, UK*
[2]*Harvard Biorobotics Laboratory, Harvard University, USA*
f.rodriguez@imperial.ac.uk

INTRODUCTION

The use of robotic motion limiting devices to provide force feedback in surgical applications is a well-developed field (e.g. active constraints in knee surgery [1]). However, the use of active devices such as motors to provide force feedback can potentially introduce safety concerns; any motor which can provide enough torque to enforce a 'hard stop' is also capable of causing the manipulator to move autonomously during a malfunction. This can be a safety concern in critical environments such as the operating theatre, where the surgeon has to have a full control of the motion of the instruments. Hence, the use of passive components, which are designed to dissipate energy, such as brakes, is desirable. Nevertheless, an actuator solely comprising of brakes, whilst being able to enforce 'hard stops', cannot be used to produce an active response, for example that which would be required to produce a force on the user's hand. To address this limitation, the aim of this research is to investigate the advantages of a hybrid actuation strategy, where the use of a small motor is coupled with novel part-locking brakes.

HYBRID ACTUATOR

A novel brake for use in haptic devices was recently developed [2]. Unlike traditional braking systems which fully lock the motion of the mechanism when actuated, this brake has a programmable part-locking feature. As such, this brake can be programmed to permit movement in one direction whilst preventing movement in the other, without the need to detect the user's intention by means of an additional force sensor.

Given the limitation of a brake-based actuator, a hybrid actuator comprising of the part-locking brakes and a relatively small motor was developed. The hybrid approach allows for a much smaller (and therefore safer) motor to be used than in a purely active design, as the brakes can provide the high torque needed to enforce hard stops. This hybrid approach offers the advantages of variable force control as found in motors and the advantages of improved safety from passive devices. The hybrid approach for force feedback is not new [3], but the proposed design allows for a simpler implementation when embedded into multi-degree of freedom devices. This is because a design approach where the actuator is modular, and thus easy to use in place of motors in conventional mechanism architectures, was adopted. This main design feature differentiates the current work from that of others (e.g. [4-5]).

The novel hybrid layout is shown in Fig 1. The concentric design allows for both the brakes (2) and motor (4) to be assembled in a compact and modular design, with a single drive shaft.

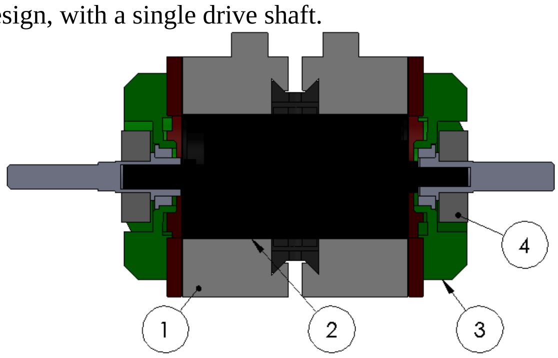

Fig. 1. Cross section of hybrid actuator design, with concentric brake (1), motor (2), block (3) and stopper (4).

The hybrid layout required a redesign and relocation of the part-locking mechanism presented in [2]. The modified stopper mechanism (parts 3 and 4 in Fig. 2), is shown in Fig. 2. In this configuration, the motor shaft (3) is attached to a rectangular stopper (1). This stopper rotates inside a block (2), which is attached to the brake pad. A spring inside the stopper (4) ensures that the stopper is preloaded and is pushed up against one side of the enclosure. When the magnetic brake actuates the block (2), the shaft is locked.

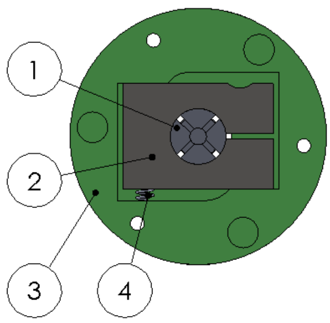

Fig. 2. Design of new stopper assembly, with motor shaft (1), stopper (2), block (3) and spring (4)

As the stopper is pushed up against one side of the enclosure, it cannot pivot in one direction, while motion in the opposite direction is allowed. The part locking mechanism operates by deactivating the brake when motion away from an intended rotary constraint, initiated by the user, is detected by means of an axis mounted position sensor. Once the brake is deactivated, the spring resets the mechanism to its initial position.

2-DOF HAPTIC DEVICE

To evaluate the performance of the hybrid actuators in a haptic environment, a 2-DOF manipulator which can generate both soft and hard constraints was developed. The soft constraints are constructed as a finite stiffness region, the force for which is provided by the motors, placed adjacent to a hard constraint, constructed as an 'infinite' stiffness boundary, enforced by the brake.

The simplest hybrid control strategy to enforce a constraint, whereby brake and motor activations are determined solely based on position, is not ideal. The delay caused by any latency in brake activation means that the hard constraint will be penetrated if the brakes are only actuated at the boundary. Instead, the concept of a braking threshold is used.

The control algorithm turns on the brake when a constraint} force greater than a certain value (the braking threshold) is required. The stiffness of the soft region is defined so that the force at the boundary of the hard region is equal to the braking threshold (in this case the maximum motor torque); hence at the wall the brake is activated. In order to prevent wall penetration a 'damping' term is added to the 'spring' term, this increases the required force with speed. This means that the braking threshold will be reached before the wall is passed and the distance from the wall at which the brake is activated increases with speed of approach, as the distance travelled during brake activation also increases with speed a suitable value of damping can be used to reduce penetration.

Fig. 3. Manufactured hybrid actuator system and actuator for 2 DoF system

RESULTS

A 2 DoF prototype (Fig. 3) has been designed, manufactured and assembled. The physical properties of the actuator, such as maximum end effector brake and motor torques, are currently being measured with a force meter for calibration purposes. The quality of the constraint is also being investigated, by requesting that test subjects attempt to penetrate a constraint while the force applied to the user and the position of the end effector are recorded. Thus the penetration achieved and the qualitative 'feel' of the feedback can be obtained.

DISCUSSION AND CONCLUSION

A hybrid haptic actuator has been designed which uses part-locking brakes. It is modular, compact and can be used to produce both hard (e.g. tool on bone), as well as soft (tool on tissue) interaction forces. A 2-DOF haptic manipulator similar in layout to the Sensable Phantom Premium haptic device (Sensable Technologies Inc.) was also developed which makes use of the novel actuators.

The design of the 2DOF mechanism allows the weight of the actuators (1.1kg in the current prototype) to be concentrated at the base of the system, thus limiting the effect of their inclusion on the quality of haptic responses. The relatively high mass of each actuator can be reduced through design optimisation, but will remain an important design factor, as each requires one motor and two brakes to operate. However, the manipulator design could be improved further, for instance by inclusion of a cable driven system, to ensure the end effector remains highly back-drivable and with low inertia. In the meantime, gravity compensation with the motors has been implemented to further improve performance. Finally, friction brakes have been employed in this work, which are difficult to control with variable torque (i.e. current control). Thus, magneto-rheological brakes, which have been used in other haptic devices [4], will be considered in future work.

REFERENCES

[1] M. Jakopec, F. Rodriguez Baena, S. J. Harris, P. Gomes, J. Cobb, and B. L. Davies, "The hands-on orthopaedic robot 'acrobot': early clinical trials of total knee replacement surgery," *IEEE Transactions on Robotics and Automation*, vol. 19, no. 5, pp. 902-911, Oct. 2003.

[2] Y. Tenzer, B. L. Davies, and F. R. y Baena, "Four-State Rotary Joint Control: Results With a Novel Programmable Brake," *IEEE/ASME Transactions on Mechatronics*, pp. 1-9, 2011.

[3] Y.-J. Nam and M.K. Park, "A hybrid haptic device for wide-ranged force reflection and improved transparency," in *2007 International Conference on Control, Automation and Systems*, 2007, pp. 1015-1020.

[4] J. An and D.S. Kwon, "Haptic experimentation on a hybrid active/passive force feedback device," in *Proceedings 2002 IEEE International Conference on Robotics and Automation (Cat. No.02CH37292)*, 2002, vol. 4, no. May, pp. 4217-4222.

Extending the Reach and Stability of Manually Steerable Neuroendoscopes Through Robotics

Pierre E. Dupont[1], Szymon Chawarski[2], Evan J. Butler[2], Robert Hammond-Oakley[2], Andrew H. Gosline[1], Patrick Codd[1], Tomer Anor[1], Joseph R. Madsen[1] and Jesse Lock[2]

[1]*Children's Hospital Boston, Harvard Medical School, Boston, MA, USA*

[2]*Sterling Point Research, Winchester, MA, USA*

pierre.dupont@childrens.harvard.edu

INTRODUCTION

Neurosurgical disease encompasses a wide range of devastating pathologies, ranging from brain tumors, epilepsy, hydrocephalus and vascular malformations to brain trauma. Over 2 million neurosurgical procedures are performed annually in the United States alone, including roughly 380,000 operations requiring intracranial access [1]. During open brain surgery, adequate visualization and tool maneuverability often require significant bone removal and harmful traction on otherwise uninvolved brain to accomplish the surgical task.

Surgeries abutting the fluid-filled spaces of the brain have provided the opportunity to reduce invasiveness through the use of endoscopy. Examples include straight rigid endoscopes inserted transphenoidally for procedures at the skull base, e.g., removal of lesions in or near the pituitary gland, and manually steerable flexible endoscopes employed through small cranial burr holes into the ventricular spaces to treat tumors, cysts, hydrocephalus and epileptogenic lesions. Despite this progress, there are many procedures in the fluid-filled regions that still require open surgery owing to limitations in the ability to navigate the endoscope to the surgical site and to provide precise tool control.

To address these limitations, this paper presents a robotic drive system for controlling the degrees of freedom of a manually steerable endoscope. By eliminating the need for the surgeon (or surgeons) to continuously maintain the manual forces and positions on the endoscope needed to achieve the desired configuration, the precision and stability of the endoscope's motion is enhanced. Furthermore, the workspace of the endoscope's tip is extended by also providing robotic control of concentric pre-curved elastic tool-delivery tubes extending through the endoscope's working channel [2]. This enables tools to reach deeper into the ventricles than existing instrumentation allows (Fig. 1).

MATERIALS AND METHODS

A robotic drive system was constructed to control the degrees of freedom of a manual neuroendoscope as well as those of a port-deployed tool (Fig. 2). In manual use, one hand controls endoscope position and orientation at the entry point into the brain while the other hand controls tip curvature and tool deployment. Not shown, a second surgeon may also assist in endoscope positioning and in tool deployment. Since the entry location into the brain is fixed, the endoscope possesses five actively controlled degrees of freedom. These correspond to two rotational axes for pivoting about the entry point, roll angle, insertion length and tip curvature.

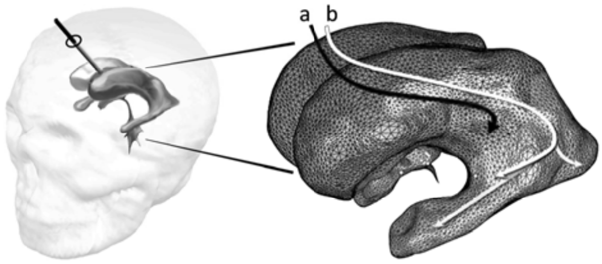

Fig. 1 Intraventricular access through cranial burr hole. (a) Workspace of manual endoscope. (b) Desired workspace.

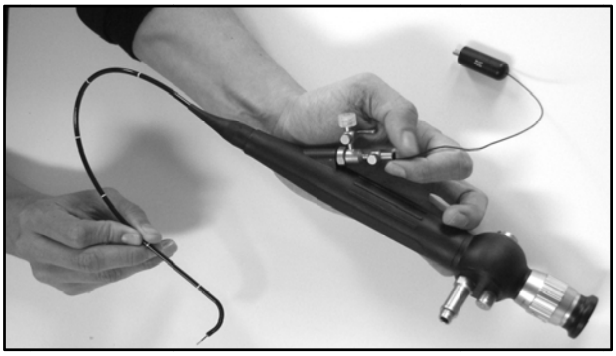

Fig. 2 Steerable manual neuroendoscope (Karl Storz). Inserted through cranial burr hole, scope tip possesses 5 degrees of freedom. Right hand controls 3 orientation axes at insertion point plus insertion length. Left hand controls tip curvature plus additional tool degrees of freedom as shown.

The robotic drive system is comprised of two major components. The first is designed to support and control the five endoscope degrees of freedom. The second component controls the concentric tube robot used for tool positioning. For the specific clinical application of choroid plexus cauterization to treat hydrocephalus, a concentric tube robot consisting of two telescoping fixed curvature segments was designed to enable navigation throughout the temporal horns of the lateral ventricles as shown by the longest white arrows of Fig. 1,which constitute the farthest reach from the frontal burr hole [3]. These sections, depicted extended in Fig.

3, conform to the curvature of the endoscope when retracted inside it. The proximal fixed-curvature section possesses two degrees of freedom corresponding to extension from the endoscope tip and rotation about its axis. The distal section is comprised of a monopolar cautery tool whose relaxed shape is straight and so possesses a single degree of freedom corresponding to extension from the proximal section.

The drive system is shown in Fig. 4 with actuated degrees of freedom labeled.The endoscope body is secured to the center of a frame that can rotate and translate along its central axis. The endoscope neck passes through a two-axis actuated gimbal cannula just proximal to the skull insertion point. The variable curvature of the endoscope is controlled via actuated rotation of the lever mounted on the endoscope body. The tool drive subsystem has three actuated degrees of freedom and has been designed to allow convenient substitution of alternate tools, such as biopsy forceps or a laser.The robot is controlled using a dual joystick master with additional input buttons. The 1 kHz controller is a Simulink model downloaded to a PC104 CPU board running the XPC Target real-time operating system (Mathworks, Inc.)

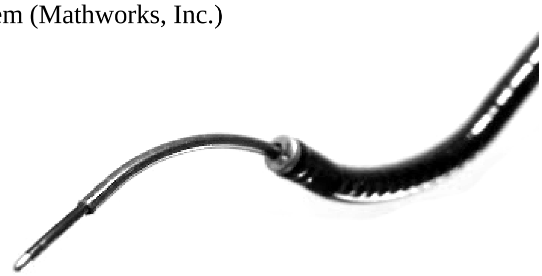

Fig. 3 Two-section concentric tube robot deployed through endoscope working channel. Distal section is monopolar cautery tool.

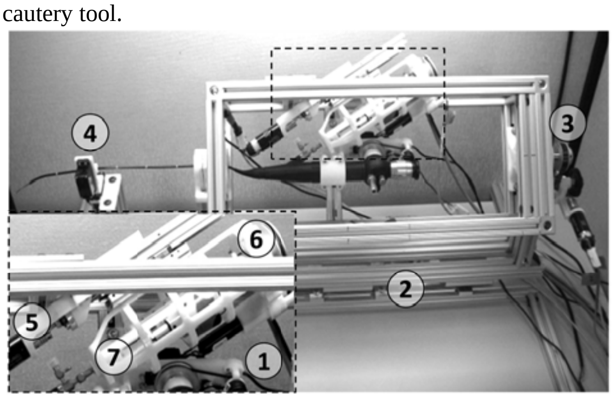

Fig. 4 Robotic drive system.(1) scope tip curvature, (2) scope insertion, (3) scope rotation,(4) two-axis actuated gimbal, (5) proximal concentric tube extension, (6) proximal concentric tube rotation, (7) distal cautery tool extension.

RESULTS

As a preliminary evaluation of the robot, the reachable workspace of the cautery tool in the temporal horns of the lateral ventricles (Fig. 1) was compared with and without the addition of the curved concentric tube of Fig. 3. This experiment was performed in a ventricle phantom produced using stereolithography from MRI images of a hydrocephalic brain. The phantom included cutouts to allow direct visualization of the endoscope and extended tools. Using a left frontal approach, the endoscope was introduced into the phantom, crossing the septum pellucidumto the contralateral lateral ventricle, and navigated inferiorly toward the temporal horn. Under joystick control, the cautery tool was positioned on a grid of points covering the inner surface of the ventricle. The sets of surface points that could be reached with and without the curved concentric tube are depicted in Fig. 5. As shown, the curved concentric tube is needed to reach the roof of the inferior horn. Note that the dashed boundary shown in Fig. 5(a) lies on the surface of the ventricle.

To provide a quantitative comparison of workspaces, the sets of reachable points were transferred to the CAD model used to produce the phantom. Using the curved concentric tube, the robot was able to reach the entire 1300 mm^2 surface area of the inferior horn and only 65%(853 mm^2) of the total area without it.

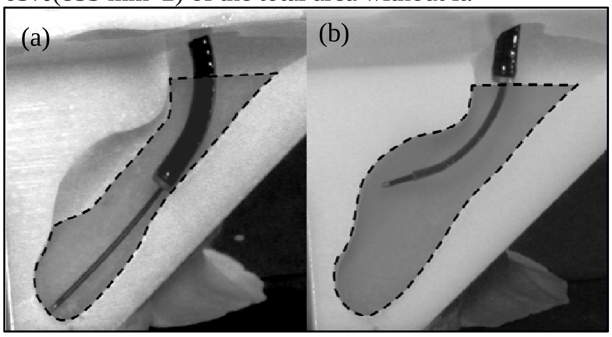

Fig. 5 Neuroendoscope workspace with and without concentric tube extension.Shaded region can be reached by cautery tool tip. (a) Cautery tool only. (b) With curved concentric tube.

DISCUSSION

To address the current limitations of neuroendoscopes, we have proposed combining robotic control of a manual neuroendoscope with concentric tube robot technology. By adapting existing endoscope technology rather than creating an entirely new device, it is anticipated that barriers to clinical acceptance and regulatory approval will be reduced. Furthermore, robotic control of a manual endoscope will likely provide safer and smoother control of its existing degrees of freedom while also providing the means to integrate the control of the concentric tube degrees of freedom.Future experiments will focus on validating our approach and on refining the user interface.

Acknowledgement: This work was supported by the National Institutes of Health under grant R43EB014063.

REFERENCES

[1] "National Neurosurgical Procedural Statistics," American Association of Neurological Surgeons, vol. Survey, 2006.

[2] Dupont P, Lock J, Itkowitz B, Butler E. Design and Control of Concentric Tube Robots. IEEE Trans Robotics 2010;26(2):209-225.

[3] Warf B. Endoscopic third ventriculostomy and choroid plexus cauterization for pediatric hydrocephalus. Clinical Neurosurgery 2007;54:78-82.

New Evaluation Metrics Applied to Robotic Anastomosis

Abdelaziz Farhat[3], Mohammed Al-Haddad[4], Georges Younes[1,2],
Tarek El-Ghazaly[3,5], Julien Abi-Nahed[1], Abdulla Al-Ansari[1,5], George Turkiyyah[2]

[1]Qatar Robotic Surgery Centre
jabinahed@qstp.org.qa

[2]American University of Beirut
[3]Weill Cornell Medical College in Qatar
[4]Carnegie Mellon University in Qatar
[5]Hamad Medical Corporation

INTRODUCTION

Despite exponential growth in robotic surgery [1,2], no standardized or widely accepted approach has been developed for clinical training [3], except perhaps recent efforts to create the "Fundamentals of Robotic Surgery"[1] which is still far from the well-established "Fundamentals of Laparoscopic Surgery." With increasing numbers of robotic surgeons not adequately trained during residency or fellowship [4], it could be speculated that an excessive number of patients may be exposed to a so-called "learning curve". Therefore, a safe and effective means of training robotic surgeons is urgently needed [5]. This partly explains the increased interest in robot-assisted surgery simulations, which have recently witnessed increased growth rate [6,7]. Furthermore, a simulator allows surgeons to continually hone their skills even for procedures that are not commonly performed. Finally, simulators provide a relatively cost-effective tool for training, as they do not require purchase of expensive robotic equipment.

This study falls within a research and development simulation program at the Qatar Robotic Surgery Centre. It aims to develop next-generation surgical simulators with more realistic representation of surgical set-ups, and improved ability to reliably differentiate between expert and novice surgeons. This will result in a useful tool for both training novice surgeons and the honing of developed expert techniques. The first step in developing our simulator (Fig. 1), which would initially be used for robotic radical prostatectomy training, will be to simulate the creation of the urethrovesical anastomosis. This paper presents evaluation metrics that will be used to assess the quality of the procedure. These are a combination of previously identified metrics, and novel metrics defined by our group.

MATERIALS AND METHODS

The purpose was to design an effective assessment tool to evaluate the performance of surgeons when performing virtual anastomosis. To this end, essential procedure-specific evaluation metrics were identified, and several novel ones were defined as detailed in the next section. First, we explored literature that specifically discussed evaluation of skills using simulators and reviewed surgery-training literature in order to identify benchmarks that are used to evaluate surgical trainees. We also viewed recordings of surgeries, noting the different techniques used and how the surgeons decided what good technique was. After compiling this data, we presented them to general and urological surgeons with experience in teaching. Based on the feedback, we formulated our own criteria for a new metric. This metric and other metrics identified by the literature search will be applied to the simulator.

RESULTS

The metrics that have been already defined and used in previous validation studies [7,8,9,10,11,12] are *total time*; *suturing time*; *ratio of times*(a ratio of the time spent on the main task—suturing—in relation to the overall time spent in the session); *number of instrument collisions*; *time out of view* (the amount of time the instruments are out of camera view); and *total motion*.

Our team defined a new hybrid metric that builds on previous validation studies and conforms to feedback from our expert panel of surgeons. The metric is *suturing quality*, which aims to identify the surgeon's skill based on the quality of sutures produced. This metric is better explained when broken down into categories encompassing smaller sub-metrics.

In the stitch and suture category, the simulator will record the *distance from edge of tissue* (Fig. 2.1), *distance between each stitch*, *number of stitches*, and *suture tension* which measures the force imparted on tissue by the suture thread.

For the tissue placement category, the simulator will record the *tissue edges overlap* (Fig. 2.2) and *tissue layer levels alignment* (Fig. 2.3) which is the alignment of different layers of tissue (muscular, connective, *etc.*) with each other from the two sides of a tissue.

Under the tissue damage category, the simulator will record *peak force* which is the magnitude of the largest force imparted onto the tissue by the subject tools; *excess force* which is the sum of forces applied to the tissue in excess of a maximum threshold; *surface damage* which measures the sum of all forces applied to the surface of the tissue in excess of the force needed to penetrate the tissue and the force needed to complete the suture; *number of needle punctures per stitch*; and the *size of tear* when needle is inserted into tissue, which includes the incident angle of the needle.

[1] Society of Robotic Surgery (http://srobotics.org)

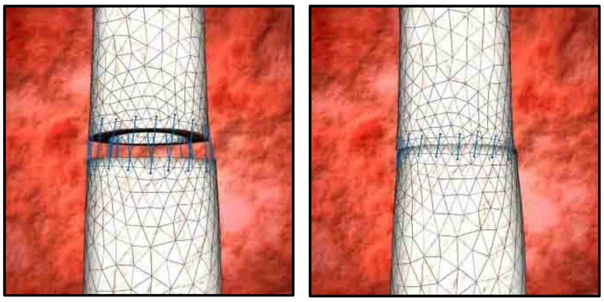

Fig. 1 Snapshots from our simulator prototype

Fig. 2.1: Distance from edge Fig. 2.2: Tissue edge overlap

Fig. 2.3: Tissue layer level alignment

Fig. 2.4: Amount of anastomosis blockage

Fig. 2 Visualization of selected metrics

Finally, the simulator will record the *amount of stress on tissue* which measures the total amount of force placed on the tissue for different purposes, including moving it, puncturing, and sewing it; *number of grasps per stitch* which is the number of grasp/release steps for each suture; *knot type and strength*; and *amount of anastomosis blockage* (Fig. 2.4).

Once the metrics are applied to the simulator, a cohort of expert urological surgeons will be invited to use the simulator. Values for the different metrics will be based on the surgeons' performance. These values will form the basis upon which novice surgeons are evaluated.

DISCUSSION

Live-case robotic prostatectomy training is estimated to require over 150 cases before expert transitioning to robotic surgery is achieved [13]. The authors in [14] demonstrated that this form of training required more procedure time, without being able to improve expected outcomes—a valid concern amidst clinical studies highlighting the impact of surgeon skill and technique on oncological and functional outcomes [15,16]. Robotic simulator training alleviates these concerns. Our long-term goal is to establish a validated, realistic, yet cost-effective tool for robotic surgical training that will give tangible enhancement of robotic surgical skill and technique in aspiring robotic surgeons. We are encouraged by the positive feedback from our expert surgeons regarding the new metrics introduced in this work. In the near future, we plan to test the metrics with surgeons from Hamad Medical Corporation and Weill Cornell Medical College in Qatar.

REFERENCES

[1] Moustris, G. et al.: Evolution of Autonomous and Semi-Autonomous Robotic Surgical Systems: a Review of the Literature. International Journal of Medical Robotics and Computer Assisted Surgery 7(4), 375–392 (2011)

[2] Schreuder, H. and Verheijen, R.: Robotic Surgery. BJOG: an International Journal of Obstetrics & Gynaecology 116(2), 198–203 (2009)

[3] Sándor, J. et al.: Minimally Invasive Surgical Technologies: Challenges in Education and Training. Asian Journal of Endoscopic Surgery 3(3), 101–108 (2010)

[4] Seixas-Mikelus, S. et al.: Content Validation of a Novel Robotic Surgical Simulator. British Journal of Urology International 107(7), 1130–1135 (2011)

[5] Albani, J. and Lee, D.: Virtual Reality-Assisted Robotic Surgery Simulation. Journal of Endourology 21(3), 285–287 (2007)

[6] Stefanidis, D. et al.: Skill Retention Following Proficiency-Based Laparoscopic Simulator Training. Surgery 138(2), 165–170 (2005)

[7] Jonsson, M. et al.: ProMIS Can Serve As a da Vinci Simulator: a Construct Validity Study. Journal of Endourology 25(2), 345–350 (2011)

[8] Kenney, P. et al.: Face, Content, and Construct Validity of dV-Trainer a Novel Virtual Reality Simulator for Robotic Surgery. Urology 73(6), 1288–1292 (2009)

[9] McDonough, P. et al.: Initial Validation of the ProMIS Surgical Simulator As an Objective Measure of Robotic Task Performance. Journal of Robotic Surgery 5(3), 195–199 (2011)

[10] Lendvay, T. et al.: Initial Validation of a Virtual-Reality Robotic Simulator. Journal of Robotic Surgery 2(3), 145–149 (2008)

[11] Halvorsen, F. et al.: Virtual Reality Simulator Training Equals Mechanical Robotic Training in Improving Robot-Assisted Basic Suturing Skills. Surgical Endoscopy 20(10), 1565–1569 (2006)

[12] Schout, B. et al.: Validation and Implementation of Surgical Simulators: a Critical Review of Present, Past, and Future. Surgical Endoscopy 24(3), 536–546 (2010)

[13] Herrell, S. and Smith, J.: Robotic-Assisted Laparoscopic Prostatectomy: What Is the Learning Curve? Urology 66(5), 105–107 (2005)

[14] Davis, J. et al.: Initial Experience of Teaching Robot-Assisted Radical Prostatectomy to Surgeons-In-Training: Can Training Be Evaluated and Standardized? British Journal of Urology International 105(8), 1148–1154 (2010)

[15] Klein, E. et al.: Surgeon Experience is Strongly Associated With Biochemical Recurrence After Radical Prostatectomy for All Preoperative Risk Categories. The Journal of Urology 179(6), 2212–2217 (2008)

[16] Ayyathurai, R. et al.: Factors Affecting Erectile Function After Radical Retropubic Prostatectomy: Results from 1620 Consecutive Patients. British Journal of Urology International 101(7), 833–836 (2008)

Skill Assessment with Proximal Force Sensing for Endovascular Catheterisation

H. Rafii-Tari[1], C.J. Payne[1], C. Riga[2], C. Bicknell[2], S.-L. Lee[1], G.-Z. Yang[1]

[1]The Hamlyn Centre for Robotic Surgery, Imperial College London, UK

[2]Academic Division of Surgery, Imperial College London, UK

{h.rafii-tari11, christopher.payne04}@imperial .ac.uk

INTRODUCTION

Due to potential advantages including reduced radiation exposure and increased stability of motion for the operator, robotic catheter navigation systems have attracted a growing interest for endovascular intervention [1]. However, most of these systems have been designed with little consideration of operator tool forces and skills, and limited studies have looked at operator behavioral data such as finger motion or catheter kinematics and dynamics [2, 3]. This paper proposes a framework for detailed analysis of operator skills, navigation cues, and manipulation strategies by using a force-torque sensor attached to the proximal end of the catheter together with a position sensor at the catheter tip for relating tool forces to tip motion. Further detailed understanding of force and motion patterns used by experienced operators during endovascular procedures is necessary for designing ergonomic catheter navigation systems, while utilizing the natural bedside catheterization skills of the operators.

MATERIALS AND METHODS

The design of the sensor and experimental setup were presented in [4] and are shown in Fig. 1. The miniature sensor measures forces (push and pull) and torques (cw and ccw) applied by the operator at the proximal end. The operator manipulates an overtube which transmits the loads to the transmission component, consisting of four load cells. A spring loaded clamp affixes the catheter to the casing and allows the operator to place the sensor anywhere along the length of the catheter.

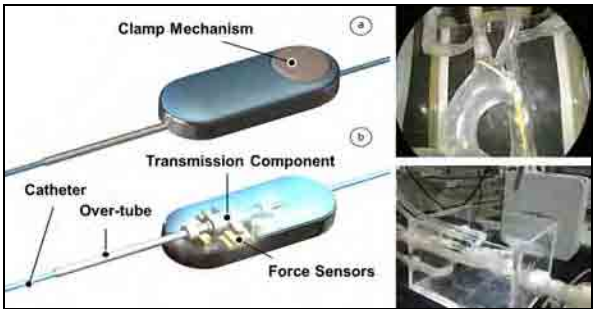

Fig. 1 Left: Force sensor mounted on the catheter top view (a) and bottom view (b) with the transmission component. Right: 2D projected phantom image and experimental setup.

Eight operators of varying endovascular experience (3 experienced and 5 inexperienced) were recruited for that study. Each was asked to cannulate the right common carotid artery in a transparent anthropomorphic phantom of a type I aortic arch three times. Catheter tip positions were obtained from a 6DOF electromagnetic position sensor attached to the tip. The procedure path was divided into three phases: the descending aorta (phase A), the aortic arch (phase B), and cannulation of the right common carotid artery (RCCA) ostium (phase C). Different performance metrics including tip displacement and velocity, mean forces and torques, sum of displacement (motion efficiency), number of twists and time were measured for each section of the procedure.

We investigate in this study by assessing other metrics including tip acceleration and smoothness of motion. A more detailed comparison of skill related patterns is performed using dynamic time warping (DTW) to allow non-linear synchronization and mapping of the signals within a common timeline between one of the most experienced and one of the least experienced operators. Differences between these are assessed using nonparametric analysis (Kruskal-Wallis test, $P < 0.05$). Further information on hand motion patterns are also obtained through attaching electromagnetic position sensors to the thumb and index finger of a single experienced interventionalist.

RESULTS

The results of DTW (Fig. 2) show distinct differences between experienced and inexperienced operators in terms of catheter tip motion, and the magnitude of forces and torques at the proximal end. The figure depicts a smoother motion pattern and less excessive movements for experienced operators. Significant push forces are seen in phase A during catheter advancement within the descending aorta, while in phases B and C torque is preferentially used to avoid contact with the vessel wall which may result in vessel trauma and embologenic sequelae. By examining the boundary conditions, it can be seen that experienced operators use push forces to enter the aortic arch curvature (between phases A and B), whereas for cannulation of the target vessel (from phase B to C) operators are mainly relying on torque.

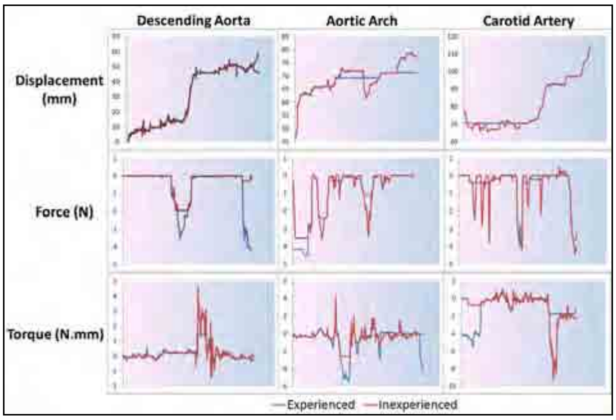

Fig. 2 Synchronised signals from DTW are shown for an experienced vs. inexperienced operator over each section of the procedure.

Table 1 shows significant differences between the experienced and inexperienced operator for the mean values of the metrics for each procedural phase. Further differences are observed in the high-risk areas (Aortic arch and RCCA) where experienced operator's superior skill is evident. The results illustrate that skilled operators rely mainly on torque, whilst achieving increased catheter displacement with smoother, less repetitive and faster motion, and thereby with higher efficiency and gain.

Table 1 Mean Values for Statistically Significant Differences between Metrics for Experienced versus Inexperienced Operators

Section	Metric	Exp.	Inexp.
Descending Aorta	Displacement (mm)	33.2	17.8
	Smoothness (mm)	342.6	529.4
Aortic Arch	Force-push (N)	2.58	0.70
	Torque – ccw (N.mm)	1.42	0.30
	# Twists	10	47
RCCA	Displacement (mm)	89.6	76.3
	Sum displacement (mm)	$9.7x10^4$	$1.9x10^5$
	Smoothness (mm)	90.5	235.2
	Torque – ccw (N.mm)	2.50	1.54
	# Twists	10	72
	Time (s)	27.0	62.7

Maximum catheter tip accelerations (on average) over all the procedures for each of the three phases were 16369.7 mm/s^2 in phase A, 10885.9 mm/s^2 in phase B, and 9185.0 mm/s^2 in phase C, for experienced operators. The corresponding values for inexperienced operators were 19436.3 mm/s^2 in phase A, 11109.7 mm/s^2 in phase B, and 15033.3 mm/s^2 in phase C, depicting smoother motion for experienced operators over all three phases of the procedure.

The average speed of motion for the thumb and index finger for a single experienced operator are given in Table 2. The speed is lower in the aortic arch and RCCA, further demonstrating dexterous operator skills in higher risk areas.

Table 2 Average Speed at Thumb and Index Finger Measurements for the Experienced Operator

	Mean thumb speed (mm/s^2)	Mean index speed (mm/s^2)
Descending Aorta	46.1	45.0
Aortic Arch	32.0	31.8
RCCA	35.2	34.9

The median force and torque values for all operators over each procedural phase are depicted in Fig. 3; significant differences in the use of catheter rotation compared to push forces between experienced and inexperienced operators are shown.

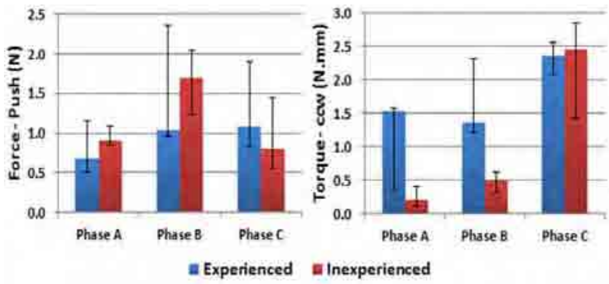

Fig. 3 Median force and torque values between groups are shown. Error bars represent the interquartile ranges.

DISCUSSION

This paper builds on our previous study using position trackers and a miniaturized proximal sensing platform for measuring detailed motion, force and torque profiles during endovascular procedures [4]. An in-depth comparison of force and motion patterns and skills between experienced and inexperienced operators is provided. DTW techniques were used for synchronization and detailed comparison of signals. Different performance metrics, including catheter tip velocities, accelerations, and motion smoothness were compared against forces and torques applied at the proximal end of the endovascular catheter. Information on finger motion patterns for an experienced operator was also provided. These results offer valuable insights into endovascular skill and navigation cues of operators, which can be valuable as design specifications for optimized robotic catheter navigation systems.

REFERENCES

[1] Riga CV, Bicknell CD, Hamady MS, Cheshire NJW. Evaluation of robotic endovascular catheters for arch vessel cannulation. J Vasc Surg 2011;54(3): 799-809.

[2] Srimathveeravalli G, Kesavadas T, Li X. Design and fabrication of a robotic mechanism for remote steering and positioning of interventional devices Int J Med Robot Comp 2010;6(2): 160-170.

[3] Thakur Y, Holdsworth DW, Drangova M. Characterization of catheter dynamics during percutaneous transluminal catheter procedures. IEEE Trans Biomed Eng. 2009;56(8): 2140-2143.

[4] Rafii-Tari H, Payne CJ, Riga C, Bicknell C., Lee SL, Yang GZ. Assessment of Navigation Cues with Proximal Force Sensing During Endovascular Catheterization. MICCAI 2012. *Accepted.*

SurgTrak: Synchronized Performance Data Capture for the da Vinci Surgical Robot

L. W. White[1], T. M. Kowalewski[2], B. H. Hannaford[2], T.S. Lendvay[3]

[1]*BioEngineering Department, University of Washington, USA*

[2]*Electrical Engineering Department, University of Washington, USA*

[3]*Department of Urology, University of Washington, USA*

leewhite@uw.edu, tmk@uw.edu, blake@uw.edu, Thomas.lendvay@seattlechildrens.org

INTRODUCTION

Rapid adoption of surgical robotics may be outpacing the ability to adequately train and maintain robotic skills. Tracking objective performance metrics of robotic surgery is paramount to ensuring safe and effective robotic surgery education and practice. Although easy to track in virtual reality (VR) simulators, performance metrics such as economy of motion, tool position and path length, and instrument grasp force data are difficult to capture from the da Vinci robot due to its closed Application Programming Interface (API) access. Thus methodologies to provide users and educators with objective metrics tracking synchronized to high definition video data for robotic surgery are required. We have developed such technology and have successfully demonstrated the ability to discriminate user skill levels.

MATERIALS AND METHODS

SurgTrak was initially developed to track surgical tool motion on the da Vinci surgical robot [1]. Since then we have added the ability to wirelessly record data streams from additional sources including electroencephalogram (EEG) and surgeon hand motion [2]. SurgTrak has also been adapted to record surgical motion data from all existing da Vinci models: Standard, S and Si models. The current system records any combinations of the following data sources:

- Surgical tool and endoscope motion – position and orientation is captured using a 3D Guidance trakSTAR magnetic tracking system (Ascension Technology Corporation), end-effector/grasper is tracked using custom electronics and a PhidgetInterfaceKit 8/8/8 (Phidgets Incorporated).
- Wireless tracking of end-effector pose (shown in Figure 1) is enabled by custom electronics featuring an Atmel ATMega328 microprocessor running the Arduino bootloader and an XBee wireless communication link.
- Video tracking – an Epiphan DVI2USB device (Epiphan Systems Incorporated) is used to record full resolution HD video from the either/both DVI outputs on the back of the da Vinci console. This enables user performance data such as tool and camera clutching or cautery activation to be synchronized with video data.
- Audio recording – From surgeon's console or other operating room sources or a simple microphone.
- Wireless hand motion tracking - AcceleGloves (Anthrotronix, Inc.).
- EEG brain monitoring for surgeon engagement, distraction, and cognitive workload – recorded wirelessly using a B-Alert X10 system (Advanced Brain Monitoring, Inc.).
- Any data source using the Transmission Control Protocol (TCP) or User Datagram Protocol (UDP).

The SurgTrak user interface is written in Visual C++ and is a flexible platform for expanding to new data sources. Measures of surgical skill (path length, economy of motion and task time) recorded by SurgTrak were shown to demonstrate construct validity by correlating with surgeon experience [3]. (Figure 2.)

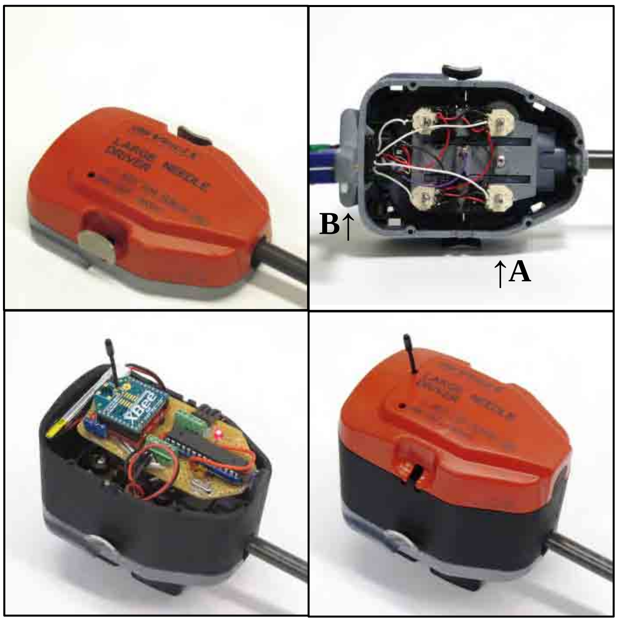

Fig. 1 (top left) da Vinci Large Needle Driver wihout modification, (top right) tool internal components including (A) potentiometers to measure spindle angles and (B) electromagnetic tracking element, (bottom left) Electronics for wireless end-effector tracking, (bottom right) complete tool.

RESULTS

SurgTrak has been used in three major studies to collect surgical performance data including 1) a recently completed study of the effect of warming up for surgery using a virtual reality simulator for dry lab tasks on the da Vinci robot, 2) a study of surgical skills of users performing robotic bladder cystotomy closures on a live porcine model and, 3) the potential benefit of VR warm-up on robotic-assisted prostatectomy procedures in humans. (See Tables 1 and 2.)

Table 1. Types of data recorded in completed and ongoing studies of surgical performance.

Data Type	Warm-Up	Cystotomy	EEG
Tool Motion	X	X	
End-Effector Tracking	X	X	
HD Video (including tool clutch, camera clutch and cautery use)	X	X	X
Hand Motion		X	
EEG			X

The objective of the three studies has been to elucidate the potential benefit of VR-based training and warm-up on surgical performance.

Table 2. Total number of sessions recorded by study using SurgTrak. FLS = Fundamentals of Laparoscopic Surgery.

Study	Warm-Up	Cystotomy	EEG
Rocking Peg Board	664		
FLS Intracorporeal Suturing Task	428		
Ring Tower	350		
FLS Block Transfer	183		
Bladder Cystotomy Closure (Porcine)		8	
Robot-Assisted Radical Prostatectomy (Human Patients)			2

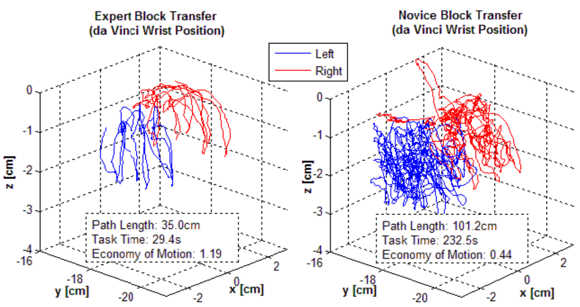

Fig. 2 (Left) Toolpath of an expert surgeon performing the FLS block transfer task and (Right) toolpath of a novice surgeon.

Fig. 3 (Left) View through the endoscope of a surgeon performing the FLS block transfer task. (Right) 3D rendering of the surgical tools and toolpath at the same moment based on a 3D model of the surgical tools and recorded position, orientation and end-effector pose data.

DISCUSSION

Collecting multiple streams of synchronized data is fundamental to objective surgical performance analysis. Our system enables flexible recording of many types of data from a variety of sources in formats enabling analysis by machine learning algorithms. Our solution includes both hardware and software components and both custom and off-the-shelf tracking sensor implementations are used.

REFERENCES

[1] White LW, Kowalewski T, Hannaford B, Lendvay TS. SurgTrak: Affordable Motion Tracking and Video Capture for the Da Vinci Surgical Robot. In: Society of American Gastrointestinal and Endoscopic Surgeons, Proceedings of the 2011 Meeting of the SAGES, San Antonio, Texas. vol. 1; 2011. p. 204.

[2] White LW, Kowalewski T, Hannaford B, Lendvay TS. SurgTrak: Evolution of a Multi-Stream Surgical Performance Data Capture System for the da Vinci Surgical Robot. Engineering and Urology Society. 2012; Submitted.

[3] Tausch TJ, Kowalewski TM, White LW, McDonough PS, Brand TC, Lendvay TS. Content and Construct Validation of Robotic Surgery Curriculum Using an Electromagnetic Instrument Tracker. Journal of Urology. 2012; #JU-12-159R1, (In Press).

AKNOWLEDGEMENTS

This technology was in part made possible with the support of the US Army Medical Research and Materiel Command Award # W81XWH-09-1-0714. Opinions, interpretations, conclusions, and recommendations are those of the authors and are not necessarily endorsed by the U.S. Army.
The authors would like to thank the numerous undergraduate researchers who have contributed to this work.

Minimally Invasive Surgical Skill Assessment by Video-Motion Analysis

Seung-kook Jun[1], Madusudanan Sathia Narayanan[1], Abeer Eddib[2], Pankaj Singhal[2], Sudha Garimella[1], Venkat Krovi[1]
[1]University at Buffalo, SUNY, Buffalo NY 14260
[2]Kaleida Health System, Buffalo, NY 14221 USA
vkrovi@buffalo.edu

INTRODUCTION

Surgical skill assessment and clinical evaluation has predominantly remained subjective [1] and developing quantitative assessment tools has become a topic of considerable importance [2]. Key challenges to assessment and accreditation of surgeons include (i) creating appropriate clinically-relevant scenarios and settings and (ii) developing uniform, repeatable, stable, verifiable performance metrics; at manageable financial levels for ever increasing cohorts of trainees. We posit that an imperfect and incomplete understanding of the underlying relationships, coupled with insufficient computational support has led to assessment regimen focused on easy-to-measure, quantitative but simplistic spatially- and temporally-aggregated measures [3].

Dexterous manipulative skill evaluation using micro-motion studies [4, 5], has roots in manipulative performance-evaluation in manufacturing industries. In this manuscript, we examine the extension of this traditional motion-study methodology to encompass assessment of minimally-invasive surgical (MIS) procedures from videorecordings. The study was conducted for representative surgical manipulation exercises (peg board and pick-and-place) on a da Vinci surgical SKILLS simulator (dVSS-Si) with a list of predefined "*Therbligs*" in order to prove its usefulness for real surgical implementation. Performance metrics were also obtained, including intra- and inter-user performance variance, by analyzing surgeons' performance over each sub-procedure.

BACKGROUND

Numerous objective methods for assessing technical skills are being considered for use in many surgical training programs today. The Objective Structured Assessment of Technical Skills (OSATS) as well as Objective Structured Clinical Examination (OSCE) emphasizes the quantitative assessment processes without relying on expert evaluators using appropriate hardware (measurement device) such as Imperial College Surgical Assessment Device (ICSAD) and Advanced Dundee Endoscopic Psychomotor Trainer (ADEPT). While the collection of quantitative raw physical measurements is very desirable, we posit that the oversimplification inherent in using aggregated measures may result in loss of desirable user-specific discriminative characteristics. Consequently, the use of such aggregated metrics (without repeatability, stability and potentially validity) to steer entire training regimen may lead to undesirable and unforeseen consequences.

Several studies in the recent past also showed that segmenting the surgical videos into sub-tasks (defined as surgemes in [2]) can aid in automated performance and skill assessment. One of the most relevant work along this aspect has been the automated motion recognition using Hidden Markov Modeling (HMM) [6] for simulated surgical tasks using da Vinci Trainer (dV-Trainer). Nonetheless, the basis and requirements of the surgical task-segmentation has not been adequately dealt with. It is essential to define these building blocks in a generalized manner, so as to allow not only segmentation and further analysis of complex surgical procedures, but also to establish clinically meaningful and relevant metrics for skill and expertise.

MOTION STUDIES

In this work, we seek to examine the applicability and usefulness of micro-motion studies to assess robotic-surgical performance and help create a viable quantitative basis for grounding the training process. At its core, these *Therbligs* allow for decomposition of a large complex manual job sequence into sub-parts that could then be individually examined. This decomposition allows for a finite state automaton representation of a complex activity that could provide linguistic representation as well as fault-detection. A detailed list of *Therblig* vocabulary extended to surgeries is discussed in detail in our prior work [7, 8]. 3D motion capture techniques are widely used in the field of biomechanics and robotics to accurately estimate the kinematics of a system – we use this modality to 'digitize' the videos to obtain raw quantitative manipulative-performance information.

EXPERIMENTAL SETUP

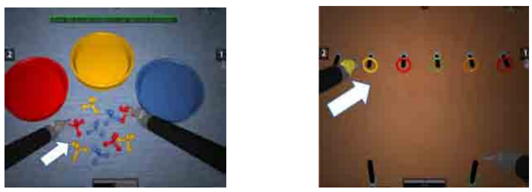

(a) (b)

Fig. 1 (a) Pick and Place (PnP) (b) Peg Board I (PegI)

In this study, the dVSS-Si with its SKILLS simulator [9] provided a standardized testbed, see Fig. 1. Since, our primary objective was to develop skill assessment methods for a generic surgical task, only the video feeds were used as input to our evaluation scheme, without requiring any information from the robotic system.

RESULTS

Using the motion analysis methods, the kinematic estimates (Cartesian positions and velocities) of virtual surgical tools were obtained [8]. Though, at present it involves manual placement of markers, pose-tracking methods are being developed to aid automated estimation of uncertain poses directly from videos.

Table 1 Automated Therblig Recognition Rates

	Pick and Place		Peg Board	
E_1 (expert)	86.3%	79.6%	77.8%	80.7%
E_2(expert)	83.1%	88.7%	74.3%	67.8%
I_1(intermediate)	77.4%	72.1%	70.4%	74.9%
I_2(intermediate)	49.7%	75.8%	52.3%	76.4%
N_1(novice)	60.0%	64.2%	63.5%	62.5%
N_2(novice)	67.2%	72.4%	70.2%	67.9%

AUTOMATED THERBLIG RECOGNITION

Based on the computed 3D trajectories for each task and each subject, a decision-tree type classification scheme is established in order to conduct studies for automated recognition of *Therbligs*. The four primary variables found to be effective for automated determination of these *Therbligs* are: tool position & velocity (translation component only) and tool finger tip. The recognition performance of *Therbligs* was determined for each case and summarized in Table 1. However, additional kinematic information extracted from the videos could be used to improve the accuracy of automated classification in future studies.

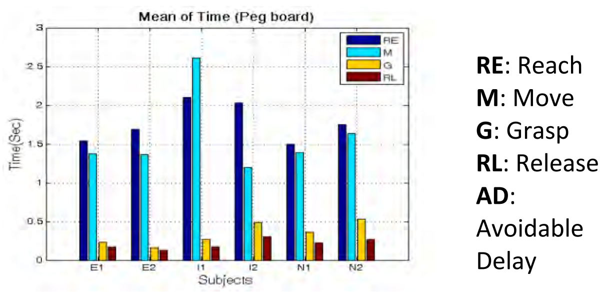

Fig. 2 Skill Estimation for Pick-and-Place Task

Table 2 Inefficient Therbligs and Bimanual Synchronization for Peg Board Tasks

	AD (sum)	Inefficient	Synchronized
E_1 (expert)	17.8%	27.9%	65.4%
E_2(expert)	18.4%	25.1%	64.9%
I_1(intermediate)	25.9%	41.8%	50.6%
I_2(intermediate)	36.2%	39.9%	56.9%
N_1(novice)	26.4%	34.1%	55.0%
N_2(novice)	33.6%	45.8%	37.7%

Comparing the estimated *Therblig* cycles with a standard template, it is possible not only to evaluate the effectiveness and efficiency of each motion elements but also identify bimanual synchronization and ineffective motion measures in order to quantify and evaluate surgical expertise. The skill identification results for surgeons with different levels of experience and expertise for Peg board task is shown in Fig. 2. By building on top of our motion bases, it is now possible to define newer metrics that is related to both the experience and expertise of surgeons and trainees as in Table 2. We note that avoidable delays (AD) and inefficient motions decrease with increase in expertise. In addition, bimanual synchronization which is a form of quantified measure for surgical dexterity is observed to vary with skill expertise.

DISCUSSION

These preliminary studies helped us gain insight into skill-evaluation, based on dexterity as well as motion economy, at the micro-motions level. In addition to applying for simulated tasks, the power of *Therbligs* was demonstrated by using it for a real-robotic surgical scenario [7]. It should also be noted that complete set of 2D and 3D kinematic data estimated from stereoscopic feeds (obtained from dVSS-Si as well as other commercial trainers) has not yet been incorporated into our analysis. With this additional information not only the discriminative performance of our method is expected to improve further but also makes it possible to implement automated recognition of these *Therbligs* from the kinematic data. Current studies on extending this framework to accommodate natural variance between users and tests via stochastic sampling methods are already underway.

REFERENCES

[1] Tsue, T.T., J.W. Dugan, and B. Burkey, *Assessment of Surgical Competency.* Otolaryngologic clinics of North America, 2007. **40**(6): p. 1237-1259.

[2] Reiley, C., et al., *Review of methods for objective surgical skill evaluation.* Surgical Endoscopy, 2011. **25**(2): p. 356-366.

[3] Lerner, M.A., et al., *Does training on a virtual reality robotic simulator improve performance on the da Vinci surgical system?* Journal of Endourology, 2010. **24**(3): p. 467-72.

[4] Salvendy(ed), G., *Handbook of Industrial Engineering: Technology and Operations Management*, ed. G. Salvendy. 2001: Wiley-Interscience.

[5] Barnes, R.M., *Motion and Time Study: Design and Measurement of Work.* August 1980, Univ. of California, Los Angeles: Wiley.

[6] Rosen, J., et al., *Generalized approach for modeling minimally invasive surgery as a stochastic process using a discrete Markov model.* Biomedical Engineering, IEEE Transactions on, 2006. **53**(3): p. 399-413.

[7] Jun, S.-K., et al. *Evaluation of Robotic Minimally Invasive Surgical Skills using Motion Studies.* in *Performance Metrics for Intell. Systems Workshop (PerMIS'12)*. 2012.

[8] Jun, S.-K., et al. *Robotic Minimally Invasive Surgical Skill Assessment based on Automated Video-Analysis Motion Studies.* in *4th IEEE RAS/EMBS International Conference on Biomedical Robotics and Biomechatronics: Surgical Robotics Symposium*. 2012. Roma, Italy.

Eye-Tracked Vergence Response During Active-Stereo Display

A.T. Duchowski, B. Pelfrey, D.H. House, R. Wang

School of Computing, Clemson University
duchowski@clemson.edu

INTRODUCTION

This paper extends previous work concerning measurement of gaze depth with an eye tracker during stereoscopic display. Earlier work demonstrated eye vergence response during stereoscopic scene viewing using a Wheatstone-type haploscope [1,2]. Here, we show that vergence reacts similarly during stereoscopic scene viewing using an active-stereo display.

Fig. 1 Measuring gaze with a Mirametrix binocular eye tracker when viewing an active stereo display.

MATERIALS AND METHODS

The purpose of the study was to measure the error between vergence (estimated *z*-component of the viewer's gaze coordinates) and the stereographically projected depth of an arbitrary screen object (a small sphere in this case). While two-dimensional gaze position estimation by an eye tracker is common, estimation of vergence is not, much less so when using active stereo shutter glasses. The experiment conducted tested whether: (a) the eye tracker could continue to function in the presence of the shutter glasses, and (b) estimated gaze depth was as reliable as when obtained previously with our Wheatstone apparatus.

Active stereo display was rendered by an NVidia Quadro 6000 graphics card installed in an Intel Xeon 5130 Quadcore PC running CentOS. The display used was a Samsung SyncMaster 2230 running at 120 Hz, and it was viewed by wearing active stereo shutter glasses included in NVidia's 3D Vision Pro Kit. The Pro Kit synchronizes the shutter glasses to the display via a radio frequency transmitter, which does not interfere with the near-infra-red light source used by the eye tracker (see Fig. 1). Note that our first attempt with NVidia's 3D Vision Kit was not successful as this consumer-level kit uses an infra-red transmitter for synchronization which does interfere with the eye tracker. The eye tracker used was the S1 model from Mirametrix. The monitor was set to 1680×1050 resolution (476×292 mm physical screen dimensions).

The Mirametrix eye tracker, using a single camera sampling at 60 Hz, measures binocular gaze position, from which an estimate of gaze depth is derived [3]. For vergence measurement, a two-step eye tracker calibration procedure is required. First, two-dimensional calibration is conducted following traditional display of 5 points on the screen. Second, calibration of the gaze depth estimate (gaze *z*-coordinate) was performed with a single small sphere shown to the viewer as the sphere spiraled through positions varying in the *xy*-plane as well as depth, as shown in Fig. 2. A similar but post-hoc *z*-coordinate data fitting procedure was used previously [2].

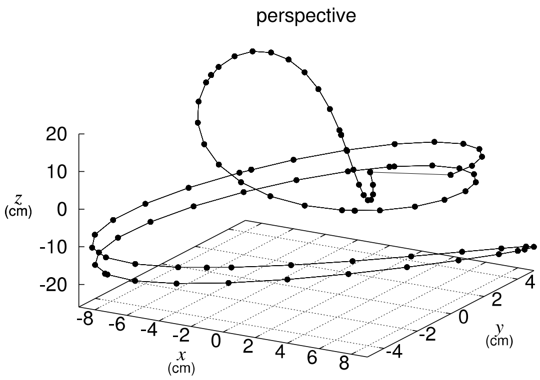

Fig. 2 Volume through which a small sphere was animated to effect 3D depth calibration.

The task given to viewers was to fixate a highlighted sphere in a field of spheres shown on an inclined plane that, when projected, extended from z = 20 cm in front of the screen to z = -20 cm receding into the screen (using a right-handed coordinate system); see Fig. 3.

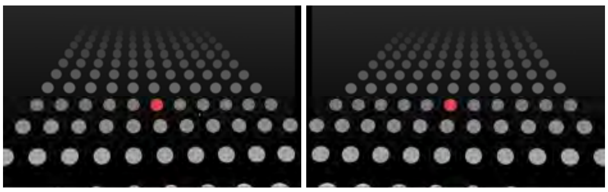

Fig. 3 Left and right projections of stereo stimulus.

RESULTS

Results of gaze depth estimation, following filtering by a 6th order Butterworth filter whose cutoff frequency was set to 0.15 Hz against the tracker's sampling frequency of 60 Hz [2], are reported in terms of mean root-mean-squared (RMS) error of the (squared) difference between measured gaze depth and the known depth of the projected target. RMS error was calculated at each of 5 depth levels (z = -20, -10, 0, 10, 20 cm) for each of 8 of our participants. A representative example of data collected from an individual is shown in Fig. 4.

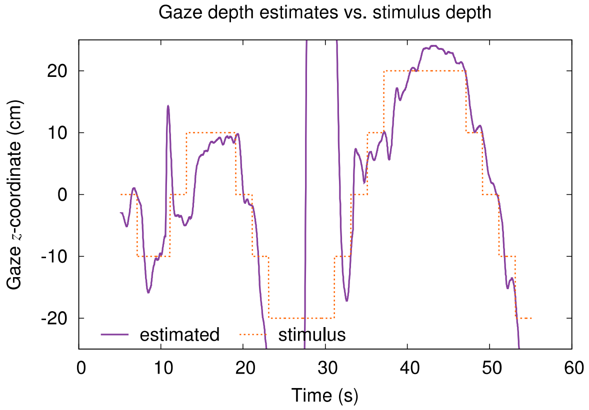

Fig. 4 Representative example of gaze depth measured for an individual. The red trace shows the depth of the target object, the green trace shows the measured depth of gaze.

Treating the known depth as a fixed factor (of 5 levels), with mean RMS error serving as the random factor, a repeated-measures ANOVA reveals a marginally significant effect of stereoscopic depth on RMS error ($F(4,28) = 3.30$, $p < 0.05$). In-line with previous results with the Wheatstone haploscope, and as shown in Fig. 5, RMS error tends to increase proportionately with projected stereo distance from the screen (i.e., either in front or behind the screen).

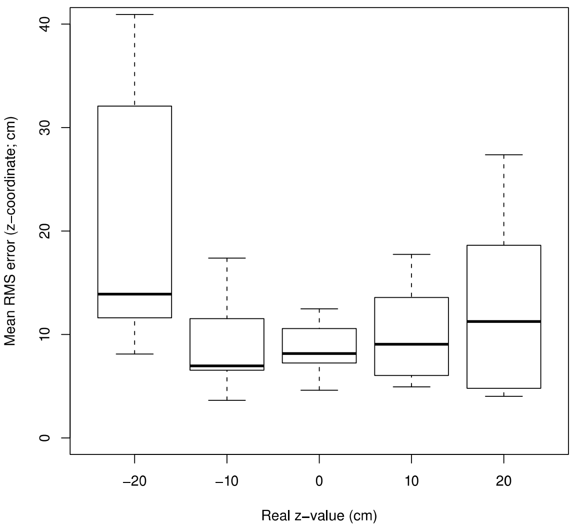

Fig. 5 Mean RMS error per stereo depth.

DISCUSSION

Results of vergence measurement using an active stereo system are consistent with those obtained with our Wheatstone-style haploscope. In both instances, measured vergence response is unexpectedly noisy, and in both reports vergence is subject to filtering by the Butterworth filter.

The Wheatstone haploscope requires that binocular eye tracking optics are split apart so that the tracker operates as a combination of two tracking units. Results of the present experiment show that more common, but still binocular, eye trackers can be used with an active stereo display to measure vergence response. However, increasing disparity beyond ±20 cm either in front of or behind the screen plane is likely to increase vergence error. Anecdotally, although vergence is more readily measured during convergence (projection in front of the screen), objects shown at +20 cm were difficult to fuse. This suggests a potential tradeoff: "fishtank" stereoscopic displays (stereo effect behind the screen plane) may be easier for viewers to fuse, but measurement of vergence is likely to be less accurate.

These results have implications for stereoscopic displays, whether viewing tomographic content or content obtained through telerobotic stereo cameras, where disparity beyond ±20 cm may lead to discomfort when viewing outside this range [4].

ACKNOWLEDGMENTS

This material is based upon work supported by the National Science Foundation under Grant No. 0915085. Any opinions, findings, and conclusions expressed in this material are those of the author(s) and do not necessarily reflect the views of the NSF. We are grateful to NVidia for their generous equipment donations.

REFERENCES

[1] Wheatstone, C. Contributions to the physiology of vision. Part the first. On some remarkable and hitherto unobserved phenomena of binocular vision. *Philosophical Transactions of the Royal Society*. 1838; 128: 371-394.

[2] Duchowski, A. T., Perlfrey, B., House, D. H. & Wang, R. Measuring Gaze Depth with an Eye Tracker During Stereoscopic Display. In *Proceedings of the Symposium on Applied Perception in Graphics and Visualization (APGV)*. Toulouse, France, 2011.

[3] Daugherty, B. C., Duchowski, A. T., House, D. H., & Ramasamy, C. Measuring Vergence Over Stereoscopic Video with a Remote Eye Tracker. In *Proceedings of the Symposium on Eye Tracking Research & Applications (ETRA)*, Austin, TX, 2010.

[4] Shibata, T., Kim, J., Hoffman, D. M., and Banks, M. S. The zone of comfort: Predicting visual discomfort with stereo displays. Journal of Vision, 2011: 11(8): 1-29.

Intraoperative Analysis of Locations for 3D Ultrasound-Guided Capture of Foreign Bodies from a Beating Heart

Paul Thienphrapa[1,2,*], Bharat Ramachandran[2], Haytham Elhawary[2], Aleksandra Popovic[2], Russell H. Taylor[1]

[1]*ERC CISST/LCSR, Johns Hopkins University;* [2]*Philips Research North America*
[*]*pault@cs.jhu.edu*

INTRODUCTION

Free moving foreign bodies in the heart pose serious health risks, having the potential to cause arrhythmia, occlusion, and even death[1,2]. The condition is common in both civilian and military populations[3,4]. Thrombi can emerge following myocardial infarction, and debris can enter heart through the venous system after a soft tissue injury in the chest, abdomen, or extremities. Small caliber bullets and small shell fragments with low velocity tend to circulate freely in the right atrium and can become entrapped in the pericardial trabeculations and fatty tissue[2]. Symptomatic, free moving cardiac foreign bodies must be removed surgically.

Treatment traditionally involves open surgery via median sternotomy and incision of the pericardium to expose the pertinent heart chamber[3,5-7]. The highly invasive procedure requires a long recovery period and incurs numerous risks, such as bacterial mediastinitis, inflammation, and bone fracture. A standard surgical setting may employ cardiopulmonary bypass (CPB), which introduces additional health risks.

We propose a minimally invasive surgical approach using an image-guided robotic end effector, to avoid the disadvantages of sternotomy and CPB. In the envisioned scenario (Fig. 1), a robotic tool is inserted transapically into the heart after detection of the foreign body using preoperative imaging. Under intraoperative ultrasound guidance, the robot moves to secure the target.

In previous work we used 3D transesophageal echocardiography (TEE) to track a foreign body in a beating heart phantom; results suggest that the abrupt, irregular motion of a cardiac foreign body precludes robotic retrieval based on direct pursuit of the projectile. We thus proposed to have the robot wait at a *capture location* and ambush the particle upon its arrival. Salient capture locations were considered based on spatial probability[8], dwell time, and visit frequency[9] to support the viability of the approach. In this work, we address the irregular nature of the motion by examining the time dependency of the capture location measurements. Our study is aimed at quantifying the tracking duration required to produce actionable estimates of capture locations, as well as determining the predictability of future figures based on past measurements. In a broader sense, improved understanding of the problem will aid in the design of retrieval systems and strategies.

This work was funded in part by Philips Research North America and in part by Johns Hopkins University.

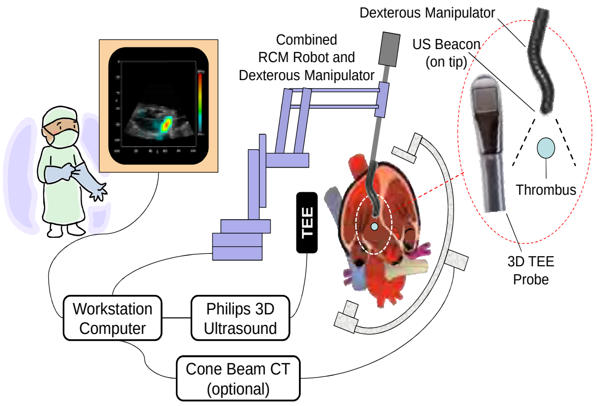

Fig. 1 Robotic fragment retrieval from the heart under 3D TEE guidance.

MATERIALS AND METHODS

As pictured in Fig. 2, the experimental setup consists of a Philips X7-2t 3D TEE probe and a heart phantom with programmable heartbeat in a water tank; a future goal is to transition to *in vivo* studies. A 3.2-mm steel ball representing a foreign body is placed in the phantom, and the scene is imaged using the probe at a rate of 20 volumes per second. Tracking of the foreign body is performed using a modified normalized cross-correlation method; previous reports[8] describe the setup in greater detail.

We previously defined different criteria for selecting a location at which to capture a cardiac foreign body, namely spatial probability, dwell time, and visit frequency, but reported measurements based on the full duration of the 20-second data sets (n=5). Here we present the time evolution of the figures in order to illustrate the intraoperative behavior of the foreign body and how the system might respond in real time.

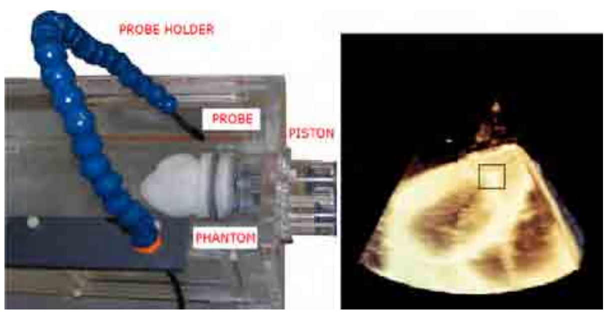

Fig. 2 (*Left*) Arrangement of the TEE probe and beating heart phantom; (*Right*) a sample 3D ultrasound image with foreign body outlined.

RESULTS

Spatial Probability: The spatial probability of foreign body location is given by the histogram of its positions over time. This metric reveals that the foreign body has preferential regions of presence, as depicted in Fig. 3 (*top row*). Fig. 4 (*top*) shows how the most probable location develops over time; on average, 18.5 seconds of tracking is needed until the most probable location reaches an estimate of 50%.

Dwell Time: A retrieval system may require that the foreign body remain at a location for a certain amount of time to facilitate capture. The dwell time of a location in the heart describes amount of time the foreign body is expected to remain there before ultimately leaving. Based on Fig. 4 (*center*), the most dwelled location can be determined after 6–8 seconds of tracking.

Visit Rate: On the other hand, a foreign body may be more amenable to capture while in transit; in this case the chance of success can be increased by determining the location that the object traverses most frequently, without regard to how long it remains there overall. Fig. 4 (*bottom*) indicates that such a measurement stabilizes after 14–16 seconds of tracking.

Table 1 lists minimum time intervals for which capture location measurements repeat, determined by dividing the data into equal time intervals and finding the maximum correlation between intervals. Spatial probability prediction requires a longer observation period, implying that the behavior is fairly consistent, albeit along varying trajectories. This is a preliminary finding to be more rigorously examined in the future.

DISCUSSION

Though a foreign body in the heart moves erratically, existence of special capture locations suggest the feasibility of using a slow robot to retrieve it. This work explores the real-time evaluation of these locations.

The results provide insight on the time required to discover capture locations, a possible issue being the linearly increasing spatial probability over the 20-seconddataset duration. Future work will examine the reachability of primary and secondary locations, as well as the tracking of heart walls to prevent damage by the robot.

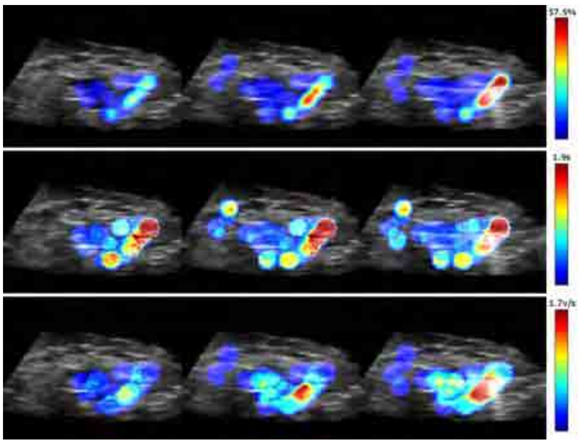

Fig. 4 Capture location values from left to right at *t*=6, 12, and 18 s. (*Top row*) Map of spatial probabilities, showing distinct regional preferences of the foreign body. (*Center row*) Map of dwell times showing faster evolution than spatial probability. (*Bottom row*) Map of visit rates; highly-traveled sections are not necessarily the most probable or most dwelled.

REFERENCES

[1] Marshall AJ, Ring NJ, Newman PL. An unexplained foreign body in the myocardium. J. Royal Soc. Med. 2002; 95: 250–251.

[2] Symbas PN, Picone AL, Hatcher CR, Vlasis-Hale SE. Cardiac missiles. A review of the literature and personal experience. Ann. Surg. 1990; 211(5): 639–48.

[3] United States Department of Defense. Emergency War Surgery: Third US Rev, s.l., 16: Thoracic Injuries 2004.

[4] Williams JC, Elkington WC. Slow progressing cardiac complications—a case report. J. Chiropr. Med. 2008; 7: 28–33.

[5] Actis Dato GM, Arslanian A, Marzio PD, Filosso PL, Ruffini E. Posttraumatic and iatrogenic foreign bodies in the heart: report of 14cases and review of the literature. J. Thorac. Cardiovasc. Surg. 2003; 126(2): 408–414.

[6] Evans J, Gray LA, Rayner A, Fulton RL. Principles for the management of penetrating cardiac wounds. Ann. Surg. 1979; 189(6): 777–784.

[7] Nessen SC, Lounsbury DE. War Surgery in Afghanistan and Iraq: A Series of Cases, 2003-2007, s.l. Department of the Army, Office of the Surgeon General and Borden Institute, 14: Thoracic Trauma 2008.

[8] Thienphrapa P, Elhawary H, Ramachandran B, Stanton D, Popovic A. Tracking and characterization of fragments in a beating heart using 3D ultrasound for interventional guidance. Medical Image Computing and Computer-Assisted Intervention 2011; 6891: 211–218.

[9] Thienphrapa P, Ramachandran B, Elhawary H, Taylor RH, Popovic A. Multiple capture locations for 3D ultrasound-guided robotic retrieval of moving bodies from a beating heart. SPIE Medical Imaging 2012; 8316.

Table 1 Minimum independent time intervals with repeating capture location estimates.

Spatial Probability	Dwell Time	Visit Rate
4.5 seconds	3.5 seconds	3.5 seconds

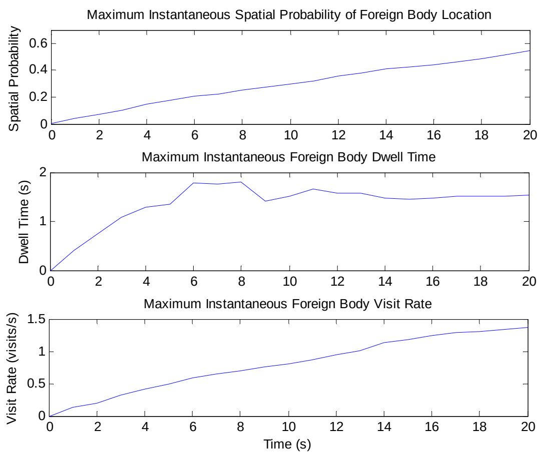

Fig. 3 Development of capture locations over time (averaged over five datasets). Previous work considered only the final estimates at *t*=20 s. (*Top*) Spatial probability. (*Center*) Dwell time. (*Bottom*) Visit rate; the slightly plateauing trend at *t*=14–16 s appears more clearly in plots of maxima, not shown here.

Fusion of Visual and Inertial Measurements for 3D Tissue Reconstruction in Minimally Invasive Surgery

Stamatia Giannarou, Zhiqiang Zhang, Guang-Zhong Yang

Hamlyn Center for Robotic Surgery, Imperial College London,
stamatia.giannarou@imperial.ac.uk

INTRODUCTION

In Minimally Invasive Surgery (MIS), 3D reconstruction of the operating field is essential for providing enhanced visual cues that aid the navigation and orientation during Natural Orifice Transluminal Endoscopic Surgery (NOTES) and for controlling the motion of surgical instruments by visual servoing in robotically assisted laparoscopic surgery. With increasing miniaturization and reliability of Microelectromechanical Systems (MEMS) based inertial sensors and gyroscopes, their integration with normal surgical instruments is a reality. The integration of information from vision and inertial sensing offers the possibility of developing more practical approaches for surgical scene reconstruction based on the complementary nature of these two sensing modalities.

The aim of this paper is to present a novel approach to robust 3D reconstruction of a surgical scene observed with a projective monocular camera. A novel adaptive Unscented Kalman Filter (UKF) parameterization scheme is proposed to fuse vision information with data from an Inertial Measurement Unit (IMU). A simplified UKF process model has been designed to reduce the computational complexity, thus making it more amenable to real-time implementation. Measurement drift of the inertial sensor is adaptively compensated and the UKF also incorporates angular velocity measurements from the gyroscope of the IMU. Detailed validation is provided on both synthetic and phantom data.

MATERIALS AND METHODS

For reliable content representation, affine-invariant anisotropic regions are tracked over a series of frames using an Extended Kalman Filter (EKF) parameterization scheme [1]. To avoid tracking across temporal discontinuities, coherent episodes which represent distinct surgical actions are detected [2]. Each surgical episode is reconstructed individually. In this work, the 5-point algorithm [3] is applied on the first and the last frame of a detected episode. For subsequent episode frames where the camera baseline is not wide enough for triangulation, the method switches to the PnP method proposed in [4] for perspective pose estimation in order to derive the relative camera pose. For outlier removal, both the 5-point algorithm and the PnP method are used in conjunction with Random Sampling Consensus (RANSAC). Each camera pose and the estimated structure are refined by an iterative non-linear optimization step on the inlier subset.

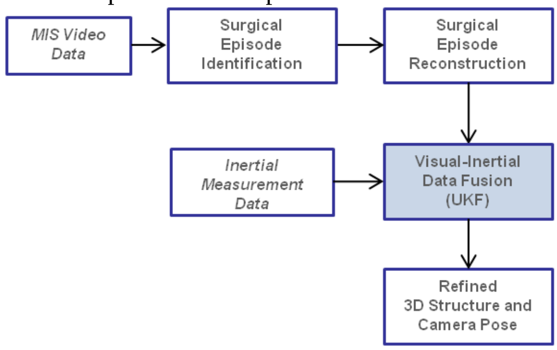

Fig. 1 Schematic representation of the proposed framework.

In order to further increase the robustness of the camera pose estimation, inertial and vision measurements are fused using the Unscented Kalman Filter (UKF) framework. The state of the system is composed of the position and orientation of the camera as $\left(b_t, \dot{b}_t, \ddot{b}_t, q_t\right)$, where b_t , $\dot{b}_t$, $\ddot{b}_t$ are the camera position, velocity and acceleration in the reference coordinate system, respectively. q_t is the orientation of the camera with respect to the reference coordinate system. The relationship between x_t and x_{t-1} can be written as $x_t = Fx_{t-1} + e_t$, where

$$F = \begin{bmatrix} I_{3\times3} & I_{3\times3}\Delta t & I_{3\times3}\,{\Delta t^2}/{2} & 0 \\ 0 & I_{3\times3} & I_{3\times3}\Delta t & 0 \\ 0 & 0 & I_{3\times3} & 0 \\ 0 & 0 & 0 & \Theta_t(\Delta t) \end{bmatrix}$$

Here, $I_{3\times3}$ is the identity matrix of order 3, Δt is the sampling rate, and e_t is the process noise which is assumed to be zero mean Gaussian noise with covariance matrix Q and

$$\Theta_t = \cos\left(\frac{|\omega_t|\Delta t}{2}\right)\cdot I_{4\times4} + \frac{1}{|\omega_t|}\sin\left(\frac{|\omega_t|\Delta t}{2}\right)\cdot \Re(\omega_t).$$

The position $z^{v}_{b,t}$ and orientation $z^{v}_{q,t}$ measurements obtained from the SFM and the acceleration $z^{imu}_{a,t}$ and orientation $z^{imu}_{q,t}$ measured by the accelerometer and gyroscope measurement integration, respectively, are combined in the following measurement model:

Table 1 Linear Regression Model parameters for camera pose estimation error using the Least Squares Method

	Varying Rotation and Constant Trans. Noise				Varying Trans. and Constant Rotation Noise			
	Rotation Error		Trans. Error		Rotation Error		Trans. Error	
	Regres. Coef.	*Intercept*	*Regres. Coef.*	*Intercept*	*Regres. Coef.*	*Intercept*	*Regres. Coef.*	*Intercept*
SFM	0.78	1.10	0	0.058	0.03	0.85	0.017	0
SFM+IMU	0.31	0.58	0	0.042	0.01	0.48	0.012	0

$$z_t = \begin{pmatrix} z^v_{b,t} \\ z^v_{q,t} \\ z^{imu}_{a,t} \\ z^{imu}_{q,t} \end{pmatrix} = h(x_t) + v_t = h(x_t) + \begin{pmatrix} v^v_{b,t} \\ v^v_{q,t} \\ v^{imu}_{a,t} \\ v^{imu}_{q,t} \end{pmatrix}$$

where v_t is assumed to be zero mean Gaussian noise with covariance matrix V. At slow motion, the MEMS accelerometer is unable to sense accurately the camera movement which is drowned in noise. In that case, the acceleration $\ddot{b}_t$ should be ignored for the measurement $z^{imu}_{a,t}$ estimation. In order to compensate the interference from the accelerometer an adaptive model is proposed for $z^{imu}_{a,t}$, defined as:

$$z^{imu}_{a,t} = \begin{cases} q_t^{-1} \otimes (\ddot{b}_t + g) \otimes q_t + v_{a,t} & \left\| \|g\| - \|z^{imu}_{a,t}\| \right\| > \varepsilon \\ q_t^{-1} \otimes g \otimes q_t + v_{a,t} & \text{otherwise} \end{cases}$$

$\varepsilon = 0.1g$ in our work. The proposed framework is illustrated in Fig. 1.

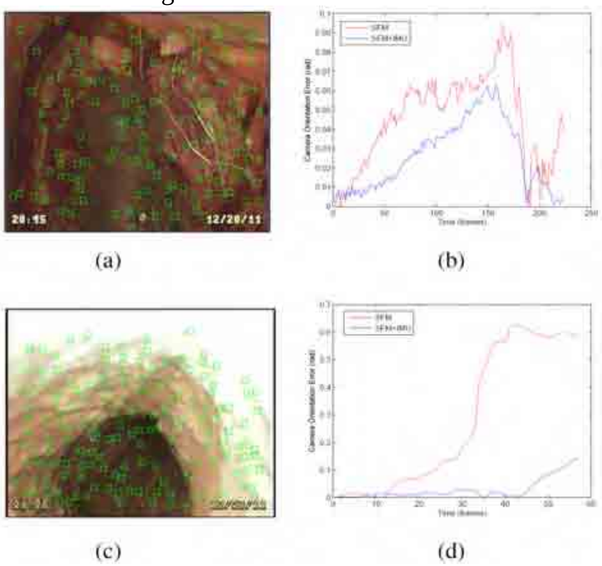

Fig. 2 (a) Sample frames with tracked points represented by green squares and (b) camera orientation error for the liver phantom data. (c) Sample frames with tracked points represented by green squares and (d) camera orientation error

RESULTS

The proposed framework had been validated on synthetic and phantom data. For the synthetic data, camera trajectories were generated using an optical tracking device (Northern Digital Inc., Ontario, Canada). To obtain the position of the camera, a rigid stereo laparoscope fitted with eight optical markers was used. IMU measurements were collected by attaching a Xsens IMU on the rigid body. Observation error was added to the camera trajectories in the x, y and z-axes, in the form of Gaussian noise with zero mean and standard deviation ranging from 0 to 15 mm. Gaussian noise with zero mean and standard deviation ranging from 0 to 0.25rad was also added to the camera orientation with respect to the x, y and z-axis. The camera rotational error is estimated as the smallest angle of rotation that can bring the estimate to the true value. The translational error is the deviation of the estimated translation direction from the true value. For performance evaluation, the parameters of the Linear Regression Model fitted to the pose estimation error for varying noise are presented in Table 1.

Phantom data was generated using the liver phantom shown in Fig. 2(a) and a laparoscope navigating around it. Ground truth data was collected using an optical tracking device, as explained above. With the proposed adaptive fusion method the mean surface reconstruction error is reduced from 9.53mm (SFM) to 5.16mm (SFM+IMU) and the camera rotation error for the two methods is compared in Fig. 2(b). The robustness of the proposed framework in a more challenging navigation environment such as the colon phantom in Fig. 2(c) is shown in Fig. 2(d).

DISCUSSION

A novel approach for fusion of vision and inertial measurement data has been proposed to facilitate surgical navigation in MIS. This represents one of the first attempts to combine vision and inertial sensing for robust reconstruction in MIS. Results derived from validation on synthetic and phantom data demonstrate the intrinsic accuracy achievable and the potential clinical value of the technique. A direct application of the proposed framework is free-form deformation recovery to enable adaptive motion stabilization and visual servoing in robotically assisted laparoscopic surgery.

REFERENCES

[1] Giannarou, S., Visentini-Scarzanella, M., Yang, G.Z.: Probabilistic tracking of affine-invariant anisotropic regions. IEEE Trans. Pattern Anal. Machine Intell. (2012) to apprear.

[2] Giannarou, S., Yang, G.Z.: Content-based surgical workflow representation using probabilistic motion modeling. In: International Workshop on Medical Imaging and Augmented Reality. (2010) 314–323

[3] Nister, D.: An efficient solution to the five-point relative pose problem. IEEE Trans. Pattern Anal. Machine Intell. 26(6) (June 2004) 756–770

[4] Moreno-Noguer, F., Lepetit, V., Fua, P.: Accurate noniterative o(n) solution to the pnp problem. In: IEEE International Conference on Computer Vision (ICCV) (2007) 1–8

A Snapshot Endoscopic Polarisation Imaging System

N.T. Clancy[1,2] and D.S. Elson[1,2]

[1]Hamlyn Centre for Robotic Surgery, Imperial College London, UK

[2]Department of Surgery and Cancer, Imperial College London, UK

n.clancy@imperial.ac.uk

INTRODUCTION

Polarisation of light has been proposed as a contrast mechanism for imaging the scattering properties of biological tissue. This includes depolarisation of light with depth and wavelength sensitivity of polarised light scattered by cells and nuclei. Changes in cellular density in *ex vivo* samples have been identified, distinguishing adenocarcinomas from healthy tissue [1]. Analysis of changes in linear polarisation has also been used to characterise dermal pigmented lesions *in vivo* [2] and identify structural changes in cervical tissue [3]. However, measurements require sequential acquisition of multiple images using different polarisation filters, which may take tens of milliseconds or more, depending on the number of polarisation states needed [3] leading to motion artefacts *in vivo*. For rigid endoscopy the analysing optics must be placed at the distal end of the instrument due to their complex polarisation properties [4]. Previous endoscopic implementations have used optical fibre probes inserted into flexible endoscopes scanned over the tissue [5] or highly specialised illumination optics, customised endoscopes and sequential imaging [6]. However, no fast rigid polarisation endoscope has yet been presented. In this paper, a modified da Vinci stereo endoscope is reported that allows simultaneous polarisation imaging of two orthogonal states using a conventional light source.

MATERIALS AND METHODS

A da Vinci endoscope (Intuitive Surgical, Inc., Sunnyvale, USA) has been adapted using a tip attachment to provide polarised white light illumination and detection through its stereo imaging channels. A schematic of the tip attachment is shown in Fig. 1.

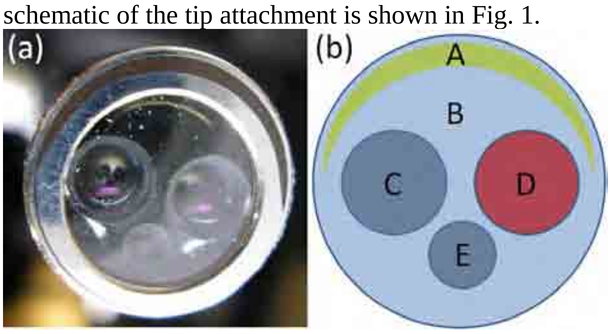

Fig. 1 (a) Tip of the da Vinci endoscope. (b) Polarisation endoscope tip attachment schematic. A: illumination fibre bundle, B: plate polariser, C: CO channel covered by plate polariser, D: CR channel covered by plate polariser and ¼ wave plate, E: unused imaging channel.

A 12.5 mm diameter plate linear polariser (FPC, CVI Melles Griot, UK) covers the entire end face of the endoscope including the illumination fibre bundle and both stereo channels. This filter is dichroic, with a high optical damage threshold (1 W cm^{-2} for polarisation perpendicular to the plate's orientation and 5 W cm^{-2} for parallel)[1] as light emitted from the xenon source at the endoscope tip may be close to 1 W. A ¼ wave plate was secured to the plate polariser using a thin bead of silicone adhesive so that it covered one of the stereo imaging channels. This wave plate rotates linearly polarised light by 90° before it passes through the plate linear polariser. The result is that one stereo channel detects light parallel to its incident polarisation (CO) while the other detects the perpendicular component (CR). Colour cameras (DCU 223C, Thorlabs Ltd., UK) recorded images from both channels simultaneously.

The CR and CO images were used to create an orthogonal states contrast (OSC) image [7] by detecting the relative amounts of parallel and perpendicularly polarised light reflected from the sample:

$$OSC = \frac{CO - CR}{CO + CR} \quad \textbf{(1)}$$

Equation 1 provides a measure of how much of the reflected light has retained its initial polarisation. If a smooth, highly reflective surface is illuminated, the reflected light will retain its initial polarisation, pass through the CO channel and be completely blocked by the orthogonal CR channel resulting in a high OSC. However, if the sample causes the light to be multiply scattered before travelling back to the endoscope, the randomisation of its polarisation will mean less CO light is transmitted and more CR light, reducing the OSC.

Since colour cameras were used for data acquisition, it was possible to examine the variation of the OSC signal in different spectral bands using the red, green and blue colour planes.

Initial results from the system are presented here showing images of objects with varying optical properties including skin (normal and nevus) and metal. Raw colour and OSC images in each colour plane are shown and the resulting OSC values analysed.

RESULTS

Figure 2 shows polarisation images of a finger with a metal ring. The raw colour images show that the regular

---

[1] https://www.cvimellesgriot.com/Products/High-Contrast-Plate-Polarizers.aspx

reflection of light from the surface of the skin and from the surface of the metal are sharply defined in the CO image. Rejection of this light in the CR image shows a loss of definition in the surface features of the skin and a significantly reduced reflection from the metal ring.

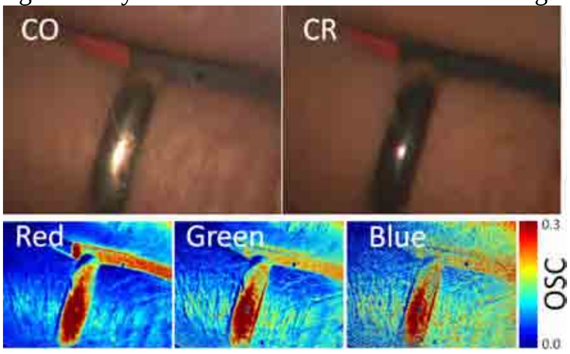

Fig. 2 Raw colour images of finger with metal ring in the CO and CR channels, along with OSC images calculated in the red, green and blue colour planes.

The OSC images in each of the three colour planes reveal the highest contrast on the metal ring, where the incident polarisation has been maintained, while the surrounding skin is much lower. Within the surrounding skin however, there appears to be a slight increase in OSC from the red to the blue colour planes along with an increase in noise.

A small lightly pigmented nevus in the skin is shown in Fig. 3, which is faintly visible in the raw colour images. Again, the sharp surface contours of the skin's surface are visible in the CO image but not the CR image.

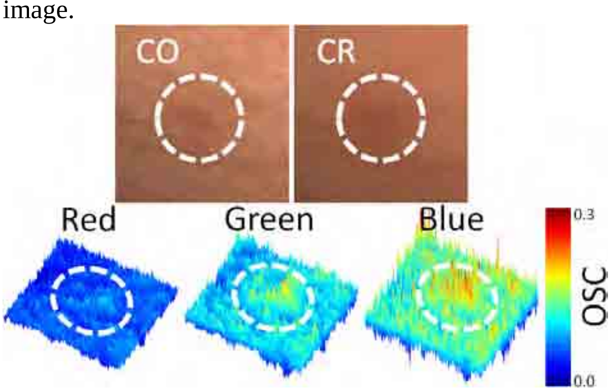

Fig. 3 Raw colour images of a small pigmented nevus in skin in the CO and CR channels. The OSC images show that the signal from the nevus becomes more visible in going from red to blue.

The OSC signal from the area containing the nevus increases from the red (where it is invisible) to the blue regions of the spectrum (visible but noisy).

DISCUSSION

A da Vinci compatible stereo endoscopic system capable of acquiring OSC images in three spectral bands simultaneously has been presented. Light regularly reflected from skin tissue and a metallic object maintains its initial polarisation resulting in a high OSC. However, light that penetrates deeper into the tissue becomes randomly polarised, producing a lower OSC.

The observed increase in OSC from the red colour plane to the blue is explained by the fact that red light penetrates tissue deeper than green or blue due to relatively low absorption by blood. Therefore, a red photon will travel farther than a blue one and have a correspondingly higher probability of being multiply scattered and randomly polarised. Conversely, any blue photons re-emerging from the skin will have undergone less scattering and are more likely to retain their initial polarisation, resulting in a higher contrast.

Wavelength-dependent effects are also evident in the lightly pigmented nevus as red light penetrates deeper into the region of high melanin content than green or blue, becoming depolarised and resulting in a low OSC of a similar value to the surrounding skin. Higher absorption of green and blue light ensures that only superficially penetrating photons are reflected from the nevus resulting in higher OSC.

Future work will focus on obtaining images of tissue during surgery and identifying superficial microvasculature structures that would be otherwise difficult to visualise using conventional endoscopic imaging. Calibration of the stereo cameras will also be carried out to automatically register the CR and CO images and correct for radial distortions. This would also allow quantification and correction of the disparity between each view due to their 5 mm separation, which may become significant at very close working distances.

ACKNOWLEDGEMENTS

We gratefully acknowledge the loan of the endoscope by Intuitive Surgical, Inc. Funding for this project was provided by ERC grant 242991, and an Intuitive Surgical Technology Research Grant.

REFERENCES

[1] Pierangelo A, Benali A, Antonelli M-R, *et al*. Ex-vivo characterization of human colon cancer by Mueller polarimetric imaging. Opt Express. 2011: 19(2): 1582-93.

[2] Kim J, John R, Wu PJ, *et al*. In vivo characterization of human pigmented lesions by degree of linear polarization image maps using incident linearly polarized light. Lasers Surg Med. 2010: 42(1): 76-85.

[3] Sviridov AP, Chernomordik V, Hassan M, *et al*. Polarization imaging system for colposcopy. OSA Biomedical Optics and 3D Imaging. Miami, FL, USA, 2012: BSu3A.34.

[4] Wood TC, Elson DS. Polarization response measurement and simulation of rigid endoscopes. Biomed Opt Express. 2010: 1(2): 463-70.

[5] Qiu L, Pleskow DK, Chuttani R, *et al*. Multispectral scanning during endoscopy guides biopsy of dysplasia in Barrett's esophagus. Nat Med. 2010: 16(5): 603-7.

[6] Qi J, Elson DS, Barriere C. Polarized multispectral imaging in a rigid endoscope based on polarized light scattering spectroscopy. OSA Biomedical Optics and 3D Imaging. Miami, FL, USA, 2012: BW4B.7.

[7] Fade J, Roche M, Alouini M. Computational polarization imaging from a single speckle image. Opt Lett. 2012: 37(3): 386-8.

Quantitative Tissue Measurements in Transoral Robotic Surgery

D. Stoyanov[1], P. Pratt[2], E. Edwards[2], G.-Z. Yang[2], A. Arora[3], A. Darzi[2,3], N. Tolley[3]

[1]Center for Medical Image Computing, University College London,[2]Hamlyn Centre for Robotic Surgery, Imperial College London, [3]St. Mary's Hospital, Imperial College Healthcare NHS Trust

danail.stoyanov@ucl.ac.uk

p.pratt, eddie.edwards, a.arora, a.darzi, g.z.yang, n.tolley@imperial.ac.uk

INTRODUCTION

Transoral robotic surgery (TORS) is a new treatment option for patients with obstructive sleep apnea (OSA). TORS overcomes the limitations of suboptimal access associated with the conventional transoral approach particularly when the tongue base (BOT) is involved. Preliminary results suggest higher cure rates compared with both conventional transoral and external surgical techniques yet with significantly less morbidity [1]. Flexible thulium laser fibres are typically used during TORS for bloodless tissue resection and vaporization to de-bulk tissue volume. However, it is not possible to measure the volume of tissue reduction *in vivo.* The surgeon uses subjective evaluation to qualitatively estimate the desired tissue volume which needs to be removed. The extent of tongue base reduction required can significantly impact on surgical success and patient morbidity including pain, dysphagia and aspiration.

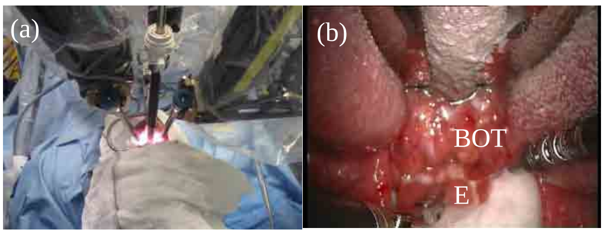

Fig. 1 (a) TORS set up in the operating room (b) the intra-operative view following insertion of a Boyle Davis mouth gag demostrating the epiglottis (E) and bulky tongue base (BOT) prior to performing tongue base reduction.

A means of computing the volume removed during surgery is therefore desirable and optical 3D reconstructions of the intra-operative stereoscopic laparoscope images represent a potential solution (Figure 1b). Optical computation of 3D tissue shape and motion using stereo-laparoscope images has been shown to be a practical approach towards making *in vivo* metrical measurements at the surgical site [2,3].Optical methods only rely on images from the laparoscope and do not require additional equipment to be introduced into the theatre or the patient. Such methods rely on the parallax between stereoscopic images to compute the distance between the camera and the tissue. For scenes where the variation in depth is large and there are multiple occlusions techniques that do not make explicit use of tissue surface models are more suitable. The robustness of parallax methods is dictated by the presence of prominent surface texture and, in practice, they are susceptible to view dependent highlights and structural discontinuities between the tissue and surgical instruments.

In this paper, we report a method for recovering 3D tissue shape at the surgical site at the start of ablation and at the end. These measurements are used to estimate the volume change caused by laser de-bulking at the BOT. Preliminary results on *in vivo* TORS video show that the approach is practical and can potentially be transferred to clincial practice.

MATERIALS AND METHODS

To compute the 3D surface shape of the region of interest at the BOT we assume that the stereo-laparoscope is calibrated such that the intrinsic and extrinsic camera parameters are known. For each incoming stereoscopic image pair at time t the images are transformed to remove lens distortions and to align the epipolar geometry by rectification using the known geometric calibration parameters of the cameras [4]. From the rectified images the disparity $d(x,y,t)$ at an image pixel in the left image $\mathbf{m}_t^l = [x,y]^T$ which provides the correspondence to the projection in the right image $\mathbf{m}_t^r = [x + d(x,y,t), y]^T$ is calculated by using an implementation of the algorithm in [2]. This is based on a growing scheme from an initial set of seed points that are matched across the stereoscopic view using any sparse matching algorithm. The search space is restricted to 1D by rectification and a symmetry constraint is added to ensure left-right disparity map consistency. Any feature point detection and feature matching strategy can be used to generate seed points for the growing method. We use the Shi and Tomasi features [5] as they can be computed efficiently and have been previously shown to work well for short-term tracking in MIS images with a stereoscopic Lucas-Kanade tracking method. More complex strategies can be adapted to work within the framework at the cost of additional computational demands. When the set of all computed matches stop growing the quasi dense reconstruction is complete.

By recovering the 3D shape of the tissue surface at the BOT before de-bulking, during and after the laser has been used, we can compute the change in shape and hence the volume of tissue removed. However, it is

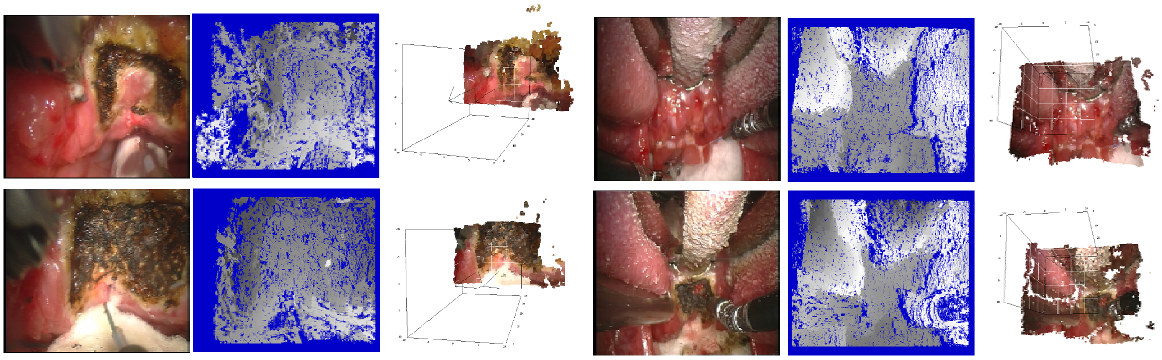

Fig. 2 Two examples of 3D reconstruction of the surgical site for measurement of the ablated volume during BOT reduction. The top row shows images at the start of the laser ablation and the bottom row shows images and at the end of the operation. Exemplar views of the surgical site are shown along with the corresponding disparity map and a 3D rendering of the recovered surface. Note the difference between the position of the scope at the start and end of each procedure as well as the variability across procedures where the working volume can be up to three times larger as shown in the images on the right.

common for the camera position and orientation to change during the procedure in order to optimise the surgical field-of-view. Computing this change in camera pose is required in order to register the recovered tissue shape for comparison. This can be achieved using techniques such as SLAM[6] or Structure-from-Motion (SfM) but the problem is ill posed as the surgical site is not rigid [7]. We therefore use a manual technique for this pilot study where the alignment is performedby the user with the laparoscopic images as shown in Figure 2. We assume the tissue surface is frontoparallel to the orientation of the camera. The surface comparison is then done on the 2D aligned disparity images.

RESULTS

In order to achieve real-time performance, the proposed reconstruction method was implemented using C++ and currently can operate at approximately 10 frames per second. However, with further optimization more computationally efficient performance is feasible especially when using hierarchical solutions with image pyramids and multithreading. Manual registration of the 2D images for calculating the surface difference volume is currently performed offline but an interface can easily be implemented for the operating room while we strive towards an automated solution.

Example results of surface reconstructions before and after ablation are shown in Figure 2 for two TORS cases. We calculated the volume of removed tissue in for case one to be approximately 412mm^{3}and for case two 273mm^3. These measurements are difficult to validate as there is no ground truth available for *in vivo* data. It is likely that the error due to the assumption of a fronto-parallel scene and due to tissue deformation both influence the calculation. Nevertheless these initial results indicate that with the proposed method we can make metrical measurements of the change in tissue volume due tovaporization of the BOT using ablation. Additionally, we are also able to measure the surface area of the ablation site, which in the case shown in the left of Figure 2 was 210 mm^2 and for the one shown on the right 140 mm^2.

It is easy to observe that there is a large variation in the viewing orientation of the surgical site in the two cases. The reconstruction in one case is of a surface located approximately 50mm from the camera which is an appropriate set up for optical reconstruction. In the second case, however, the surface of interest is over 150mm away from the camera and in this case the 5mm stereo baseline of the surgical scope imposes inherent limitations to reconstruction accuracy. In addition, it is important to note the variation in viewing orientation between the start of tissue reduction and the final scene.

DISCUSSION

In this study, we propose a method for computing the volume of tissue removed using laser ablation during TORS. The method is based on computational stereo using the stereoscopic laparascope images to compute metrical 3D measurements at the surgical site. Preliminary results indicate that the proposed method is promising but further work is required to enhance its robustments and to allow for automatic camera adjustment between the start of the procedure and the final ablation. The results of this study provide a platform for ongoing research which includes computationally optimising themethod using GPU hardware to enable us to providereal-time feedback for the surgeon *in vivo*.

REFERENCES

[1] Arora A*et al*. “Clinical applications of Telerobotic ENT-Head and neck surgery”*Int J Surg*9: 277-84, 2011

[2] Stoyanov D *et al*. "Real-time Stereo Reconstruction in Robotic Assisted Minimally Invasive Surgery" in *MICCAI*, 275-282, 2010

[3] Röhl S *et al*. “Real-Time Surface Reconstruction from Stereo Endoscopic Images for Intraoperative Registration” in *SPIE Medical Imaging*, 2011

[4] R. Hartley and A. Zisserman, Multiple View Geometry in Computer Vision: Cambridge Press, 2000

[5] Shi J *et al*. "Good features to track" in *IEEE CVPR*, 593-600, 1994

[6] Mountney P *et al*. “Motion Compensated SLAM for Image Guided Surgery“ in *MICCAI*, 496-504, 2011

[7] Collins T*et al*. “Towards Live Monocular 3D Laparoscopy using Shading and Specularity Information“ in *IPCAI*, 2012

Author Index

A

Abi-Nahed, J. 91
Acharya, A. 59
Ahn, J. 65
Akhtar, K. 12
Al-Ansari, A. 91
Al-Haddad, M. 91
Alizai, N. 11
Allen, P. 29
Althoefer, K. 52, 79, 81, 85
Ando, T. 42
Anor, T. 89
Arora, A. 21, 54, 59, 65, 107
Arujuna, A. 19
Ataollahi, A. 81
Atkins, R. 40
Awad, Z. 54, 65

B

Bajo, A. 29, 33
Bark, K. 50
Bayona, S. 12
Bello, F. 12
Bergeles, C. 83
Bicknell, C. 38, 93
Billia, M. 35
Boggi, U. 55
Bonnema, G.M. 25
Bowyer, S. 87
Broeders, I.A.M.J. 25
Budge, J. 54
Burgner, J. 77
Burns, A. 73
Butler, E.J. 3, 89

C

Cappelli, C. 55
Carbone, M. 55
Challacombe, B. 35, 85
Chauhan, S. 14, 61
Chawarski, S. 89
Chen, R. 3
Cheng, L. 23
Choset, H. 2
Chu, M.W.A. 46
Clancy, N.T. 105
Clark, J. 36
Cleary, K. 71, 73
Cobb, J. 12
Codd, P. 89
Coelho, R.F. 14, 61
Cohen, A. 3
Cohen, D.C. 63
Correa, J. 69
Currie, M.E. 46

D

Darzi, A. 21, 36, 54, 59, 63, 67, 107
Dasgupta, P. 35, 85
Davenport, K. 71
De Lio, N. 55
Deguet, A 44
Dehghani, A. 75
Del Nido, P. 3
Di Marco, A. 36
Dodds, A. 12
Dogramadzi, S. 40
Duchowski, A.T. 99
Dumon, K.R. 50
Dupont , P. 3, 15, 83, 89

E

Eddib, A. 97
Edwards, P. 21, 63, 107
El-Ghazaly, T. 91
Elhawary, H. 101
Elson, D.S. 105
Emery, R. 12

F

Farhat, A. 91
Ferrari, V. 55
Feussner, H.D. 36
Folk, C. 3
Fowler, D. 29
Friedman, D. 23

G

Gangloff, J. 17
Garimella, S. 97
Gary, K. 71

Gattas, N. 11, 57
Giannarou, S. 103
Giedelman, C. 14, 61
Gilbert, H.B. 77
Gillardin, J.P. 31
Gillen, S. 36
Glozman, D. 23
Goldie, J. 73
Gomez, E.D. 50
Gosline, A.H. 3, 89
Gupte, C. 12

H

Hammond-Oakley, R. 89
Hannaford, B. 23, 95
Hassaan, A. 54
Herrell, S.D. 33
Hinitt, A. 40
Hirose, S. 1
Hohenberg, K. 87
Housden, J. 19
House, D.H. 99

I

Ikeuchi, M. 27
Ikuta, K. 27
Iseki, H. 42

J

James, D.R.C. 36
Jayne, D. 75
Johns, E. 69
Jun, S.-K. 97

K

Karim, R. 19
Khemani, S. 59
Khoubehi, B. 63
Kiaii, B. 46
King, H.H. 23
Ko, Y.H. 14
Kobayashi, E. 42
Koike, J. 42
Kojcev, R. 71
Kooiman, G. 35
Kosari, S.N. 23
Kotecha, B. 54, 59
Kotecha, J. 59
Kowalewski, T.M. 95
Krovi, V. 97
Krupa, A. 15, 17
Kuchenbecker, K.J. 50
Kwok, K.-W. 38

L

LaBrecque, B. 73
Lee, D.I. 50
Lee, L.-S. 9
Lee, S.-L. 38, 93
Leff, D.R. 67
Lendvay, T.S. 95
LeRoy, K. 73
Li, J. 85
Liao, H. 42
Liu, H. 79, 85
Liu, J. 69
Liu, W.P. 44
Lock, J. 3, 89
Luo, H. 71, 73
Luzzato, V. 65

M

Ma, J. 23
Ma, Y.-L. 19, 81
Madsen, J.R. 89
Maes, H. 31
Martin, T. 48
Maruyama, T. 42
Mayer, E.K. 63
McKeague, S. 69
McMahan, W. 50
Mizumura, K. 42
Montellano López, A. 75
Moreira, P. 17
Mosca, F. 55
Muragaki, Y. 42
Murayama, K.M. 50

N

Nadeau, C. 15, 17
Najmaldin, A. 11, 57
Narayanan, M.S. 97
Neal, D. 9
Neville, A. 75

O

O'Brien, T.S. 35
Oldfield, M. 48, 65
Oliver, C. 35
O'Neill, M. 19
Oonk, S. 71
Orihuela-Espina, F. 67
Ostovari, F. 65

P

Palmer, K. 14, 61
Patel, A. 35
Patel, R. 46
Patel, V. 5, 14, 61
Payne, C. 93
Pelfrey, B. 99
Pereira, A. 87
Perrone, V. 55
Peters, C.A. 73
Peters, T. 46
Pickens, R.B. 33
Poignet, P. 17
Popovic, A. 101
Pratt, P. 21, 63, 107

Q

Qin, L. 83

R

Raabe, D. 40
Rafii-Tari, H. 93
Ramachandran, B. 101
Rayman, R. 46
Razavi, R. 19, 81
Reaugamornrat, S. 44
Reiter, A. 29
Remington. A.C. 50
Ren, H. 15
Rhode, K. 19, 81
Richardson, R. 75
Richmon, J. 44
Riga, C. 38, 93
Rinaldi, C.A. 19
Rivera, C. 50
Roan, P. 23
Rodriguez y Baena, F. 48, 65, 87
Rosen, J. 23
Roshan, R. 75
Ruiter, J.G. 25
Russell, P.T. 77

S

Sakuma, I. 42
Samavedi, S. 14, 61
Sargeant, R. 79
Satava, R. 7
Schaeffter, T. 19, 81
Schatloff, O. 14, 61
Schmitz, G. 3
Schwingshackl, C.W. 48
Sellors, J. 11
Seneviratne, L.D. 52, 81, 85
Shah, N. 9
Shaw, G. 9
Shetty, K. 67
Shier, D. 12
Siewerdsen, J.H. 44
Signori, S. 55
Simaan, N. 29, 33
Singhal, P. 97
Sivaraman, A. 14, 61
Skinner, A. 87
Smith, C. 11
Sobhani, M. 40
Sodergren, M. 36
Sorger, J.M. 44
Sridhar, A.N. 63
Sriskandarajah, K. 36
Stoyanov, D. 107
Swaney, P.J. 77

T

Talasaz, A. 46
Taylor, R.H. 44, 101
Tenzer, Y. 87
Thienphrapa, P. 101
Tolley, N. 21, 54, 59, 65, 107
Trejos, A.L. 46
Turkiyyah, G. 91

V

Vale, J. 63
van der Voort, M.C. 25
Van Slycke, S. 31
Van Wyk, C. 11
Vartholomeos, P. 83
Vasilyev, N. 3

Veeramani, A. 3
Vermeersch, H. 31
Vicente, A. 69

W

Wang, R. 99
Wanninayake, I.B. 52
Weaver, K.D. 77
Webster, R.J. 77
White, A. 57
White, L.W. 95
Whiteley, S. 11, 57
Williams, N.N. 50
Wilson, E. 71, 73
Wong, C. 69
Wu, M. 3

Y

Yang, G.-Z. 21, 36, 38, 63, 67, 69, 93, 103, 107
Yasui, M. 27
Younes, G. 91

Z

Zemiti, N. 17
Zhang, Z. 103
Zirjakova, J. 85